DOCTORAL SCHOOL
UNIVERSITÀ *MEDITERRANEA* DI REGGIO CALABRIA

DIPARTIMENTO DI INGEGNERIA DELL'INFORMAZIONE, DELLE INFRASTRUTTURE E DELL'ENERGIA SOSTENIBILE (DIIES)

PHD IN
INFORMATION ENGINEERING

S.S.D. ING-INF/01
S.S.D. ING-ICAR/04
XXXI CICLO

STRUCTURAL HEALTH MONITORING OF STRUCTURES AND INFRASTRUCTURES THROUGH ACOUSTIC SIGNATURE ANALYSIS

CANDIDATE
Rosario FEDELE

ADVISORS
Prof. Filippo G. PRATICÒ
Prof. Riccardo CAROTENUTO

COORDINATOR
Prof. Tommaso ISERNIA

REGGIO CALABRIA, FEBRUARY 2019

Finito di stampare nel mese di **febbraio 2019**

Edizione 

Quaderno N. 40
Collana *Quaderni del Dottorato di Ricerca in Ingegneria dell'Informazione*
Curatore *Prof. Claudio De Capua*

ISBN 978-88-99352-30-1

Università degli Studi *Mediterranea* di Reggio Calabria
Salita Melissari, Feo di Vito, Reggio Calabria

ROSARIO FEDELE

STRUCTURAL HEALTH MONITORING OF STRUCTURES AND INFRASTRUCTURES THROUGH ACOUSTIC SIGNATURE ANALYSIS

The Teaching Staff of the PhD course in
INFORMATION ENGINEERING
consists of:

Tommaso ISERNIA (Coordinator)
Pierluigi ANTONUCCI
Giovanni ANGIULLI
Giuseppe ARANITI
Francesco BUCCAFURRI
Rosario CARBONE
Riccardo CAROTENUTO
Salvatore COCO
Maria Antonia COTRONEI
Claudio DE CAPUA
Francesco DELLA CORTE
Aimè LAY EKUAKILLE
Pasquale G. F. FILIANOTI
Patrizia FRONTERA
Sofia GIUFFRÈ
Antonio IERA
Gianluca LAX
Giacomo MESSINA
Antonella MOLINARI
Andrea F. MORABITO
Rosario MORELLO
Fortunato PEZZIMENTI
Sandro RAO
Domenico ROSACI
Giuseppe RUGGERI
Maria Teresa RUSSO
Valerio SCORDAMAGLIA
Domenico URSINO
And also:
Antoine BERTHET
Dominique DALLET
Lubomir DOBOS
Lorenzo CROCCO
Ivo RENDINA
Groza VOICU

Abstract

Vehicular traffic load is one of the main causes that lead to the road pavements failure, i.e. the worsening of the road pavement's performances that are mainly caused by internal (concealed) cracks. These cracks are generated in the bottom layers of the road pavements and propagate toward the upper layer leading to the failure of the road pavements. Because of their location, this type of damage is difficult to be detected. Future smart cities need smart infrastructures and Intelligent Transportation Systems (ITS) able to provide high levels of performance and comfort, and to share information with their users in a sustainable and an efficient way. Unfortunately, despite the current high number of solutions designed for the structural health monitoring, there is a lack in implementation of these solutions in real contexts or in installation on road infrastructures. Exceptionally, some solutions are able to: i) monitor the structural conditions of the internal layers of the road pavements; ii) detect any variations over time of the road conditions due to the occurrence or the propagation of internal cracks; iii) share information with the appropriate authorities. In fact, the authorities that are responsible for the management of road pavements need more sustainable, efficient, and reliable methods and technologies to improve the current management process. In particular, Pavement Management Systems (PMSs) are currently used to carry out failure-based maintenance, by mean of destructive tests and measurements that not represent the real structural conditions of the road infrastructures. Such approach has by now become unsustainable and unreliable and an improvement is needed. For these reasons, the objectives of this thesis are: i) to design and set up a new non-destructive test (NDT)-based method for the structural health monitoring (SHM) of road pavement based on the concept of vibro-acoustic signature; ii) to design an electronic system that is able to apply the new NDT-SHM method, based on the principles of simplicity, efficiency, and sustainability; iii) to estimate the effect of the proposed solutions on the current road infrastructure management process.

A thorough literature review, simulations, and several in-lab and on-site experimental investigations were used to design and set up the method and the system proposed in this thesis. The proposed method is innovative because of the fact it considers the road pavement as a filter for the vibration and the sound that propagate from a mechanical source to a specially designed receiver. The microphone-based receiver is able to detect the acoustic response of a road pavement to a mechanical load (e.g., a vehicle pass-by), which is therefore considered the vibro-acoustic signature of the monitored pavement. It is expected that any variation of the structural conditions of the filter will lead to a detectable variation of the road vibro-acoustic signature. Specific algorithms were designed to detect and monitor road signature variations using Fourier Transform, Wavelet Transform, and Hierarchical Clustering.

Results show that the proposed NDT-SHM method allows detecting and monitoring the presence of cracks (internal and external) into the road pavements. Meaningful features can be extracted from road pavement's acoustic signatures by using Fourier and Wavelet Transforms. Algorithms based on hierarchical clustering recognize, from the extracted features specific variations of the signals transmitted (e.g., by using the wavelet coefficient's energy as feature), or the worsening of the transmission capability of the transmission medium (e.g., by using the Shannon's entropy of the wavelet coefficients as feature).

The proposed method has been implemented in a prototype of Wireless Sensor Network (WSN) system. It consists of several renewable energy-powered, wireless, low-consuming sensor units (modular system), which are able to detect in real-time both the vibro-acoustic signatures of the monitored structures and the significant environmental conditions (e.g., the temperature of the propagation medium that affects the signal propagation).

The proposed method and system can improve the current road infrastructure management process (PMSs), because of the fact they switch from the failure-based to the predictive-based maintenance paradigm using innovative smart, sustainable, efficient, reliable, and properly designed technologies.

Summary

List of Figures

List of Tables

1
Introduction

Vehicular traffic load is one of the main causes that lead to the road pavements failure, i.e. the worsening of the road pavement's performances that are mainly caused by internal (concealed) cracks. These cracks are generated, by the traffic load, in the bottom layers of the road pavements and propagate toward the upper layer leading to the road pavement failure. Because of their location, this type of damage is difficult to be detected. Furthermore, the future smart cities will need smart infrastructures, i.e. assets that are able to provide high performances, information sharing, and high level of comfort in a sustainable and efficient way. This chapter aims at providing an overview of the problem to be faced, the objectives of the thesis, and the main tasks that were identified to face the problem by designing a suitable solution.

1.1. Problem statement

The main problem faced in this thesis refers to the failures of the road pavements. In more detail, in this section are reported the main causes of failure (e.g., traffic load, environmental conditions, boundary condition, manufacturing conditions), the effects of the above-mentioned causes (generation of several types of distresses, and their propagation/expansion), and the current solutions that were proposed and are commonly used to face causes and effects (e.g., Pavement Management System based on different solutions such as methods, devices, systems, etc.).

Road pavements are multi-layer structures that may consist (from the top to the bottom) of a top layer (usually called wearing course layer), a base, a subbase, and a subgrade. The thickness and the number of layers depend on the type of road pavement (e.g., the highway usually include all the above mentioned layers). Road pavements belong to the macro-category of the flexible pavements and usually consist in asphalt concrete.

A flexible pavement is a pavement with asphalt concrete (AC) layers on the top (Solanki and Zaman 2017) that responds to the vertical loads by distributing the pressure over the volume of subbase near to the loaded area (cf. Fig. 1.1, left). This characteristic makes this type of pavement different from the semi-rigid and rigid pavements. In fact, the semi-rigid ones (which consist of a chemically stabilized layer on the subbase, e.g., using pozzolanic) spread the vertical pressure in the subgrade in a more diffused way than the flexible ones. While, the rigid ones (which consist of a top layer made of cement concrete material) spread the vertical pressure over all the lower layers (cf. Fig. 1.1, right).

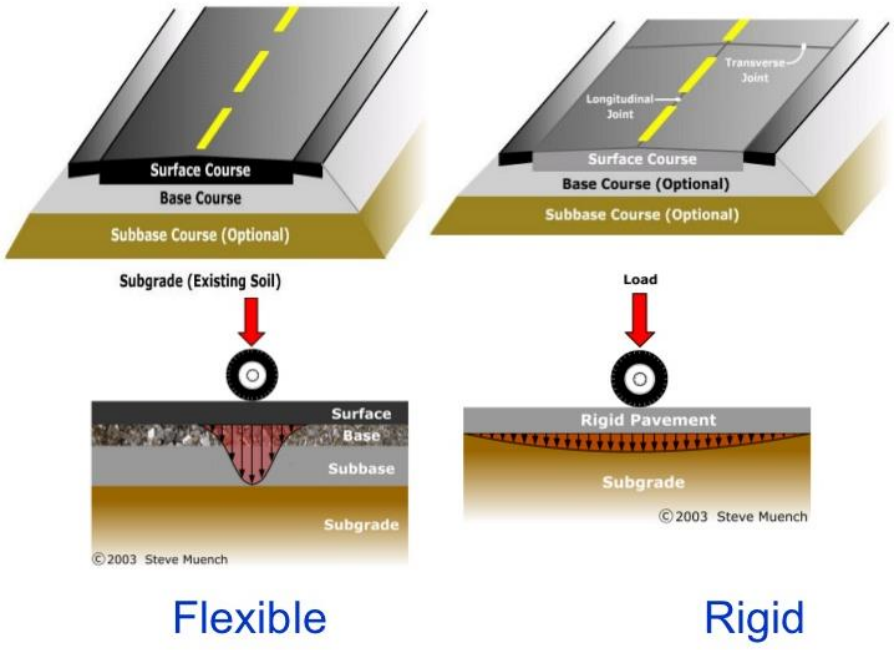

Fig. 1.1 Representation of flexible and rigid road pavements and their responses to a vertical load (Muench, Mahoney, and Pierce 2003).

The "flexibility" of the road pavement is due to the asphalt concrete (AC). AC is composite material with viscoelastic behavior (Soenen, Redelius, and De La Roche 2003), which consists of mineral aggregate and asphalt binder (Harcourt 2011). The most used AC is the Hot Mix Asphalt Concrete (HMA; warm and cold process are also available). To build the HMA, aggregates and bitumen are heated (in order to increase the viscosity of the asphalt binder and to remove the moisture from the aggregate), bonded together, laid in

layers, and compacted at about 150°C. Aggregates are the skeleton of the AC and are derived from crushed natural rocks and natural deposits. They can be classified as a function of size (e.g., stone, sand, and gravel), or of the geological origin (i.e., igneous, sedimentary, and metamorphic)(Papagiannakis and Masad 2012). Asphalt binder (or bitumen) is a binder that consists of a mixture of hydrocarbons and a small percentage of heteroatoms (i.e., nitrogen, sulfur, oxygen, and metals such as vanadium, nickel, iron, etc.)(Papagiannakis and Masad 2012). It can be classified based on its rheological and mechanical properties that relate to the field performances and that are particularly influenced by temperature (temperature susceptibility), and time (aging)(Papagiannakis and Masad 2012).

It is possible to identify two main AC sub-categories, as a function of the Air Void (AV) content of the mixture, i.e. the dense-graded surface course (e.g., the Dense Graded Friction Course, DGFC, with AV < 12%, usually 4-8%) and the open-graded surface course (e.g., Porous European Mixes, PEM, or Open Graded Friction Course, OGFC, which have AV > 12%, usually 15-25%)(Huang 2003; Papagiannakis and Masad 2012). The main differences refer to three abilities of the open-graded, i.e.: i) drainability (drain the rainwater); ii) sound-absorbing (absorb the traffic noise in specific frequency band); iii) opaqueness (i.e., they are less reflective than the dense-graded).

The main causes of failure of the flexible road pavements (Gedafa 2007; Moghaddam, Karim, and Abdelaziz 2011; Pavementinteractive.org 2018) can be attributed at:

1) inadequate mix design (e.g., excessive asphalt binder, or poor quality asphalt binder or aggregates);
2) inadequate structural design (e.g., unsuitable road geometry, underestimated traffic load, insufficient layer thickness, poor joint construction or location);
3) inadequate construction quality (e.g., poor compaction, poor patching after utility cuts);
4) the increase in the traffic volume or of the number of vehicles with high axle loads;
5) repeated traffic loading (fatigue);

6) asphalt binder aging (i.e., oxidation of the binder resulting in a stiffer, more viscous material that is not able to hold the superficial aggregates that are pulled away by traffic);
7) temperature (e.g., temperature cycling, freeze-thaw cycle, low temperatures);
8) moisture (e.g., excessive moisture in the subgrade);
9) decreasing in pavement load supporting characteristics (i.e., loss in base, subbase or subgrade);
10) reflective crack from an underlying layer (e.g., due to bottom-up cracking propagation, or presence of rigid objects);
11) traffic start and stops;
12) mechanical dislodging by uncommon traffic (e.g., studded tires, snowplow blades, or tracked vehicles).
13) vibrations induced by the traffic, work zones, or natural events (e.g., earthquakes);
14) maintenance policy pursued (e.g., failure- or condition-based).

Based on the main causes listed above, it is possible to state that: 1) they relate to intrinsic (e.g., inadequate design) or extrinsic (i.e., due to the interaction or the road pavement with the traffic or the environment); 2) the road pavement failures can be classified in surface and concealed; 3) sometime surface failures are generated by concealed failures, or problems.
Concealed failures are, by definition, difficult to be identified and localized. Hence, it seems clear that they need greater attention than the surface ones, and should be promptly detected, carefully classified, and monitored.
The effects of the above-mentioned causes refer to the generation of several types of distresses, and to their propagation/expansion over space and time.
Fig. 1.2 provides a summary of the main distresses that affect the road pavements (Pavementinteractive.org 2018), especially along the wheel paths (i.e., the areas of the road pavement where the vehicle load is more concentrated and intensive).

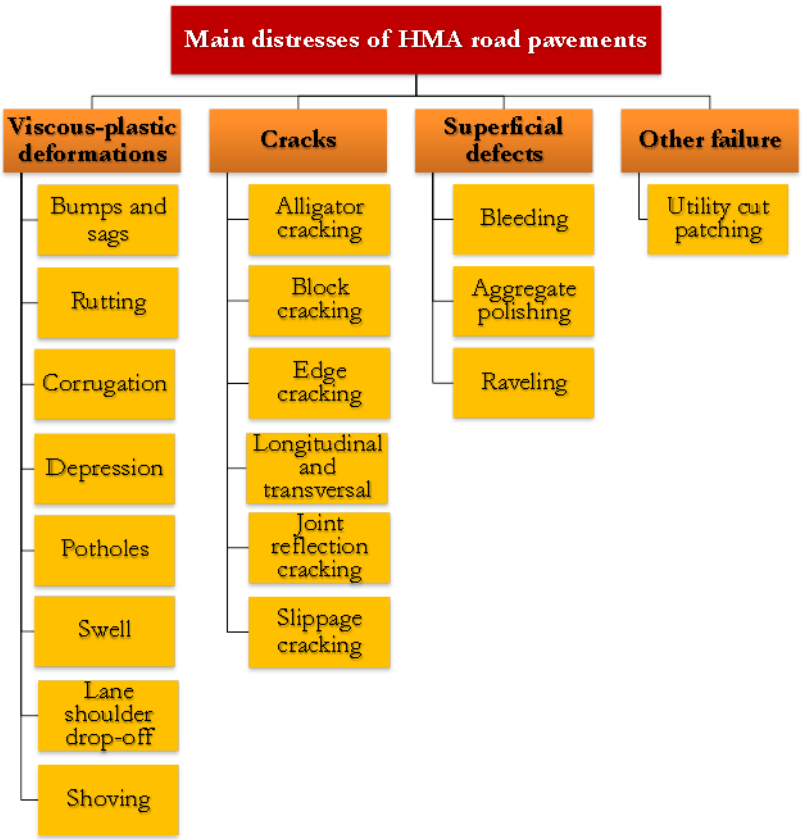

Fig. 1.2 Main distresses that affect the road pavements.

The figure below shows some examples of the distress reported in the previous figure.

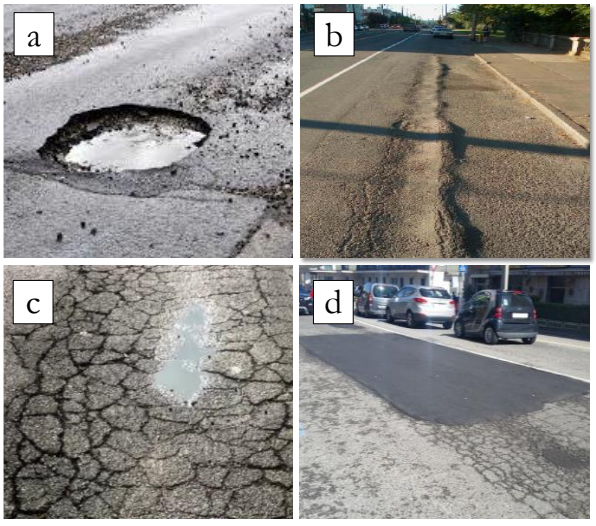

Fig. 1.3 Examples of road pavement distresses: a) pothole; b) rutting; c) alligator or crocodile cracking; d) utility cut patching.

The propagation or expansion of the distresses reported above is caused by different phenomena (e.g., top-down and bottom-up propagation, or moisture infiltration into the base and subgrade, etc.)

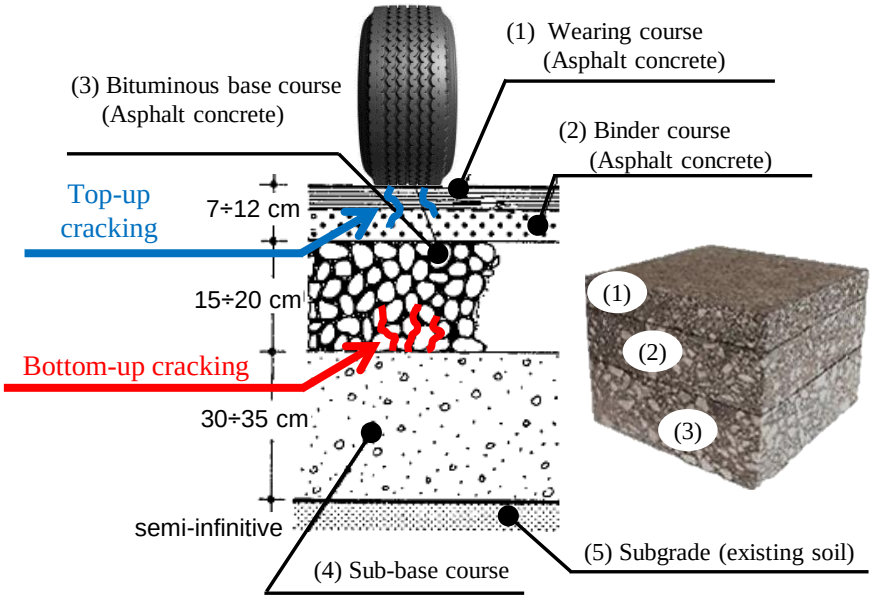

Fig. 1.4 Representation of two causes of crack propagation, i.e., top-down and bottom-up.

In order to reduce the above-mentioned causes and mitigate the related effects, several solutions were proposed and are commonly used. Furthermore, in order to satisfy current and future requirements of the Smart Cities (e.g., sustainability, connectivity, efficiency, etc.; cf. (Pop and Proştean 2018)), the widespread field of the Information and Communication Technology (ICT), and the emerging field of the Internet of Things (IoT), are merging aiming at proposing more and more innovative solutions. These solutions were identified during the literature review supporting the current thesis, and are reported in the next chapter. Among the above-mentioned solutions, the creation of Intelligent Transportation System (ITS) is strongly encouraged, even at high organization levels. In fact, the Directive of the European Union 2010/40/EU (European Union 2010) was issued in order to provide an official framework for the deployment of ITS, and, also, to obtain more connected transport modes. The above-mentioned Directive defines the ITSs as "…*advanced applications, which without embodying intelligence as such, aim to*

provide innovative services relating to different modes of transport and traffic management, and enable various users to be better informed and make safer, more coordinated and 'smarter' use of transport networks." ITSs are considered as the official answer to the increase in road transport volume in the European Union, which was attributed to the growth of economy- and mobility-related problems. In more detail, to face problems such as: i) the increasing congestion of road infrastructures; ii) the rising energy consumption; iii) the emerging environmental and social problems. Furthermore, the ITSs are needed to all the involved stakeholders (authorities and agencies that are responsible for the assets' management, users, service providers, etc. (European Union 2010)), which can use this solution to: 1) gather and collect both road data (e.g., infrastructure characteristics), and traffic/travel data (e.g., traffic characteristics); 2) optimize the use of the collected data through processing that aims at extracting important information from them; 3) use the information extracted to improving environmental performance, and the efficiency (in terms of energy, safety, and security) of current road infrastructures, ensuring the functioning of the internal market as well as increased levels of competitiveness and employment (European Union 2010).

Despite the current high number of solutions proposed in the last decades (analyzed in Chapter 2), and the requirements of the authorities, there is a lack in implementation of these solutions in real contexts. Exceptionally, some solutions are able to: i) monitor the structural conditions of the internal layers of the road pavements; ii) detect any variations over time of the road conditions due to the occurrence or the propagation of concealed distresses; iii) share information with the appropriate authorities.

Consequently, the main objective of this thesis is the design and set up a new solution that is able to solve the problems mentioned above (i.e., detect and recognize the concealed distress in flexible road pavements) and, at the same time, satisfy the requirements of the authorities (i.e., obtain more efficient, sustainable, and user-connected transportation infrastructures).

The following section (section 1.2) provides all the objectives of this thesis, while the section 1.3 describes the tasks that were designed and carried out to achieve the objectives cited above.

1.2. Objectives

Based on the problem statement presented in the previous section, the objectives of the thesis are the following:

- Define the state of the art of the methods, techniques and devices used in the field of the Structural Health Monitoring (SHM) of civil engineer structures and infrastructures (focusing on those designed and used on road pavements, and including those based on data processing and data meaning).
- Design a new solution for the SHM of road pavements, specially designed for detecting and monitoring concealed failures.
- Set up the solution cited above by means the definition of a new, efficient, and sustainable way to gather data (signals) from road pavements.
- Set up the proposed solution through experimental investigations aimed at gathering data from road pavements.
- Set up the proposed solution defining the best way to analyze the data gathered during the above-mentioned experimental investigations, and to extract information about the structural health status (presence/growth of concealed failures) from the data above (solution validation).
- Design a system that is able to apply the new proposed solution, based on the principles of simplicity, efficiency, and sustainability.
- Estimate the effect of the proposed solution on the current road infrastructure management process (e.g., on Pavement Management Systems, PMSs).

1.3. Tasks definition

The thesis is the description of the following tasks (see Fig. 1.5). In particular, the activities were carried out starting from a thorough literature review that was mainly focused on the current approaches that are used to

manage the civil engineering structures and infrastructures (e.g., the Pavement Management Systems, PMSs).

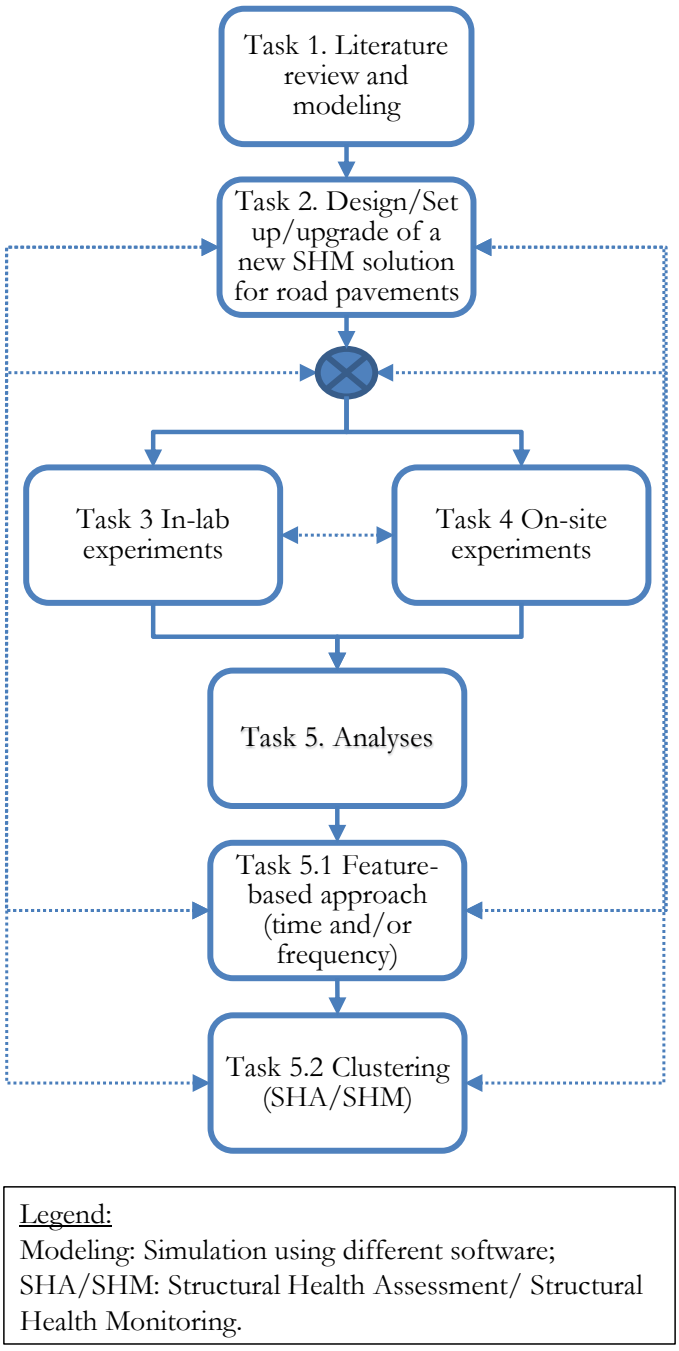

Fig. 1.5 Main tasks carried out in the thesis.

The literature review was flanked by simulations related to the interaction vehicles-pavement-cracks, which were carried out to better understand the phenomena behind the concealed failures. Based on the two activities

mentioned above, a new SHM solution was designed, set up, and upgraded using the results of several experimental investigations, which were carried out on road pavements (on-site experiments), and on dense-graded asphalt concrete samples (in-lab experiments) in different structural health statuses (SHSs). The data collected during the investigations were analyzed using a feature-based approach. Finally, hierarchical clustering-based algorithms were used to define a pattern between the data collected and the SHSs of the road pavements (i.e., to carry out the Structural Health Assessment, SHA, and the Structural Health Monitoring, SHM).

Note that, all the above-mentioned activities are described in detail in the following chapters.

2
Literature review

The objective of this Chapter is to provide an overview of the main results of the literature review that was carried out during the research activities. The literature review aimed at defining and analyzing the state-of-the-art of the solutions (e.g., methods, techniques, devices, systems, etc.) that are currently used to improve the sustainability and the efficiency of the road pavements during their service-life (from the design and construction, to the operations and replacement).

2.1. Topics definition

This Chapter of the thesis contains the results of the literature review that was carried out to support the research activities (defined in section 1.3). Fig. 2.1 provides an overview of the solutions that are currently adopted to improve the sustainability and efficiency of the road pavements, which can be associated to two different phases of this infrastructure, i.e. the Construction and the Operational (see Fig. 2.1, top). Several solutions can be associated to each phase. In particular, the solutions associated to the Construction phase are: i) the optimization of the construction process (e.g., acting on the mixing temperatures); ii) the use of innovative materials (e.g., wastes) in addition to the traditional ones (i.e., the aggregates and the asphalt binder; cf. section 1.1); iii) the improvement of the existing vehicles (e.g., electric vehicles); iv) design mixtures that include recycled or reused traditional construction materials (i.e., milled asphalt concrete); v) design roads that include intelligent solutions (e.g., using embedded sensors). While, the solutions related to the Operational phase are: a) the management of the traffic (e.g., aiming at reducing the travel times); b) the replacement of an old road with a new one that consists of materials that come from the old one; c) the transformation of the present roads in smart roads (i.e., Intelligent Transportation System, ITS).

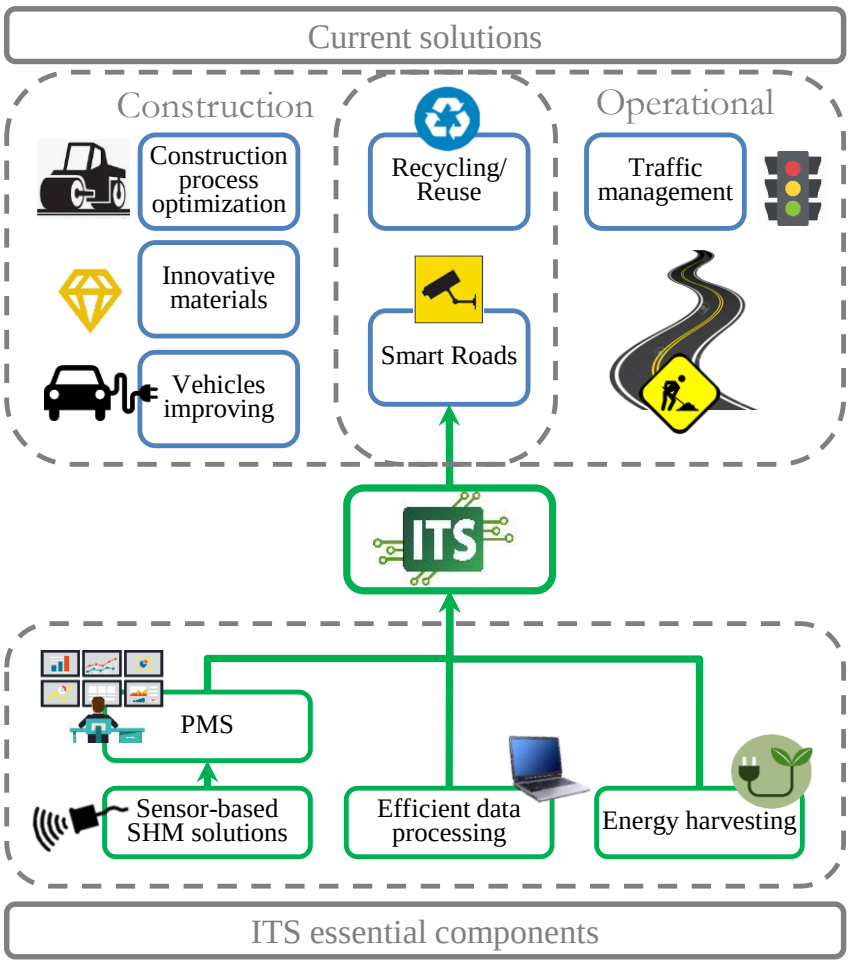

Fig. 2.1 Current solutions used to increase the sustainability and the efficiency of the road infrastructures during the construction and the operational phases.

Furthermore, Pavement Management Systems (PMSs), based on Structural Health Monitoring (SHM) solutions, are commonly adopted by the authorities as decision support in the road infrastructure management process. For these reasons, two of the following sections are related to PMS and SHM solutions. In addition, these last two topics are assumed in this thesis as one of the three essential components of an ideal ITS (see Fig. 2.1, bottom), which should include also efficient data processing method (e.g., Wavelet Transform-based) and technologies that are able to gather the energy required by the ITS using sustainable ways (e.g., energy harvesting technologies, EHTs). Hence, particular attention was paid to define the state-of-the-art of these last two topics.

2.2. Current solutions for sustainable and efficient roads[1]

The field of the transportation is gradually changing because of the new solutions offered by: i) automotive industries; ii) construction enterprises; iii) Internet of Things (IoT); iv) sensor-based structural health monitoring (SHM) systems; v) international regulations.

These continuous upgrading call for a careful analysis of the current situation and a proper tuning of the design and management of the transportation infrastructures. It should aim at finding a trade-off between the ever-growing request of innovation (smart cities), and the never-ending depletion of the available resources.

This section of the thesis illustrates several relevant examples of current solutions that are/should be implemented to improve the existing/future road infrastructures (i.e., to reduce the need of resources, such as energy, materials, money, time, and workers).

2.2.1. Construction process optimization

Recent studies show that it is possible to optimize the road construction process acting on three important phases of the Hot Mix Asphalt (HMA) production, i.e., aggregates drying, and bitumen/bituminous mixture heating (Peng et al. 2017). In particular, by using natural gas as fuel, energy savings (more than 60 MJ), carbon emission reduction (more than 30%), and costs reduction (more than 35%) can be achieved.

Warm and Cool Mix Asphalt were proposed as an alternative to HMA. They allow saving energy and reduce greenhouse gas (GHG) emissions (i.e., carbon footprint) because of lower temperatures, using alternative binders (e.g., emulsified bitumen or cement) and new technologies (Du et al. 2018; Raab, Camargo, and Partl 2017). Even though WMAs often show a good performance over time in terms of fatigue resistance (durability), their design must be improved in terms of rutting behavior (Raab et al. 2017).

[1] This section mainly refers to the papers 1.9 (see Scientific production).

2.2.2. Innovative materials

In the last years, studies have been carried out aiming at using waste materials as construction materials (i.e., Asphalt Concrete, AC). Road construction alternative materials have been proposed and analyzed in terms of Lifecycle Cost Analysis (LCA; (Balaguera et al. 2018). By-products (e.g., crumb rubber, plastics, blast furnace slag, fly ash, leachate, glass, concrete, wood ash) have been recently taken into account as alternative materials because of the restrictions on landfill disposal (Appiah, Berko-Boateng, and Tagbor 2017; Jamshidi et al. 2017; Poulikakos et al. 2017; F.G. Praticò et al. 2016; T. Wang et al. 2018). The effects of including these materials might have positive or negative consequences on road pavements and their lifetime, but there are unquestionable positive effects in terms of raw material needs/processing and carbon footprints. The success related to this solution is greatly influenced by the technical readiness level, the obstacles from legislation, and the involvement of several stakeholders (e.g., the waste management professional, or the scientific community) (Poulikakos et al. 2017). The improvement in oil refinery technology has had negative effects on bitumen-based binder quality (C. Wang et al. 2018; Yang and Suciptan 2016). For this reason, studies are investigating the possibility of creating and using bio-oil by-products (e.g., waste cooking oil) as a substitute for bitumen (bio-binders). Bio-binders may have higher recovery ability and fatigue performance than conventional petroleum-based binders, but this success strictly depends on their inner characteristics, which influence the heating and mixing processes (C. Wang et al. 2018; Yang and Suciptan 2016). A noteworthy effort was dedicated to include Crumb Rubber (CR) and fibers in AC mixtures. CR is used to increase the properties of the asphalt binder or as substitute for aggregates (wet and dry process, respectively; cf. (Hassan et al. 2014; Wulandari and Tjandra 2017) Finally, Fiber-Reinforced Asphalt Concrete (FRAC) were proposed to try to improve the mechanical properties of the AC (e.g., using randomly-included glass fibers, or geo-synthetic oriented materials), to obtain electrically conductive mixtures (e.g., using metallic fibers), and to increase the waste recycling (e.g., using plastic fibers)

(Abtahi, Sheikhzadeh, and Hejazi 2010; Vasudevan et al. 2012; H. Wang et al. 2016).

2.2.3. Vehicle optimization

Different approaches have been adopted by the automotive industry to design more sustainable and less consuming vehicles, for example: 1) based on fuel type and/or quality; 2) based on engines technology; 3) having lighter and aerodynamic vehicles; 4) using automated vehicles or self-driving cars (Moriarty and Wang 2017; Wenlong, Xiaokai, and Lu 2016; Wilberforce et al. 2017).

Electric vehicles will likely represent the future of the automobile industry because they seem to be environmentally friendly (zero GHG emission), to reduce operational costs compared to traditional vehicles (i.e., an electric vehicle costs 10 cents per mile less than a petrol powered vehicle; cf. (Wilberforce et al. 2017)). They need 1 kWh to travel for 4-8 miles and they have an energy efficiency of around 75% while the traditional ones use only the 15% of the total fuel energy (Wilberforce et al. 2017). Nonetheless, there are still problems related to their overall high costs (due for 1/3 to the cost of the electricity used to power the car; cf. (Wilberforce et al. 2017)), to their powertrain (i.e., type, size, charging protocol, battery size, timing, etc.), to the energy management approach used (i.e., battery size, or the vehicle velocity), and to the driving cycles (i.e., how the driver doses the speed), and to the current infrastructure performance (i.e., to service and maintain electric cars) (Grauers and Upendra 2016; Hu, Zou, and Yang 2016; Wilberforce et al. 2017; Zheng et al. 2015). Electric cars powered by fuel cells fed with hydrogen from clean renewable sources (e.g., wind or solar) represent a promising solution for the current problems related to the electric cars mentioned above (Wilberforce et al. 2017). Actually, their development and diffusion depend on high costs, low durability, and hydrogen storage problems (i.e., refueling infrastructure-related). Automated vehicles were proposed to optimize fuel consumption, but recent studies demonstrate that they lead to poor results in terms of energy use and GHG emissions (Moriarty and Wang 2017), and that they will probably arrive too late to make

an impact. Besides these drawbacks, there are also problems related to i) the safety of passengers, pedestrians, and cyclists; ii) cyber security (e.g., terrorism, or malicious hacking); iii) their dimensions because now they are perceived as mobile offices or entertainment centers; iv) marketability.

2.2.4. Traffic management improvement

Traffic management is often considered as a key solution to tackle congestion, to reduce travel times, to improve flows, to reduce emissions (and save energy), and to exploit the effective road capacity (Calvert et al. 2018). Nevertheless, if stochastic uncertainty and fluctuations related to the traffic flow (connected to human driving behavior) are not carefully considered on a case-by-case basis, the effectiveness of this solution may be reduced. Real time traffic management systems have been proposed in order to intelligently pilot the vehicles, discourage the formation of gridlock, and optimize power requirement of hybrid vehicles (e.g., fuel cell-based, or autonomous) (Saikar et al. 2017; Zheng et al. 2015).

2.2.5. Recycling and reuse of construction materials

The most common way to recycle road pavement materials is to reuse Reclaimed Asphalt Pavement (RAP) (Praticò et al. 2013). In a recent study (Chen and Wang 2018), to quantify energy consumption and GHG emissions of asphalt pavement containing RAP, a thorough analysis about raw materials acquisition, plant production, construction, maintenance, and pavement end-of-life was carried out. The authors concluded that the energy consumption strictly depends on RAP and moisture contents, blending efficiency, and performance levels. This study underlines the fact that this is an efficient and well-established solution to reduce consumption in transportation, but a proper design is needed in order to avoid a subsequent increase of the maintenance activities that lead to an increase of GHG emission and energy consumption.

2.2.6. Smart roads

Future cities must be able to improve the daily life of their citizens and, to achieve this goal, in the last years, the concepts of Intelligent Transportation System (ITS), and "smart city" emerged (Pop and Proştean 2018). These ideas have all the potentialities to succeed because they combine the world of Internet of Things (IoT) with the Information and Communication Technologies (ICTs). Despite its potential, this approach is very complex because it involves several sectors, stakeholders, authorities, services, and its implementation must take into account: i) innovative ways to share the information (e.g., mobile applications); ii) alternative transportation modes (e.g., bike or car sharing); iii) sustainable strategies (e.g., free electric charging stations for electric vehicles); iv) intelligent traffic lights systems or parking; v) adopting innovative and efficient Pavement Management Systems (PMSs). Smart street lighting entails traffic safety, visual comfort, and energy-savings at the same time (He et al. 2017; Qin et al. 2017; Yoomak and Ngaopitakkul 2018)t is important to note that, even if street lighting is governed by a huge number of parameters, new technologies (e.g., LED luminaries, or simulation software; cf. (Yoomak and Ngaopitakkul 2018)) can ensure good performance and high energy/economic savings. On the other hand, this solution introduces non-disruptive innovations to solve the problem of the energy consumption in transportation.

2.3. Pavement Management System (PMS)

The preservation of the infrastructure assets is commonly accomplished through the Pavement Management System (PMS) approach, which is likely the most widespread and cost-effective tool used by officials and practitioners (Scarpati and Guerra 2013). *"A Pavement Management System is a set of defined procedures for collecting, analyzing, maintaining, and reporting pavement data, to assist the decision makers in finding optimum strategies for maintaining pavements in serviceable condition over a given period of time for the least cost"* (Vitillo 2018). PMSs are used to gather information from the asset, to identify backlog work, to set goals, and schedule maintenance and rehabilitation (e.g., for 3-5 years) in order to

prioritize and limit the interventions, and saving time, energy, and money (as budget stretching and return on investment). Usually, a PMS consists of two main levels (see Fig. 2.2), i.e. the higher (network + project) and the lower (data processing). At the Network level (bird's eye view), decisions about the whole pavement network are taken (e.g., the budget; cf. (Vitillo 2018)). While, at the project level, different interventions can be locally carried out (e.g., preventive maintenance, resurfacing, etc.). The lower level includes data collection (i.e., several tools are used to derive road-related conditions, costs, traffic level, and intervention frequency), modeling and analysis (i.e., estimation and prediction of performances, serviceability, budgeting by means of, e.g., deterioration curves; cf. Fig. 2.3), and data management (i.e., reporting).

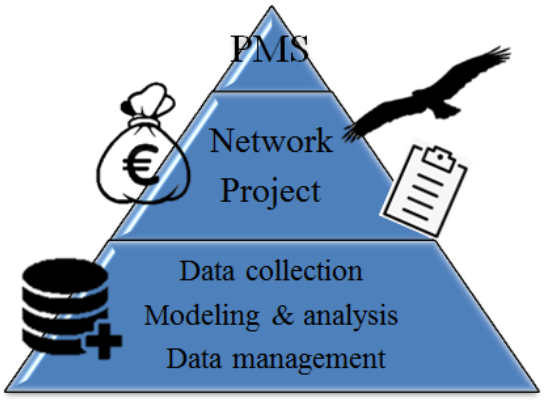

Fig. 2.2 Pavement Management System (PMS): main levels and tasks.

Usually, the approach "worst-first" is considered as the best way to fix a road pavement, but using a PMS is possible to clearly see that is less expensive to maintain pavement in decent condition than completely reconstruct it, when it is in bad conditions (e.g., reconstruct 1 mile of road corresponds to preserve or treat 8 miles; cf. (Scarpati and Guerra 2013)). In order to give an idea of the advantages provided by the adoption of a PMS, Tab. 2.1 and Fig. 2.3 are here included.

One of the main results of the PMS is the estimation, over time, of road pavement condition variation (see Fig. 2.3). Commonly, pavement conditions are expressed through deterioration curves, which show the variation over

time of indices such as the Present Serviceability Index (PSI), the Present Serviceability Rating (PSR), the Mean Panel Rating (MPR), the Pavement Condition Index (PCI), the Pavement Condition Rating (PCR), the Ride Number (RN), the Profile Index (PI), and the International Roughness Index (IRI) (Scarpati and Guerra 2013)(Morova et al. 2013).

Tab. 2.1 PMS economic advantages

Pavement condition	Cost/sy[1]	Reference
PCI=60% PCI=20%	1 $ 8-10 $	(Scarpati and Guerra 2013)
40%Road Lifetime (PCI≈100-80%) 70%Road Lifetime (PCI≈80-60%) 90%Road Lifetime (PCI≈60-20%) 100%Road Lifetime (PCI≈20-0%)	0.85 $ 4.25 $ 7.50 $ 16.75 $	(Smadi 2004)
Good (PCI≈80%) Poor/Fair (PCI≈50%) Very Poor (PCI<20%)[2]	7-9 $ 15-20 $ 50-55 $	(Hebel and Dorbit 2018)
PCI≈90% PCI≈30%	1 $ 6-10 $	(Lonbar, Nasrazadani, and Shafaghat 2015)
75%Road Lifetime (PCI≈60%) 83%Road Lifetime (PCI≈20%)	1 $ 4-5 $	(Technology 2013)
75%Road Lifetime (PCI≈60%) 88%Road Lifetime (PCI≈20%)	1 $ 6-14 $	(National Center for Pavement Preservation (NCPP) 2018)
Good-Excellent (PCI≈90%) Good (PCI≈80%) Fair (PCI≈60%) Very Poor(PCI<20%)[2]	1-2 $ 6-9 $ 10-14 $ 60 $	(Springfield Department of Public Work 2009)

Notes: 1. Cost of preventive maintenance *per* Square yard; 2. Costs referred to the road pavement reconstruction. 1square yard= 0.836127 square meter.

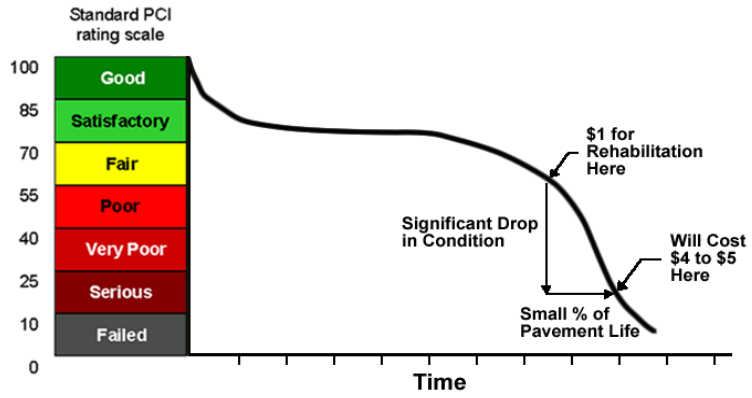

Fig. 2.3 Example of deterioration curve (Vanderhawk Consulting LLC 2011).

Pavement deterioration can be studied using the same approach used to carry out the machine fault monitoring, i.e. in terms of P-F interval. The P-F curves report the reduction of the functional capability of a system (y-axis) over time (x-axis; cf. (J. Moubray 1997)). The time interval between the point P and the point F indicates the exposure to stress between the instant at which a potential failure, P (i.e., a detectable symptom, a warning sign, a potential failure symptom) can be detected, and the time when a functional failure, F, occurs (see Fig. 2.4).

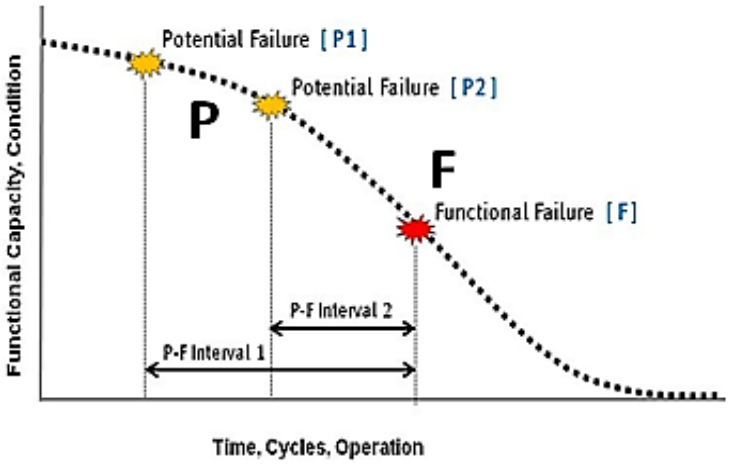

Fig. 2.4 Example of P-F curve (Asset Insights.net 2018).

Despite the advantages shown by the deterioration curves and the P-F curves, different replacement strategies (Asset Insights.net 2018) can be selected and assumed in the PMS. In more detail, the replacement can be carried out after the failure (failure replacement; cf. Fig. 2.5, left) or before that the failure occurs (preventive replacement; cf. Fig. 2.5, right). In the first case, the authorities (i.e., the owner of the asset) are conscious of the fact that the asset will be neglected until it will fail (run to failure; see point 1 in Fig. 2.5), or they simply react to a failure (unintended failure replacement; see point 2 in Fig. 2.5). In the second case, the replacement can be carried out at pre-defined intervals (time-based replacement; see point 3 in Fig. 2.5), or at a pre-defined asset age (age-based replacement; see point 4 in Fig. 2.5), or when the measured performances indicate that a pre-defined threshold is exceeded (condition-based replacement; see point 5 in Fig. 2.5).

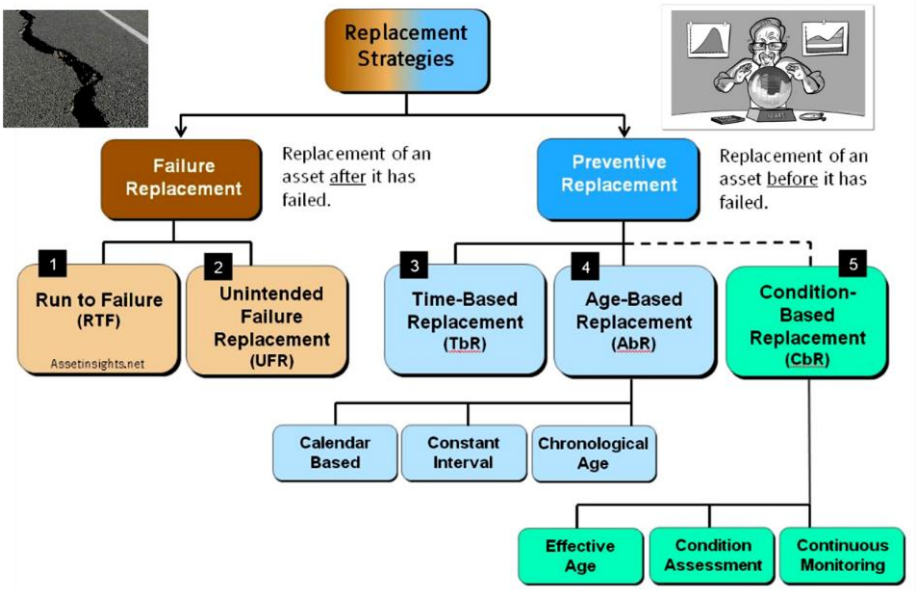

Fig. 2.5 Replacement strategies (Asset Insights.net 2018).

When a PMS plans to use the condition-based replacement (see point 5 in Fig. 2.5), three different tasks (cf. Fig. 2.5, bottom) can be selected: 1) estimate the effective asset age; 2) assess the asset conditions; 3) use the continuous monitoring. Regardless of the task chosen, different factors, such as material type, age, geometry, drainage, substructure conditions and construction history, basic geophysical segmentation, average daily traffic, functional class, and thickness should be taken into account (Scarpati and Guerra 2013). Hence, the asset conditions are estimated from the above-mentioned factors, and information about the asset practicability, availability, and safety (during normal and emergency situations) are derived. Finally, this information can be used by the authorities (public or private) that are deputed to the construction and maintenance of the asset, to improve the management process (e.g., defying the proper maintenance intervention), or by the users to optimize their trips in terms of travel time, costs, safety, and consumptions.

Several solutions can be used to carry out the three tasks mentioned above, and are described in the following section of the thesis.

2.4. Sensor-based SHM solutions for civil engineering assets

Infrastructure monitoring can be carried out using (Hola and Schabowicz 2010) traditional destructive testing (DT), or innovative semi-destructive testing (SDT) and non-destructive testing (NDT). Usually, DT-based monitoring is the most used because of the fact that (i) it is based on well-established and accurate methods, (ii) it derives the characteristics of the road pavement from samples of the pavement (e.g., after coring), (iii) technology requirements and worker's knowledge and skills (e.g., to carry out the measurements, or to process the data) are usually already in place. Despite the above-mentioned strengths, beside the fact of providing sample-based information (i.e., discrete points of the pavement), DT requires energy and money for extracting (e.g., coring), analyzing, and landfilling pavement samples. On the other hand, SDT- and NDT-based methods, driven by the increasingly insistent demand for smart cities, are growing in relevance *versus* traditional DT methods, offering high performance (e.g., extended measurements), sustainability (e.g., energy and time savings), and efficiency (e.g., high measurement frequency, and/or technologically advanced devices). The main NDT-based monitoring drawbacks are related to the costs (i.e., instrumented infrastructures are more expensive than traditional ones), and to the worker's skill (i.e., skilled worker are required to set up, use, and tune sophisticated devices/systems, and/or to handle and analyze huge amounts of data). From an energy point of view, it should be underlined that the NDT methods tend to be more sustainable than the DT methods, because they use efficient and advanced systems (see e.g., (Nazarko et al. 2015)).

Consequently, the thesis was developed focusing principally on the NDT solutions, and the following tables aim at providing an overview of the state-of-the-art by including most of the scientific research papers and the patents that were taken into account during the research project. They refer to structures built using two of the most common construction materials, i.e., cement concrete and asphalt concrete.

Finally, it is important to remember that the Structural Health Monitoring (SHM) may have different purposes (Farrar and Worden 2010; Lu and Yang 2017; Worden et al. 2007) characterized by growing difficulty level, i.e.: i)

damage detection; ii) damage localization; iii) damage type identification; iv) damage quantification. For this reason, it should be noted that the descriptions provided in the tables below underline which is the main purpose of each type of method.

The following table (Tab. 2.2) reports recent and relevant NDT-SHM solutions designed or commonly applied on cement concrete structures like building and bridges.

Tab. 2.2 NDT-SHM solutions for cement concrete (CC) assets.

Type of method	Description	Reference
Audio-visual inspections and image analysis	Apparent and superficial problems identification, with or without devices (e.g., computer vision-based tools).	(German, Brilakis, and Desroches 2012; Hüthwohl and Brilakis 2018; Kashif Ur Rehman et al. 2016; Koch et al. 2015)
Sclerometric tests	CC strength assessment, and monitoring (especially in building).	(Hola and Schabowicz 2010)
Pachometer tests	Reinforcements localization, and corrosion assessment in terms of diameter (especially in building).	(Hola and Schabowicz 2010)
Stress- and wave-based	Vibration- and acoustic-based techniques, including impact echo, acoustic emission, and ultrasonic guided waves.	(Behnia, Chai, and Shiotani 2014; Choi et al. 2016; Hola and Schabowicz 2010; International Atomic Energy Agency 2002; Kashif Ur Rehman et al. 2016; Wang and Chan 2009; Yu et al. 2013)
Electro-magnetic, Radiological (radiometric and radiographic), thermographic, and tomographic	Reinforcements localization, and corrosion assessment, structural elements dimensions assessment, defects and damage localization, by means of Ground Penetrating Radar (GPR), conductivity tests, potential tests, electrical resistivity measurements, Nuclear and Non-Nuclear gauge, thermo-cameras, and 3D scanner, respectively.	(Aggelis et al. 2010; Choi et al. 2016; Hola and Schabowicz 2010; Kashif Ur Rehman et al. 2016; Liu et al. 2014)
Chemical and physical	Assessment of dampness, thermal properties, and material degradations.	(Hola and Schabowicz 2010)

Tab. 2.3 NDT-SHM solutions for asphalt concrete (AC) assets.

Type of method	Description	Reference
Audio-visual inspections and image analysis	Used to identify apparent and superficial problems (e.g., roughness, texture, sound absorption, distress), with or without devices (e.g., computer vision-based tools).	(Cafiso et al. 2017; Harjit K.; Rajandeep K. 2017; Koch et al. 2015; Masino et al. 2017; Mubaraki 2016; Oliveira and Correia 2013; Ouma and Hahn 2017; Praticò and Vaiana 2013; Praticò, Vaiana, and Fedele 2015; Wang, T., Gopalakrishnan, K., Smadi, O. Somani 2018; T. Wang et al. 2016; Wright 2014; Yousaf et al. 2018; Zelelew, Papagiannakis, and De León Izeppi 2013; Zhang et al. 2018)
Mobile scanning	Mobile scanning technologies based on heavy and light instrumented vehicles, unmanned aerial vehicles, satellite, smartphones on vehicles to detect image of road pavement, pavement roughness, profile, sound absorption, and traffic noise level using several devices (e.g., the smartphone's gyroscope).	(Cafiso et al. 2017; Carlos et al. 2018; Chen et al. 2011; International Atomic Energy Agency 2002; Licitra, Teti, and Cerchiai 2014; Morgan and Watts 2003; Radopoulou and Brilakis 2016; Schnebele et al. 2015; Tedeschi and Benedetto 2017; Wright 2014; Yi, Chuang, and Nian 2015; Yousuf, M.; Morton 2014)
Ultrasonic	Detecting distress (e.g., delamination) by mean of ultrasonic guided waves, ultrasonic wave propagation, and ultrasonic tomography.	(Hoegh, Khazanovich, and Yu 2011; Mounier, Di Benedetto, and Sauzéat 2012; Pahlavan, Mota, and Blacquière 2016)
Electromagnetic	Estimation of geometric properties of pavement layers and detection of concealed damages, using radargrams from GPR. Nuclear and non-nuclear electromagnetic gauge to measure AC density and homogeneity. Microwave imaging to scan the surface layers.	(Benedetto et al. 2017; Bevacqua and Isernia 2018; Krysinski and Sudyka 2013; Lin, Ashlock, and Williams 2016; Liu et al. 2014; Pedret Rodés, Pérez-Gracia, and Martínez-Reguero 2015; Porubiaková, Grinč, and Slabej 2014; Praticò, Moro, and Ammendola 2009; Solla et al. 2014; Tong, Gao, and Zhang 2017; Tosti et al. 2018; Uddin 2014)
Seismic	Multichannel Analysis of Surface Waves, MASW, and Multiple Impact of Surface Waves, MISW to derive the stiffness studying the wave propagation. Measuring mechanistic properties (e.g., stiffness) using the Light Weight Deflectometer (LWD), the Falling Weight Deflectometer	(Gosk 2016; Iodice, Muggleton, and Rustighi 2016; Katicha et al. 2014; Pitoňák and Filipovsky 2016)

	(FWD), the Rolling Wheel Deflectometer (RWD).	
GPR and Thermo-cameras	Surface and concealed cracks detection using GPR and thermographic cameras.	(Solla et al. 2014)(Ouma and Hahn 2016)
Sensor-based	Sensor networks wirelessly connected sometimes self-powered, or low- and ultralow-powered to detect, quantify, localize, and monitor surface and concealed failures.	(Le Cam et al. 2013; Grace 2015; Hasni et al. 2017; Lajnef, N., Chatti, K., Chakrabartty, S., Rhimi, M. & Sarkar 2013; Lenglet, Blanc, and Dubroca 2017; Miraliakbari, Hahn, and Maas 2014; F G Praticò, Della Corte, and Merenda 2016; Smarsly and Law 2013; Yang 2014; Yu et al. 2013; Zhou et al. 2012)

Intelligent solutions should be able to detect, in real-time, changes of the response of a monitored complex structure to stresses and loads, in the pursuit of linking these changes to information about its structural health status (Posenato et al. 2008). In order to achieve this goal, a SHM system needs to use proper digital signal processing algorithms (tools) to: i) identify any even slight variations (e.g., shape, amplitude, time-lag, etc.) of the signals collected from the monitored body over time; ii) derive the frequency components corresponding to the variations above; iii) detect the "development" of new frequencies in the signals due to changes in the structural dynamics (Reda Taha et al. 2006).

In the field of transportation, there are two main "schools of thought" concerning the data processing, i.e. statistical (e.g., multivariate statistics) and computational intelligence (e.g., machine learning)(Karlaftis and Vlahogianni 2011). Statistic aims at collecting, organizing and interpreting numerical data. This latter is particularly suited when the data characteristics are inferred from sampling, while it is not recommended for the analysis of complex and highly nonlinear data. Computational intelligence combines learning, adaptation, evolution and fuzzy logic to structure from unstructured data (Karlaftis and Vlahogianni 2011). Consequently, the more appropriate data process should be selected case-by-case. The following table reports relevant examples found in the literature, which refers to both the approaches mentioned above.

Tab. 2.4 NDT-SHM solutions based on efficient data processing approaches.

Type of method	Description	Reference
Fuzzy c-means clustering and morphological reconstruction.	Pothole detection on asphalt pavements from 2D-colour pothole images.	(Ouma and Hahn 2017)
Frequency response functions	Analyses in the frequency domain to damage detection and identification.	(Bandara, Chan, and Thambiratnam 2014; Nozarian and Esfandiari 2008)
Independent component analysis	Statistical-based damage detection.	(Zang, Friswell, and Imregun 2004)
Wavelet Transform (WT)	Wavelet-based data processing (Discrete or Continuous Wavelet Transform) to measure road pavement macro-texture, damage detection, and signal denoising.	(Katicha et al. 2014; Ouma and Hahn 2016; Reda Taha et al. 2006; Subirats et al. 2006; Zelelew et al. 2013)
Artificial Neural Network (ANN)	Machine learning-based data processing using supervised (e.g. Convolutional Neural Network) and unsupervised approaches to: i) evaluate pavement surface characteristics; ii) detect surface (visual or image analyses) and concealed (e.g., using GPR) damages; iii) predict pavement condition, performance, and distresses; iv) support pavement management and maintenance strategies; v) support pavement materials modeling.	(Ceylan, Bayrak, and Gopalakrishnan 2014; Koch et al. 2015; Tong et al. 2017; Zhao, Ivan, and DeWolf 1998)
ANN and WT	Structural damage detection (e.g., road cracks) using deep learning and WT.	(Carr et al. 2018; Moghadas Nejad and Zakeri 2011; Shi and Yu 2012; Wang and Hu 2017)
ANN and Finite Element Method (FEM)	Cracks propagation in structures paved with bituminous layers.	(Gajewski and Sadowski 2014)
Filter-based	Crack detection using visual features extracted by Gabor filters, and particle filter.	(Hassan, Mathavan, and Kamal. 2017; Salman et al. 2013; Zalama et al. 2014)
Miscellaneous	Combination of the above-mentioned data processing techniques.	(Gajewski and Sadowski 2014; Moghadas Nejad and Zakeri 2011; RPB HealTec, Review of highway standards and manuals 2016; Sheerin Sitara, Kavitha, and Raghuraman 2018)

Finally, the following table reports the patents that were taken into account during this research project and that were included as relevant examples in the

patent that was derived from this thesis (see section Scientific production-patents).

Tab. 2.5 Patents related to the SHM of solid bodies.

Type of method	Description	Reference
Active (i.e., need a source and a receiver) and frequency analysis-based.	Method and system to detect discontinuities in structures with wideband vibrational frequencies to produce a propagating wave field in the structure.	WO9428388A1
Active (i.e., need a source and a receiver) and frequency analysis-based.	Non-destructive method and system for the identification of time changes of signal frequency. It uses only the Wavelet Transform to obtain the envelope of amplitude and phase of the recorder signals, which are used to derive a characteristic parameter (feature), i.e. the instantaneous variation of the recorded signals in the time-frequency domain.	US 2012/0186349 A1
Ultrasounds-based	Method and apparatus for the detection of the thicknesses of cracks in reinforced cement concrete through the assessment of the phase variation between different ultrasonic waves transmitted and reflected, because of the interaction with a crack.	US5675085A
Guided-waves-based	System and method that aim at identifying failures in flat structures (plate and plate-like structure). Guided waves are generated, and their reflections, are analyzed using images (subtraction and suppression) to localize possible defects.	US 2015/0073729 A1
Vibration-based	Detection of vibration through one or more accelerometers (placed on one or more parts of the monitored structure) used to monitor the evolution of alterations, discontinuities, and defects of civil engineering structures and infrastructures.	RM2009A000387
Vibration-based and sound and ultrasound sensors	Method and sound/ultrasound-based apparatus to monitor the parts of a body that vibrates under transient loads, and to classify these loads based on the analysis of characteristic frequencies (resonance frequencies) of the part of the structure monitored along its main inertial axes.	US4901575A
Acoustic emissions (AE)-based	Method that aims at characterizing, dynamically and quantitatively, the aging of solid materials from the acoustic emission signals, due to mechanical vibration at any frequency (from ultrasound to seismic vibration), through statistical analyses based on hammer	RM2011A000151

	diagrams.	
Acoustic emissions (AE)-based	Non-destructive monitoring method and a system that aim at identifying structural actions (acoustic emissions), and characterizing them, through an acoustic sensor network. The characterization of the acoustic signals is carried out in terms of waveform, symmetric and asymmetric components of the loading waves, and using the Wavelet Transform.	US2009326834A1
Acoustic signature-based	Method and system based on the acoustic signature that aim at monitoring the structural health status and the operating status of the mechanical parts of the unmanned vehicles that emits sounds.	US8775013B1
Acoustic signature-based	Apparatus to identify the vehicle pass-by using neural network to analyze airborne sounds.	US2011169664A1
Image analysis-based	Non-destructive method to determine the residual tension-deformation status of welded artifacts by mean of the elaboration (using WT and envelopes obtained through the Hilbert transform) of images derived from heated artifacts and detected using a thermal imaging camera.	NA2012A000007
Object decomposition-based (i.e., large objects considered as a set of parts separately analyzed)	Apparatus and method for the remote detection of forthcoming failures in large structures composed of a set of elements. This patent is based on sensors capable of generating vibrations (active method) in the audible frequency range. The localization of a defect in a structure is carried out analyzing the alteration of the structure response (both compression and bending waves) to a unitary impulse, by mean of the inverse Fourier Transform of the spectrum of the measured acceleration.	WO0216926A1
Concealed condition –based (i.e., monitoring of internal parts of a structure).	Monitor some parameters related to the structural conditions (e.g., the temperature, the levels of pressure, tension, and distress) at given points (i.e., sensors placed on structure's nodes).	EP1863317A2
Crystalline materials-related	Method and system for detection and the propagation monitoring of cracks in solid bodies, generated by load cycles and overloads on materials that consist of crystalline structure, using wireless cracks detectors.	US2010094566A1

2.5. Wavelet Transform for data processing and data meaning

As shown in table Tab. 2.4, Wavelet Transform (WT)-based data processing and data analysis were applied in the field of the road pavement SHM, in order to measure pavement characteristics (e.g., macro-texture), to carry out damage detection and signal denoising.

Wavelet Transform (WT) is a signal processing tool based on a windowing approach of dilated (scaled) and shifted wavelets, which demonstrated its ability to overcome many of the limitations of the widely used Short Time Fourier Transform (STFT) in the time-frequency domain of analysis (Reda Taha et al. 2006). In fact, by comparing these two transforms, WT resulted to be the most suitable method to detect signal changes in both time and frequency domain (Kumar and Foufoula-Georgiou 1997; Reda Taha et al. 2006) This is the main strength of the WT and is called time-frequency localization (Kumar and Foufoula-Georgiou 1997). This property of the WT is related with the Heisenberg's uncertainty principle, which dictates the minimum area of the windows (or time-bandwidth product; cf. (Reda Taha et al. 2006)) used to decompose the time-frequency plane (multiplying the signal to be analyzed with variable-sized window functions; see Fig. 2.6) but does not indicate the shape of these windows (Kumar and Foufoula-Georgiou 1997).

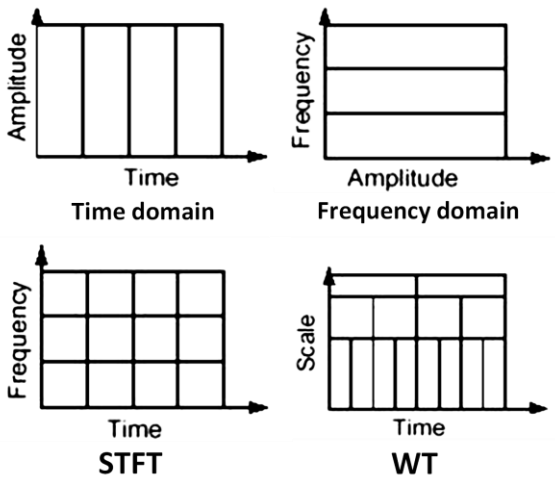

Fig. 2.6 Top: Plan of analysis decomposition during time and frequency analysis; Bottom: time-frequency plane decomposition using Short Time Fourier Transform (STFT), and Wavelet Transform (WT).

Fig. 2.6 shows that WT allows working with high frequency resolution (and low time resolution) for low frequencies, and high time resolution (and low frequency resolution) for high frequencies (Reda Taha et al. 2006). This strength makes this tool especially suitable for the analysis of non-stationary phenomena and signals with short-lived transient components (Kumar and Foufoula-Georgiou 1997), which are the combination of transient high frequency components and long lasting low frequency components. In addition, it is important to note that this ability makes the WT more similar to the human ear than other "too much artificial" tools. All these abilities make the WT a perfect tool when the purpose is to monitor a certain phenomenon over time (Reda Taha et al. 2006).

Importantly, the quality of the WT application is strictly related with the type of transformation used to analyze the data (i.e., Continuous Wavelet Transform, CWT, and Discrete Wavelet Transform, DWT), and the Mother Wavelet (MW) chosen for the same purpose (Reda Taha et al. 2006). In particular, the main difference among continuous and discrete WT is the discretization of the scaling factor, which affects the representation of the processed signal (Kim and Melhem 2004) . In fact, CWT provide results more detailed than DWT ones, because of the fact that CWT uses fine discretized scales (i.e., the scaling factors used by the CWT produce significantly overlapped daughter wavelets, which were defined in the following).

The CWT is obtained using the expression (Shoaib, Shamseldin, and Melville 2014):

$$CWT(a,b) = \int_{-\infty}^{+\infty} x(t) \cdot \psi_{a,b}^{*}(t) dt, \qquad (2.\ 1)$$

where a is the scaling parameter and is a vector of positive elements, which allows dilating or contracting the basic function or mother wavelet ψ (cf. (Abdolmaleki et al. 2017; Kumar et al. 2014)); b is the shifting parameter, which permits the translation of the mother wavelet ψ along the x-axis (time); $x(t)$ is the signal to be transformed; t stands for time; ψ^* is the complex conjugate of the MW function ψ chosen.

When a MW is scaled (stretched or dilated through scaling function called "father wavelet"; cf. (Alhasan, White, and De Brabanterb 2016)) a family of "daughter wavelets" is originated. This family is first shifted (translated) along the signal, and then multiplied by the signal during the application of the WT. The result of these operations is a matrix of coefficients, usually called "wavelet coefficients" (Continuous Wavelet Coefficients, CWCs, in this case), which represent the projection (convolution; cf.(Y. Wang et al. 2016)) of the signal on the family of functions (Reda Taha et al. 2006). A strong correlation value means that the signal, at that instant, looks like the daughter wavelet. The CWCs are contained in a N×A matrix, where N and A are the lengths of the signal, *x(t)*, and of the scaling vector, *a*, respectively. Summarizing, CWT returns the CWCs after the convolution of the signal, *x(t)*, with ψ^*, properly scaled and shifted varying *a*, and *b*. The CWCs can be used to represent the signal. The mother wavelet (MW) can be expresses as follows (Shoaib et al. 2014):

$$\psi_{a,b}(t) = \frac{1}{\sqrt{a}}\psi\left(\frac{t-b}{a}\right), \tag{2. 2}$$

where ψ is the mother wavelet (MW), which depends of *a*, *b*, and *t*.

In order to reduce the amount of computations, the Discrete Wavelet Transform were introduced. The DWT is derived from the CWT by discretizing the dilation parameter, *a*, and translation parameter, *b*. The discretization of the two parameters mentioned above is more efficient if a dyadic values are used (Ouma and Hahn 2016). In particular, the parameter *a* is replaced by the term 2^j, while *b* by $2^j \times k$, where j and k are positive real numbers. Using the DWT, the high frequencies of the signal are filtered through a series of high-pass filters, while the low frequency ones through a series of low-pass filters. The results are approximated and detailed coefficients, which can be used to represent the signal. The DWT can be calculated using the expression (Shoaib et al. 2014):

$$DWT(a,b) = 2^{-j/2} \cdot \int_{j=1}^{j=J} x(t) \cdot \psi^*\left(2^{-j/2} - k\right) dt, \tag{2. 3}$$

where *J* is the predefined level of decomposition of the signal, *x(t)*.
In this case the general expression for the MW becomes:

$$\psi_{j,k}(t) = 2^{j/2}\,\psi\left(2^{j/2} - k\right). \tag{2. 4}$$

After the wavelet decomposition, the signal, *x(t)*, can be represented as follows (Ouma and Hahn 2016):

$$x(t) = A_J + \sum_{j \le J} D_j = \sum_{j \ge J} D_j + \sum_{k \in Z} a_{j,k} \cdot \psi_{j,k}(t). \tag{2. 5}$$

The following figure shows the decomposition of the signal carried out using the DWT.

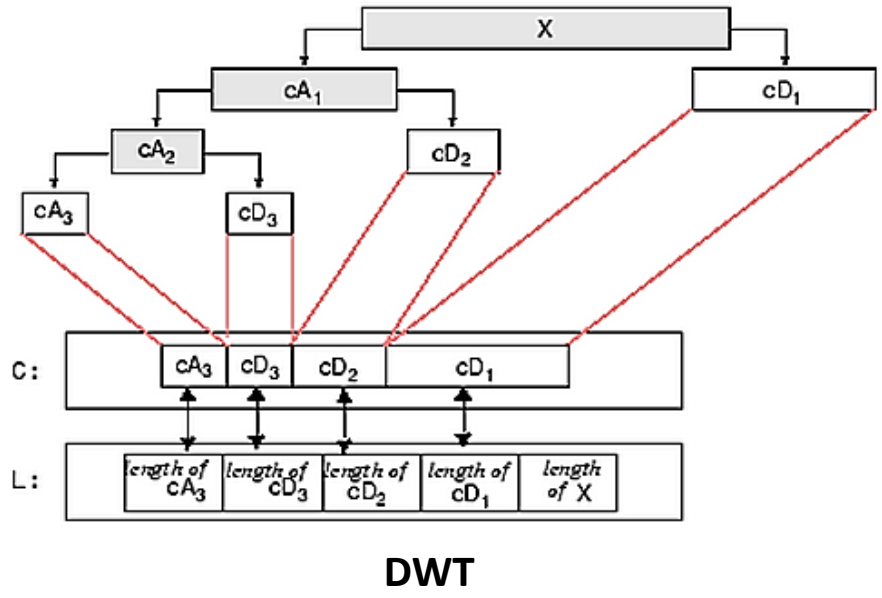

Fig. 2.7 Signal decomposition using Discrete Wavelet Transform (DWT)(Mathworks 2018b).

A typical 2-D graphical representation of the wavelet coefficients in the time-frequency domain is the "scalogram". It shows the scaled percentage of energy of the wavelet coefficients (different colors or intensity variation of a color) with respect to time (or shift; x-axis), and scale variables (y-axis) (Reda Taha et al. 2006).

Usually, scalograms show on the y-axis the scaling parameter, *a*. However, a pseudo-frequency (see Fig. 2.8) can be derived from the scaling parameter using the following expression (Alhasan et al. 2016):

$$F_a = \frac{F_c}{a} \cdot F_S, \tag{2. 6}$$

where *Fa* is the pseudo-frequency (Hz) corresponding to the scale factor *a* (dimensionless); *Fc* is the central frequency of the mother wavelet ψ used (Hz); F_S is the sampling frequency (Hz). Finally, the x-axis of the scalogram shows the duration of the signal (seconds).

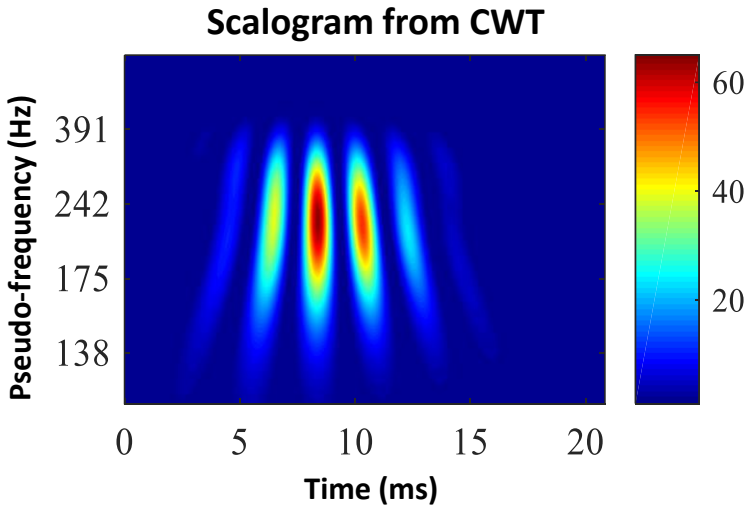

Fig. 2.8 Example of scalogram obtained applying the CWT on an acoustic signal.

Mather Wavelet selection

The choice of the Mother Wavelet (MW) is a crucial aspect of the application of the WT and should be carefully done on a case-by-case basis in order to avoid useless or unrepresentative results. The WT gives the possibility to use different types (e.g., real, analytic, orthogonal) of MW (e.g., Daubechies, Morlet, Coiflet, etc.; see Fig. 2.9) (Kumar et al. 2014; Kumar and Foufoula-Georgiou 1997).

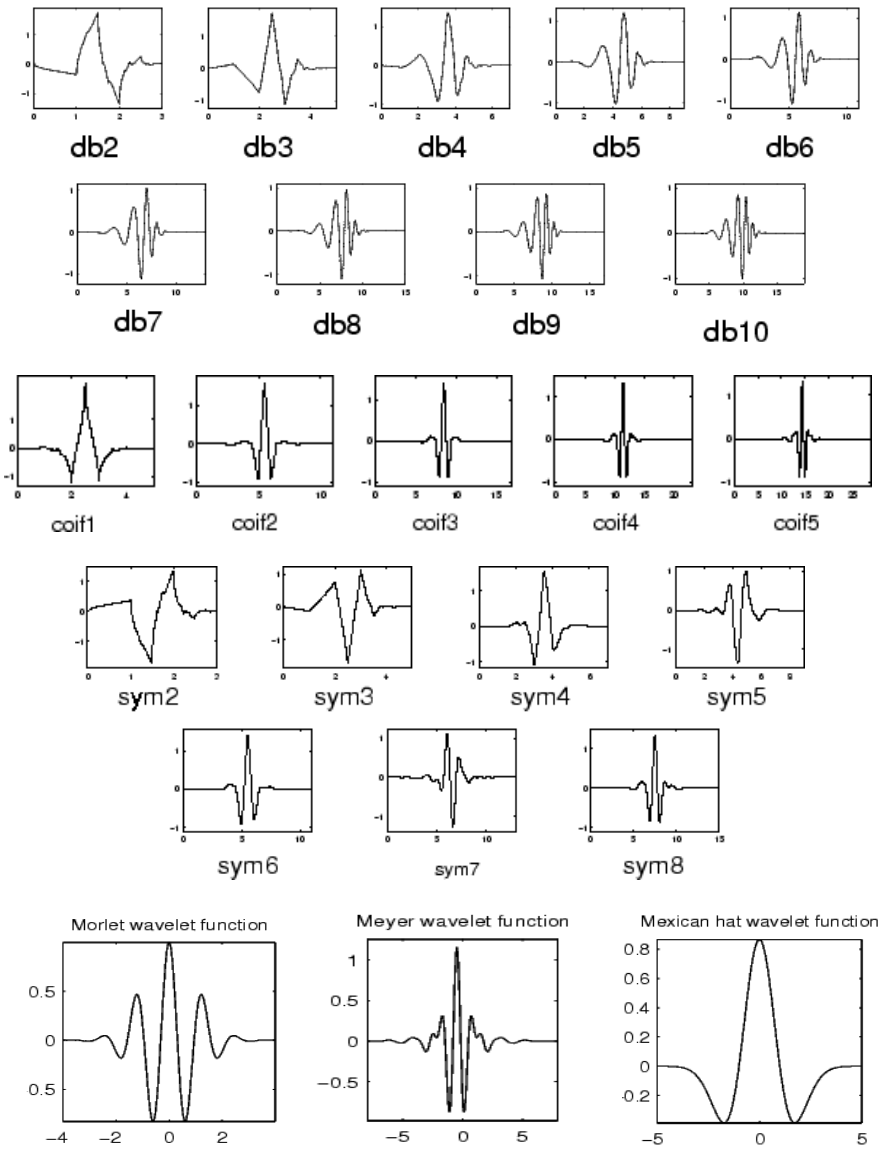

Fig. 2.9 Examples of Mother Wavelets, where db = Daubechies; coif = Coiflet; sym = Symlet, and the number represent the MW order (Mathworks 2018b).

The efficiency of a mother wavelet (MW) is measured by evaluating its ability to approximate particular classes of functions with few nonzero wavelet coefficients (Maheswaran and Khosa 2012; Mathworks 2018b). This depends on the regularity of the function under analysis, on the size of the MW support, and on the number of the vanishing moments of the MW. In more detail: a) the regularity can be intuitively considered as the measure of the function smoothness (i.e., if it is differentiable mathematically in each point of its domain). The more the MW is regular, the more abrupt changes in the data

can be easily detected (Mathworks 2018b); b) the support of a function is the set of points where the function is non-zero. Using a MW with a compact support (support with minimum size, in the time-domain) the number of the high-amplitude coefficients can be reduced (Maheswaran and Khosa 2012); c) the vanishing moment is the MW's ability of representing polynomial behavior or information in a signal. A MW with p vanishing moments is orthogonal to any polynomial of degree $p-1$ (i.e., a MW with 3 vanishing moments, for example, suitably encodes any quadratic signal, which has constant, linear and quadratic components; cf. (Maheswaran and Khosa 2012)). When the p is greater, the MW oscillates radically (Y. Wang et al. 2016). The higher the order of vanishing moments is, the higher the MW accuracy is in detecting punctual signal mutations (despite the high number of computations required). The number of vanishing moments of a MW is often called "order" (Mathworks 2018b; Y. Wang et al. 2016), and some of the MW families have order greater than one (e.g., the maximum order of the Symlet families is 45, correspondent to "sym45"). There are relationships among the above-mentioned properties. In particular, a MW with higher regularity has higher vanishing moments (Y. Wang et al. 2016), and if an orthogonal MW has p vanishing moments, then its support should be at least $2p-1$ (Mathworks 2018b). Usually, a MW with many vanishing moments should be chosen if the function to be analyzed has few isolated singularities and is very regular among these singularities (a less number of smaller wavelet coefficients will be obtained). On the other hand, if a high number of singularities must be detected through high-amplitude wavelet coefficients, a MW with compact support (and reduced vanishing moments) should be preferred.

The choice of the MW can be carried out by mean of several mother wavelet selection criteria and methods, which can be classified as qualitative and quantitative (Ngui et al. 2013). The qualitative methods allow picking up the proper MW considering its properties (i.e., regularity, vanishing moment, degree of shift variance, compact support, orthogonally, bi-orthogonally, symmetry, explicit expression, filter order), or the shape matching by visual inspection (Bigerelle et al. 2013; He, Jianchun, and Yang 2014; Y. Wang et al. 2016). On the other hand, the quantitative methods take into account

quantities such as cross correlation, variance, standard deviation, energy, entropy. The following table reports the scientific papers related to quantitative MW selection method and criteria, which were taken into account in this thesis.

Tab. 2.6 Review (2004-2017) about quantitative MW selection methods and criteria.

Method – Criterion	Reference
Minimum Description Length (MDL) criterion.	(Saito 1994)
Cross correlation coefficient (CC) method.	(Abdolmaleki et al. 2017; Al-Qazzaz et al. 2015; He, Tan, and Wang 2015; Pal et al. 2011; Rodrigues, D'Mello, and Srinivasa 2016; Saraswathy et al. 2014; Seljuq, Himayun, and Rasheed 2014; Singh and Tiwari 2006; Yang, Judd, and Bennoch 2004)
Symmetric divergence or Relative entropy method.	(Tsui and Basir 2006)
Maximum Energy to Shannon Entropy Ratio criterion (MEER).	(Abdolmaleki et al. 2017; He et al. 2015; Kankar, Sharma, and Harsha 2011; Kumar et al. 2014; Li et al. 2009; Rodrigues et al. 2016; Saraswathy et al. 2014; Vakharia, Gupta, and Kankar 2017; Yan 2007; Yan and Gao 2009)
Minimum Shannon Entropy criterion (MSEC).	(Kulkarni and Sahasrabudhe 2017; Kumar et al. 2014; Y. Wang et al. 2016; Wang, Miao, and Xie 2011; Zheng and Washington 2012)
Comprehensive entropy criterion (E_{com}) (integrates 8 different criteria based on energy and entropy of the wavelet coefficients).	(He et al. 2015)
Mean Square Error (MSE) (of wavelet coefficients before and after the WT application and/or original signal and/or reconstructed signals).	(Al-Qazzaz et al. 2014; Blache et al. 2017; He et al. 2015; Kulkarni and Sahasrabudhe 2017; Seljuq et al. 2014; Zhang, Bao, and Wu 2005)
Evaluation criterion (EC).	(Rafiee et al. 2011)
Signal to noise ratio (SNR).	(Al-Qazzaz et al. 2014; He et al. 2015)
Multiple index method (uses MSE, EC, and SNR).	(He et al. 2014)
MinMax information criterion.	(Yan 2007)
Maximum Relative Wavelet Energy.	(Kankar et al. 2011; Saraswathy et al. 2014)
SUMVAR criterion.	(Rafiee, Rafiee, and Tse 2010; Rafiee and Tse 2009; Rodrigues et al. 2016)

Genetic algorithm.	(Rafiee et al. 2009)
Deviation between percentage energies (of the harmonics and discrete wavelet coefficients).	(Morsi and El-Hawary 2008)
Energy of the wavelet coefficients at higher scales.	(Nair and Kiremidjian 2009)
Wavelet Transform (WT)-Filtering-Inverse WT.	(Cheng, Min, and Zhang 2010)
Root Mean Square (RMS) error of reconstructed signals.	(Bigerelle et al. 2013; Chompusri, Dejhan, and Yimman 2012; He et al. 2015; Maheswaran and Khosa 2012; Megahed et al. 2008)
Minimum energy of wavelet coefficients.	(Kulkarni and Sahasrabudhe 2017)
MAXERR method (maximum absolute squared deviation).	(Kulkarni and Sahasrabudhe 2017)
Peak Signal to Noise Ratio (PSNR).	(Adamo et al. 2013; Al-Qazzaz et al. 2014; Kulkarni and Sahasrabudhe 2017; Seljuq et al. 2014)
Information Quality Ratio (IQR).	(Wijaya, Sarno, and Zulaika 2017)
Mean Absolute Error (MAE).	(Maheswaran and Khosa 2012)
Nash Sutcliffe Criteria (NSC).	(Maheswaran and Khosa 2012)
Compression Ratio (CR).	(Chompusri et al. 2012)
Adaptive discriminant Wavelet Packet Transform (WPT) algorithm.	(Qureshi, Wilson, and Rajpoot 2008)
Support Vector Machine (SVM)- and/or Probabilistic Neural Network (PNN)-based (using as features energy, entropy, RMS, and wavelet coefficients standard deviation).	(Ferroudji et al. 2012; Gandhi, Panigrahi, and Anand 2011; Saraswathy et al. 2014; Shoaib et al. 2014)
Equal Error Rate (EER) in percentages, and the optimal Detection Cost Function.	(Ganchev et al. 2014)

Based on a literature survey reported in Tab. 2.6, which covered 13 years (between 2003 and 2017), the following considerations on the quantitative methods for the MW selection can be stated:

1. They are based on: i) the comparison between original and elaborated signals or their wavelet coefficients (e.g., CC method, RMS method, MSE method, SUMVAR method; cf. (Rodrigues et al. 2016)); ii) the entropy and the energy of the wavelet coefficients (e.g., E_{com} method, MEER method, MSEC method; cf. (He et al. 2015)); iii) the characteristics of the signal (e.g., SNR method, (He et al. 2015)); iv) the potentialities of the Support Vector Machine (SVM) and the Probabilistic Neural Network (PNN) in terms of classification, extraction and analysis of feature, and modeling (Shoaib et al. 2014).

2. The quantitative MW selection methods are applied on different type of data, but are frequently used to improve the data analysis of biomedical signals (e.g., ECG, EEG, etc.; cf. (Al-Qazzaz et al. 2015; Seljuq et al. 2014), vibration, images, acoustic signals, geophysical data (Pal et al. 2011; Shoaib et al. 2014; Y. Wang et al. 2016)
3. Commonly, these methods are used to improve WT-based applications that aim at carrying out signal denoising, data compression, feature classification, and structural health monitoring.
4. The DWT and its variants (Multi Resolution Analysis, MRA, and Wavelet Packet Transform, WPT) are usually preferred over the CWT because they allow saving computational time even if they provide less accurate results (Qureshi et al. 2008). However, it is frequent to find studies where the CWT is applied together with the DWT (e.g., (Reda Taha et al. 2006)).

2.6. Energy harvesting in transportation[2]

As mentioned in the section "Topics definition" (2.1), in this thesis were assumed as three essential components of an ideal ITS (see Fig. 2.1, bottom): 1) PMSs based on SHMs; 2) efficient data processing method; 3) Energy Harvesting Technologies (EHTs). The first two topics were discussed in the previous sections, while this section aims at providing a description of the last one, i.e. the main EHTs that are able to gather energy and can be used to power the ITS in a sustainable way.

The efficiency, sustainability, connectivity, and durability of transportation infrastructures are properties strongly requested by users and authorities, and are going to become essential characteristics of the future smart cities (Pop and Proştean 2018). One of the most powerful ITS tool is represented by the Internet of Things (IoT) solutions, such as Wireless Sensor Network (WSN) monitoring systems that use Micro Electro-Mechanical Systems (MEMS) sensor (Grace 2015)(Perles et al. 2018). These latter have small size, are easy to be installed and used, are able to carry out monitoring-related activities and

[2] This section mainly refers to the papers 2.2 (see Scientific production).

wireless data transmission with low power consumption. The sustainability of these solutions can be further increased if EHTs are implemented (Dhakar 2017; F G Praticò et al. 2016; Saadona and Othman 2015)

In the following, recent and relevant examples of EHTs, implemented in road-related applications, were reported. Different approaches were used to gather energy from road infrastructures (including vehicles). Based on (Duarte and Ferreira 2016; H. Wang, Jasim, and Chen 2018) EHTs include systems based on several effects, i.e. photovoltaic, thermal, thermoelectric, geothermal, piezoelectric, electromagnetic, and electrostatic. Through these devices, electric energy can be produced, heating or cooling can be carried out, and sensors-based systems can be powered.

Solar-based EHTs for road applications include solar pavements (see e.g., (Dezfooli et al. 2017)), asphalt solar collectors (e.g., hydronic asphalt pavement, a.k.a. HAP; cf. (Pan et al. 2015)), and photovoltaic thermal hybrid solar collectors (Xiang et al. 2018). They aim at producing electricity (through photovoltaic systems), and/or heat (through pipes embedded into the pavement in which water flow gathers heat). Photovoltaic (PV) applications have a high level of efficiency and maturity (Duarte and Ferreira 2016; H. Wang et al. 2018). Solar road (Dezfooli et al. 2017), solar trees (Hyder, Sudhakar, and Mamat 2018), and bus shelters are some of the recent and promising ideas and applications of the PV technology that were proposed in the last years.

(a) (b) (c)

Fig. 2.10 Example of (a) solar road (Silva 2016), (b) bus shelters, and (c) PV tree (Bucket.sunshineworks.com 2018).

Compared to traditional PV applications, they were designed (Hyder et al. 2018) to: i) optimize space/land management (especially in urban areas, and

open spaces); ii) reduce land carbon footprint compared to the traditional PV solar panel (i.e., solar trees need less land to be installed); iii) reduce grazing angles of solar irradiation (i.e., the acute angle of incidence of a beam almost parallel to a surface); iv) offer mobile/laptop/electric vehicles charging, street lighting, household/industrial supply, grid support; v) increase the aesthetics of PV, aiming at improving public perception.

Collectors in road pavements (a.k.a., Asphalt Solar Collectors, ASC; cf. (Duarte and Ferreira 2016)) take advantage from the thermal effect (see Fig. 2.11).

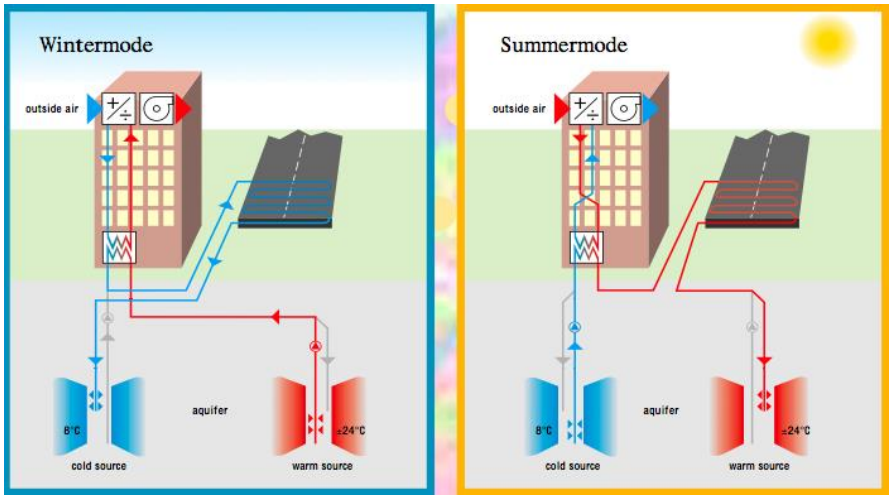

Fig. 2.11 Example of Asphalt Solar Collectors (ASC) (Ooms Avenhorn Holding BV 2003).

Collectors allow a better control of the pavement temperature (e.g., urban heat island effect reduction, snow melting/deicing on road surface, or air conditioning of buildings (Pan et al. 2015; Xiang et al. 2018). Unfortunately, they need an accurate design (pipe size and distribution, fluid type, and flow rate) and high solar radiation (Pan et al. 2015; Xiang et al. 2018) The main unsolved problems that affect the diffusion of this solar-based EHTs refer to: i) costs (e.g., photovoltaic panels have high investment costs due to the need for inverters and storage batteries; cf. (H. Wang et al. 2018)); ii) energy performances (e.g., solar road energy efficiency is about 11%; cf. (Xiang et al. 2018)); iii) surface performance (e.g., solar pavements have to guarantee suitable roughness, resilience, stiffness, sustainability, etc.; cf. (Dezfooli et al.

2017; H. Wang et al. 2018); iv) construction optimization (e.g., using reinforcing grid to reduce the stress concentration on the pipe of a HAP system (Pan et al. 2015)); v) the need for specific designed maintenance processes and long-term performance evaluation (Pan et al. 2015); vi) environmental impact (e.g., toxic chemical in the production process, difficulties during recycling and disposal (H. Wang et al. 2018)). Furthermore, they are more suitable where high solar radiation is present (H. Wang et al. 2018).

A noteworthy attempt to optimize the energy production of solar roads consists in photovoltaic thermal hybrid solar collectors (Xiang et al. 2018) (see Fig. 2.12). The hydronic part of the hybrid system proposed allows decreasing the photovoltaic cell temperatures (by around 24°C) and this increases the electrical efficiencies (by 6%) compared to conventional solar roads.

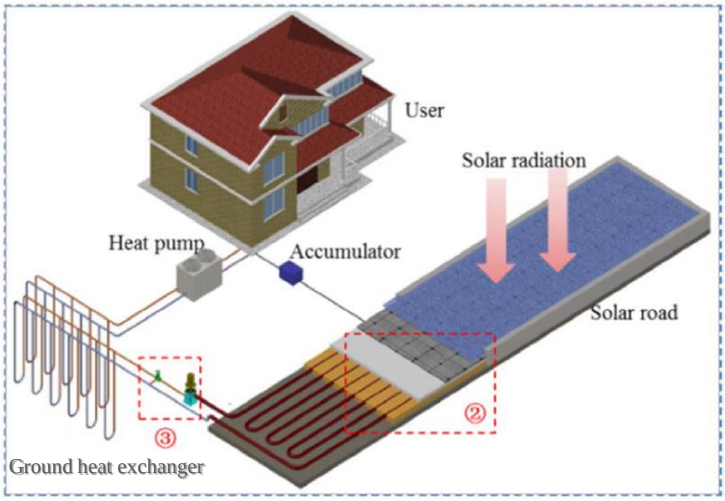

Fig. 2.12 Example of photovoltaic thermal hybrid solar collectors (Xiang et al. 2018).

Geothermal EHTs (Fig. 2.13, a) are technologically advanced, but geologically and geographically limited (H. Wang et al. 2018). Thermoelectric EHTs (i.e., ThermoElectric Generators, TEGs; cf. (Duarte and Ferreira 2016), and Fig. 2.13, b) are not energetically profitable (i.e., their global efficiency is about 1.6-2.0%; (Duarte and Ferreira 2016; H. Wang et al. 2018)), and

expensive at present (i.e., equipping one linear mile of road with a typical TEG system, and maintain it for all its lifetime, costs 3 times the cost of a typical PV system, and 1.3 times the cost of a solar collector-based system; cf. (H. Wang et al. 2018)). Despite this weaknesses, current improvements in materials and structure design are making this technology promising (H. Wang et al. 2018).

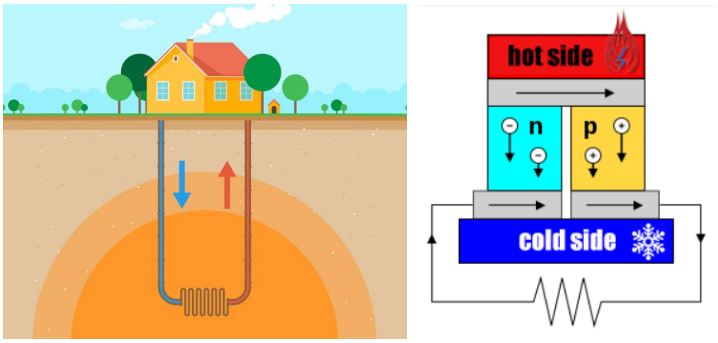

(a) (b)

Fig. 2.13 Example of (a) Geothermal, and (b) Thermoelectric EHTs.

Energy from traffic-induced vibrations can be harnessed through piezoelectric-based devices, which are based on piezoelectric, electromagnetic, and electrostatic effects (H. Wang et al. 2018). Piezoelectric energy harvesters, where the power is generated by mechanical stresses, allow stress- or vibration-based energy harvesting, but need repeated traffic load, and, because of their low energy conversion efficiency, a large number of units to gather the energy required from roadways applications. Furthermore, piezoelectric materials undergo structural and electrical degradation due to cycling loading. This calls for proper investigations on long-term durability and service life (H. Wang et al. 2018). Besides, significant efforts were made to embed Piezoelectric Energy Harvesters (PEHs) into the road pavement (see Fig. 2.14).

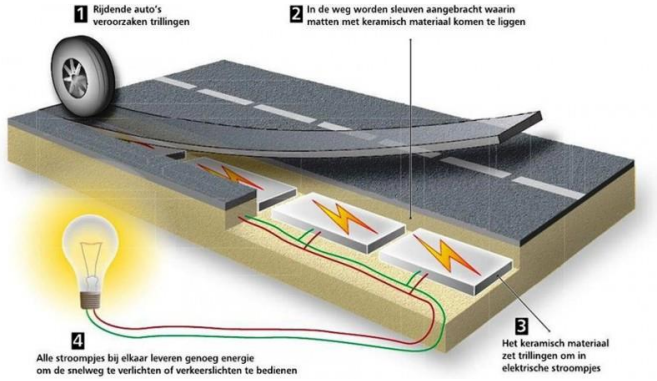

Fig. 2.14 Example of Piezoelectric Energy Harvesters (PEHs) into the road pavement (Engineersonline.nl 2012).

In fact, it should be considered that: i) embedded devices require tough packaging; ii) vibrations affect their efficiency; iii) their duty cycles should be accorded to the traffic; iv) their design and durability are strictly related to the boundary conditions (e.g., temperature, stress, strain, vibration, etc.); v) standard specifications for their installation into the road, and appropriate management are needed (i.e., implementation of these systems and maintenance (Guo and Lu 2017; Hasni et al. 2017; Papagiannakis et al. 2016; H. Wang et al. 2018; Xiong and Wang 2016; Xu et al. 2018; Yang et al. 2018). Despite these problems, these devices allow avoiding the long-distance electricity transmitting, and the energy produced by them might be used to power traffic facilities (e.g., signs, or LED traffic lights), or low-power sensors able to get real-time traffic information (e.g., vehicle driving speed and/or load) (Papagiannakis et al. 2016; Xu et al. 2018).

Electromagnetic (EM) systems are easy installable and they are largely applied to bridges (i.e., an EM generator is a velocity-induced transducer that produce energy because of the oscillations of a coil in a magnetic field, induced by the low-frequency traffic-induced vibrations/oscillations of the bridge; cf. (H. Wang et al. 2018)), but they are not able to produce energy from pavement vibrations (Duarte and Ferreira 2016; H. Wang et al. 2018).

Electrostatic energy harvesters (i.e., using variable capacitors, induced charges from an external voltage bias, or pre-charged) have advantages (e.g., high voltage, low cost, high coupling coefficient, size reduction, etc.) that make them more appropriate for small-scale embedded sensor-based applications

(i.e., less 10 cm^3) than electromagnetic and piezoelectric ones (H. Wang et al. 2018).

Wind turbine on highways medians can produce energy (especially for in series configuration), and reduce accidents (i.e., reduce glare from oncoming vehicles) (H. Wang et al. 2018).

Fig. 2.15 Examples of wind turbines on highways (Chapa 2007)(Intmensorg.com 2018).

Vehicle-based EHTs were designed to gather energy from the vehicle vibration. Examples of these devices include piezoelectric system to harness thermoelectric or piezoelectric energy from the car engine and damper (Lafarge et al. 2015), or to power wireless sensors on the tire (Lee and Choi 2014), respectively (see Fig. 2.16). Research is growing in this field, aiming at improving electromagnetic generators and hydraulic systems (Duarte and Ferreira 2016).

(a) (b)

Fig. 2.16 Example of (a) thermoelectric and (b) piezoelectric EHT for cars.

Finally, the application of EHTs mostly depends on power output, cost-effectiveness, technology readiness level, strengths and weaknesses, and support from government and industry (H. Wang et al. 2018). It should be noted that none of the EHTs above mentioned have been fully developed, validated, and are today complete and certified products (except for the ASCs, that do not produce electrical energy; cf. (Duarte and Ferreira 2016)).

2.7. Summary of the literature review

Based on the contents of the previous sections related to the literature review, it is possible to state that:

- Several solutions are currently adopted to improve sustainability and efficiency of the road pavements construction and operational phases, and one of the most effective refers to the Intelligent Transportation Systems (ITSs).
- Three essential components of an ideal ITS were defined, i.e.: 1) Pavement Management Systems (PMSs) based on Structural Health Monitoring (SHM) solutions; 2) efficient data processing methods; 3) Energy Harvesting Technologies (EHTs).
- The authorities that are responsible for the management of road pavements need more efficient and reliable PMSs than the current ones. In order to achieve this result, it is needed to switch from the failure-based to the condition- or predictive-based maintenance, and to move from the destructive, un-sustainable, and limited traditional measurement systems to non-destructive, sustainable, and specially designed innovative ones.
- Despite the high number of solutions designed for the SHM of civil engineering assets, like building, bridge, and roads, there is a lack in implementation of these solutions in real contexts. In addition, it is difficult to find solutions applied on road infrastructures that are able to: i) monitor the structural conditions of the internal layers of the road pavements; ii) detect any variations over time of the road

conditions due to the occurrence or the propagation of concealed failures; iii) share information with the appropriate authorities.

- Efficient data processing can be carried out using Wavelet Transform and Artificial Neural Network. The first one can be used for different purposes (time-frequency analyses, signal decomposition, denoising, compression, etc.), but it is recommended when signal singularities, which can be related with the occurrence of asset distresses, should be detected and monitored. While, the second one can be used to implement algorithm that are able "to learn" from the signals gathered from the monitoring system, and this ability can be effectively used to recognize the occurrence of asset distresses, and define the distress type.
- Efficient, sustainable, connected, and durable ITSs can be obtained using Internet of Things (IoT) solutions, such as Wireless Sensor Network (WSN) monitoring systems that use Micro Electro-Mechanical System (MEMS) sensors powered using specially designed Energy Harvesting Technologies (EHTs).

3
Pavement modeling and method set up

This Chapter aims at: i) describing the simulations carried out to characterize the concealed fatigue cracks in road pavements; ii) presenting the main objective of this thesis, i.e. a new monitoring method specially designed for road pavements; iii) presenting the experimental plan that was designed to set up and validate the proposed method.

3.1. Pavement modeling simulations using KENPAVE

In this section of the thesis, the simulations carried out to characterize the most common concealed failures affecting the road pavement are described. In more detail, these simulations were performed to better understand the phenomena (fatigue) that lead to the generation and propagation of concealed cracks in the bottom layers of the road pavements.
The main causes of failure of road pavements are reported in section 1.1, and can be mainly attributed to intrinsic (e.g., inadequate design) or extrinsic (i.e., due to the interaction or the road pavement with the traffic or the environment). Importantly, the analysis carried out in section 1.1 led to the conclusion that concealed failures need greater attention than the surface ones, and should be promptly detected, and carefully classified and monitored. Furthermore, the literature review (cf. Chapter 2) shows that a multitude of solutions are currently adopted to improve the sustainability and efficiency of the road pavements, which can be associated to two different phases of this infrastructure, i.e. the Construction and the Operational. Most of the thesis is focused on the second phase, while this section is used to: 1) provide an example of solution that can be used to improve the road pavement Construction phase; 2) characterize the traffic-induced concealed failures (in terms of position, dimensions, and main causes).

First of all, it is important to underline that several failure models are available in the literature. These models aim at predicting the failure of a road pavement, and in the following two are reported to show how is possible to predict two critical phenomena that lead to the generation of concealed distresses, namely the fatigue and the rutting (AASHTO 1993; Asphalt-Institute 1991; Beskou, Tsinopoulos, and Hatzigeorgiou 2016; Pokorski, Radziszewski, and Sarnowski 2016; Sivakumar Babu, Saride, and Munwar Basha 2016).

Fatigue Cracking Models

Miner's cumulative damage concept (Sivakumar Babu et al. 2016) has been widely used to predict fatigue cracking. It is generally agreed that the allowable number of load repetitions is related to the tensile strains at the bottom of the asphalt layer. The amount of damage is expressed as a damage ratio, which is the ratio between predicted and allowable number of load repetitions. Damage occurs when the sum of damage ratio reaches 1. The major difference in the various design methods refers to the transfer functions that relate the tensile strains present in flexible road pavements to the allowable number of load repetitions. The allowable number of load repetitions, N_f, can be computed using the following equation:

$$N_f = f_1(\varepsilon_t)^{-f_2}(E)^{-f_3}, \tag{3.1}$$

where ε_t is the tensile strain at the bottom of the flexible pavement, E is modulus of elasticity of the pavement and f_1, f_2, and f_3 are constants obtained by calibration (e.g., $f_1 = 0.414$, $f_2 = 3.291$, and $f_3 = 0.854$ using the software KENPAVE).

Rutting Models

Rutting models are used to limit the vertical compressive strains on the top of the subgrade and are widely used (Sivakumar Babu et al. 2016). The allowable number of load repetitions N_d to limit rutting is related to the vertical compressive strains, ε_c, on top of the subgrade by the following equation:

$$N_d = f_4(\varepsilon_c)^{-f_5}, \tag{3.2}$$

where f_4 and f_5 are calibrated values using predicted performance and field observation (e.g., f_4 = 1.365e-09, and f_5 = 4.477 using the software KENPAVE).

Based on the two models reported above, the distress can be estimated by the software KENPAVE (Huang 2003). By means of KENLAYER (the section of the KENPAVE used to design asphalt concrete pavements and applying the multi-layer elastic theory), it is possible to calculate the structural response of a multi-layer flexible road pavement in terms of stresses, strains, and deflections in various layers of several hypothetical pavement sections.

KENLAYER considers the fatigue cracking caused by the combination of two tensile strains (Al-Khoury et al. 2002) (see Fig. 3.1) horizontal tensile strain (ε_t , see Eq. 3.1) at the bottom of the asphalt layer that cause permanent cracks; 2) vertical compressive strain (ε_c , see Eq. 3.2) on the surface of subgrade that cause permanent deformation (or rutting).

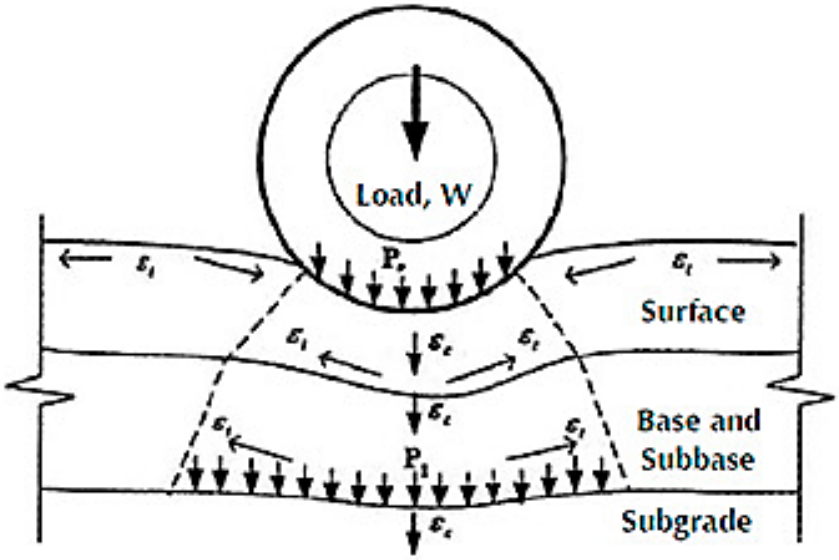

Fig. 3.1 Stresses (P) and stains (ε) generated by a vehicle wheel on the road pavement layers, i.e. surface stands for bounded asphalt concrete layer (subjected to horizontal tensile strain, ε_t), while subbase and subgrade are the un-bounded layers (subjected to vertical compressive strain ε_c).

The above-mentioned software can be also used to predict the life of new pavement based on the failure models mentioned above, on a given pavement configuration.

The software KENLAYER makes the "damage analysis" using the Eqs. 3.1, and 3.2. After the determination of stresses, strains and displacements that occurs at each layers, it calculates the values of the parameter N_f and N_d for each layers (indicating both of them as "allowable load repetitions"). These values are utilized to determine the Damage Ratio (*DR*) at the bottom of the layers and at the top of the layers, respectively. This parameter is defined by the following ratio:

$$DR = \frac{N}{N^*}, \tag{3.3}$$

where *N* comes from an estimation of the number of vehicles passing on the road section under analysis in a year (called "load repetitions" by the software KENLAYER), while *N** is the number of load repetition that lead to the failure of the pavement, i.e. N_f or N_d previously calculated. The highest value of the *DR* is used to estimate the "Design life" of the pavement (year) through the following expression:

$$Design\ life = \frac{1}{DRmax} \tag{3.4}$$

The simulations, which were carried out using the software KENLAYER, consists of the following four cases study:

I. Thick pavement loaded by heavy vehicles;
II. Thick pavement loaded by light vehicles;
III. Thin pavement loaded by heavy vehicles;
IV. Thin pavement loaded by heavy vehicles.

Hence, two different road pavements were designed (i.e., thick and thin) and loaded using two different loads (i.e., heavy and light). In order to correctly design the road pavement, the values reported in the following table (related to layer thicknesses and elastic moduli) were taken into account.

Tab. 3.1 Road pavement layer thicknesses and elastic moduli.

Type of layer	Layer thickness (cm)	Elastic modulus (MPa)	Reference
Asphalt concrete (as-designed)	27	2.29e03	(Praticó 2011)
Asphalt concrete (as-designed)	25	2.65e03	
Asphalt concrete (as-constructed)	27	1.00e03	
Cement treated (as-designed)	20	1.00e03	
Cement treated (as- constructed)	20	1.30e03	
Subbase + subgrade (as-designed)	semi-infinite	1.0e02	
Subbase + subgrade (as-constructed)	semi-infinite	1.3e02	
Asphalt concrete	4	1.7e03	(Gedafa 2007)
Dense Bituminous macadam (DBM)	5	1.5e03	
Crack relief layer (CRL)	5	1.0e03	
Bitumen Macadam (BM)	6	7.0e02	
Water Bound Macadam (WBM)	30	4.0e02	
Moorum	150	0.6e02	
Semi-dense bituminous concrete	2.5	2.6e03	(Selvi 2015)
Dense Bituminous macadam (DBM)	7	2.4e03	
Base	25	0.74e02	
Subbase	45	0.74e02	
Compacted Subgrade	500	0.12e02	
Asphalt	15	1.0e03	(Al-Khoury et al. 2002)
Subbase	25	2.0e02	
Subgrade (fully saturated of water)	infinite	0.25e02	

I. Thick pavement loaded by heavy vehicles

The characteristics of the thick road pavement are described in the following table, and were designed considering the requirement of the Italian standard for the highway (ANAS S.p.a. 2008). In more detail, the surface course (i.e., wearing course layer) consists of a porous asphalt concrete layer, and the road section includes three bounded layers (asphalt concrete; see black cells in Tabs. 3.2, and 3.3) and 3 un-bounded layers (see white cells in Tabs. 3.2, and 3.3).

The following inputs were implemented in the software (see Fig. 3.2, and Tab. 3.2):

- Number of layers = 6 (linear elastic material, all layer interfaces are bonded);
- Poisson's ration $\nu = 0.35$ (dimensionless);

- Number of passages of the vehicles in 1-year N = 5 million (considered as a single period, i.e. without any season or temperature change in a year);
- Contact pressure = 490 kPa (derived considering a vehicle weight of about 8 ton = 8000 kg);
- Contact radius r = 11.46 cm;
- Points of analysis = 2 (indicated in Fig. 3.2 with 1 (0, 0), i.e. under the external wheel, and 2 (0, 17), i.e. in the middle of the space between the two wheels, which are 34.5 cm from each other).

Tab. 3.2 Characteristics of the thick road pavement.

Layer number	Layer name	Layer thickness (cm)	Layer elastic modulus (MPa)
1	Surface Course	5	1000
2	Binder	7	2500
3	Base	15	1500
4	Cement treated base	20	5000
5	Subbase	20	100
6	Sub-grade	Semi-infinite	90

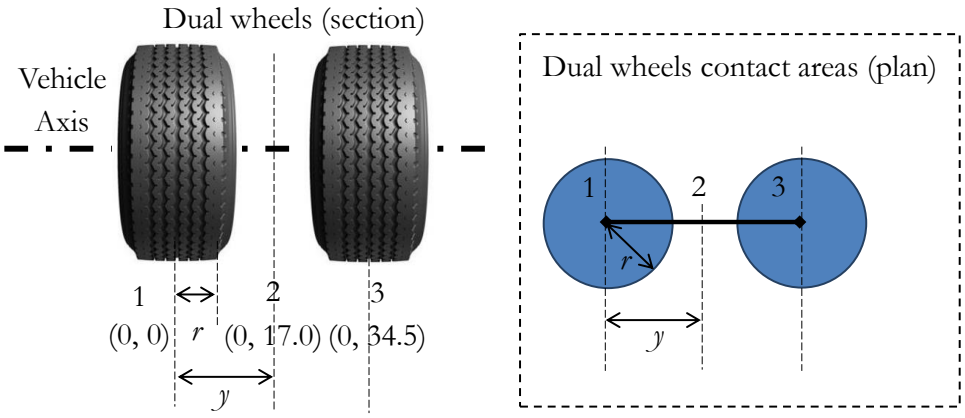

Fig. 3.2 Section and plan schemes of a typical configuration of a heavy vehicle axis that consists of a couple of dual wheels.

Using the software KENLAYER the following values were derived (see Tab. 3.3). Note that positive strains correspond to compression-shrinkage, while negative strains correspond to tensile stresses.

Tab. 3.3 Results of the simulation I (thick pavement-heavy vehicles).

Point of analysis	Depth (cm)	Disp. (mm)	σ_V (kPa)	$\sigma_{V,max}$ (kPa)	ε_V (-)	ε_H (-)
1	0	0.216	512	512	2.3e-04	7.8e-05
	5	0.204	459	459	2.7e-04	1.5e-05
	12	0.196	303	304	1.1e-04	-4.1e-05
	27	0.181	117	129	4.8e-05	-2.6e-7
	47	0.176	13	13	3.7e-05	-3.8e-05
	67	0.156	9	9	8.8e-05	-3.1e-05
2	0	0.184	93	112	1.5e-05	3.8e-05
	5	0.191	33	96	2.5e-05	2.5e-05
	12	0.191	128	209	1.5e-05	-2.6e-05
	27	0.184	99	99	3.7e-05	1.4e-7
	47	0.180	13	13	4.1e-05	-4.1e-05
	67	0.160	10	10	9.3e-05	-3.2e-05

Symbols: Disp. = layer displacement; σ_V = vertical stress; $\sigma_{V,max}$ = maximum vertical stress; ε_V = vertical strain (dimensionless); ε_H = horizontal strain (dimensionless).

Based on the results contained in the Tab. 3.3, the software calculate the Damage Ratio (*DR*) of each layers (at the top and at the bottom) for the thick pavement loaded by heavy vehicles, which was shown by the software dashboard as follow (see Fig. 3.3).

```
*****************************
* SUMMARY OF DAMAGE ANALYSIS *
*****************************
AT BOTTOM OF LAYER  1     SUM OF DAMAGE RATIO = 0.000E+00
AT BOTTOM OF LAYER  2     SUM OF DAMAGE RATIO = 1.295E-02
AT BOTTOM OF LAYER  3     SUM OF DAMAGE RATIO = 4.844E-10
AT BOTTOM OF LAYER  4     SUM OF DAMAGE RATIO = 2.244E-02
AT BOTTOM OF LAYER  5     SUM OF DAMAGE RATIO = 3.766E-04
AT BOTTOM OF LAYER  6     SUM OF DAMAGE RATIO = 3.442E-04
AT TOP OF LAYER  1        SUM OF DAMAGE RATIO = 2.013E-01
AT TOP OF LAYER  2        SUM OF DAMAGE RATIO = 3.750E-03
AT TOP OF LAYER  3        SUM OF DAMAGE RATIO = 4.236E-02
AT TOP OF LAYER  4        SUM OF DAMAGE RATIO = 7.052E-07
AT TOP OF LAYER  5        SUM OF DAMAGE RATIO = 1.097E-02
AT TOP OF LAYER  6        SUM OF DAMAGE RATIO = 4.463E-03

MAXIMUM DAMAGE RATO =   2.013E-01   DESIGN LIFE IN YEARS = 4.97
```

Fig. 3.3 Damage ratio values for the simulation I (thick pavement-heavy vehicles) as shown by the KENLAYER dashboard, together with the estimated design life.

The software, based on the values of *DR* and using the Eq. 3.4, estimated a Design life of the thick pavement loaded by heavy vehicles (dual wheel axis) of about 5 years. The maximum value of *DR* (2.013e-01) refers to the wearing course layer (top of the layer 1), and this means that it is the first layer that fails under the design load and after a number of passage equal to N (i.e., 5 million). The maximum *DR* corresponds to the allowable load repetitions *Nd* = 2.484e07 ≈ 25 million of cycles of the design load. Because of the fact that *Nd* is a function of the vertical compressive strain ε_V, it is possible to state that the pavement fails because of permanent deformation (or rutting) of its surface course layer.

II. Thick pavement loaded by light vehicles

The second case study refers to the thick road pavement (see Tab. 3.2) loaded by light vehicles. The characteristics of the vehicle chosen to derive the light load are reported in the following figure.

Vehicle characteristics

Model: Fiat 500 1.4 16v Fire
Type of wheel: 185/55 R15;
Tire pressure (P) = 2 atm ≈ 203 kPa;
Weight of the vehicle (car + driver + all tanks full)= 930 kg
Carrying capacity (driver included) = 440 kg
Approximate Weight (W) = 1250 kg = 1.250 ton
Number of wheels(n)= 4

$$\text{Contact radius (r)} = \sqrt{\frac{\left(\frac{W}{n}\cdot g\right)}{\pi \cdot P}} = \sqrt{\frac{\left(\frac{1250}{4}\cdot 9.81\right)}{\pi \cdot 203000}} = \sqrt{\frac{3066}{637743}} \approx 6.93\ cm$$

Fig. 3.4 Light vehicle characteristics (FIAT 2016).

The inputs that were implemented in the software were the following:

- Number of layers = 6 (linear elastic material, all layer interfaces are bonded);
- Poisson's ration ν = 0.35 (dimensionless);

- Number of passages of the vehicle in 1 year (N) = 5 million (considered as a single period, i.e. without any season or temperature change in a year);
- Contact pressure = 203 kPa;
- Contact radius r = 6.93 cm;
- Points of analysis = 1 (i.e., under one wheel).

The following values (see Tab. 3.4) were calculated by the software.

Tab. 3.4 Results of the simulation II (thick pavement-light vehicles).

Point of analysis	Depth (cm)	Disp. (mm)	σ_V (kPa)	$\sigma_{V,\,max}$ (kPa)	ε_V (-)	ε_H (-)
1	0	0.030	203	204	1.4e-04	3.3e-05
	5	0.021	174	80	1.2e-04	-9.1e-06
	12	0.018	71	-17	3.3e-05	-4.1e-05
	27	0.014	20	9	8.9e-6	-5.9e-07
	47	0.014	1	-27	4.0e-06	-3.6e-06
	67	0.012	0.7	0	7.6e-06	-2.6e-06

Symbols: Disp. = layer displacement; σ_V = vertical stress; $\sigma_{V,max}$ = maximum vertical stress; ε_V = vertical strain (dimensionless); ε_H = horizontal strain (dimensionless).

Even in this case (simulation II), the software returned the values of the *DR* of the pavement layers, and estimated the Design life of the pavement.

```
******************************
* SUMMARY OF DAMAGE ANALYSIS *
******************************
AT BOTTOM OF LAYER  1     SUM OF DAMAGE RATIO = 4.129E-05
AT BOTTOM OF LAYER  2     SUM OF DAMAGE RATIO = 4.139E-04
AT BOTTOM OF LAYER  3     SUM OF DAMAGE RATIO = 7.038E-09
AT BOTTOM OF LAYER  4     SUM OF DAMAGE RATIO = 7.597E-06
AT BOTTOM OF LAYER  5     SUM OF DAMAGE RATIO = 9.487E-08
AT BOTTOM OF LAYER  6     SUM OF DAMAGE RATIO = 8.671E-08
AT TOP OF LAYER  1        SUM OF DAMAGE RATIO = 2.183E-02
AT TOP OF LAYER  2        SUM OF DAMAGE RATIO = 2.675E-04
AT TOP OF LAYER  3        SUM OF DAMAGE RATIO = 1.257E-04
AT TOP OF LAYER  4        SUM OF DAMAGE RATIO = 7.993E-10
AT TOP OF LAYER  5        SUM OF DAMAGE RATIO = 2.455E-07
AT TOP OF LAYER  6        SUM OF DAMAGE RATIO = 6.069E-08

MAXIMUM DAMAGE RATO =   2.183E-02   DESIGN LIFE IN YEARS = 45.8
```

Fig. 3.5 Damage ratio values for the simulation II (thick pavement-light vehicles), together with the estimated design life.

Fig. 3.5 shows that the weaker layer is the first one because of the fact that the highest *DR* value (2.183e-02) refers to the top of the layer 1. This critical value depends on the allowable load repetitions *Nd* = 2.290e08 ≈ 229 million of cycles of the design load. The design life of the pavement is about 46 years and the pavement fails because of permanent deformation (or rutting) of the surface course layer.

III. Thin pavement loaded by heavy vehicles

In this case study, the thin pavement (e.g., poor urban section) consisting of three layer (one bounded and two un-bounded) with the characteristics reported in the table below. The heavy load is the same of the simulation I.

Tab. 3.5 Characteristics of the thin road pavement.

Layer number	Layer name	Layer thickness (cm)	Layer elastic modulus (MPa)
1	Surface Course	3	1000
2	Subbase	20	100
3	Subgrade	Semi-infinite	90

The inputs that were implemented in the software were the following:

- Number of layers = 3 (linear elastic material, all layer interfaces are bonded);
- Poisson's ration ν = 0.35 (dimensionless);
- Number of passages of the vehicle in 1 year (*N*) = 5 million;
- Contact pressure = 490 kPa (derived considering a vehicle weight of about 8 ton = 8000 kg);
- Contact radius *r* = 11.46 cm;
- Points of analysis = 2 (indicated in Fig. 3.2 with 1 (0, 0), i.e. under the external wheel, and 2 (0, 17), i.e. in the middle of the space between the two wheels, which are 34.5 cm from each other).

The software returns the following results (see Tab. 3.6).

Tab. 3.6 Results of the simulation III (thin pavement-heavy vehicles).

Point of analysis	Depth (cm)	Disp. (mm)	σ_V (kPa)	$\sigma_{V,max}$ (kPa)	ε_V (-)	ε_H (-)
1	0	1.084	694	1930	-6.3e-04	9.4e-04
	3	1.051	464	464	8.2e-04	-5.0e-04
	23	0.573	129	131	1.3e-03	-5.9e-04
2	0	0.768	-17	383	7.1e-05	-7.6e-04
	3	0.768	64	909	-2.8e-04	-2.7e-04
	23	0.594	113	113	1.1e-03	-6.1e-04

Symbols: Disp. = layer displacement; σ_V = vertical stress; $\sigma_{V,max}$ = maximum vertical stress; ε_V = vertical strain (dimensionless); ε_H = horizontal strain (dimensionless).

```
*******************************
* SUMMARY OF DAMAGE ANALYSIS *
*******************************
AT BOTTOM OF LAYER  1      SUM OF DAMAGE RATIO = 2.215E+01
AT BOTTOM OF LAYER  2      SUM OF DAMAGE RATIO = 5.815E+00
AT BOTTOM OF LAYER  3      SUM OF DAMAGE RATIO = 5.314E+00
AT TOP OF LAYER  1         SUM OF DAMAGE RATIO = 9.338E-04
AT TOP OF LAYER  2         SUM OF DAMAGE RATIO = 3.361E+04
AT TOP OF LAYER  3         SUM OF DAMAGE RATIO = 6.167E+02

MAXIMUM DAMAGE RATO =   3.361E+04   DESIGN LIFE IN YEARS = 0.
```

Fig. 3.6 Damage ratio values for the simulation III (thin pavement-heavy vehicles), together with the estimated design life.

In this case of study, the weaker layer is the second one because of the highest *DR* value (3.361e+04) that occurs at its top. This high value leads to an extremely low Design Life of the pavement (3.0e-05 years, i.e., almost 20 min under the heavy load repeated 150 times cf. design life in years = 0 in Fig. 3.6). Moreover, this *DR* is function of *Nd* = 1.487e02 ≈ 149 cycles of the design load. Hence, the pavement fails because of permanent deformation or rutting of the subbase layer.

IV. Thin pavement loaded by light vehicles

The last case study refers to the thin pavement (see simulation III) and the light load (see simulation II). Hence, the inputs that were implemented in the software were the following:

- Number of layers = 3 (linear elastic material, all layer interfaces are bonded);

- Poisson's ration ν = 0.35 (dimensionless);
- Number of passages of the vehicle in 1 year (*N*) = 5 million (considered as a single period, i.e. without any season or temperature change in a year);
- Contact pressure = 203 kPa;
- Contact radius *r* = 6.93 cm;
- Points of analysis = 1 (i.e., under one wheel).

The results of the simulation IV are reported in Tab. 3.7.

Tab. 3.7 Results of the simulation IV (thin pavement-light vehicles).

Point of analysis	Depth (cm)	Disp. (mm)	σ_V (kPa)	$\sigma_{V,max}$ (kPa)	ε_V (-)	ε_H (-)
1	0	0.186	203	712	-2.1e-04	3.6e-04
	3	0.180	148	-353	3.9e-04	-2.8e-04
	23	0.063	20	-2	2.2e-04	-8.7e-05

Symbols: Disp. = layer displacement; σ_V = vertical stress; $\sigma_{V,max}$ = maximum vertical stress; ε_V = vertical strain (dimensionless); ε_H = horizontal strain (dimensionless).

```
*******************************
* SUMMARY OF DAMAGE ANALYSIS *
*******************************
AT BOTTOM OF LAYER  1      SUM OF DAMAGE RATIO = 3.311E+00
AT BOTTOM OF LAYER  2      SUM OF DAMAGE RATIO = 9.827E-03
AT BOTTOM OF LAYER  3      SUM OF DAMAGE RATIO = 8.981E-03
AT TOP OF LAYER  1         SUM OF DAMAGE RATIO = 0.000E+00
AT TOP OF LAYER  2         SUM OF DAMAGE RATIO = 3.383E+02
AT TOP OF LAYER  3         SUM OF DAMAGE RATIO = 2.113E-01

MAXIMUM DAMAGE RATO =   3.383E+02   DESIGN LIFE IN YEARS = 0.
```

Fig. 3.7 Damage ratio values for the simulation IV (thin pavement-light vehicles), together with the estimated design life.

Analyzing the figure above is possible to assert that the weaker layer is the second one because of the highest *DR* value (3.383e+02) that occurs at its top. As a consequence of this, the pavement fails because of permanent deformations (or rutting) of the subbase layer. The Design life of the pavement is very low (3.0e-03 years, i.e., almost 26 hours under the heavy load repeated 15000 times; cf. design life = 0 in Fig. 3.7), as well as the

allowable load repetition Nd = 1.478e04 ≈ 15 thousand of cycles of the design load.

The tables below summarize the results of the four simulations, aiming at characterizing the cause of failure (e.g., horizontal or vertical stain, position, magnitude), and the effects of each occurred failure in terms of maximum displacement of a given layer.

Tab. 3.8 Summary of the maxima horizontal stains ε_H at the bottom of the bounded layers (responsible for the fatigue failures).

Load / **Pavement**	***Light (2 wheels for axis)***	***Heavy (4 wheels for axis)***
Thick pavement (6 layers)	-4.1e-05	-4.1e-05
Thin pavement (3 layers)	-2.8e-04	**-5.0e-04**

Tab. 3.9 Summary of the maxima vertical stains ε_V at the top of the first un-bounded layers under the bounded ones (responsible for the rutting).

Load / **Pavement**	***Light (2 wheels for axis)***	***Heavy (4 wheels for axis)***
Thick pavement (6 layers)	8.9e-6	4.8e-05
Thin pavement (3 layers)	2.2e-04	**1.3e-03**

Bearing in mind that positive strains correspond to compression-shrinkage, while negative strains correspond to tensile stresses, the maxima vertical and horizontal strains were analyzed (see also Fig. 3.1).

First of all, it is important to notice that all the maxima horizontal strains are negative, i.e. they produce tensile strains. Secondly, the horizontal strains at the bottom of the asphaltic layers of the thick road pavement are the same for both load conditions, i.e. -4.1e-05. This means that the response of the thick pavement is independent from the type of load. While, the thin pavement shown a different behavior under different loads that is proportional to the load magnitude.

On the other hand, the maxima of the vertical strains on the top of the first un-bounded layer under the bonded ones resulted almost negligible in comparison with those of the thin pavement. Furthermore, the horizontal

strains are almost always bigger, in absolute value, than the vertical strains, in all the simulations.

In addition, these results show that: i) in the thick pavement, the occurrence of concealed cracks can be mainly attributed to tensile horizontal strains (about -4e-05) that affect the lowest bounded layer if traffic consists of light vehicles; ii) in the thick pavement, the occurrence of concealed cracks can be mainly attributed to the combination of tensile horizontal strains (about -4e-05) that affect the lowest bounded layer, and of compressive vertical strains (about 5e-05) that affect the highest un-bounded layer if traffic consists of heavy vehicles; iii) in the thin pavement, the occurrence of concealed cracks can be mainly attributed to the interaction between of tensile horizontal strains (about -3e-04) that affect the lowest bounded layer and of compressive vertical strains (about 2e-04) that affect the highest un-bounded layer if traffic consists of light vehicles; iv) in the thin pavement, the occurrence of concealed cracks can be mainly attributed to compressive vertical strains (about 1e-03) that affect the highest un-bounded layer if traffic consists of heavy vehicles

The results of the simulations discussed in this section of the thesis are consistent with the literature and provide a characterization of the main causes that lead to the generation and propagation of concealed distresses in road pavements.

3.2. Design of a new NDT-SHM method for road pavements

The objective of this section is presenting a new Non-Destructive Test (NDT)-based Structural Health Monitoring (SHM) method specially designed for road pavements.

First of all, it is important to state that the non-destructivity was chosen to obtain the sustainability required by the current and future smart cities, as discussed in the previous chapters. In addition, this method was designed aiming at providing an innovative, and alternative solutions to those reported in the state-of-the-art analysis carried out in the Chapter 2. In fact, the literature review shows that despite the high number of SHM solutions

designed for the civil engineering assets, there is a lack in implementation of these solutions in real contexts (e.g., on road infrastructures).

The innovation related to the new method mainly refers to: i) the target of the method; ii) the concept of vibro-acoustic signature. In particular, the target of the method is the identification of the concealed distresses that, as discussed in the sections above, are difficult to be detected and monitored, and often are the cause of the surface distresses that affect the flexible road pavements. In this thesis, the structural health condition refers to the structural integrity, which can range from that of a new pavement (as-built, hence without external or internal cracks) to the one of a damaged pavement (where it is ease to identify deep cracks, potholes, or other surface distress).

The method is based on the concept of vibro-acoustic signature. This concept is widely used by process and fabrication industries in order to estimate the availability, the reliability, and the efficiency of the key components of machineries through real time and not invasive monitoring techniques, and advanced signal processing (see e.g., (Hemmati, Orfali, and Gadala 2016; Vujnovic, Djurovic, and Kvascev 2016)). These industries use this method to monitor their productivity, to control their products in terms of quality and safety, and also to optimize the management process. But, it is easy to understand that this concept can be extended to other fields.

The new method should be able to detect, at an early point, the internal cracks of an apparently intact pavement, starting from acoustic signals analysis. Hence, it should identify the cracks that were generated in the subbase-base layers' interface, when they are not already propagated through all the pavement layers up to the wearing course layer.

The core idea of the method is to consider the road pavements as filters, i.e. media in which there is a transmission of vibration and sound waves from a mechanical source (see Fig. 3.8) to a receiver system that is able to derive the vibro-acoustic signature of the monitored road pavement.

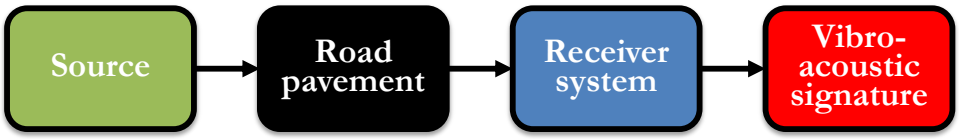

Fig. 3.8 Schematic representation of the main parts of the new NDT-SHM method.

The method involves a source of noise and vibration and a receiver of the signals generated by the source. The method can be classified as "passive" (cf. section 2.4) because of the fact that it considers as sources those already present around the road pavement, i.e. aims at taking advantage from all the seismic waves that travel into the road pavement during the use of these infrastructures (Operational phase; cf. section 2.1). Thus, the method considers the traffic (vehicles pass-by) as the preferred mechanical source.

The receiver system must be able to detect the vibro-acoustic response of the monitored road to the stresses generated from the source. A properly isolated broadband microphone was selected as main sensor of the receiver system. For this reasons the proposed method can be classified as "acoustic method" (or stress- and wave-based method; cf. section 2.4). Importantly, the method needs a microphone that is isolated from the airborne noise and that is able to detect the acoustic signals transmitted by the pavement (filter) only, acting as a "stethoscope". Hence, the sound pressure detected by the microphone derives by the transformation of the vibration that travelling in the road into sound, due to a change of medium of propagation (from solid, i.e. the road, to fluid, i.e. the air around the microphone).

As is well known, the propagation of both vibrations and sound in solids is a function of different parameters (Achenbach 1973), such as the type of source, the distance between source (of noise and vibrations) and receiver (which causes geometric attenuation (Kim and Lee 2000)), and the material damping that is a function of the medium properties, the amplitude and the frequency band of the seismic waves (Woods and Jedele 1985). One of the main properties of a transmission medium it the elastic modulus (Esfandiarpour and Shalaby 2017; Lin et al. 2016). This latter is a key factor of the waves propagation because it is in turn function of the several factors,

such as the temperature of the medium (which affects the geometry because of can generate thermal expansion; cf. (Lamothe, Perraton, and Di Benedetto 2015; Taha et al. 2013)), the thickness of the material, the boundary conditions (e.g., the status of the foundation layers, or the presence of water), and the structural integrity (structural health conditions). In addition, the vibration phenomena, caused by tire-road interaction, depend on air temperature, pavement structure and moduli (Heisey et al. 1982). Furthermore, it is important to underline that experimental procedures (e.g. sampling process, experimental setup used, etc.) can affect the received signals, and this can lead to errors due to misinterpretation.

The new method proposed in this thesis is focused on the identification of the variations of the road pavement structural health status by means of the monitoring of the vibro-acoustic signatures of the pavement. It is expected that many characteristics of the recorded signals are related to the level of deterioration of the road pavement (filter). The relationship between the deterioration of the pavement and the variation (temporal and spectral) of the recorded signals can be properly recognized by specially designed and efficient (see section 2.5) data processing methods. Consequently, each and every level of deterioration can be associated to a specific acoustic signature.

3.3. Design of experiments

In order to set up, improve, and validate the new NDT-SHM method presented in the section above, the experimental plan shown in the following figure was carried out during the research project. In particular, different experimental investigations were carried out in-lab (on samples of asphalt concrete) and on-site (on un-damaged and specifically damaged road pavements, hereafter called Un-Cracked, UC, and Cracked, C), using different devices, as described in the following two chapters of the thesis.

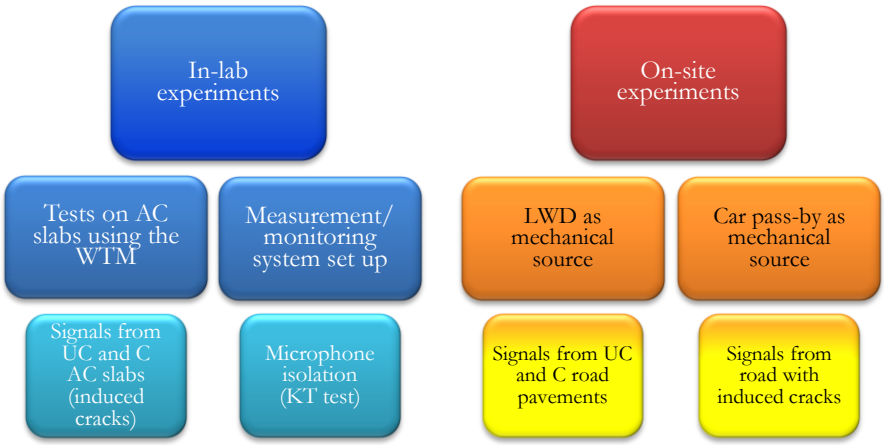

Fig. 3.9 Experimental plan..

4
In-lab experiments and data analysis

Several experimental investigations were carried out in laboratory and on site to validate the structural health monitoring method presented in this thesis. This section refers to the experiments carried out in laboratory on asphalt concrete samples (slabs). These experiments aimed at gathering the vibro-acoustic signature of the slabs, characterized by different structural health statuses (SHSs). A Wheel Tracking Machine was used as conventional load. The main objective of this experiments was to understand if it is possible to recognize the SHS of a slab from its vibro-acoustic signature using a proper data analysis.

4.1. In-lab experiments using the Wheel Tracking Machine[3]

The first approach (Fedele, Della Corte, et al. 2017; Fedele, Praticò, et al. 2017; Fedele R., Praticò F. G., Carotenuto R. 2017) used to assess the feasibility of the non-destructive-test-based (NDT), Structural Health Monitoring (SHM) method, presented in this thesis, aimed at trying to control as many parameters of the problem (e.g., the boundary conditions, the composition of the asphalt concrete, etc.) as possible. For this reason, the experimental investigation consisted of tests carried out in laboratory on asphalt concrete (i.e., Dense Graded Friction Course mix, DGFC) slabs using a Wheel Tracking Machine (hereafter called WTM) as conventional load. A microphone to gather the vibro-acoustic signatures of the slabs under test.
Several experiments were carried out according to the following procedure:

Task 1. Mechanistic analysis of the DGFC slabs under test (Tab. 4.1).
Task 2. Hardware set up (i.e., slab, microphone, cable, and laptop).
Task 3. Matlab coding for acoustic signals recording and analysis.
Task 4. Preliminary tests, and design of the final tests.
Task 5. Final tests.
Task 6. Results analysis.

[3] This section mainly refers to the papers 1.1, 1.2, and 1.7 (see Scientific production).

The WTM is a machine that was designed to produce (i.e., compact) slabs according to the standards UNI EN 12697-33 (UNI 2007b) (or Colorado Procedure – Laboratory 5116-10 (Colorado Department of Transportation 2015)), and UNI EN 12697-35:2016 (UNI 2016), and to carry out the rutting test according to the standard EN 12697-22:2007 (UNI 2007a).

The WTM used in this research (see Fig. 4.1) consists in a chamber where a metallic housing (that contains the material to be compacted or the slab to be tested) is moved back and forth while a rubber wheel apply a given load. It is important to notice that this machine allows to work under controlled conditions, and for this reason was chosen for this tests. In particular, it is possible to set and control the following parameters: i) the load applied by the rubber wheel (which simulate a properly scaled passage of one vehicle's tire on the road pavement); ii) the number of passage of the wheel; iii) the speed of the wheel; iv) the temperature of the chamber using two thermocouples, which must be put into the sample.

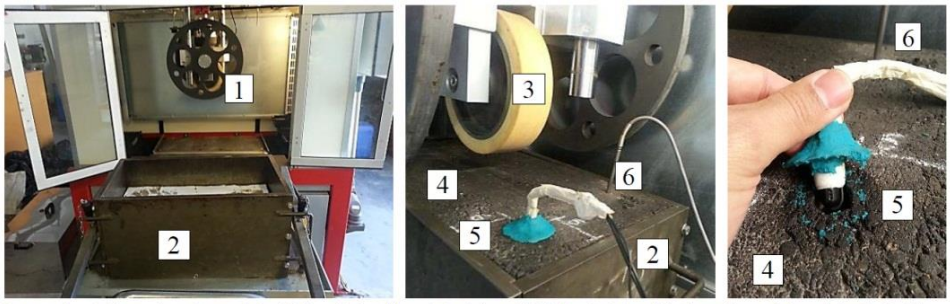

Legend: 1:Test chamber of the Wheel Tracking Machine (WTM); 2: Metallic housing of the slab; 3: Rubber wheel of the WTM; 4: Hot mix asphalt slab; 5: Microphone placed in the hole drilled in the slab, held in place by modeling clay; 6: Thermocouple into the drilled hole.

Fig. 4.1 Wheel Tracking Machine used to produce and test different DGFC slabs.

During the compaction process (UNI EN 12697-33; (UNI 2007b)) a single slab (see point 4 in Fig. 4.1), with a rectangular base of 500×260 mm^2 and variable thicknesses (e.g., 50 mm), can be produced. Briefly, the hot mixture (determined according to the standard UNI EN 12697-35; (UNI 2016)) is put into the metallic housing (which consists of a steel box with sides 16 mm thick; see point 2 in Fig. 4.1), this latter is placed in the chamber (see point 1 in Fig. 4.1) and is covered with metallic sticks. At this point, the rubber wheel (which has a diameter of about 200 mm, and a width of 5 mm; see point 3 in

Fig. 4.1) of the WTM presses, at 0.7 kN, the metallic sticks simulating a real roller compactor (i.e., the machine that is deputed to the compaction of the road pavement) until the pre-defined thickness of the slab is reached (e.g., 50 mm). In order to assure a proper compaction process, two thermocouples (see point 6 in Fig. 4.1) are insert in the hot material and are used to monitor the temperature.

During the rutting test (EN 12697-22:2007; (UNI 2007a)) the rubber wheel rolls back and forth on a slab, which is held in place by a metallic housing, under controlled conditions (i.e., the parameters mentioned above).

In this experimental investigation, the WTM was chosen: i) to produce and compact, under controlled conditions, three DGFC slabs, which were considered as samples of a road surface (according to the standard: UNI EN 12697-22; (UNI 2007a)); ii) to generate realistic conditions in terms of both the load applied by a vehicle's wheel, and the waves (seismic and sound) generated by a rolling wheel on a road surface, in order to record the vibro-acoustic signature (acoustic signals) of the produced slabs.

The experimental investigation described in this section of the thesis was carried out following the procedure defined above, which starts with the Task 1, i.e. the mechanistic analysis of the DGFC slabs under test. The results of this first laboratory tests are reported in the following table.

Tab. 4.1 Results of the mechanistic analysis of the slabs under tests

Mix type	Bitumen percentage (%)	G_{mb} (g/g)	AV (%)	Filler percentage (%)
DGFC	5	2.3	8	4

Task 2 refers to the setup of the hardware, i.e. the slabs and the electronic system used to gather the vibro-acoustic signature (acoustic signal) of the slabs.

First of all, a set of three slabs were produced using the WTM. Secondly, these slabs were prepared to be tested. On two corners of each slab (on the face where the wheel of the WTM runs), two holes were drilled (diameter of 8 mm and depth of 25 mm) to place the thermocouples (cf. Fig. 4.2). On the

same faces of the slabs, one hole (diameter of 20 mm, 60 mm far from the sides of the slabs, and 25 mm depth) was drilled to place the microphone of the electronic system (cf. Fig. 4.2). Note that, although the SHM method presented in this thesis is non-destructive, during the experiments described in this section a semi-destructive approach was carried out, which relates to the holes drilled on the slabs.

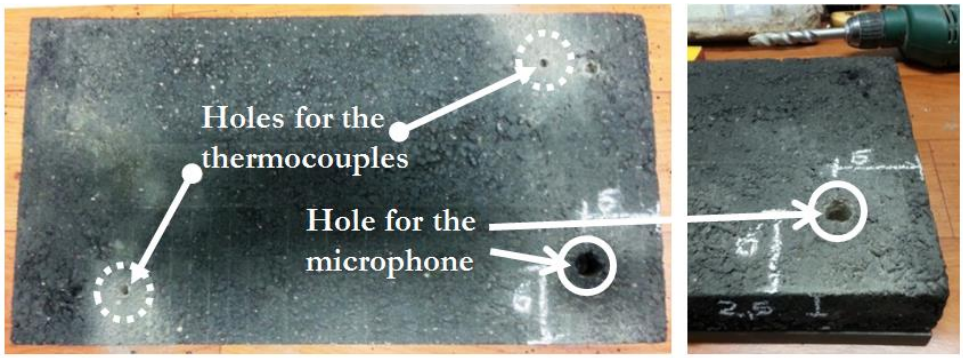

Fig. 4.2 Holes drilled on the DGFC slabs before the WTM tests.

The electronic system used during the tests consisted of: i) a microphone (omnidirectional, sensibility: -42 dBA, impedance: 2200 Ohm, rated current: 0.5 mA, diameter: 4 mm); ii) a laptop where a proper Matlab code was executed to record and analyze the acoustic signals gathered during the tests.
Task 3 consists of the writing of a Matlab code that aimed at recording and analyze the data collected using the microphone. Fig. 4.3 shows the main tasks of the Matlab code (which are defined in detail in the following).

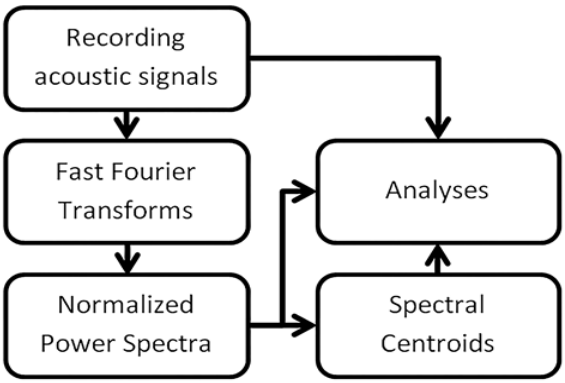

Fig. 4.3 Flow chart of the Matlab codes (Task 3).

Preliminary tests (Task 4) were carried out to: a) get more confident with the WTM; b) setup all the boundary conditions (e.g., the load to be applied, the temperature of the WTM chamber, the number of passages of the WYM wheel, etc.); c) set up the Matlab code used to record the data (e.g., duration of the recording, sampling frequency, etc.). These tests allowed to highlight that: i) higher loads seem to correspond to higher peak amplitudes; ii) peak frequency does not undergo appreciable variations based on load. For these reasons the tests were carried out according to the rutting test, i.e. using a load of 0.7 kN.

The main task of the experimental investigation consisted of the tests carried out on the three slabs using the WTM using the electronic system (Task 5). Three slabs were used because of the fact that three different structural health conditions were investigated. In particular, the first one was called UC (Un-Cracked slab), the second one LC (Lightly-Cracked slab), and the last one HC (Highly-Cracked slab). In the LC and HC slabs, two different macro cracks (grooves) were made in the lower surface (the one opposite to the upper where the wheel rolls). The cracks dimensions are 260×3×10 mm^3 for the LC, and 260×3×20 mm^3 for the HC. Consequently, they differ only for their depth, i.e. 10 mm and 20 mm, respectively (cf. Tab. 4.2).

Tab. 4.2 Factorial plan of the experimental investigation (Task 5 and 6).

Test ID	Groove dimensions (mm^3)	Slab ID	Type of groove	Type of load (kN)
1	0x0x0	UC*	TR	0.7
2	260x10x3	LC*	TR	0.7
3	260x20x3	HC*	TR	0.7

*UC, LC, HC stand for Un-Cracked, Lightly, and Highly Cracked, respectively.

**TR: Transversal to the wheel path. The grooves have a length of 260 mm, a width of about 3 mm and two different depths, i.e. 10 mm for the LC slab and 20 mm for the HC slab.

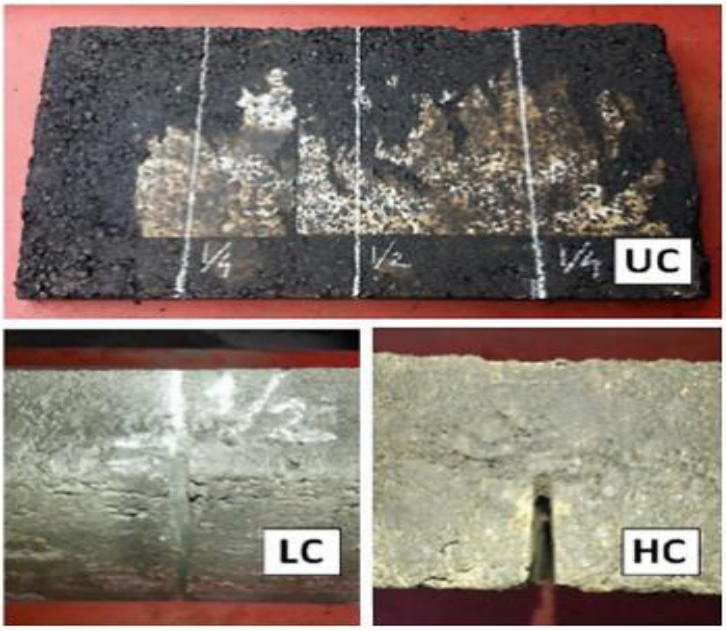

Fig. 4.4 The three slabs under investigation. UC = Un-Cracked; LC = Lightly Cracked; HC = Highly Cracked.

Subsequently, the tests were carried out using the WTM on the three slabs, according to the following steps: i) the slab was put in the metallic housing to prevent any undesired displacement; ii) the two thermocouples were placed into the two holes located on two opposite corners of the up-per slab face; iii) the microphone was placed in a suitable hole and held in place by a sufficient amount of modeling clay (deputed to the sound insolation; cf. point 5 in Fig. 4.1); iv) the test chamber was sealed by closing its two doors; v) using the control panel of the WTM (Fig. 4.5), the test parameters have been set, i.e. the temperature of 30°C, the load of the wheel (0.7 kN, corresponding to about 0.3 MPa; cf. Eq. 4.1), and the number of passages of the wheel on the slab (200); vi) the WTM and the signal recording were started at the same time. It is important to notice that the value of the load of the wheel is the same of the load used during the rutting test. Computations were carried out in order to estimate the load of a wheel (cf. section 3.1) of a heavy vehicle (about 500 kPa) and of a wheel of a light vehicle (about 200 kPa), using the following expression:

$$Load = \frac{0.7kN}{0.05 \cdot 0.05m^2} = \frac{0.7kN}{0.0025m^2} = 280kPa \cong 0.3\frac{kg}{cm^2}. \qquad (4.1)$$

Fig. 4.5 Control panel (dashboard) of the WTM.

Fig. 4.5 shows the control panel of the WTM, where are indicated: a) the temperature measured using the thermocouples; b) the maximum strain of the slabs (i.e., 1.5 mm in this case); c) the load applied by the wheel (i.e., 0.7 kN); d) the maximum number of cycle of the wheel (i.e., 100, which means 200 passages).

An appropriate Matlab code was started together with the WTM, and this code was used to records the signals at the sampling frequency of 192 kilo samples *per* second (kS/s). One signal, with a duration of about 280 s, was recorded *per* each slab, and Fig. 4.6 shows one set of acoustic signatures related to one slab recorded during the tests. In particular, Fig. 4.6b, shows a detail of the, Fig. 4.6a, in which is possible to see a couple of passages of the wheel that represents a single cycle of the WTM wheel.

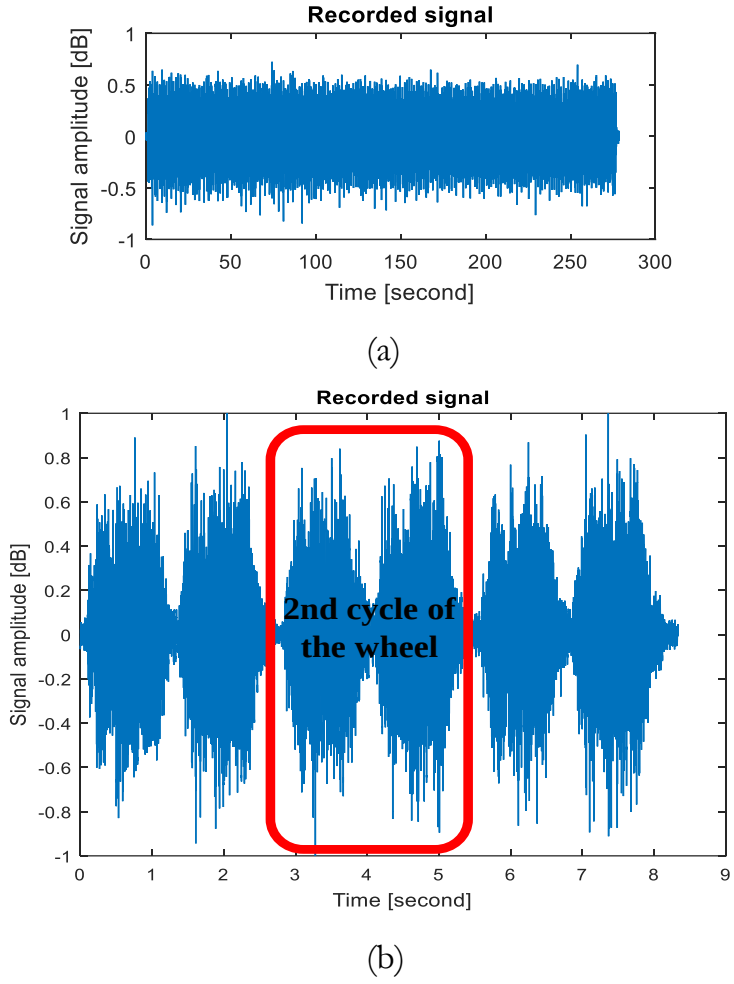

Fig. 4.6 Vibro-acoustic signatures of one slab during the test using the WTM, related to (a) 200 passages, and (b) 6 passages of the WTM wheel.

Finally, in Task 6, the acoustic signal recorded were analyzed in the frequency domain as reported in the following section. Fig. 4.7 shows the results of preliminary analyses that were carried out to define the spectral content of the signals recorded during the tests. As it is possible to see, the signals have a spectral content that mainly refers to low-frequencies (i.e., lesser than 200 Hz).

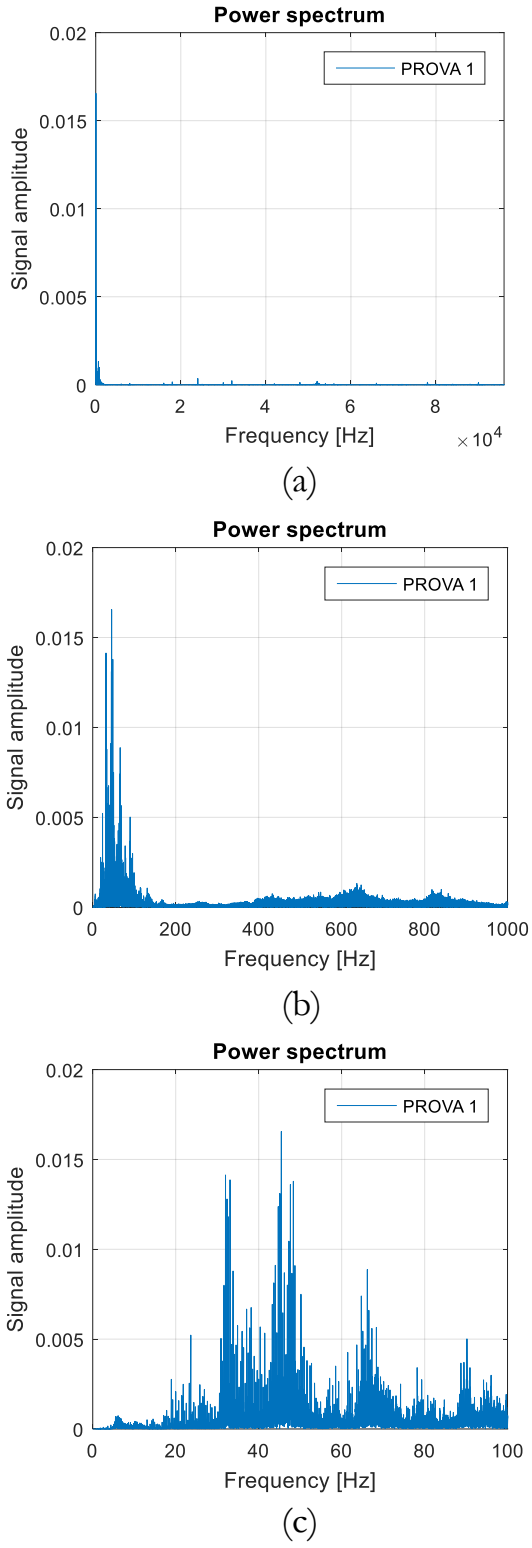

Fig. 4.7 Spectral content of the vibro-acoustic signature of the UC slabs, at different frequency ranges, i.e. (a) 0-96 kHz, (b) 0-1 kHz, and (c) 0-100 Hz.

4.2. Results of the WTM application

During the experiments performed using the WTM, described in the previous paragraphs, a set of signals were recorded. These signals were assumed as the vibro-acoustic signatures of three classes of slabs, which differ from each other for their structural health status (presence or absence of induced grooves), hereafter called UC, LC, and HC. The terms vibro-acoustic signature was used to indicate the response of a slab to the load applied by the rubber wheel of the WTM, which were transmitted (as sound and seismic waves) by the parts of the slabs that are not affected by the induced grooves.

This set of signals were analyzed in the frequency domain using periodograms (Power Spectral Density versus Frequency) obtained applying the following equations.

As is well known (Bendat and Piersol 2000), the power spectral density (or auto-spectral density function, $Gxx(f)$) can be derived using the finite Fourier Transforms $X(f, T)$:

$$G_{xx}(f) = 2 \lim_{T \to \infty} \frac{1}{T} E\left[|X(f,T)|^2 \right], \tag{4.2}$$

or simply

$$G_{xx}(f) = \frac{2}{T} E\left\{ |X(f,T)|^2 \right\}, \tag{4.3}$$

where $Gxx(f)$ is the one-sided, auto-spectral density function (which is twice the two-sided auto-spectral density function) that is defined for $0 < f < \infty$, where f is the frequency, T is the record length, $E[\,]$ is the ensemble average, $X(f, T)$ is the finite Fourier Transform of the signal $x(t)$ of length T, t stands for time, and the absolute value of the finite Fourier Transform is squared.

Note that, for $f < 0$ results:

$$G_{xx}(f) = 0. \tag{4.4}$$

The finite Fourier Transform $X()$ does not have the same units of measure (and dimensions) of the signal, $x(t)$, being:

$$X(f,T)=\int_0^T x(t)e^{-j2\pi ft}dt. \tag{4.5}$$

Furthermore, the two-sided auto-spectral density function *Sxx(f)* can be defined for $-\infty < f < \infty$, by setting, when $f > 0$ (Bendat and Piersol 2000):

$$S_{xx}(f)=\frac{1}{2}\cdot G_{xx}(f), \tag{4.6}$$

and

$$S_{xx}(-f)=S_{xx}(f). \tag{4.7}$$

If the Fast Fourier Transform (FFT) is used, then the sampling frequency must be used and the above formula becomes:

$$PSD = 2\cdot\frac{|FFT|^2}{N\cdot Fs}, \tag{4.8}$$

where *Fs* is the sampling frequency (Hz), and *N* is the length of the recorded signals.

Based on the literature and based on the above, PSD expresses the power (Watt) *per* unit of frequency (Hz). The logarithm scale is usually used for the y-axis.

The high sampling frequency used (i.e., 192 kS/s) allowed obtaining periodograms in the frequency range 0-96 kHz. It is important to note that, each periodograms refer to all the passages (i.e., around 200) of the WTM's wheel over each of the three slabs under tests.

The periodograms show the frequency (Hz) on the x-axis, while the y-axis refers to the PSD in a logarithmic scale (dBW/Hz; see Fig. 4.8a). This latter was preferred to the normal one (Fig. 4.8b) because it allows to better highlight the behavior of the PSD at each frequency, as shown in Fig. 4.8.

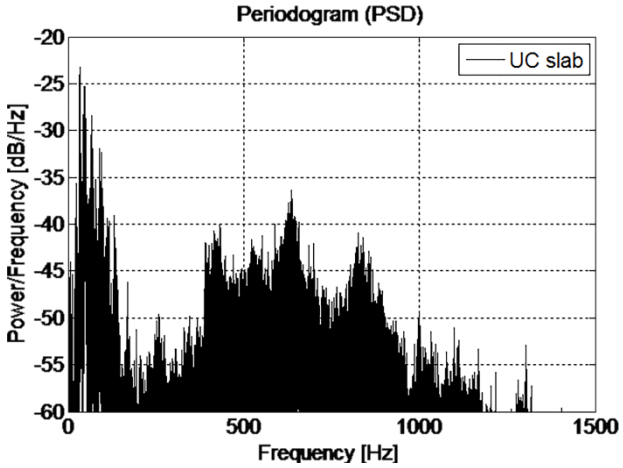

(a)

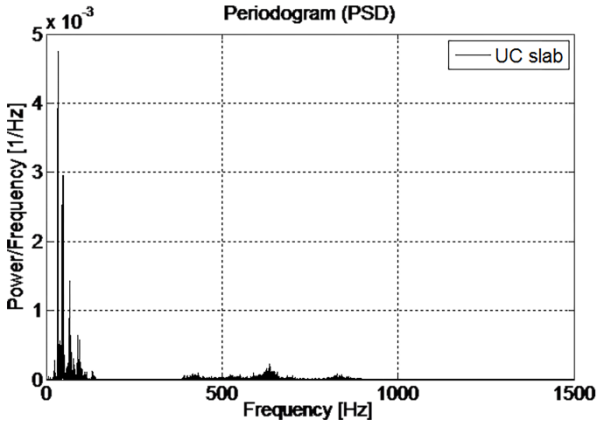

(b)

Fig. 4.8 Example of test results for the Un-Cracked (UC) slabs with the y-axis in: a) logarithmic scale; b) linear scale.

In the pursuit of better analyzing the plots, when the logarithmic scale for the y-axis was used, a value of -60 dBW/Hz was considered as the lower bound (cf. Fig. 4.8a). This allowed at focusing on the frequency range 20-1500 Hz, where the PSD has its highest values (cf. Fig. 4.8a). Trying to identify a pattern or one or more features of the spectrum, six main "peaks" of the periodograms related to the UC slab were marked (see Fig. 4.9). Each peak was associated to a specific frequency range (note that the terms peak is herein used in the sense of area of the plot between relevant minima, or valleys). Hence, the whole frequency range (20-1500 Hz) was divided in 6 new ranges. Consequently, in each new frequency range, the relative peak was calculated, and used to compare the three periodograms (Fig. 4.9).

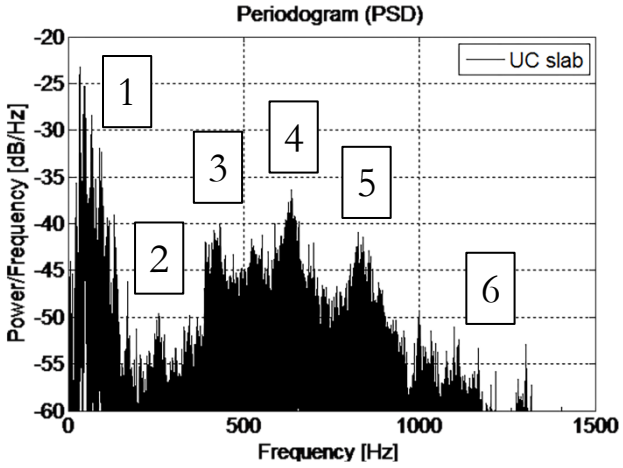

(a)

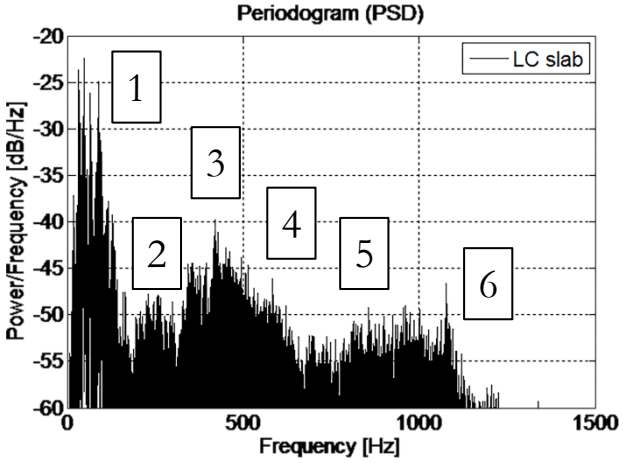

(b)

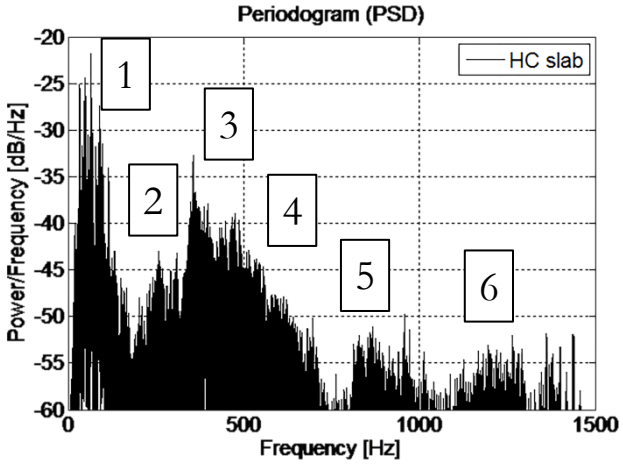

(c)

Fig. 4.9 Periodograms that refer to (a) the Un-Cracked (UC) slabs, (b) the Lightly-Cracked (LC) slabs, and (c) the Highly-Cracked (HC) slabs, where six main picks are marked.

Based on the analyses of the six main peaks of the three periodograms (see Fig. 4.9), it is possible to outline the following observations:

- The peak N. 1, which belongs to the frequency range 20-200 Hz, does not undergo appreciable variations. The maximum is almost constant (25 dBW/Hz), as well as its frequency position (47-54 Hz).
- The peak N. 2, located in the frequency range 200-380 Hz, increases of about 5 dBW/Hz, while its spectral position moves from 305 Hz to 356 Hz.
- The peak N. 3, which refers to the range 380-500 Hz, increases of about 10 dBW/Hz, while its frequency position stays almost constant (427-436 Hz).
- The peak N. 4 (500-750 Hz) undergoes significant deviations in terms of both level and frequency. Its maximum decreases of 10 dBW/Hz, while its frequency decreases (620 to 539 Hz).
- The peak N. 5 (from 750 Hz to 1000 Hz) has variations in terms of both y-axis (-10 dBW/Hz) and x-axis (834-892 Hz), becoming almost negligible.
- The peak N. 6 (1-1.5 kHz) undergoes a slight reduction in terms of PSD (-3 dBW/Hz), but resulted shifted of about 200 Hz (1-1.2 kHz).

In summarizing, the presence of the two grooves in the slabs seems to cause different variations of the PSD. In particular, an absorption of the power of the acoustic signals that pass through the slabs (almost 20 dBW/Hz around 700 Hz) appears evident especially for 600-900 Hz. On the other hand, there is an increase of the power density level (almost 20 dBW/Hz around 350 Hz) in the range 200-400 Hz. While the power density level is almost the same in the range 400-600 Hz.

The considerations reported above suggested that: i) it is possible to define some regions of the periodograms that are almost not influenced by the presence and the increase of the grooves depth (e.g., in this case study, 20-200 Hz, and 380-500 Hz); ii) some frequency band may be used to identify the presence of cracks on the slabs (e.g., in this case study, 200-400 Hz, and

600-900 Hz); iii) it seems difficult to define an overall clear pattern of the PSD (i.e., define a variation of structural health status of the slabs due to the presence of the cracks from the analysis of the PSD) by using only the PSD peaks.

The above-mentioned conclusions led to research a new parameter (feature) that that can be used to describe the overall change of the magnitude of the spectral contents of the signals recorded. This research led to take into account the parameter usually called "spectral centroid", which could be defined as the "center of mass or barycenter" of the spectrum (Schubert and Wolfe 2006), and can be calculated using the following algorithm:

$$f_c = \frac{\sum_{n=0}^{N-1} p_n \cdot f_n}{\sum_{n=0}^{N-1} p_n}, \tag{4.9}$$

where *fc* is the spectral centroid (Hz); *N* is the sample length of the signal; *pn* represent the weights (e.g., the values on the y-axis of the periodogram, dBW/Hz); *fn* are the frequencies (e.g., the values on the x-axis of the periodogram, Hz).

The spectral centroid (feature of the Periodograms) was calculated by considering (i) the frequency range 200-1000 Hz, and (ii) the six frequency range used to define the peaks defined above (different range between 20 and 1500 Hz). Fig. 4.10 shows the feature *fc* as a triangle included in the Periodograms reported above.

The spectral centroids *fc* was calculated where the PSD undergoes the main variations, i.e. in the range 200-1000 Hz. They assumed the value 592 Hz for UC (no cracks), 444 Hz for LC (10-mm crack), and 377 Hz for HC (20-mm crack). These values show that there has been a migration of the spectral centroids toward the low frequencies, due to the presence and the increase of the groove depth. This migration may be related to the vibro-acoustic response of the material of the slabs that is affected by the above-mentioned grooves. In more detail, *fc* undergoes an overall reduction (shift toward the low frequencies) of about 215 Hz. It seems that the presence of a groove depth 10 mm (LC slab) led to a shifting of 148 Hz toward the low

frequencies, and that a groove depth 20 mm led to a supplementary shift of 67 Hz in the same direction.

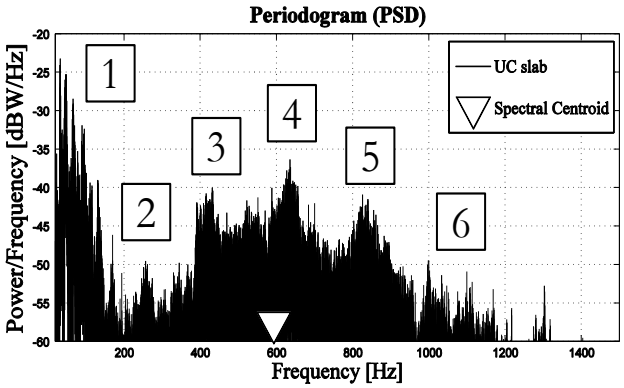

(a)

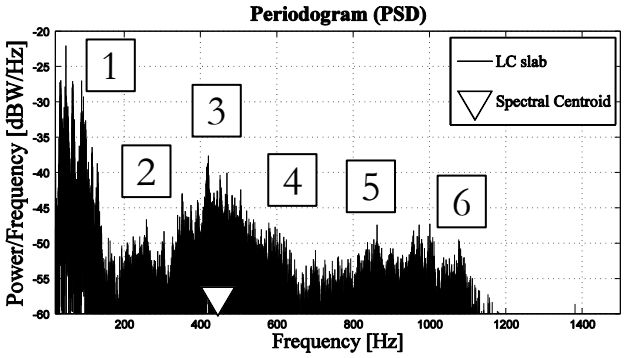

(b)

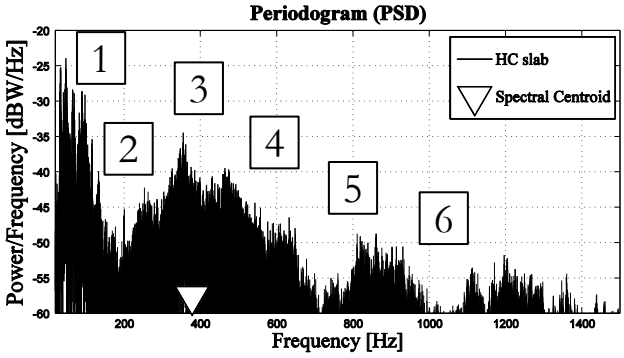

(c)

Fig. 4.10 Variation of the periodogram feature *fc* (triangle), from (a) the Un-cracked (UC) slabs, to (b) the Lightly-cracked (LC) ones, to (c) the Highly-cracked (HC) ones.

A further analysis is reported in Tab. 4.3. In particular, the spectral centroid was calculated in the six frequency ranges used to determine the six peaks of PSD used in the previous analyses.

Tab. 4.3 PSD peaks and spectral centroids (*fc*).

Type of slabs	Peaks of PSD					
	1	*2*	*3*	*4*	*5*	*6*
	Frequency range around the peaks [Hz]					
	20-200	*200-380*	*380-500*	*500-750*	*750-1000*	*1000-1500*
	Spectral centroids (*fc*) [Hz]					
UC*	47	305	427	620	834	1089
LC**	54	333	436	551	892	1062
HC***	53	356	430	539	880	1274

Symbols: * Un-Cracked slab; ** Lightly Cracked slab; *** Highly Cracked slab.

The results contained in Tab. 4.3 confirm the results of the previous analysis, and provides more detailed information. In particular, it should be noted the behavior of the spectral centroid of the range 200-380 Hz (associated to the peak of PSD number 2) that moves to the high frequencies (from 305 to 356 Hz) with two almost constant steps of about 25 Hz (linear behavior). Noteworthy is the migration (620-539 Hz) towards the low frequencies of the spectral centroid of the range 500-750 Hz (associated to the peak of PSD number 4). Unlike the spectral centroids of the range number 2, the latter one does not show a linear behavior because of the fact that it undergoes a considerable initial reduction (about 69 Hz), and, then, a further decrease of about 12 Hz. This two different steps may be attributed to two different causes, i.e. the presence of the first groove (depth 10 mm in the LC slab), and to the increase of 10 mm of the groove depth (from the LC to the HC slab), respectively.

It should be noted that the most meaningful frequency ranges are the second and the forth, and this latter corresponds to frequencies that are almost double in comparison to those of the second intervals. This may be attributed

to the first and second resonance frequencies of the longest side (500 mm) of the slabs under investigation.

By comparing the behavior of the spectral centroid (hereinafter called *fc1*) calculated in the frequency range 200-1000 Hz with the two spectral centroids calculated in the frequency ranges associated to the peak of PSD number 2 and 4, it is possible to observe that the first one (hereinafter called *fc2*) undergoes a shifting of 215 Hz in a range of 800 Hz (200-1000 Hz), while the second one (hereinafter called *fc3*) of 51 Hz in a range of 180 Hz, and the third of 81 Hz in a range of 250 Hz. This means that *fc1* shows a variation of -0.23 Hz/Hz (i.e., = - 215/800 Hz/Hz), *fc2* of +0.28 Hz/Hz, and *fc3* of -0.32 Hz/Hz. In addition: i) *fc1* undergoes a reduction of the 69% because of the first groove, and of 31% because of the second groove; ii) *fc2* increases of the 55% because of the first groove, and of 45% because of the second groove; iii) the percentages for *fc3* are 85% and 15%, respectively. Averaging the percentages related to the first and second groove of *fc2* and *fc3*, it is possible to obtain the values 70% and 30% (i.e., average between 55% and 85%, and 45% and 15%, respectively). These latter are consistent to the percentages related to *fc1*, and, for this reason it is possible to conclude that the overall variation of *fc1* may be principally attributed to the variation of the spectral content of the signals in the frequency ranges 200-380 Hz and 500-750 Hz.

All these results show that, despite the uncertainties and the limitation related to this approach (i.e., use of the WTM on slab, instead of real traffic and road pavements), if the objective is the identification of cracks and/or the monitoring the growth of cracks in structures consisting in asphalt concrete from their vibro-acoustic signature, one feature extracted from the periodogram (analysis in the frequency domain), i.e. the spectral centroid, seems to have the potentialities to allow the achievement of this objective.

4.3. Conclusions and recommendations of the WTM application

In order to identify the presence of cracks and/or monitor the growth of cracks already present in structures consisting in asphalt concrete a new

method has been designed. This method is based on proper analyses of the vibro-acoustic signature of the above mentioned structures. A Wheel Tracking Machine (WTM)-based approach was used as first application of the new method.

First of all, a set of three hot-mix asphalt concrete slabs were built using the WTM (according to the standard EN 12697-33:2007; (UNI 2007b)). On two of the three slabs (herein called Lightly-cracked, LC, and Highly-cracked, HC), two grooves with different depths (10 mm and 20 mm) were created transversally to the largest dimension on one face of the two slabs. The third has not been changed after the production and was called Un-cracked, UC.

Secondly, the three slabs were repeatedly loaded (on the faces opposite at those where the grooves were created) through the WTM (according to the standard used to carry out the rutting test, i.e. the EN 12697-22:2007; (UNI 2007a)), which was used as source of vibration and noise. During the application of the load the vibro-acoustic response of the slabs (acoustic signals) to the WTM load were recorded using a microphone placed in a hole drilled to the face where the WTM rubber wheel apply the load.

Finally, the acoustic responses recorded during the tests were analyzed in order to identify the presence and the growth of the induced grooves. Periodograms (Power Spectral Density vs. Frequency) were used to analyze the spectral content of the recorded signals in the frequency domain. In more detail, the analysis aimed at seeking for, at least, a meaningful feature that could be used to assess and monitor the structural health status of the slabs (and subsequently the status of a real road).

This experimental investigation led to the following conclusions:

- The magnitude of the applied load affects the peak amplitude of the recorded signals, while, in contrast, it does not influence the peak frequency.
- The most relevant changes in the periodograms, which were used to represent and analyze the spectral content of the recorded signals, has been shown in the frequency range from 20 Hz to 1.5 kHz.

- It is possible to define regions of the periodograms (within the range 20-1500 Hz) that are almost not influenced by the presence and the increase of the grooves depth, and other regions that may be used for these purposes. Base on the peaks amplitude, an overall reduction of the average PSD (about -8 dBW/Hz) is observed passing from the slab UC to the slab HC. This reduction may be attributed to a dissipation of energy of the waves that while travelling through the slabs have encountered the grooves.
- The influence of the grooves on some regions of the periodograms can be read in term of variation of the peak amplitude and of the peak frequency.
- It is quite difficult to define a variation of the structural health status of the slabs due to the grooves using only the peak amplitude variation.
- The spectral centroid (one feature of the periodogram) may be effectively used to better represent the variation of the peak frequency of the recorded signals. It shows the potentialities to recognize the presence and the change of dimensions of the induced grooves.
- The higher is the depth of the grooves, the higher is the shift of the spectral centroid toward the low frequencies.
- Results are encouraging about the possibility to associate to a given asphalt concrete pavement its vibro-acoustic signature based on its structural health status (structural health assessment, SHA). Each vibro-acoustic signature can be characterized by one or more parameters (features) extracted from single or multiple domains of analysis (e.g., the frequency domain). Furthermore, this/these feature/s can be used for the structural health monitoring (SHM) of the pavement above to identify the occurrence of cracks, or the propagation of the cracks already present on their layers.

Based on above, the following recommendations may be outlined:

- Despite the WTM allows to work simulating almost real conditions (i.e., material tested, temperature, pressure, and number of passage applied by the wheel), the main drawbacks of this machine refer to the noise produced that affects the signal spectral content.
- This method can be considered as semi-destructive, because of the installation of the microphone that requires a hole drilled on the slab. In order to make the method non-destructive, the microphone may be installed on the surface, but this configuration calls for further research to isolate this transducer from the airborne noise and to couple it to the pavement. These two issues might emerge when implementing the method in full scale.
- The information contained in the vibro-acoustic signatures of the slabs is influenced by several factors (i.e., dimensions of the slabs, absence of layers, material and mixture used to build the slab, intrinsic properties of the mixes, and the experimental set up used).
- Frequency range may affect the reliability of results shown above. Further research could be carry out in the full frequency range (in this case study the range 20-1.5 kHz was used for the data analysis).
- This case study represents the first approach used to validate the proposed NDT-SHM method. The analyses carried out in the frequency domain through periodograms and their related features should be developed integrating more features extracted from more domain of analysis (i.e., time domain, or time-frequency domain), or using approaches that allow to carry out a vibro-acoustic signature-based SHM that is independent from the features used (e.g., machine learning approach).
- On-site tests are needed to verify the effectiveness of the new method and to face real boundary conditions (e.g., presence of air-borne noise, vibration, wind, temperature changes, etc.).
- The vibro-acoustic signatures of different types of road pavements (e.g., pavements with different mixes properties, thicknesses, elastic

moduli, structural health status, etc.) loaded with traditional (real vehicular traffic) and customized loads, may be collected to create a sound database that would be a useful instrument for the estimation of the health condition of a road (SHA).

5
On-site experiments and data analysis

Several experimental investigations were carried out in laboratory and on site to validate the structural health monitoring method presented in this thesis. This section refers to the experiments carried on site on several real road pavements. These experiments aimed at gathering the vibro-acoustic signature of road pavements, which were characterized by different structural health statuses (SHSs). A Light Weight Deflectometer (hereinafter called LWD) and the vehicular traffic were used as un-conventional and conventional load, respectively. The main objective of this experiments was to understand if it is possible to recognize the SHS of a road pavement from its vibro-acoustic signature using a proper data analysis.

5.1. On-site experiments using the LWD as source

The following pieces of equipment were used in the experiments: Light Weight Deflectometer (LWD), microphones, laptop, software for data analysis (Matlab).

The Light Weight Deflectometer (LWD) is a device primarily used to evaluate the dynamic modulus of the unbound layers of a pavement (e.g., subgrade) according to the standard ASTM E 2583-07 (ASTM 2015), as an alternative to the static plate bearing test (ASTM D1196 (ASTM 2016); ASTM D1194-94; (ASTM 2003); BS 1377:9 (British Standards Institution 1990), 1990; CNR 146, 1992 (Consiglio Nazionale delle Ricerche (CNR) 1992)).

Usually, during the LWD test, the pavement is loaded with an impulse load generated by a fixed mass (e.g., 10 kg), dropped from a fixed height (e.g., 830 mm). The mechanical energy is transferred from the mass to the pavement through a damping system, which causes a controlled transient load in the interface plate-pavement (e.g., load = 7 kN, pulse time = 15-30 ms, plate diameter = 300 mm, and pressure about 100 kPa). The resulting road surface deflection in the interface pavement-plate is detected by one or more

geophones (or accelerometers located into the LWD plate), while the impulse force is measured by a load cell. Forces and deflections are used to derive the stiffness, also called modulus or dynamic modulus, of the underneath pavement layers layer until a depth of about 1/3 the diameter of the LWD base plate (Commuri et al. 2012)(Siekmeier et al. 2009)(Marecos et al. 2017)(Ryden and Mooney 2009).

The LWD PRIMA100 (Fig. 5.1) produced by Grontmij (Carl Bro A/S, Pavement Consultants, Denmark) was used during the experimental investigation carried out in the following sections.

Fig. 5.1 Light Weight Deflectometer (LWD) used in the on-site experiments.

The LWD allows to measure the dynamic modulus of a pavement. The value of the modulus is calculated automatically by the LWD, which uses the following expression:

$$E_{LWD} = \frac{A \times \left(1 - \nu^2\right) \times R \times P}{D}, \tag{5. 1}$$

where A is the stress distribution factor (A = 2 for inverse parabolic stress distribution); ν is the Poisson's ratio (ν = 0.35 for HMA road pavements); R is the radius of the base plate of the LWD (in this case R=150 mm); P is the peak applied pressure measured by the LWD (kPa); D is the peak vertical deflection measured by the LWD (mm).

5.1.1. Road pavement cracks versus elastic modulus, PSD magnitude, and distance source-receiver[4]

In this section is described the first on-site application of the proposed NDT-SHM method (Fedele, Pratico, et al. 2017). This application aimed at understand how the waves transmission capacity ((Nguyen, To, and Vu 2017; Rahman, A., and Tarefder 2016)) of HMA road pavements is effected by surface and concealed cracks.

In particular, a reduction of the pavement's stiffness (expressed by the dynamic modulus) due to the presence of cracks is expected, and this may affect the spectral content of the signals that are generated by a source, travel through this medium, and are detected by a microphone placed on the pavement.

Similar to the in-lab tests (cf. section 3.2), the data set collected during this experimental investigation was analyzed in the frequency domain, and periodograms (i.e., Power Spectral Density, PSD, *versus* frequency) were used to represent the spectral content of the recorded signals. The PSD was related to both pavement moduli (stiffness of the medium), and the distance between impulse force and receiver (waves transmission capacity of the medium).

Based on the considerations about the signal propagations reported in the section 3.2, the following conceptual models were defined:

$$S_p = F_{S_p}\left(d_{SR},\ T,\ E^*,\ p_1,\ldots,\ p_n\right), \tag{5. 2}$$

$$f_c = F_{fc}\left(dSR,\ T,\ E^*,\ p_1,\ldots,\ p_n\right), \tag{5. 3}$$

$$\overline{PSD}_{f_1-f_2} = F_{PSD}\left(dSR,\ T,\ E^*,\ p_1,\ldots,\ p_n\right), \tag{5. 4}$$

where Sp is acoustic spectrum, dSR is the distance Source-Receiver, T is the temperature of the road pavement, E^* is the dynamic modulus of the road pavement, fc refers to the spectral centroid (as defined in Eq. 4.9), $PSD_{f1\text{-}f2}$ is the average amplitude of the Power Spectral Density (PSD, cf. Eq. 4.8) in a specific range of frequency ($f_1 - f_2$), p_1, …, p_n stand for other parameters that are function of the boundary conditions.

[4] This section mainly refers to the paper 1.3 (see Scientific production).

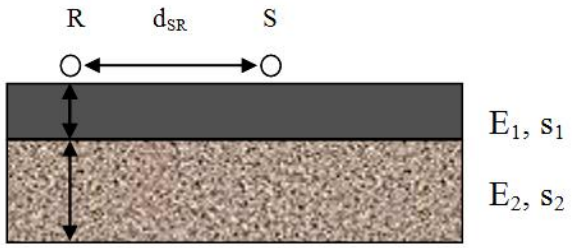

Symbols. R: Receiver (microphone); S: Source (e.g., load impulse, vehicle passage); s_i: Thickness of the layer; E_i: Elastic modulus of the i-th layer; d_{SR}: Distance between source and receiver.

Fig. 5.2 Main components and parameters involved during the on-site experiments.

The models above might be used for structural health monitoring (SHM), and structural health assessment (SHA) purposes. Particularly, deriving the elastic modulus from the characteristics of the periodogram, e.g. the spectral centroid, it would be possible to estimate the variation of the conditions of the structural conditions of a road pavement (SHM):

$$\frac{\partial f_c}{\partial t} \Rightarrow \frac{\partial E}{\partial t} \Rightarrow SHM\,. \tag{5. 5}$$

On the other hand, the assessment of the structural conditions of the internal layers of a road pavement (SHA) may be carried out by extracting the one or more features (e.g., the spectral centroid) from the periodogram (or the spectrum). Then, by using a proper pattern recognition technique, this/these feature/s can be associated to elastic moduli who belong to a proper class (e.g., Un-Cracked, UC, or Cracked, C, road pavements). For instance, if the spectral centroid is used as feature, the Structural Health Assessment (SHA) can be modeled as follows:

$$f_c \Rightarrow E \in \left(class_1\ ,\ class_2\ ,\ldots,\ class_n\right) \Rightarrow SHA. \tag{5. 6}$$

In order to preliminary assess the influence of the above-mentioned parameters on the signal, experiments were planned as follows:

- The pavement was loaded by using dynamic impulses generated according to the standard ASTM E 2583-07 (ASTM 2015) by the LWD at a given distance from the microphone.

- The same standard cited above was used to assess the mechanistic properties of the pavements (dynamic moduli), along different sections of the test road.
- Impulses were organized in order to control and monitor the distance between receiver (microphone) and source (LWD) (see Fig. 5.3c).
- Air and pavement temperatures were monitored and recorded.
- Tests were carried out on the different road sections: i) one superficially cracked; ii) one superficially un-cracked road pavements; iii) one re-habilitated (herein called UC, C, and R sections, respectively), placing the same broadband microphone (Omnidirectional, Sensibility: -42 dBA, Impedance: 2200 Ohm, rated current: 0.5 mA, Diameter: 4 mm) used for the in-lab tests (cf. previous chapter) on the wearing course using modeling clay (Fig. 5.3c).
- Tests were carried out using as sources the device LWD.
- Four case studies were considered.
- Audio recordings were converted into time-series, and then PSD.

(a) (b) (c)

Fig. 5.3 The three sections under investigation: a) Un-Cracked; b) Cracked; c) Re-habilitated. M=Microphone attached on the road pavement using modeling clay.

Experiments proved to be complex and highly dependent on a number of remaining environmental and operational variables. This notwithstanding,

preliminary analyses can be carried out and are briefly discussed in the following.

The following parameters are herein considered:

- *E*: modulus measured through the LWD device (ASTM E2583-07; (ASTM 2015)), (MPa);
- *Eav*: average value of the modulus above in the given section, between source and receiver, (MPa);
- *dSR*: distance between Source (S) and Receiver (R), (m);
- *fc*: spectral centroid (see Eq. 4.9), (Hz);
- *PSD20-200*: averaged amplitude of the Power Spectral Density in the frequency range 20-200 Hz, calculated from the acoustic signals gathered from a road pavement, (dBW/Hz);
- *PSD200-1500*: averaged amplitude of the Power Spectral Density in the frequency range 200-1500 Hz, calculated from the acoustic signals gathered from a road pavement, (dBW/Hz);
- *PSD1500-96k*: averaged amplitude of the Power Spectral Density in the frequency range 1500-96000 Hz, calculated from the acoustic signals gathered from a road pavement, (dBW/Hz).

Note that, the parameters related to the PSD were considered in this study because of the conclusions and recommendations of the in-lab experiments (cf. section 4.3). In fact, the frequency band considered to analyze the data from the in-lab tests (20-1500 Hz), was extended by including the parameter herein called *PSD1500-96k*. Furthermore, in order to make the method non-destructive, the microphone was attached on the road pavement.

Tab. 5.1 summarizes the factorial plan of experiments, and provides an overview of the main results obtained, while the dependency on single parameters is discussed below.

Tab. 5.1 Overview of the experimental results.

Moduli and Spectral characteristics (PSD and *fc*) *per dSR*=0.5-2.5 m					
Road section's Structural Health Status	*E* (GPa)	*PSD20-200* (dBW/Hz)	*PSD200-1500* (dBW/Hz)	*PSD1500-96k* (dBW/Hz)	*fc* *(200-1500 Hz)* (Hz)
Un-Cracked (UC)	0.6~0.9	-74~-82	-69~-83	-102~-111	602~832
Cracked (C)	0.1~0.3	-71~-76	-60~-75	-95~-100	468~1030
Re-habilitated (R)	0.1~0.2	-91~-92	-90~-97	-116~-120	570~656

By considering the main results of Tab. 5.1, it is possible to state the following considerations:

- The elastic moduli (*E*) measured on the damaged road section (i.e., where internal and surface cracks were present) resulted lesser that those measured on the un-cracked one.
- The main variation of the spectral content of the acoustic signals recorded during the on-site tests (expressed in terms of PSD) refers to the frequency range 200-1500 Hz (i.e., between 7 and 15 dBW/Hz for the range 200-1500 Hz, compared to 1-8 dBW/Hz and 4-9 dBW/Hz for the ranges 20-200 Hz and 1500-96k Hz, respectively). For this reason, the spectral centroid, *fc*, was calculated in this range.
- At this level of detail, it is not possible to define how the spectral centroid varies as a function of the structural health status of the road pavements under investigation. Tab. 5.2 provides a greater level of details for the results above.

Tab. 5.2 Trend of the features extracted (frequency domain) as a function of the distance source-receiver (*dSR*) and the structural health status (UC = Un-Cracked; C = Cracked; R = Re-habilitated).

Feature	**Structural Health Status**	***dSR* (m)**				
		0.5	**1**	**1.5**	**2**	**2.5**
fc **(Hz)**	UC	602	674	729	581	832
	C	468	631	624	1064	1030
	R	570	656	n.a	n.a.	n.a.
PSD20-200 **(dBW/Hz)**	UC	-74	-79	-82	n.a.	n.a.
	C	-71	-72	-76	n.a.	n.a.
	R	-91	-92	n.a.	n.a.	n.a.
PSD200-1500 **(dBW/Hz)**	UC	-69	-78	-83	n.a.	n.a.
	C	-60	-66	-75	n.a.	n.a.
	R	-90	-97	n.a.	n.a.	n.a.

***PSD1500-96k* (dBW/Hz)**	UC	-102	-105	-111	n.a.	n.a.
	C	-95	-94	-100	n.a.	n.a.
	R	-116	-120	n.a.	n.a.	n.a.

Based on the content of Tab. 5.2, it is possible to assert that:

- The experimental set up used was affected by the environmental noise, and, for this reason, it was not impossible to obtain reliable results for distances greater than 1.5 m. This observation calls for the improvement of the experimental set up towards more effective isolation of the microphone from the airborne noise, and a more performing microphone.
- For distance *dSR* lesser than 1.5 m, the cracked section has spectral centroids lower than the un-cracked one. This result is consistent to the results obtained during the in-lab experiments (cf. previous chapter).
- The spectral centroids related to the re-habilitated section have values that are included between those of the sections UC and C. This may be attributed to poor re-habilitation, which involved the wearing course only.
- The UC section always has PSDs lesser than the C section. This result is not coherent with the results of the in-lab tests (where the presence of the grooves in the slabs led to an overall reduction of the average PSD), and may be associated to the poor coupling between the metallic plate of the LWD and the cracked section (C). In fact, the macro-cracks present on the C section have produced acoustic waves with greater variability and amplitude than those associated to the sections UC and R. Furthermore, this conclusion is confirmed by the PSD of the signals gathered from the section R, which had a smoother surface (lower macro-texture) and, therefore, PSDs that are the lowest of the three sections under investigation. This result calls for further investigations about the proper coupling between the LWD and the road pavements.

The following sections show the mutual relationship between the parameters that have been taken into account in this case study. The following figures illustrate the relationship among two parameters, which were derived from the on-site experimental investigation described in this section, and the distance between the source (i.e., the dynamic impulse of the LWD) and the receiver (microphone attached on the road pavements under test), herein called *dSR* (m). In particular, one of them, i.e. the elastic modulus of the road pavement, *E* (MPa), was measured using the LWD, while, the second one, i.e. the spectral centroid, *fc* (Hz), was derived from the periodogram obtained following the same procedure used in the previous chapter. In more detail, *fc* was calculated in the frequency range 200-1500 Hz, which includes the part of spectrum which presents greater variations in terms of frequency and magnitude (PSD).

Fig. 5.4 illustrates that, while the distance *dSR* (between source and receiver) varies from 0.5 m to 2.5 m (x-axis), the Un-Cracked section (UC) had: i) dynamic modulus, *E*, which ranged from 677-932 MPa (max/min=1.4); ii) progressive average value of the dynamic modulus, *Eav*, with values in the range 677-875 MPa; iii) spectral centroids that vary in the range 0.5-1.1 kHz (y-axis). It should be noted that, the variation of the spectral centroid as a function of the distance *dSR* seems to follow a quasi-monotonic behavior.

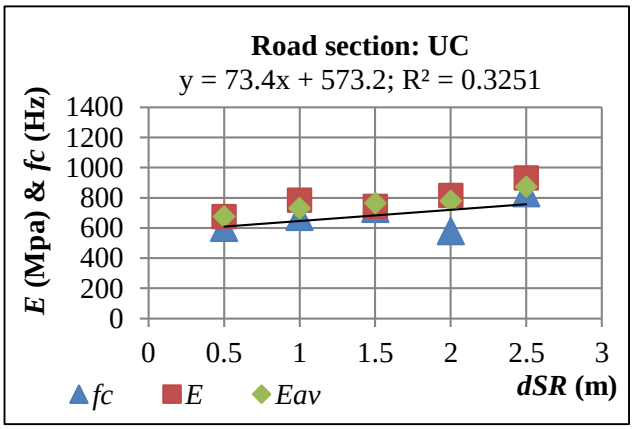

Fig. 5.4 Distance (*dSR*) *versus* Spectral Centroid (*fc*) and Stiffness (*E* & *Eav*) (section UC = Un-Cracked).

Similarly, in Fig. 5.5, the variation of the spectral centroids (y-axis, Hz) as a function of the distance (x-axis, m) is illustrated for the cracked section (C). In this section: i) the modulus (E) had values in the range 109-299 MPa (max/min=2.7); ii) the modulus *Eav* had values included in the range 299-180 MPa; iii) the spectral centroids ranged the values 468-1030 Hz.

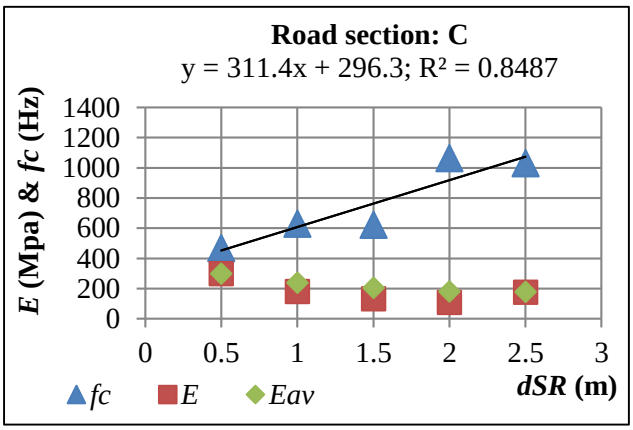

Fig. 5.5 Distance (*dSR*) *versus* Spectral centroid (*fc*) and Stiffness (E and Eav) (section C = Cracked).

Fig. 5.6 illustrates how the PSD (y-axis) of the section C, estimated in a given frequency range (e.g., 200-1500 Hz), varies as a function of the distance between source and receiver (x-axis). As expected, the higher the distance is, the lower the signal becomes.

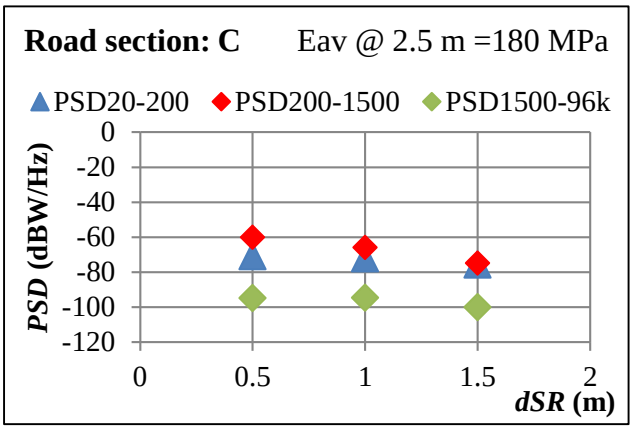

Fig. 5.6 PSD amplitudes *versus* distance, *dSR* (section C = Cracked).

Fig. 5.7 illustrates how the PSD amplitudes (in the given range of frequency, e.g., 20-200 Hz, cf. y-axis), vary as a function of the modulus (*E*, x-axis, MPa),

for two given distances *dSR* (0.5, and 1 m). These plots involve all the structural health status (i.e., UC, C, and R), because it refers to two distances and to the corresponding relationship between spectrum features (e.g., *PSD200-1500*, y-axis) and the corresponding moduli (*E*, MPa, x-axis). First derivatives result quite similar for the features under investigation.

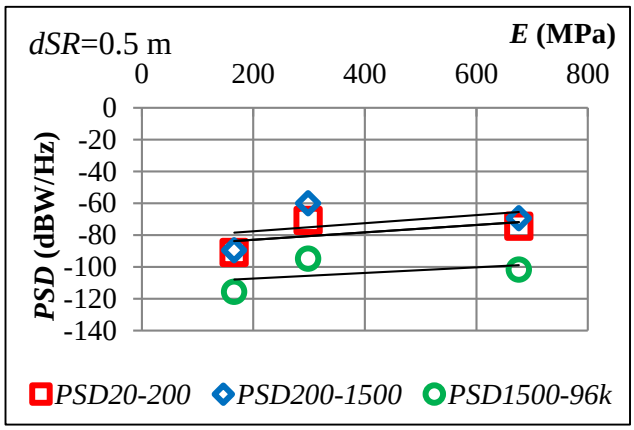

(a)

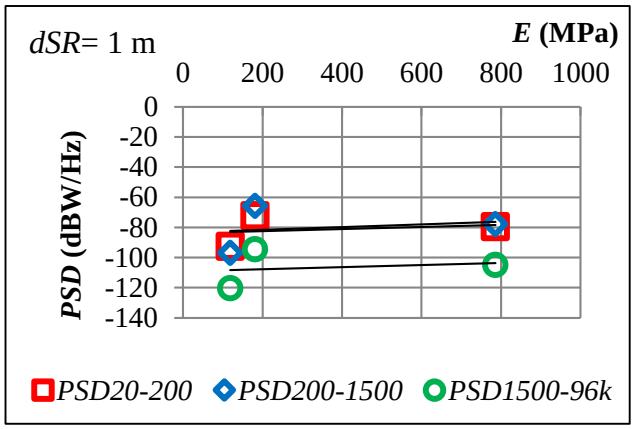

(b)

Fig. 5.7 PSD *versus* Modulus, *E*, for (a) *dSR* = 0.5 m, and (b) *dSR* = 1 m.

Importantly, Fig. 5.7 underlines that in the range 200-1500 Hz, PSD amplitudes are higher than in 20-200 Hz range, which in turn are higher than in 1.5-96 kHz. This fact points out that the interaction between LWD drops and the pavement under investigation generated acoustic signals with spectral content consisting in frequencies lower than 1500 Hz.

Fig. 5.8 focuses on the dependency of *fc* (Hz) on the modulus (x-axis). Even if only a few points are available, results seem to point out that the lower the

distance the higher the first derivative is. This fact may be due to the relationship between the level of the desired signal (i.e., the one which correlates with moduli) and the level of background noise. Indeed, this relationship may depend on the distance between source and receiver, or on the isolation of the microphone.

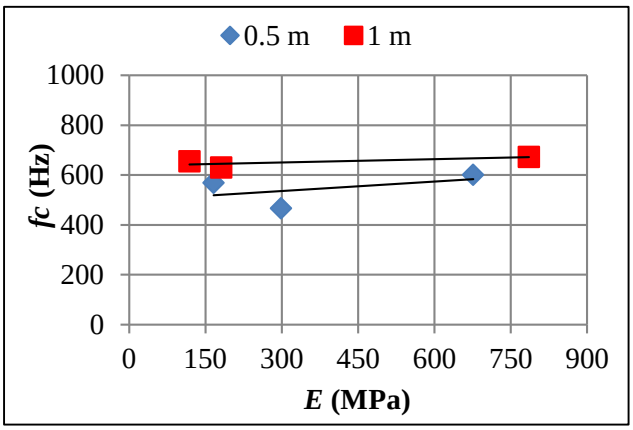

Fig. 5.8 Spectral centroid, *fc, versus* Modulus, *E*, for *dSR* of 0.5, and 1 m.

Based on the above, the following conclusions may be drawn:

- The system used during this experimental investigation provided reliable results for distance source-receiver (*dSR*) lesser than 1.5 m.
- Further studies are needed to isolate the microphone from the airborne noise.
- A specific study is needed to find a proper way to couple the metallic plate of the LWD to the road pavements, in order to avoid the generation of un-desirable noise.
- The elastic modulus of a road pavement is reduced by the presence of surface and internal cracks.
- The attenuation with the distance of the acoustic signal PSD appears to be significant for differences ranges of frequencies.
- The main variation of the spectral content of the vibro-acoustic responses of differently cracked road pavements can be restricted to a given range of their spectrum (e.g., 200-1500 Hz). In this range, different features can be recognized and extracted (e.g., the spectral

centroid), and then used to monitor the structural health status of the road pavements.

- The PSD-based features shown the limitation of the experimental set up used in this case study, and it is important to improve them for further applications. On the other hand, these features were very helpful to recognize the frequency range in which the spectral centroid had to be extracted.
- Spectral centroids undergo increase when the dynamic moduli increase. In other words, the presence of cracks, which lead to a reduction of the modulus of a pavement, can be associated to spectral centroids lower than those of an un-cracked road.

5.1.2. Innovative deterioration curves to improve the PMSs[5]

As described in the Chapters 1 and 2, the current Pavement Management Systems (PMSs) are widespread and consolidated tools that represent a decision support for the authorities that are responsible for the maintenance and rehabilitation of the transportation infrastructures.

Unfortunately, as discussed in the section 2.1, the main drawbacks of the PMSs refer to: i) the failure-based approach applied to carry out maintenance interventions and schedule the tasks of the management process; ii) the limitations of the measurement systems used to detect the failure of the infrastructures above.

As a consequence of these drawbacks, authorities entail un-sustainable delays in prioritizing investments, and are not able to control and forecast the consequent increase of agency and user costs.

Consequently, more efficient and reliable PMSs are needed and this goal may be reached acting on the current approaches applied and systems used. Possible ways to obtain improved PMSs may be (a) switching from the failure-based to the condition- or predictive-based maintenance, and (b) moving from the destructive, un-sustainable, and limited traditional

[5] This section mainly refers to the paper 1.9 (see Scientific production).

measurements systems to non-destructive, sustainable, and specially designed innovative ones.

For these reasons, in this section, is described how the NDT-SHM method presented in this thesis can be used to improve the current PMSs (Fedele, Praticò, et al. 2018). In more detail, it contains the description of how it is possible to build P-F curves (defined in the section 2.3) using the most reliable and meaningful features extracted in the previous section (e.g., the spectral centroid), and how these curves may be used to monitor the structural health status of road pavements, to improve the current PMSs, and to save resources (e.g., time, money, workers, materials, energy, etc.) at the same time.

Sustainable monitoring systems that are able to implement the proposed NDT-SHM method, may be used to define, extract, and use innovative PMS input parameters (features) derived from the signals recorded by the system. In order to obtain a sustainable SHM system for road infrastructures, the following characteristics should be considered during the design process: a) the system should be hopefully based on non-destructive, and ultra-low- or, at least, low-power electronic devices (i.e., sensors placed on the road pavement, or embedded in the pavement during the road laydown); b) it should not interfere with traffic (i.e., sensors installed outside the carriageway); c) it should not need skilled workers, i.e. it should be able to automatically extract the required information from the signals gathered through the sensors; d) instead of traditional PMS input parameters, it should use the information (features), extracted from the acoustic signatures of the road pavement; e) it should allow detecting, in real time and with a high sampling frequency, potential failures that occur in pavement layers.

Fig. 5.9 summarizes the results of the experimental investigation described in the previous section (cf. paragraph 5.1.1). In particular, it reports the trends of the two most important parameters used as a function of the distance between the source of noise and vibration (S, i.e., the LWD), and the receiver (R, i.e., the microphone attached on the road pavements under test). In more detail, it shows the trends of: i) the values of the dynamic moduli (histogram) of two road pavements, one Un-Cracked (UC) and one Cracked (C, i.e.,

where both surface and internal cracks were easily recognized through a visual inspection); ii) the values of the spectral centroids (circles) derived from the vibro-acoustic response of the two road pavements under tests (calculated using the Eq. 4.9 from the periodogram obtained by the Eq. 4.8).

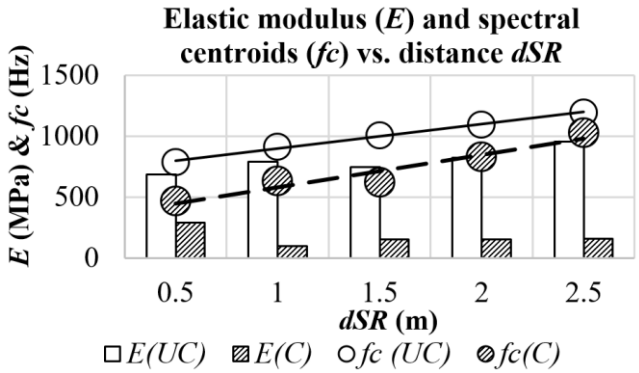

Fig. 5.9 Moduli, *E,* and spectral centroids, *fc*, of the Un-Cracked (UC), and the Cracked (C) road sections, as a function of the distance Source-Receiver (*dSR*).

Based on results of Fig. 5.9 and the considerations reported in section 5.1.1, the average of the elastic moduli of the two road sections under test were derived obtaining E = 800 MPa for the section UC, and E = 200 MPa for the section C. At the same time, the spectral centroids were derived taking into account the most reliable values, i.e. the values included in the range 0.5-1.5 m, obtaining the values 668 Hz and 574 Hz for the sections UC and C, respectively.

Fig. 5.9 illustrates how centroids (*fc*) and moduli varied as a function of the distance between source and receiver (*dSR*). For a given distance, the section UC yield a spectral centroid and a modulus that were lower than the ones of the corresponding cracked section C. Consequently, there is a correlation between the reduction of the stiffness (expressed by the elastic modulus) due to the presence of cracks, and the variation of the spectral content (in terms of spectral centroid) of the acoustic responses of the pavements. This leads to the conclusion that the spectral centroid can be used as input parameter for the estimation of the pavement condition. For these reasons, the average values mentioned above (moduli and spectral centroids) were used to build the deterioration curves (cf. section 2.1) that are shown in Fig. 5.10.

Fig. 5.10 shows three curves as a function of time, and four couples of points: i) deterioration curve in terms of moduli (solid curve); ii) deterioration curve in terms of spectral centroids (dashed curve); iii) curve of management costs (dotted curve); iv) couple of points P (overlaid triangles, potential failure symptoms of solid and dashed curves); v) couple of points F (asterisks, functional failure of the solid and dashed condition curves); vi) couple of circles (solid and dashed, symptoms detected on the dashed curve); vii) couple of squares (solid and dashed, symptoms detected on the solid curve). The deterioration curves (solid line and dashed line in Fig. 5.10) illustrate how the structural properties of the pavement decay over time. They were built using the four average values derived from the experimental investigation, based on the following hypotheses: i) the experimentally derived modulus, E, and centroid, fc, of the section UC refer to a 10 years old pavement and are close to the point P ("fair-to-good" conditions, cf. section 2.3); ii) the experimentally derived E and fc of the section C refer to a pavement in poor to very poor conditions, where PC ≈ 20% in terms of modulus. They are close to the point F (PC≈ 10%); iii) the expected life (i.e., the as-design life time) of the road pavement is about 25 years.

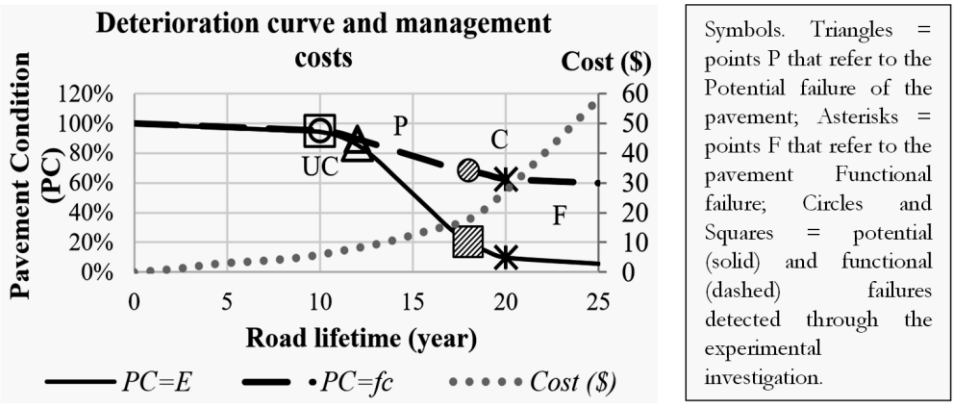

Fig. 5.10 Deterioration curves built in terms of elastic moduli, E (solid curve), and spectral centroid, fc (dashed curves); Management costs (dotted curve).

By analyzing Fig. 5.10, it is possible to state that the variation of the Pavement Conditions (PC) of a road pavement can be expressed using deterioration curves built using "traditional" parameters, e.g. the elastic modulus, E, of the road pavement (PC = E), but also through "innovative" parameters, e.g. the

spectral centroid, *fc*, extracted from the spectral content of the vibro-acoustic signature of the pavement (PC = *fc*), hopefully gathered by using innovative NDT-SHM systems.

It is important to underline that the spectral centroid is just one out of the countless number of parameters that can be derived from the vibro-acoustic signatures of the pavements. Based on these "innovative" parameters, specifically designed and weighted indices (cf. section 2.3) can be derived to express the pavement degradation. Hence, the proposed method has the potentialities to improve the current PMSs.

In addition, the dotted curve in Fig. 5.10, which refers to the maintenance and reconstruction costs, was built using the information reported in section 2.3. It shows that using an efficient monitoring system, i.e. able to identify automatically, and in real-time the variation of the pavement condition, it is possible to save money, and so, improve the overall sustainability of the management process. In more detail, maintenance costs 4 $ when potential failure has been early detected (PC = 70% for *E*), but 18 $ are needed if the maintenance is carried out when functional failures are present and easily detectable (PC = 20% for *E*). In other words, the sooner the symptom is detected, the higher the savings are. This result can be easily seen in terms of energy saving and carbon footprint reduction, because of the fact that money savings are mainly due to the energy saved reducing the maintenance interventions and, especially, avoiding the reconstruction of the road pavement.

In summarizing, a trade-off between the ever-growing request of Intelligent Transportation System (ITS) and the never-ending depletion of the available resources is needed. Several possible solutions that may be implemented in road infrastructures to reduce the current need of resources (in terms of energy, materials, money, time, and manpower) were presented and analyzed (see sections 2.2, and 2.3). The motivations behind the study are related to one of the possible solutions presented, i.e. PMSs optimization. The current PMSs aim at predicting and using deterioration curves of the road pavement, and for this reason they require input parameters (cf. section 2.3). Unfortunately, "traditional" parameters are derived through methods that

have usually need destructive, time-consuming, and expensive operations. Consequently, in this section of the thesis, an innovative and sustainable method to improve the current PMSs was proposed. The prototypical validation of the method was carried out using two different parameters, one "traditional" and one "innovative", related to the structural health conditions of an Un-Cracked (section UC) and a Cracked (section C) road pavement. A Light Weight Deflectometer (LWD) was used to measure the "traditional" parameter, i.e. the elastic modulus, E, and as a source of vibration and sounds. The spectral content of the acoustic response of the pavements to the impulse loads was analyzed through periodograms (PSD vs. Frequency). Among the entire set of features that might be extracted from the periodograms, the spectral centroids, fc, were selected as "innovative" parameter in this study. The results of the experimental investigation show that the degradation of the pavement conditions (from the UC to C condition) can be represented by the two above-mentioned parameters. In particular, the road pavement elastic modulus (stiffness) undergoes a reduction as well as of the spectral centroid. Bearing in mind that, the spectral centroid is just one out of the countless number of parameters that can be derived from the signals recorded using a SHM system, and, under given conditions, the "innovative" parameters might replace the "traditional" ones.
In conclusion, the following considerations can be listed:

1) "more sustainable" indices that represent the pavement conditions might be formalized and derived using innovative (e.g., non-destructive, or less-consuming) system, and alternative ways to analyze the data gathered by the above-mentioned systems;
2) based on the more sustainable indices above, innovative deterioration curves might be drawn to the identify, monitor, and forecast the structural health condition of road pavements over time, covering all the expected life of these infrastructures;
3) the innovative deterioration curves mentioned above may be used to upgrade and develop the current PMSs;
4) the PMSs improvement increases the efficiency of the road management and rehabilitation process, and, as a consequence of

this, effects can be seen in the short (i.e., timeliness in potential failure detection), middle (i.e., energy/money saving in maintenance and rehabilitation), and long term (i.e., carbon footprint reduction).

5.1.3. Feature-based approach: road pavement classification from LWD-related signals[6]

The last two sections above were included to provide an overview about: i) the relationships among crucial characteristics of the road pavements e.g., stiffness), and meaningful features (e.g., spectral centroid) that can be extracted from the vibro-acoustic signatures of the pavements using suitable data-analyses; ii) the potentialities of the features extracted to improve processes and systems (e.g., the PMSs) that are currently used to manage the road infrastructures.

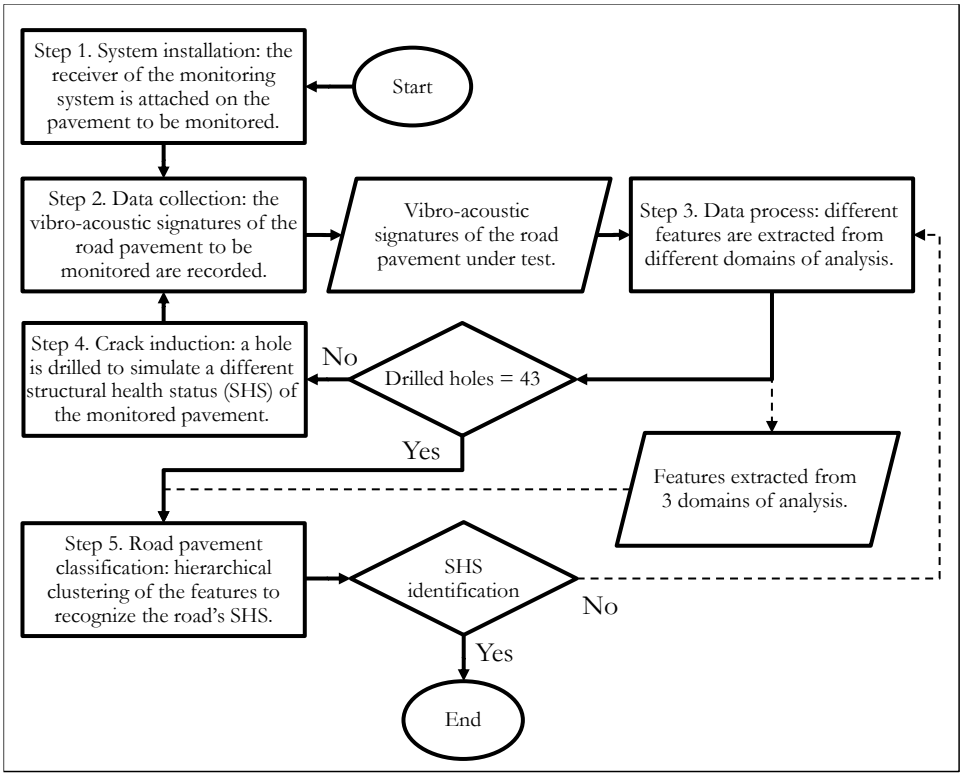

Fig. 5.11 Main steps of the feature-based approach for road pavement classification.

[6] This section mainly refers to the papers 3.2, and 3.9 (see Scientific production).

After the overview cited above, this section contains the description of the feature-based approach used to classify a differently cracked road pavement based on the changes of its vibro-acoustic signature. Fig. 5.11 reports the main steps of the above-mentioned approach.

In order to set up the proposed SHM method, and bearing in mind the conclusions of the previous experimental investigations (cf. sections 4.3, 5.1.1., and 5.1.2), an attempt of improvement of both the measurement system and the data analysis was made. This attempt consisted in: 1) using a more performing receiver module (isolated microphone, sound card, isolated cable); 2) improving the coupling LWD-pavements; 3) inducing damages (drilled holes) to simulate the generation and propagation of cracks into the road pavement; 4) extracting more features from different domains of analysis; 5) using a hierarchical clustering algorithm to try to recognize the structural health status of the road pavement under investigation through the features extracted (classification problem).

First of all, aiming at properly detecting the sound propagating in the road pavement, a more performing receiver module was used. It consists of (Fig. 5.12): i) an acoustic transducer, i.e. one insulated broadband microphone (Model: Audix TM1, Omnidirectional, Frequency response: 20 Hz-25 kHz +/- 2 dB, Sensitivity: 6 mV/Pa at 1 kHz, Maximum SPL: 130 dBA, Pre-polarized condenser, Impedance: 200 Ohm, Diameter: 8 mm); ii) one external sound card (Model: Roland Quad-capture, 4 channels, AD/DA conversion: 24-bit, Maximum sampling frequency: 192 kHz, current draw: 480 mA, headroom: 14 dB); iii) one isolated cable (Model: Reference Laboratory RCM-GBK-Plolite); iv) one laptop (Model: Sony Vaio) running Matlab dedicated to the gathering and processing of the data.

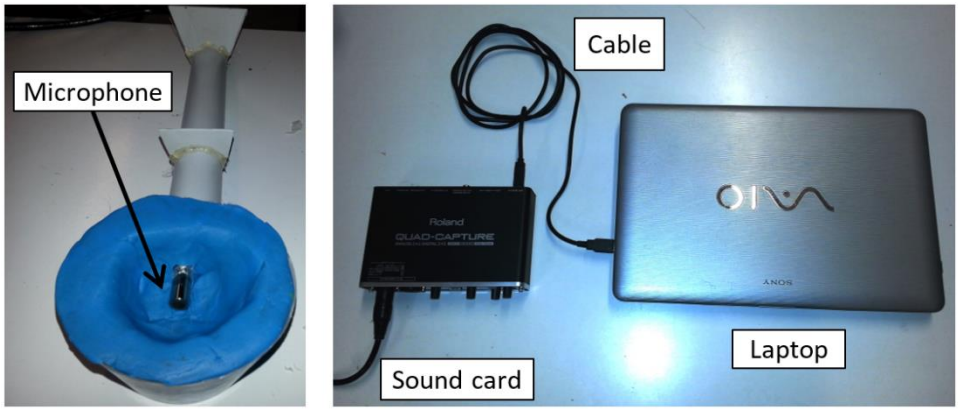

Fig. 5.12 Receiver module (isolated microphone, sound card, isolated cable) of the measurement system.

It is important to underline that a noteworthy effort was made to obtain an acoustic receiver that is able to detect preferably the sounds transmitted through the internal structure of the monitored pavement. Several experiments were carried out for this purpose. Satisfying results have been achieved insulating the transducer (from the environmental airborne noise and the action of the wind) by using a proper amount of modeling clay (cf. Fig. 5.13), a sound absorbing coverage (see Fig. 5.13b), and placing the transducer in close contact with the pavement surface.

Fig. 5.13a shows the sound absorption spectra, i.e., the sound absorption coefficient (α; dimensionless) in the frequency domain (Hz), obtained using the Kundt's tube (applying the transfer-function method according to standard ISO 10534-2 (ISO 1998)), of samples of different materials used as noise absorbers. In particular, discs of different materials, such as wadding (raw cotton), or modeling clay (plasticine), were stacked to form a cylinder, and this cylinder was put in the Kundt's tube in order to measure its ability to absorb the noise in a given frequency range (200-1600 Hz).

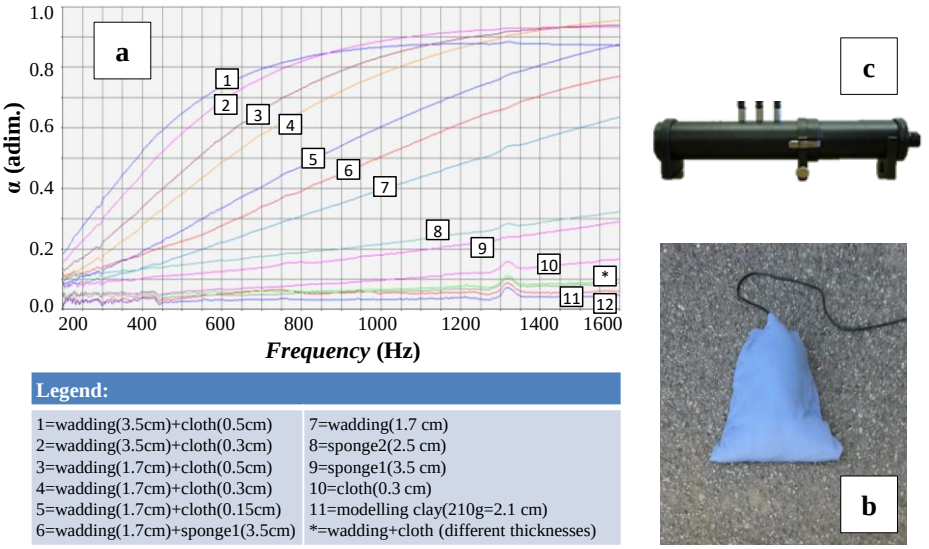

Fig. 5.13 Microphone sound isolation: (a) sound absorption spectra (sound absorption coefficient (α) vs. frequency), obtained using the Kundt's tube (b), of samples of different materials used as noise absorbers; (c) microphone covered by the absorbing coverage during the on-site tests.

As it is possible to see in the Fig. 5.13a, the best results in terms of sound absorption were obtained using the combination of wadding and cloth (4 cm thick). For this reason, a first prototype of sound absorbing coverage was built using these materials, and was used to isolate the microphone from the airborne noise and the wind during the on-site tests (as shown in Fig. 5.13, c). As repeatedly said, the method aims at detecting and monitoring the acoustic response of the pavement to an excitation (due for example to a vehicle or an impulse load), and, for this reason, the presence of a proper source of noise and vibration (i.e., a source that is able to produce the sound and seismic waves that after the propagation into the road pavement are detected by the microphone) is required. During the experimental investigation described in section 5.1.1, an LWD was used as source and it has been noticed that the metallic plate of the LWD often generates undesirable sound components. To solve this problem, different attempts were made to properly couple the metallic plate to the road surface. Good results were obtained using thin layers of sands, or modeling clay, or rubber mats, or cloth disc (see Fig. 5.14).

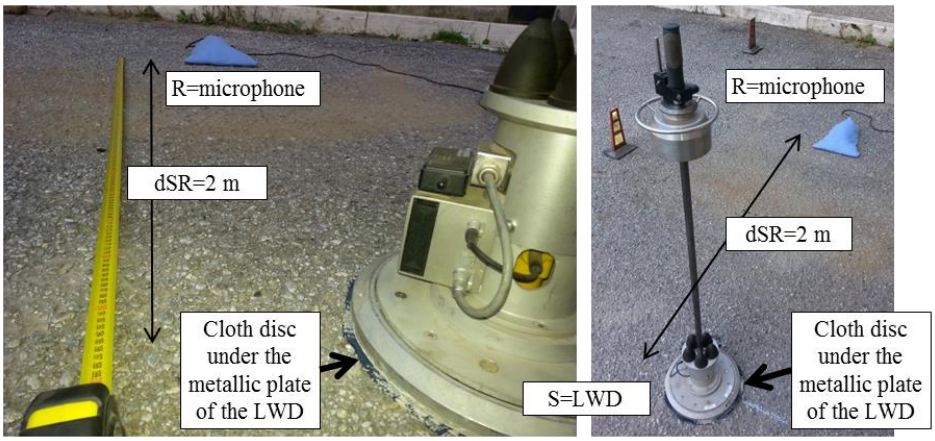

Fig. 5.14 Installation of the source (S) of sound and vibration, i.e., LWD) using a cloth disc to improve the coupling LWD-pavement, and the receiver (R), i.e. the microphone isolated using the absorbing coverage, distant 2 m to each other (*dSR*).

Step1. System installation:

In this step, after the selection of the proper place to carry out the measurement (based on the regularity of the road pavement, and the presence of reflecting objects), the microphone was attached on the pavement using sufficient modeling clay, and it was covered with the absorbing coverage described above. Then, a cloth disc was placed on the pavement 2 m distant from the microphone. On this cloth disc, the metallic plate of the LWD was placed paying attention to the stability of the LWD and to the similarity among the signals received by the microphone (in terms of peaks amplitude and signal to noise ratio, SNR). In addition, to increase the LWD stability and improve the reproducibility of the signals, a small amount of modeling clay was laid between the metallic parts of the LWD base, and, finally, the LWD rod (where the loading mass flows) was smeared with grease.

Step 2: Data collection: recording vibro-acoustic signatures of the road pavement

In this step, a set of 50 acoustic signals, generated through the LWD and received by the microphone placed on the road pavement, were recorded running a specific Matlab code. These signals represent the vibro-acoustic responses of the pavement to the impulse loads produced by the LWD, herein called ARs.

The temperature of the pavement and the air were measured during the experiments, and they resulted included in the ranges 9-12°C and 12-16°C, respectively.

The first set of ARs, recorded during this step, were properly pre-processed (i.e., alignment using autocorrelation, and averaging) in order to obtain the Average Acoustic Response (AAR) of the road pavement without cracks (Un-Cracked, UC section). This AAR was assumed as baseline data (i.e., the signal related to the original pavement state).

Step 3. Data process: different features are extracted from different domains of analysis.

The data analysis was carried out in time, frequency, and time-frequency domains in order to extract meaningful features from the above-mentioned AAR. The use of the features is necessary because of the fact that the proposed method aims at extracting important pieces of information (i.e., the occurrence or the growth of internal cracks into the road pavement) from acoustic signals that are expected to be too complex and large to be used as such, i.e. without preliminary processing. Furthermore, this information is used during the monitoring process, and for this reason it should consist in data suitable to be easily stored and processed. Consequently, several features were taken into account considering the shape, and the main characteristics of the AARs of the pavement under test (time domain), and their transformations expressed by periodograms and scalograms in frequency and time-frequency domains, respectively). Among all the possible features, we selected the best three ones for each domain, which are listed in Tab. 5.3.

Tab. 5.3 Features considered in this study (mechanical source: LWD).

Symbol	Feature	Unit of measure	Domain/ Feature Source
Δa	Amplitude difference between the absolute maximum P and the absolute minimum N of the AAR amplitudes.	a.u.	Time/Signal
Δt	Time Delay of N from P	ms	
σ	Standard deviation of the AARs.	a.u.	

PSD_{min}	Minimum of the PSD of the AARs into the range 50-150 Hz.	dBW/Hz	Frequency/ Periodogram
S	Slope of the linear regression model of the PSD of the AARs into the frequency range 20-250 Hz.	dBW	
f_c	Spectral centroid of the periodogram (PSD vs. frequency) in the frequency range 20-450 Hz.	Hz	
Ent_{CWC}	Maximum Entropy of the CWCs.	a.u.	Time-Frequency/ CWT scalogram
$p\text{-}f_{WR}$	Pseudo-frequency of the WR (from the y-axis of the scalogram).	Hz	
$Eng_{CWC,max}$	Energy of the CWCs above a given threshold (60 out of 64, i.e. red areas of the scalogram).	a.u.	

Symbols. *AAR* = Average Acoustic Response; a.u. = arbitrary unit; dim. = dimensionless; ms = milliseconds; dB = decibel; dBW/Hz = decibel Watt *per* Hertz; Hz = Hertz; s = seconds; *Ent* = Entropy; CWCs = Continuous Wavelet Coefficients; *p-f* = pseudo-frequency; WR = Wavelet Ridges; *Eng* = Energy; max =maximum; min = minimum.

Note that, simple equations were used to derive the features in the time domain (i.e., basic Matlab functions, such as "min", "max" and "std"). While, for the analyses in the frequency domain, the Eqs. 7 and 8 were used to derive, from the AARs of the pavement under test, the periodograms and the related spectral centroids, respectively. In the same domain, the feature herein called *S*, i.e. the slope of the linear regression of the PSD shown in the periodograms in a given frequency range, was derived using a Matlab code based on the function "polyfit". Finally, the features in the time-frequency domain were identified from the Continuous Wavelet Coefficients (CWCs) and the scalograms, which are the representation of the CWCs.

The reasons behind the choice of the CWT refers to the main strength of the WT that is called time-frequency localization (Kumar and Foufoula-Georgiou 1997), which was discussed in detail in the section 2.5. Furthermore, the CWCs were analyzed in order to extract meaningful information such as the Energy and the Entropy of the CWCs. In particular, as is well known, the Shannon's entropy measures the amount of information in messages (Chai, Zhang, and Duan 2018; Jose, Neil, and Curt 2001). If the message is known the information carried is zero (and the probability associated with the message is the highest, i.e., is equal to 1), while if the message is unexpected, the information content becomes large (and the probability of occurrence of

the message is lesser than 1). Hence, the Shannon's entropy is able to quantify the disorder, or the uncertainty of a probability distribution. For these reasons, in this thesis, the Shannon's entropy was used to recognize the increase of information contained in the signals that can be associated to the occurrence of a variation of the transmission medium (i.e., the road pavement). In this thesis the Shannon's Entropy was calculated using as input the Continuous Wavelet Coefficients (herein called Ent_{CWC}). It was calculated, *per* each scale factor, *a*, using the following expression (Abdolmaleki et al. 2017):

$$Ent_{CWC}(a) = -\sum_{i=1}^{N} p_i \cdot \log_2 p_i, \tag{5. 7}$$

where N is the length of each AAR, and pi is the energy probability distribution of the continuous wavelet coefficients (CWCs), for $i = 1, 2, \ldots, N$, which can be calculated through the following expression:

$$p_i = \frac{|CWC(a,i)|^2}{Eng(a)}, \tag{5. 8}$$

where $Eng_{CWC}(a)$ represents the energy content of the CWCs *per* each scale factor, *a*. In more detail (Abdolmaleki et al. 2017), the variable $Eng_{CWC}(a)$ can be calculated from the matrix CWC, for $b = 1, 2, \ldots, N$ (with N equal to the length of each AR), using the following expression:

$$Eng_{CWC}(a) = \sum_{b} |CWC(a,b)|^2. \tag{5. 9}$$

It should be noted that last expression was used to determine the seventh and the ninth features used in this study (cf. Tab. 5.3).

Step 4: Cracks induction

Longitudinal cracking in wheel paths, "alligator" cracking in wheel paths, block cracking, transverse and longitudinal cracking outside wheel paths, and rutting are surface distresses that usually originate behind/on a road pavement, in surface or base layers (e.g., fatigue cracking and bottom-up cracking, cf. (Huang 2003), and section 1.1). Importantly, the main effects of

the vehicles wheels (especially of the heavy ones) on a road lane can be localized, in two stripes along the traffic direction called wheel paths. Note that distress in the outer wheel path may be severer than the one in the inner wheel path (Huang 2003), and that by paving the road shoulders is likely to mitigate this occurrence. Overall, to this end, equations (cf. Chapter 3) are used for predicting the allowable number of load repetitions when cracks occur over 10% and 45% of the area in the wheel path (Huang 2003)(Finn et al. 1986). Based on what was said above, it is possible to assume that the change of the structural health status of the road pavement is likely to be assessed by referring to the wheel path volumes (deep layers), i.e. where it is more probable to detect early cracks.

In order to simulate the presence of cracks along the wheel paths, three lines of holes were drilled between the source and the receiver (i.e., half of the distance LWD-microphone, *dSR*). In more detail (see Figs. 5.15, and 5.16), 44 Structural Health Statuses (SHSs) were created, which consist of: i) the first line of 15 holes was drilled at half of the distance *dSR*; ii) the second line of 14 holes was drilled between the first line of holes and the microphone, in such a way to obtain distances among the holes of approximately 5 cm (i.e., a group of three neighbor holes forms an equilateral triangle); iii) the third line of 14 holes was drilled between the LWD and the first line of holes. Each hole has a diameter of 10 mm, and a height equal to the thickness of the asphalt concrete layers of the pavement (i.e., 15 cm). The 43 holes were made with a distance of 5 cm from each other.

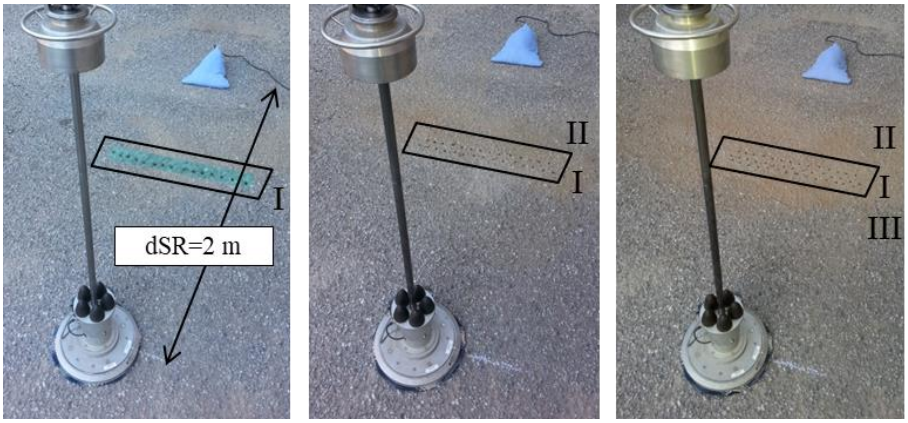

(a) (b) (c)

Fig. 5.15 Lines of holes drilled in the road pavement to simulate the cracks induced by the vehicles under a wheel path: (a) first line of holes; (b) first, and second line of holes; (c) first, second, and third line of holes.

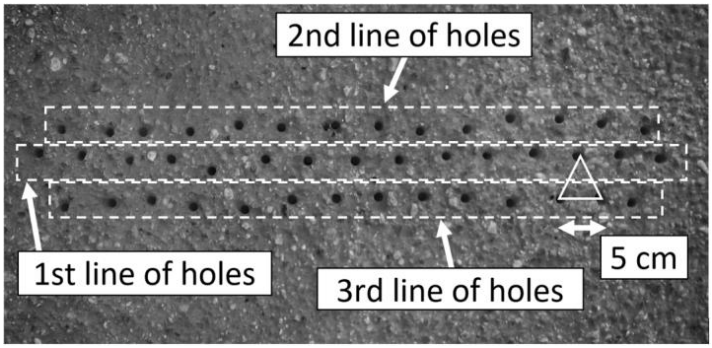

Fig. 5.16 Detail of the three lines of holes drilled in the road pavement under test.

After the creation of each hole in the road pavement, this latter was loaded by the LWD and a set of 50 vibro-acoustic signatures of the pavement were recorded. At the end of the experiment 44 series of 50 signatures (i.e., 2200 acoustic signals) were recorded, i.e.: a) 1 series from the un-cracked pavement; b) 15 related to the holes of the first line; c) 14 related to the second line of holes; d) 14 related to the third line.

Features extracted in the Time domain

Fig. 5.17 shows all the 2200 Acoustic Responses (ARs, i.e. signal amplitude vs. time) recorded from the road pavement under investigation in each of the 44 SHSs in which it was tested. Furthermore, the same figure shows the graphical representation of two out of three features extracted in the time

domain, i.e. the amplitude difference between the absolute maximum P and the absolute minimum N of the AR, herein called Δa, and the time delay of N from P, herein called Δt.

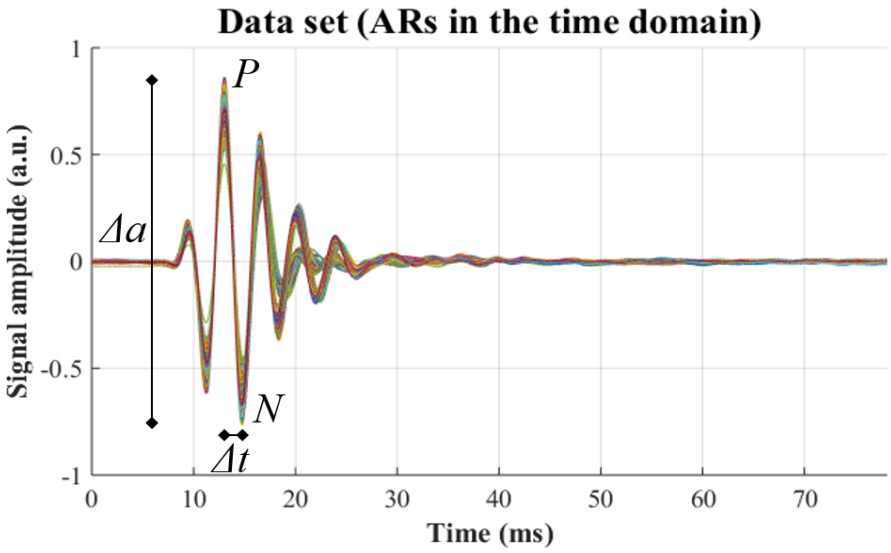

Fig. 5.17 Acoustic Responses (ARs) of the road pavement in 44 different SHSs in the time domain, and the representation of two out of the three features extracted in the time domain.

Tab. 5.4 reports the values of the features extracted from the AARs in the time domain for each SHS.

Tab. 5.4 Values of the features extracted in the Time domain.

SHS	Δa (a.u.)	Δt (ms)	σ (a.u.)
SHS0	1.34	1.86	13.21%
SHS1	1.44	1.81	13.91%
SHS2	1.35	1.72	13.32%
SHS3	1.28	1.71	12.55%
Mean	**1.35**	**1.77**	**13.25%**
Max	**1.44**	**1.86**	**13.91%**
Min	**1.28**	**1.71**	**12.55%**

Symbols. SHS = road pavement Structural Health Status; SHS0 = pavement without holes; SHS1 = pavement with 1 line of holes (i.e., 15 holes); SHS2 = Cracked pavement with 2 lines of holes (i.e., 29 holes); SHS3 = pavement with 3 lines of holes (i.e., 43 holes); Δa = amplitude difference between the absolute maximum P and the absolute minimum N of the Average Acoustic Responses (AARs) (a.u.); Δt = time delay of N from P (ms); σ = standard deviation of the AARs (%).

Importantly, the value of the features related to the SHS1, SHS2, and SHS3 are the average of 15, 14, and 14 values, respectively (which refer to the number of holes *per* SHS). Note that, the same operation was carried out fot

the values of the Tabs. 5.5, and 5.6. $\measuredangle a$ is a dimensionless amplitude, $\measuredangle t$ is a time delay measured in milliseconds, while the standard deviation σ of the AARs that was reported in percentage terms.

Features extracted in the Frequency domain

The AARs of the road pavement under investigation were elaborated using Eq. 4.8 and 4.9 in order to obtain periodograms (and two out of three features considered in this domain; cf. Fig. 5.18), and spectral centroids (third feature extracted from this domain). The results are reported in the table below (Tab. 5.5). In this study, in the pursuit of better analyzing the Power Spectral Density (PSD) of the AARs of the pavement under investigation, the logarithmic scale for the y-axis (dBW/Hz) was used, and a value of −100 dBW/Hz was considered as the lower bound. For this reason, the periodogram (Fig. 5.18) shows the PSD between 0 and -100 dBW/Hz in the frequency range 20-450 Hz.

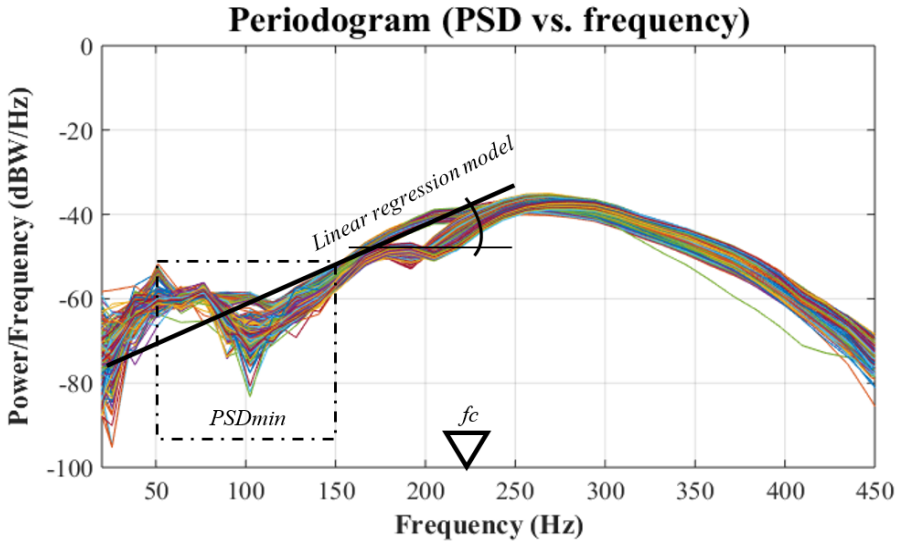

Fig. 5.18 Periodogram (PSD *versus* Frequency) of the Acoustic Responses (ARs) of the road pavement under investigation, and representation of all the features extracted from the frequency domain.

Furthermore, Fig. 5.18 shows: i) the section of the periodogram where local minima of the PSD were calculated (i.e., the feature herein called PSD_{min}); ii) an example of linear regression line of the PSD into the frequency range 20-250 Hz, and its slope (i.e., the feature herein called S); iii) the spectral

centroids of the periodogram (i.e., the feature herein called *fc*, which is represented by a triangle).

Tab. 5.5 Values of the features extracted in the Frequency domain.

SHS	PSD_{min} (dBW/Hz)	S (dBW)	f_c (Hz)
SHS0	-51.56	0.132	239
SHS1	-52.57	0.134	242
SHS2	-54.91	0.130	250
SHS3	-55.56	0.127	251
AV	**-53.65**	**0.131**	**246**
Max	**-51.56**	**0.134**	**251**
Min	**-55.56**	**0.127**	**239**

Symbols. SHS = road pavement Structural Health Status; SHS0 = UC = pavement, i.e. without holes; SHS1 = C1 = Cracked pavement with 1 line of holes (i.e., 15 holes); SHS2 = C2 = Cracked pavement with 2 lines of holes (i.e., 29 holes); SHS3 = C3 =Cracked pavement with 3 lines of holes (i.e., 43 holes); *PSDmin* = minimum of the Power Spectral Density (PSD) of the Average Acoustic Responses (AARs) in the range 50-150 Hz (dBW/Hz = dBWatt/Hz); *S* = Slope of the linear regression model of the PSD of the AARs into the frequency range 20-250 Hz; *fc* = spectral centroid of the periodogram (Hz) in the range 20-450Hz.

Features extracted in the Time-Frequency domain

Time-frequency domain analysis involved: i) aligning (by means of cross-correlation) the AARs in order to optimize the comparison of the graphic results (spectrograms); ii) choosing of the mother wavelet (i.e., the wavelet "Meyer" was selected because of its similarity with the ARs); iii) calculating the Continuous Wavelet Coefficients (CWCs) using the Continuous Wavelet Transform (CWT), through the Eqs. 2.1 and 2.6, in a given pseudo-frequency range; iv) extracting the CWT-related features through the Eqs. 5.7-5.9.

The corresponding graphical results are the scalograms (Fig. 5.19), which refer to the road pavement under investigation in two conditions: 1) un-cracked (i.e., no holes); 2) 43 times cracked (i.e., 3 lines of holes). X-axis refers to time (milliseconds), y-axis refers to the pseudo-frequency (Hz), while colors point out the percentage of energy for each CWC (cf. (Mathworks 2008)) (arbitrary unit), scaled as shown by the color palette that was plotted together with each scalogram.

Note that one out of three features considered in the time-frequency domain, i.e. the feature herein called $p\text{-}f_{WR}$, refers to the pseudo-frequency of the Wavelet Ridges (WR) of the scalogram, which can be defined, according to

(Reda Taha et al. 2006), as *"the maxima points of the normalized scalogram representing the wavelet coefficients with respect to different time and scale values."* In particular, the scalogram shows the percentage of energy for each CWC (cf. (Mathworks 2008)) in the pseudo-frequency range 110-700 Hz, and the feature $p\text{-}f_{WR}$ is included in this range. Furthermore, the other two features taken into account in this domain, i.e. the Entropy of the CWC (herein called Ent_{CWC}), and the Energy of the CWC above a given threshold (i.e., 60 out of 64, which refer to the red areas of each scalogram) herein called Eng_{CWC}, were chosen aiming at taking advantage from the CWCs and their graphical plots, i.e. the scalograms. Tab. 5.6 shows the values of the features extracted in the time-frequency domain.

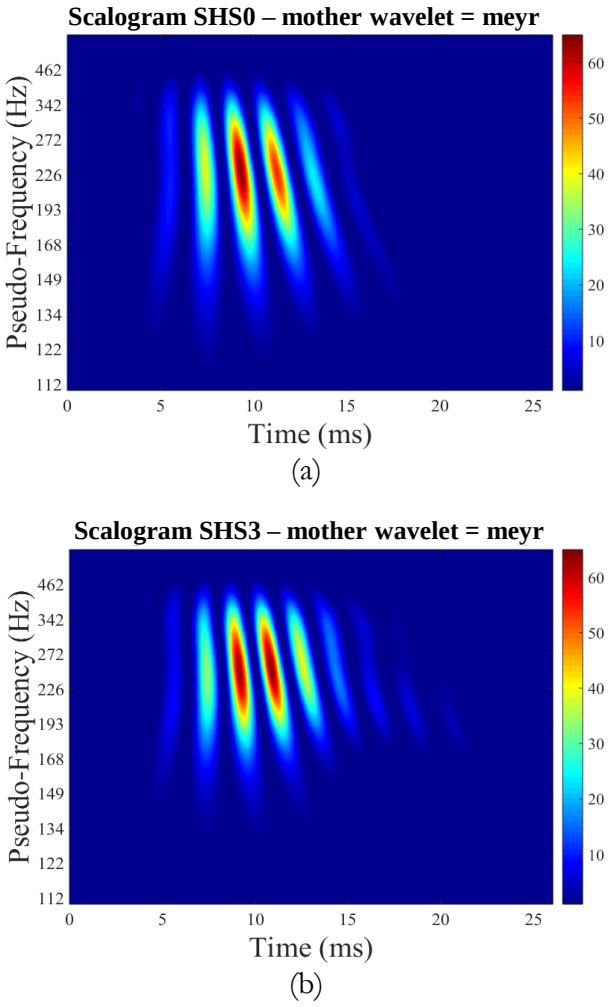

Fig. 5.19 Example of scalograms derived from the Average Acoustic Responses (AARs) of the road pavement in two different SHSs: (a) un-cracked (SHS0), and (b) cracked with 3 lines of holes (SHS3).

Tab. 5.6 Values of the features extracted in the Time-Frequency domain.

SHS	Ent_{CWC} *(a.u.)*	$p\text{-}f_{WR}$ *(Hz)*	$Eng_{CWC,max}$ *(a.u.)*
SHS0	11.54	262	2.61%
SHS1	11.76	280	1.97%
SHS2	11.90	284	1.88%
SHS3	11.93	287	2.14%
AV	**11.78**	**278**	**2.2%**
Max	**11.93**	**287**	**2.6%**
Min	**11.54**	**262**	**1.9%**

Symbols. SHS = road pavement Structural Health Status; SHS0 = pavement without holes; SHS1 = pavement with 1 line of holes (i.e., 15 holes); SHS2 = pavement with 2 lines of holes (i.e., 29 holes); SHS3 = pavement with 3 lines of holes (i.e., 43 holes); Ent_{CWC} = Maximum Entropy of the Continuous Wavelet Coefficients (CWCs) (a.u.); $p\text{-}f_{WR}$ = pseudo-frequency of the Wavelet Ridge (WR) from the y-axis of the scalogram (Hz); $Eng_{CWC,max}$ = Energy of the CWCs from the z-axis (i.e. the colors) of the scalogram (a.u.).

Based on the results reported in the previous three paragraphs of this chapter, the following overall observations can be made:

- The presence and the increase of the number of cracks into the road pavement seams to lead to a dissipation of the energy of the sound and of the seismic waves traveling from the source, through the road pavement, to the receiver. This dissipation is caused by the complex interactions (adsorption, reflection and diffraction) between the mechanical waves and the drilled holes. This statement was derived analyzing the behavior of the features: i) $\measuredangle a$, and σ in the time domain, which undergo a reduction; ii) Ent_{CWC} and $Eng_{CWC,max}$, extracted in the time-frequency domain. These last two features show that: 1) the maximum entropy of the system (Ent_{CWC}) increases when the number of cracks increases (underling the increase of the chaos in the transmission medium that leads to an increase of the information contents of the signals); 2) the dissipation of the signal's energy leads to an overall reduction of the absolute maxima of the wavelet coefficients (CWCs). This reduction is clearly shown by the scalograms. In fact, by comparing the scalograms in Fig. 5.19, it is possible to see that the presence of the cracks increased the number and the extension of the wavelet ridges (WRs), which are represented by different colors into the scalograms (i.e. with values between 20

and 64; cf. color palette plotted beside the scalograms in Fig. 5.19). These increases were caused by the fact that, before the scalogram is plotted, the energy of the CWCs is normalized and scaled. These two processes lead to the appearance of hidden WRs (cf. tail of the scalogram in Fig. 5.19b) and, at the same time, the association of a greater number of WRs to the highest values of the scale (e.g., from 40 – yellow – to 50 or greater – orange/red). From these graphical results, the feature $Eng_{CWC,max}$ was extracted. This feature refers only to the extension of the red areas of the scalogram (values between 60 and 64), but is able to well represent the energy dissipation caused by the cracks induced into the road pavement during the experimental investigation.

- From a spectral point of view, the dissipation of the energy discussed above can be seen as a reduction of some spectral components in the low frequency region, which leads to an increase of the influence of the high frequency belonging to the same region. These conclusions were derived by analyzing the behaviors of the features Δt (extracted in the time domain); PSD_{min}, S, and fc (from the frequency domain); and $Eng_{CWC,max}$ (from the time-frequency domain). In more detail, the reduction of the PSD_{min} represents the reduction of the spectral content of the acoustic signals under analysis in the frequency range 50-150 Hz shown into the periodograms (cf. Fig. 5.18), and this reduction leads to a decrease of the first derivative of the linear regression model built on the periodogram in the frequency range 20-250 Hz. Hence, the spectral centroids of the periodograms in the range 20-450 Hz undergo a slight increase (from 239 Hz to 251 Hz), which was also detected by the feature $p\text{-}f_{WR}$ (230-249 Hz).

Step 5. Road pavement classification: hierarchical clustering

The validation of the proposed method is based on the experimental investigation described above, and on the following hierarchical clustering procedure. Note that, the hierarchical clustering is one of the algorithm

belonging to the "clustering" family, which is one of the families of the machine learning (O'Kelly 2016).

The hierarchical clustering procedure used in this thesis consists in: i) computing the distance matrix, which contains the Euclidean distances between pairs of observations (i.e., samples of each AR, or values of each features) (Mathworks 2006); ii) encoding a tree of hierarchical clusters (i.e., a matrix with cluster indices and linkage distances between pairs of clusters) using as input the distance matrix calculated in the first step, counting the furthest distance between two element of the distance matrix, and considering 4 clusters, i.e. one for each structural health status (SHS) of the road pavement under investigation (Mathworks 2006); iii) finding the smallest height at which a horizontal cut through the agglomerative hierarchical cluster tree (generated in the previous step), groups the observations into 4 clusters (Mathworks 2006); iv) generating the confusion matrix (i.e., a matrix that shows how many observations were associated to each cluster; cf. (Mathworks 2006)); v) verifying if the ARs associated to a given SHS is correctly clustered (identification) and associated to a single cluster (classification).

The hierarchical clustering procedure, aiming at validate the proposed NDT-SHM method, was initially applied on the dataset consisting of 44 AARs, but poor results were obtained.

Consequently, it was applied using as input the 2200 ARs, and the values of the 9 features related to each AAR define above.

Tab. 5.7 shows four clusters (columns) and four statuses (rows) of the so-called "confusion matrix", derived applying the hierarchical clustering procedure. This allows deriving: 1) the "best cluster" (herein called "predicted cluster", cf. column *PC*), i.e. the one corresponding to the highest number of observations; 2) the highest percentage of the observations associated to the *PC*, for the given status (i.e., *Max OPC*, %).

For example, the un-cracked status (SHS0) "corresponds" to the fourth cluster (SHS0~CL4, with *Max OPC* = 100%), while the most cracked status (SHS3) corresponds to the second cluster (SHS3~CL2, with *Max OPC* = 92%).

If an ideal classification were carried out, the confusion matrix would show four different "perfect" associations (SHSi~CLj, with i different from j and *Max OPC* = 100%), that is to say rows that would consist in only one non-zero element.

Tab. 5. 7 Confusion matrix derived using the hierarchical clustering procedure and, as input, the 2200 ARs of the road pavement under test.

SHS	CL_1	CL_2	CL_3	CL_4	***PC***	***Max OPC* (%)**
SHS0	0	0	0	50	**4**	**100**
SHS1	64	6	0	641	**4**	**90**
SHS2	158	519	22	0	**2**	**74**
SHS3	0	639	50	0	**2**	**92**

Symbols. SHS = Structural Health Status; SHS0 = pavement without holes; SHS1 = pavement with 1 line of holes (i.e., 15 holes); SHS2 = pavement with 2 lines of holes (i.e., 29 holes); SHS3 = pavement with 3 lines of holes (i.e., 43 holes); CLn = Cluster number n, with n=1, 2, 3, 4; *PC* = Predicted Cluster; *Max OPC* = highest percentage of observations associated to *PC* (%).

Tab. 5.7 shows that: i) 50 out of 50 ARs of the pavement in the SHS0 were associated to the cluster number 4 (i.e., CL_4); ii) the 90% of the ARs of the pavement in the SHS1 were associated to the cluster number 4; iii) the 74% of the ARs of the pavement in the SHS2 were associated to the cluster number 2; iv) the 92% of the ARs of the pavement in the SHS3 were associated to the cluster number 2.

These results allow to state that: i) if the ARs (acoustic signals) are used as input of the clustering procedure, it is not possible to validate the proposed method. In fact, the algorithm was not able to distinguish the un-cracked (SHS0) road from the road cracked with one line of 15 holes (SHS1), and the pavement cracked with 2 and 3 lines of holes (because of the fact that they are associated to the same cluster, i.e., the cluster number 2); ii) the features extracted from the ARs may be a possible solution to this misclassification, and may be used to validate the proposed method.

The results of the clustering procedure carried out using the nine features extracted from the ARs, are shown in the following tables. In more detail, for each structural status (SHS), and for a given domain (e.g., time, T, frequency,

F, and time-frequency, TF), Tab. 5.8 shows the parameters *PC* and *Max OPC* obtained using the features extracted from the ARs.

Tab. 5.8 Results of the hierarchical clustering of the nine features extracted from the ARs of the road pavement in three different domains.

Domain		SHS				*Max OPC$_{AV}$ (%)*
		SHS0	SHS1	SHS2	SHS3	
T	*PC*	2	1	2	3	n.a.
	Max OPC (%)	72	59	50	48	
F	***PC***	**1**	**2**	**4**	**3**	**71**
	Max OPC (%)	**100**	**48**	**83**	**54**	
TF	*PC*	3	4	1	1	n.a.
	Max OPC (%)	100	83	92	73	
T + F	*PC*	2	1	3	3	n.a.
	Max OPC (%)	96	65	71	88	
T + TF	*PC*	1	2	3	3	n.a.
	Max OPC (%)	100	51	99	91	
F + TF	*PC*	2	2	3	3	n.a.
	Max OPC (%)	100	65	72	84	
T + F + TF	*PC*	2	2	4	4	n.a.
	Max OPC (%)	100	52	94	91	

Symbols. ARs = Acoustic Responses of the road pavement under test in different Structural Health Statuses (SHSs); SHS0 = Un-Cracked pavement, i.e. without holes; SHS1 = Cracked pavement with 1 line of holes (i.e., 15 holes); SHS2 = Cracked pavement with 2 lines of holes (i.e., 29 holes); SHS3 = Cracked pavement with 3 lines of holes (i.e., 43 holes); *PC* = Predicted cluster; *Max OPC* = highest percentage of observations associated to *PC* (%); T = all the features extracted in the Time domain; F = all the features extracted in the Frequency domain; TF = all the feature extracted in the Time-Frequency domain; *Max OPC$_{AV}$ (%)*= average of the values *Max OPC (%)*; n.a. = misclassification.

Based on the results contained in Tab. 5.8 is possible to conclude that:

i) Carrying out the clustering by using all the nine features extracted from the three domains (last row), it is not possible to classify in a correct way the ARs (misclassification = n.a.), and the results are quite similar (and slight worse) to the results obtained using the ARs (shown in Tab. 5.7). It seems that the combination of all the extracted feature leads to an effect that is the contrary to the desired one, i.e. a loss of information instead of an extraction of information.

ii) If the feature of one domain are coupled with the features of another domain (i.e., 6 features from two domains are used together), in two cases out of three (i.e., T + F, and T + TF), it is possible to detect the

presence of the first line of cracks but it is not possible to distinguish the effect of the second and third lines.

iii) If the clustering is carried out using only three features belonging to the same domain (e.g., T = all the features extracted from the ARs analyzed in the Time domain), different results can be obtained. In particular: a) the features from the TF domain lead to results that are quite similar to the previous ones; b) the features related to the domain T lead to a misclassification; c) the features from F lead to the most efficient clustering (i.e., 71% of the ARs, in average, were correctly classified).

These results shows that: 1) better results can be obtained if the spectral content of the ARs is considered; 2) using the features extracted from the F domain, it is possible to correctly classify the ARs of the pavement, i.e. most of the ARs gathered from the road pavement in the same SHS (i.e., SHS0, SHS1, SHS2, and SHS3) were associated to a unique cluster among the 4 considered (i.e., *PC* = 1, 2, 4, 3; cf. Tab. 5.8, domain F). Based on this last result, a more in-depth analysis about the combination of the nine extracted features was carried out, and Tab 5.9 shows the related results.

Tab. 5.9 Hierarchical clustering of the features extracted from the ARs.

#F	*F*		SHS				*Max* OPC_{AV} (%)
			SHS0	SHS1	SHS2	SHS3	
1	2	*PC* *Max OPC (%)*	3 98	4 79	2 56	1 80	78
2	**2+9**	***PC*** ***Max OPC (%)***	**4** **98**	**3** **79**	**1** **82**	**2** **89**	**87**
3	*2+3+9*	*PC* *Max OPC (%)*	4 98	3 75	1 68	2 97	85
4	*2+3+5+9*	*PC* *Max OPC (%)*	4 98	3 76	1 57	2 99	83
5	*3+4+5+6+7*	*PC* *Max OPC (%)*	2 100	1 66	4 58	3 71	74
	2+3+5+6+9	*PC* *Max OPC (%)*	1 96	2 68	4 82	3 50	74
	1+2+6+8+9 *1+2+5+6+8* *1+2+3+6+8*	*PC* *Max OPC (%)*	2 100	1 67	4 68	3 61	74

6	*1+2+5+6+8+9* *1+2+3+6+8+9* *1+2+3+5+6+8*	*PC* *Max OPC (%)*	2 100	1 67	4 68	3 61	74
	1+2+4+5+7+9	*PC* *Max OPC (%)*	1 84	2 67	3 61	4 85	74
7	*1+2+3+5+6+8+9*	*PC* *Max OPC (%)*	2 100	1 67	4 68	3 61	74
8	*n.a.*	*PC* *Max OPC (%)*	- -	- -	- -	- -	-
9	*n.a.*	*PC* *Max OPC (%)*	- -	- -	- -	- -	-

Symbols. ARs = Acoustic Responses of the road pavement under test in different Structural Health Statuses (SHSs); SHS0 = Un-Cracked pavement, i.e. without holes; SHS1 = Cracked pavement with 1 line of holes (i.e., 15 holes); SHS2 = Cracked pavement with 2 lines of holes (i.e., 29 holes); SHS3 = Cracked pavement with 3 lines of holes (i.e., 43 holes); #F = number of features used as input during the clustering; F = Features from the first one of the Time domain to the last one of the Time-Frequency domain; *PC (%)*= Predicted cluster; *Max OPC (%)* = highest percentage of observations associated to *PC (%)*; *Max* OPC_{AV} *(%)*= average of the values *Max OPC (%);* n.a. = misclassification.

For each SHS, Tab. 5.9 shows: i) the number of features used in each trial (#F); ii) the cluster corresponding to the given SHS (e.g., SHS0 = *PC* = 3, with *Max OPC (%)* = 98%); iii) the average *OPC* (*Max* OPC_{AV}, %).

Note that different combinations of features imply different results, which have been expressed using the parameter herein called *Max* OPC_{AV} (a sort of key performance indicator). This parameter was calculated averaging the values of the parameter *Max OPC*.

Based on the content of Tab. 5.9, the following considerations can be derived: i) by using only the feature number 2, i.e. the time delay between the absolute maxima and minima of the ARs in the time domain (herein called $\angle t$), it was possible to classify in a correct way the ARs (on average, the 78% of the ARs were correctly clustered). This means that $\angle t$ can be considered as the best among the features taken into account in this study; ii) by combining 8 or 9 features all together, it was not possible to obtain a correct classification of the ARs (misclassification), and the misclassification increased hand in hand with the number of the features used; iii) similar results, in terms of *Max* OPC_{AV} (74%), were obtained using proper combinations of 5, 6, and 7 features; iv) good results (*Max* OPC_{AV} = 83-85%) can be achieved through the proper combination of 3 or 4 features; v) the best results were obtained when combining $\angle t$ and $Eng_{CWC,max}$. As a matter of

fact, this combination led to the highest values of the $Max\ OPC_{AV}$ (87%), which indicate that it was possible to detect the occurrence of the cracks and discriminate among different levels of cracks.

Even though these results have been derived from an experimental investigation where, in order to minimize the variables of the problem, several approximations and limiting conditions have been adopted (e.g., the same road pavement was loaded using the same source, i.e., the LWD; the distance between the source and the receiver - the insolated microphone - was kept constant; the cracks were induced affecting the entire thickness of the pavement; etc.), and bearing in mind that the features must be chosen case by case and point by point (e.g., each road pavement has a different ARs, or acoustic signature; different loads on the same pavement lead to different ARs; different points of the same pavement may have different ARs because of the boundary conditions; the AR is affected by the temperature and humidity of the pavement; etc.), this study appears sufficient to validate the proposed method, and lay the foundation for future work.

Consequently, future work will involve: i) the use of traffic as source of sound and seismic waves; ii) the application of different techniques to define the proper features to be used during the road pavement structural health monitoring (SHM) process (e.g., using methods for the selection of the best mother wavelet to carry out the CWT); iv) the use of Artificial Neural Networks to build a more powerful tool that is able to classify the acoustic signature of the road pavement as a function of the structural health status, or to identify the level of damage from the acoustic signatures.

5.1.4. Improvement of the analysis in the time-frequency domain: the mother wavelet selection [7]

In the previous section, the potentialities of the Wavelet Transform in analyzing the data in the time-frequency domain were discussed. While, this section contains the results of a study conducted to improve the proposed method by mean of the improvement of the application of the Continuous Wavelet Transform (CWT). As is well-know, although the CWT is one of the

[7] This section mainly refers to the papers 3.4, and 3.5 (see Scientific production).

most suitable tools for the identification of signal singularities, its success depends critically on the "mother wavelet" (hereafter indicated as MW) used during the data processing, and on the criterion used to select the most efficient MW (often called "best mother wavelet"). First of all, in order to make more clear which step of the proposed method was improved (through the selection of the best MW), the Fig. 5.20 was plotted. This figure shows that one additional step (i.e., the Step 3.1) was added to the steps defined in the section above (cf. Fig. 5.11). Secondly, the motivations behind this study refers to some aspects related to the choice of the MW. As mentioned in section 2.5, a MW with many vanishing moments should be chosen is the function to be analyzed has few isolated singularities, while if a high number of singularities must be detected (using high-amplitude wavelet coefficients), a MW with compact support (and reduced vanishing moments) should be preferred. In order to select the proper MW, qualitative and quantitative methods (which were reported and analyzed in section 2.5) can be used.

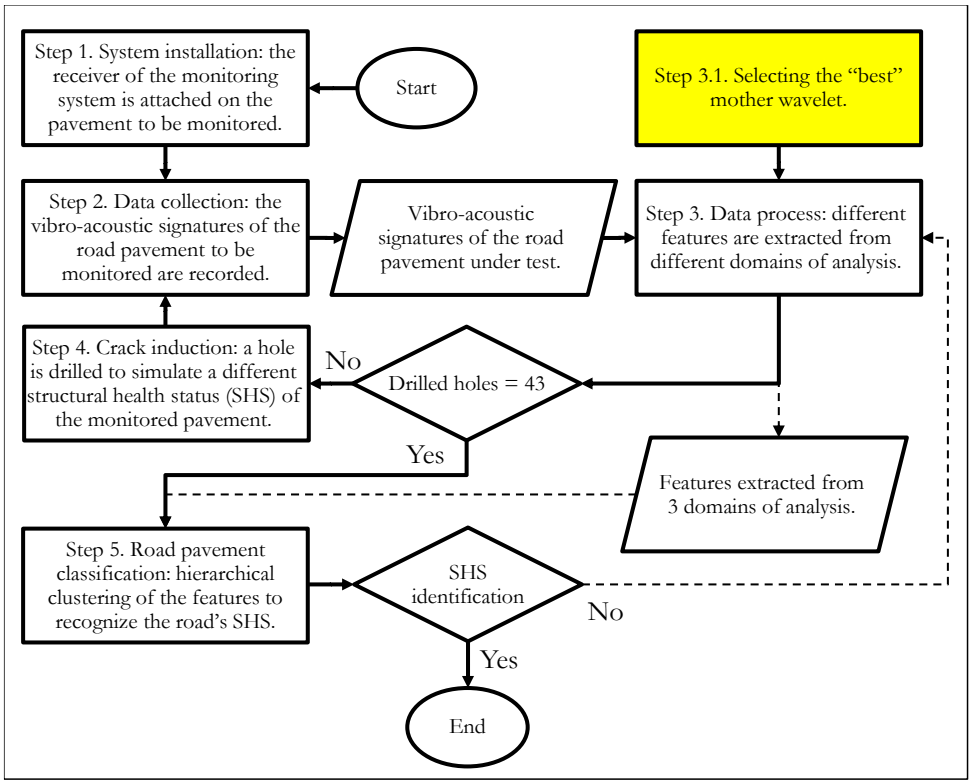

Fig. 5.20 Main steps of the feature-based approach used for the road pavement classification, which include the selection of the best mother wavelet (step 3.1).

Finally, three quantitative MW selection methods were selected among those listed in the literature review (see Tab. 2.6 of section 2.5) and applied to the same data set used in the previous section (i.e., the vibro-acoustic response to the LWD loads). Fig. 5.21 provides an overview of the study.

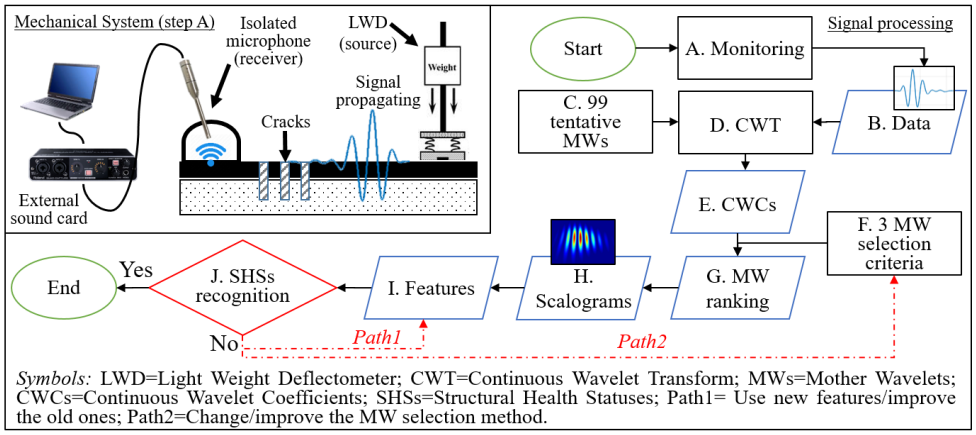

Fig. 5. 21 Summary of the study carried out to improve the SHM-NDT method.

Fig. 5.21 shows the different tasks (from A to J) that were carried out during this study. In particular, the data set (see task B. Data in Fig. 5.21) consists of 44 Average Acoustic Responses (AARs), derived from the 2200 Acoustic Responses (ARs) recorded during the experimental investigation (see task A. Monitoring in Fig. 5.21), described above; cf. section 5.1.3). This latter involved 44 different structural health status of a road pavement, i.e. from the first one (SHS0) related to the un-cracked road pavement to the last one (SHS43) that refers to the same road pavement cracked 43 times (cf. section 5.1.3). In this study, as candidate mother wavelets (MWs), the following libraries consisting of 7 families were considered: Daubechies (db), Symlet (sym), Coiflets (coif), Meyer (meyr), Discrete Meyer (dmey), Mexican hat (mexh), and Morlet (morl). Among the MW families cited above, the orthogonal MW families Daubechies and Symlet have a maximum order equal to 45 (corresponding to the maximum number of their vanishing moments), the family Coiflet has maximum order equal to 5 (each order corresponds to 2 vanishing moments), while the MW morl, dmey, meyr, mexh do not have vanishing moments (Mathworks 2018a). Considering all the families chosen and the correspondent orders, the MWs used in this study were 99 (45 db +

45 sym + 5 coif + 1 meyr + 1 dmey + 1 mexh + 1 morl; cf. task C. 99 tentative MWs in Fig. 5.21). They were selected because of the facts that (i) they are compatible with the CWT (Mathworks 2018a), and (ii) they are commonly used for similar application (cf. e.g., (Y. Wang et al. 2016)). The 99 MWs were used to process the 44 AARs of the road pavement under investigation (see task D. CWT in Fig. 5.21), in order to obtain the corresponding Continuous Wavelet Coefficients (CWCs; see task E. CWCs in Fig. 5.21).

Afterwards, three quantitative MW selection methods (cf. task F. 3 MW selection criteria in Fig. 5.21) were picked out from those listed in Tab. 2.6, and then they were applied to the AARs (vibro-acoustic signatures) in order to understand (see task G. MW ranking in Fig. 5.21) which is the MW that approximates the signals to be analyzed with few nonzero wavelet coefficients, which is the "best MW" for the particular application presented in the previous paragraphs. This means that if scalograms are used to represent the wavelet coefficients, they are able to highlight any variation of the wavelet coefficients. In this study, scalograms were used to try to recognized and quantified the variation of the structural health status (SHS) of the road pavement under test (see H. Scalograms in Fig. 5.21). In more detail, this last task was carried out identifying and extracting features from the scalograms (see I. Features in Fig. 5.21), and these features were monitored to identify their variation as a function of the SHSs of the pavement (see J. SHSs recognition in Fig. 5.21). At this point, if the scalograms and the feature extracted are able to recognize the variation of the pavement's SHS this means that the MW, ranked as the best one and the MW selection method, is actually the more efficient. While, if the variation of the SHS is not clearly recognized, it is possible to take two different path, i.e. "Path1" by refining the features used or extracting different features, or "Path 2" by changing or improving the MW selection method used (see the dotted lines in Fig. 5.21).

The following quantitative MW selection criteria were applied and compared:

- Correlation Coefficient method (herein called CC method; cf. (Pal et al. 2011; Rodrigues et al. 2016));

- Maximum Energy to Shannon Entropy Ratio criterion, herein called MEER method (cf. (Rodrigues et al. 2016; Yan and Gao 2009));
- Variance method or SUMVAR method (cf. (Rafiee and Tse 2009; Rodrigues et al. 2016)).

The methods listed above were selected among the quantitative methods reported in Tab. 2.6 because of the fact that (i) they were frequently used for SHM purposes (cf. (Kumar et al. 2014; Ngui et al. 2013; Rafiee and Tse 2009; Rodrigues et al. 2016)), and that (ii) they are based on different input parameters derived from the Continuous Wavelet Coefficients (CWCs, as in (Rafiee and Tse 2009)), such as the root mean square, the energy, the entropy, and the variance of the wavelet coefficients. In more detail:

- The CC method was chosen because of the fact that it allows combining data that refer to the structural health conditions of the road pavement under investigation (see Tab. 5.10) with the data gathered through the receiver system.
- The MEER method was chosen because it is based on the main characteristics of the CWCs, i.e. the energy and the entropy. Furthermore, the entropy-based methods are indicated as the most successful for the choice of the mother wavelet (considering the fact that pure noise signals have big Shannon's entropies, while systematic signals have almost zero entropy; cf. (Reda Taha et al. 2006)).
- The SUMVAR method was chosen because it allows carrying out statistical analysis on the CWC in terms of variance.

Note that, the three methods listed above were applied using the CWCs that were calculated using the CWT.

In the following, the procedures used in this study to apply the three MW selection methods will be presented together with the equations that are the basics of the methods.

The three procedures cited above have five common steps (from task A to task E in Fig. 5.21) consisting in:

- recording a data set of 50 acoustic signals (or Acoustic Responses, ARs) in each of the 44 structural health statuses (SHSs) of the road pavement under test (i.e., 2200 signals or ARs);
- aligning the ARs;
- averaging the ARs related to each SHS to obtaining one Average Acoustic Response (AAR) *per* SHS (i.e., 44 AARs, 9500 samples long);
- selecting one of the 99 MWs;
- building the vector of the scaling parameter, *a*, using the Eq. 2.6, for including the frequency range where the CWCs have non-zero elements (i.e., in this case, consisting of 100 elements equally spaced between 100 Hz and 1000 Hz);
- applying the CWT (through a specific Matlab toolbox that allows using Eq. 2.1) to each AAR using the selected MW.

After these five steps, *per* each MW, a series of 44 CWC matrixes was calculated, i.e. one matrix *per* each SHS (which consisted in 100 rows × 9500 columns). This means that 4356 (44×99) CWC matrixes were generated and analyzed in this study in order to find the "best" MW.

The first MW selection method that was applied, i.e. the Correlation Coefficient (CC) method, is usually applied to correlate tool wear to the root mean square (RMS) of the CWCs obtained through the Wavelet Packet Transform (WPT; cf. (Pal et al. 2011; Rodrigues et al. 2016)). In this work, the method was adapted as follows: i) instead of the tool wear, the reduction of the road pavement volume due to each drilled hole was herein interpreted in terms of pavement damage; ii) instead of the WPT, the CWT was used. Hence, the CC method was applied as follows:

1. the average root mean square (RMS) of each CWC matrix in each scale (or frequency (Pal et al. 2011)), corresponding to one SHS, (herein called *Fi*) was calculated to the transpose of the CWC matrix. A vector of 44 elements was determined;
2. the average value of F_i (corresponding to all the SHSs) was determined (i.e., 1 element, herein called F_{AV});

3. for each SHS, the corresponding pavement damage value V_i (i.e., the reduction of the pavement volume due to the presence of each drilled holes) was calculated. V_i is one vector that consists of 44 elements (i.e., i = 1, 2, …, 44). Note that the pavement damage values were assumed as positive elements, according to the literature (Pal et al. 2011; Rodrigues et al. 2016);
4. the average value of the elements of V_{AV} was calculated from the previous values (obtaining one positive value);
5. finally, the Correlation Coefficient was determined (for each MW), through the equation below (Pal et al. 2011):

$$CC = \frac{\sum_i (V_i - V_{AV})(F_i - F_{AV})}{\sqrt{\sum_i (V_i - V_{AV})^2 \sum_i (F_i - F_{AV})^2}}, \qquad (5.\ 10)$$

where CC stands for Correlation Coefficient of the CWCs *per* each MW; V_i is the reduction of volume (cm^3 see Tab. 5.10) of the pavement due to each drilled hole, or single pavement damage; V_{AV} is the average pavement damage obtained from the V_i; F_i is the average Root Mean Square (RMS) of the CWCs in each pseudo-frequency band; F_{AV} is the average RMS of the CWCs calculated from F_i.

Note that this procedure was repeated from the point 3 above to the last point, using the 99 MWs that were considered in this study. Among the 99 values of CC calculated, this method associates the highest one with the best MW due to the best correlation between the pavement damage and the acoustic signals that pass through the cracked pavement (represented by the wavelet coefficients).

Tab.5.10 illustrates the volume reduction, V_i, corresponding to the i-th structural status, SHSi. In particular, a road volume with the following characteristics was considered: i) thickness equal to the height of the asphalt concrete layers, i.e. 15 cm; ii) width equal to the first line of holes, i.e. 70 cm; iii) length equal to the distance between receiver (microphone) and source

(LWD device), i.e. 2 m. Consequently, the volume involved resulted almost equal to 377 cm^3. Furthermore, the dimension of the single hole has been considered, i.e. a diameter of 1 cm and a depth of 15 cm. Hence, the volume subtracted for each drilled hole was 11.78 cm^3. Each hole was associated to one different Structural Health Status (SHS) of the road pavement.

Tab. 5.10 Road pavement volume reduction.

SHSi	V_i (cm^3)	SHSi	V_i (cm^3)	SHSi	V_i (cm^3)	SHSi	V_i (cm^3)
SHS0	0.0	SHS11	129.6	SHS22	259.2	SHS33	388.8
SHS1	11.8	SHS12	141.4	SHS23	271.0	SHS34	400.5
SHS2	23.6	SHS13	153.1	SHS24	282.7	SHS35	412.3
SHS3	35.3	SHS14	164.9	SHS25	294.5	SHS36	424.1
SHS4	47.1	SHS15	176.7	SHS26	306.3	SHS37	435.9
SHS5	58.9	SHS16	188.5	SHS27	318.1	SHS38	447.7
SHS6	70.7	SHS17	200.3	SHS28	329.9	SHS39	459.5
SHS7	82.5	SHS18	212.1	SHS29	341.6	SHS40	471.2
SHS8	94.2	SHS19	223.8	SHS30	353.4	SHS41	483.0
SHS9	106.0	SHS20	235.6	SHS31	365.2	SHS42	494.8
SHS10	117.8	SHS21	247.4	SHS32	377.0	SHS43	506.6
Average pavement damage (V_{AV}) = 253.29 cm^3.							

Legend. SHSi=i-th Structural Health Status due to the first i-th drilled holes; V_i = i-th volume reduction due to the first i-th drilled holes; V_{AV} =Total volume reduction due to the 43 drilled holes.

The second method applied in this study is called "Maximum Energy to Shannon Entropy ratio criterion", and hereafter will be called MEER method (according to (Rodrigues et al. 2016)). This method allows calculating the ratio *R(a)* that is defined as follows:

$$R(a) = \frac{E_{energy}(a)}{E_{entropy}(a)}, \tag{5. 11}$$

where *R(a)* is the energy ratio per single scaling factor *a*; $E_{energy}(a)$ represents the energy content of the CWCs of the AAR calculated using the scale factor, *a*, and the Eq. 2.1, and $E_{entropy}(a)$ is the entropy of the CWCs of the AAR obtained at the same scale, *a*, and the Eqs. 5.7, 5.8, and 5.9.

In this study, after the above-mentioned five steps to determine the 4356 CWC matrixes, the MEER method was applied following these procedures:

1. the energy of the CWCs (E_{energy}) for each scale, *a*, was calculated applying Eq. 5.9. A vector of 100 elements (i.e., the scaling vector length) was obtained for each CWC matrix;
2. the energy probability distribution of the CWCs (*pi*) for each scale, *a*, was determined using Eq. 5.8. A matrix (100 rows × 9500 columns) was obtained for each CWC matrix;
3. the entropy of the CWCs was calculated through Eq. 5.7. A vector of 100 elements was obtained for each CWC matrix;
4. the ratio *R(a)* was determined, using Eq. 5.11 (i.e., dividing each element of the vector E_{energy} with each element of the vector $E_{entropy}$). A vector of 100 elements was obtained for each CWC matrix. For each MW and each AAR, the maximum value among the 435600 (99×44×100) parameter *R(a)* was calculated (i.e., finding the *R(a) per* each of the 7 MW families used, and then the maximum among the 7 value of *R(a)* derived above);
5. finally, according to the method, the MW that provides the highest value of the parameter *R(a)* was selected as best MW for the AARs analyzed.

The last method that was applied and compared is the SUMVAR method (Rafiee and Tse 2009). This method is based on time-series analysis of the CWCs, and allows extracting features from the autocorrelation of the CWCs. The autocorrelation of the CWCs is able to reduce the size of the data without significant information loss in the frequency domain. In this study, after the above-mentioned five steps to determine the CWCs, the SUMVAR method was applied as follows:

1. using one MW, 44 CWC matrixes were built (100 rows × 9500 columns);
2. from each of the 44 CWC matrixes, the variance of the rows (i.e., the scaling factor, *a*) were derived obtaining one vector σ (100 rows × 1 column);

3. each vector σ was averaged obtaining 44 elements σ_{AV} (44 rows × 1 column);
4. each vector σ_{AV} was sorted (descended order), and the five highest elements were summed obtaining one value, *S* (related to the MW used);
5. finally, according with the SUMVAR method, the MW associated with the maximum value of *S*, was elected as the best MW for the signals under investigation.

Results and discussions

According to the MW selection methods presented into the previous section, the most suitable mother wavelet (MW) can be identified based on their results, i.e. the maximum value of *CC* (cf. Eq. 5.10), the maximum value of *R(a)* (cf. Eq. 5.11), and the maximum value of *S* (cf. SUMVAR method). Consequently, the figures below report the values of the three coefficients above, for each of the 7 wavelet families used in this study (corresponding to 99 MWs), and for 4 different "reference" Structural Health Statuses (SHSs) selected among all the 44 SHSs. In more detail, the results refer to: i) SHS0, which corresponds to the road pavement without holes, or Un-Cracked (UC); ii) SHS15, which corresponds to the road pavement cracked with 1 line of 15 holes; iii) SHS29, which corresponds to 2 lines of holes, for a total of 29 holes; iv) SHS43, corresponding to 3 lines of holes, for a total of 43 holes. Note that, in order to make easy the comparison of the results, they were normalized.

Fig. 5.22 shows the results of the CC method (cf. Eq. 5.10). Note that, the method provides a value of the parameter *CC* for each SHS. The CC method points out that the MW morl has the best MW to analyze the acoustic signals gathered, during the experimental investigation, from the road pavement in 44 different SHSs. On the other hand, the worst ones resulted the meyr and the mexh. It is important to underline that even though the sym44 provided the second best result in terms of cross correlation (i.e., the parameter *CC* provided by this method), it was found that the high orders of the Symlet family requires a computational time higher than the other MW families used

in this study. In addition, it should be noted that: i) the CC method provides results that allow identifying the best MW to analyze all the AARs, while the other two methods point out one MW for each AAR; ii) this is the only method (among the ones used in this study) that takes into account the SHS of the road pavement by including into the equation data about the reduction of the volume of the monitored object (according to (Pal et al. 2011)) due to the induced cracks (in this case due to drilled holes in a road pavement).
Importantly, the CC method allows defining a correlation among the level of damage of the pavement and wavelet-related indicators, extracted from the signal (V_i and F_i, respectively; cf. Eq. 5.10). Hence, under the hypothesis of the applicability of this relationship to a wider spectrum of loads and conditions, it could be possible to use the CC method to predict a structural status of the pavement based on its response (AAR), this latter analyzed in terms of wavelet coefficients. This pattern could be used as a benchmark to recognize the occurrence of damage into other points of the same pavement. This important consideration calls for further, and future investigations.

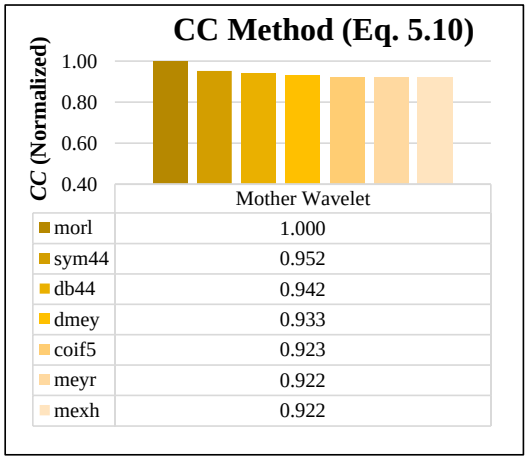

Fig. 5.22 Results of the CC method (99 MWs, 44 SHSs).

Moving on the next method, Fig. 5.23 shows the results of the MEER method. Values represent the normalized maxima values of *R(a)* (cf. Eq. 5.11) for each MW used and for each of the four SHSs considered above. It should be noted that this method, as well as the SUMVAR method, provides one result for each SHS in which the pavement was tested, and *per* each order of

the MW families used. For this reason, Figs. 5.23, and 5.24, which show the results of the last two methods, refer to the maximum value of the parameters *R(a)* and *S*, when the MW family has an order greater than 1 (e.g., for the MW family Symlet, that has a maximum order equal to 45, 44 different values of *R(a)* were calculated *per* each order, and the highest was used to select the "best" MW to analyze the above-mentioned family).

Based on MEER method, Fig. 5.23 reports the maximum values obtained by Eq. 5.11 using four MWs of order one (i.e., morl, mexh, dmey, meyr), one of order 5 (i.e., coif) and two of order 45 (i.e., db and sym).

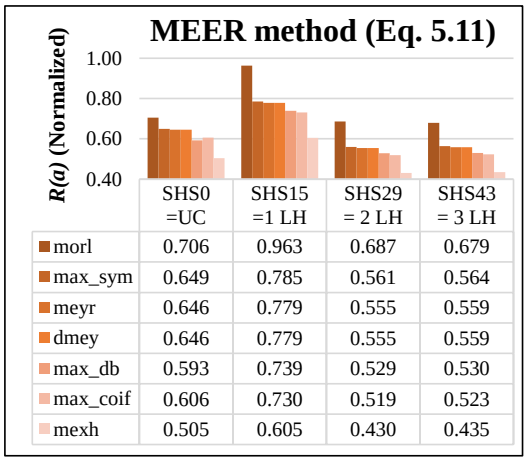

	SHS0 =UC	SHS15 =1 LH	SHS29 = 2 LH	SHS43 = 3 LH
morl	0.706	0.963	0.687	0.679
max_sym	0.649	0.785	0.561	0.564
meyr	0.646	0.779	0.555	0.559
dmey	0.646	0.779	0.555	0.559
max_db	0.593	0.739	0.529	0.530
max_coif	0.606	0.730	0.519	0.523
mexh	0.505	0.605	0.430	0.435

Fig. 5.23 Results of the MEER method (99 MWs, 44 SHSs).

In more detail, considering the MW of order greater than one, when the road pavement was in: i) SHS0 (i.e., 0 holes) the maxima were obtained for db17, sym45, and coif5; ii) SHS15 (i.e., 15 holes) the maxima were related with db23, sym45, and coif5; iii) SHS29 (i.e., 29 holes) the maxima were found for db24, sym39, and coif5; iv) SHS43 (i.e., 43 holes) the maxima correspond to db22, sym39, and coif5. However, the absolute maxima were obtained for the MW morl in each of the 44 SHSs of the roar pavement under test. In other words, the MW morl, based on the MEER method, is the best MW to analyze the signals used in this study. In contrast, the worst MW results the mexh. Noteworthy, the worst performances in terms of the computational time was obtained for sym, although, based on the MEER method, the Symlet family would appear as one of the best MWs for this study.

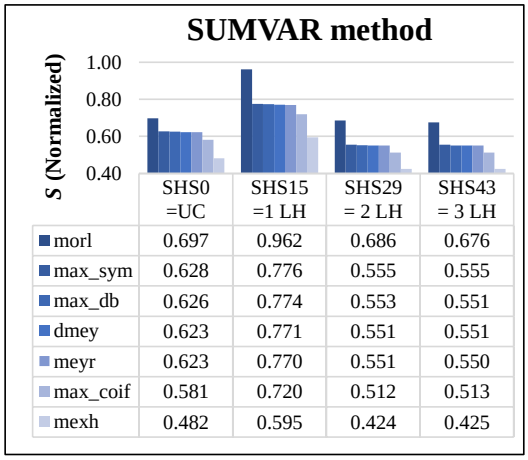

	SHS0 =UC	SHS15 =1 LH	SHS29 = 2 LH	SHS43 = 3 LH
morl	0.697	0.962	0.686	0.676
max_sym	0.628	0.776	0.555	0.555
max_db	0.626	0.774	0.553	0.551
dmey	0.623	0.771	0.551	0.551
meyr	0.623	0.770	0.551	0.550
max_coif	0.581	0.720	0.512	0.513
mexh	0.482	0.595	0.424	0.425

Fig. 5.24 Results of the SUMVAR method (99 MWs, 44 SHSs).

Fig. 5.24 illustrates the results obtained through the SUMVAR method for the 4 above-mentioned reference SHSs of the road pavement. Values refer to the SUMVAR method, represent the normalized maxima values of S for each MW used, and for the four reference SHSs defined above. Differently from the MEER method, by using the families db, sym, and coif, the maxima values were obtained for all the SHSs with the same orders, i.e. db44, sym45, and coif5. Anyway, through this method, as well as the other two methods, the absolute maxima were obtained using the MW morl, while the minima refer to the MW mexh. Noteworthy, even in this case, the computational time associated with the family Symlet resulted greater than that of the other MW families used.

The table below report the not normalized values of the three parameters calculated using the three MW selection methods.

Tab. 5. 11 Results of the three MW selection methods (not normalized).

Mother Wavelet Selection Methods					
CC method		**MEER method**		**SUMVAR method**	
MW	***CC***	**MW**	***R(a)***	**MW**	***S***
morl	-0.089	morl	20714	morl	117.14
sym44	-0.085	sym44	16867	sym44	94.45
db44	-0.084	db44	16718	db44	94.23
meyr	-0.084	meyr	16713	meyr	97.81
dmey	-0.083	dmey	15882	dmey	93.73
coif5	-0.082	coif5	15683	coif5	87.60
mexh	-0.082	mexh	12987	mexh	72.41

Based on the results shown through the figures above, it results that:

- all the MW selection methods applied in this study led to the same result, i.e. they point out the morl as the best MW for this application (consistently with (Rodrigues et al. 2016));
- all the methods indicate the mexh as the worst MW to analyze the acoustic signals used in this study;
- all the methods indicate the dmey as the intermediate quality MW to analyze the acoustic signals used in this study;
- the computational time associated with the Symlet family is much higher than the one of the other families used in this study;
- the MEER method allows a better discrimination of the AARs when MW families with order greater than 5 are used (Daubechies and Symlet), i.e. it is able to associate a given MW, with a specific order, to a given AAR. For this reason, it can be assumed, among the three applied in this study, as the most suitable for the NDT-SHM method proposed in this thesis.

As defined in the sections above, the proposed NDT-SHM method considers the road pavement as a filter of seismic and/or acoustic waves, and it is expected that the presence of the holes, induced during the experimental investigation, affects the way in which the pavement transmits the signals leading to the dissipation of their energy (due to multiple diffractions and reflections around the holes). Furthermore, based on the potentiality of the wavelet transform and on the results of the previous section of this thesis, it is expected that: i) the energy dissipation above should be well characterized by the wavelet coefficients, and shown by the scalograms; ii) the MW used to calculate the wavelet coefficients affects the quality of the results shown by the scalograms. For these reasons, the three figures below (Figs. 5.25, 5.26, and 5.27) show three set of scalograms obtained using the MWs indicated, by the three MW selection methods applied above, as: 1) the best (morl); 2) the intermediate quality MW (dmey); 3) the worst (mexh).

Note that: i) the three sets of scalograms have been plotted using the same input parameter (i.e., frequency intervals and signals); ii) the differences

among the y-axis (pseudo-frequency intervals) of the three sets of scalograms is due to the different shapes of the MWs used (i.e., different center frequency of the MW, and the conversion from scale to pseudo-frequency; cf. (Mathworks 2008)).

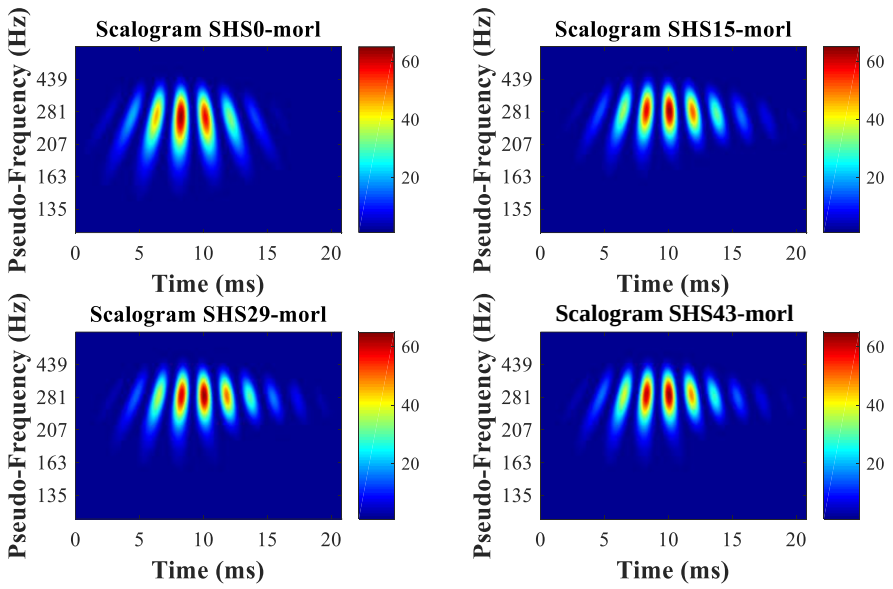

Fig. 5.25 Scalograms obtained using the "best" mother wavelet (MW) for this study, i.e. the morl, related to the 4 main SHSs.

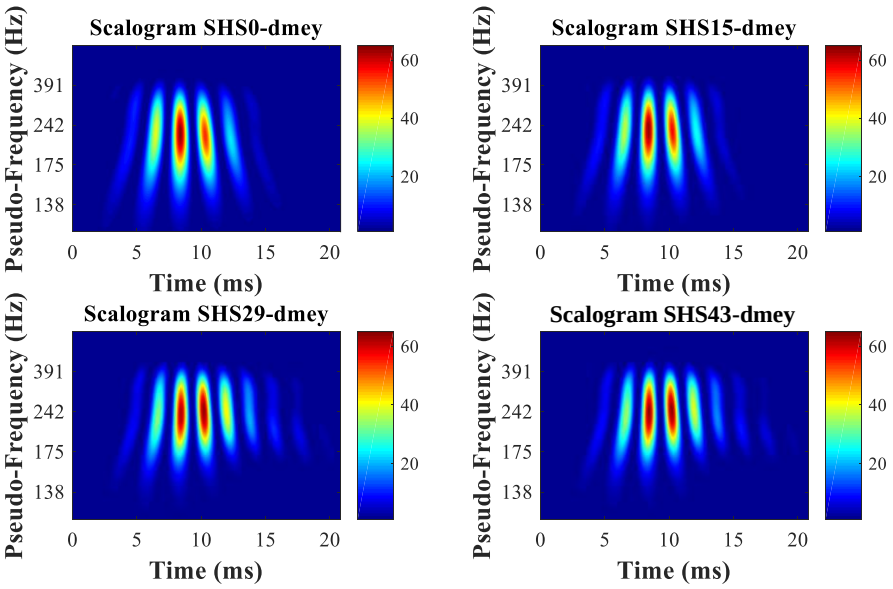

Fig. 5.26 Scalograms obtained using the "intermediate quality" mother wavelet (MW) for this study, i.e. the dmey, related to the 4 main SHSs.

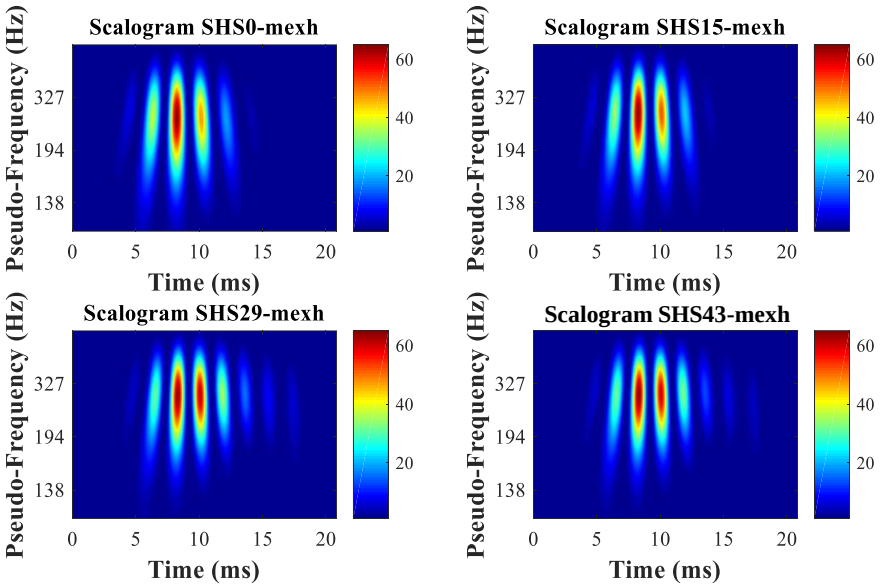

Fig. 5.27 Scalograms obtained using the "worst" mother wavelet (MW) for this study, i.e. the mexh, related to the 4 main SHSs.

By comparing Fig. 5.25, Fig. 5.26, and Fig. 5.27, and bearing in mind the expected results, it may be observed that:

a. the best MW (Fig. 5.25) corresponds to the narrowest frequency range. *Vice versa*, the worst ones (Figs. 5.26, and 5.27) correspond to the widest frequency range. This means that using the best MW it is possible to identify with more precision the spectral component of the signals;
b. the best MW allows a better definition of the primary ridges (the main red spots), and the secondary ridges (i.e., the less relevant ones associated to colors between 20 and 40; cf. color palette plotted beside each scalogram), especially into the signals tails (very high times);
c. the scalograms obtained using the best MW (morl) seem able to show the energy dissipation in comparison with the other two MWs used. This can be observed focusing on the reduction of the colored ellipsis that emerge from the background.

In order to quantify and clarify the advantages offered by the best MW and, at the same time, to demonstrate the effectiveness of the MW selection methods

applied in this study, a further analysis was carried out. In particular, from the three sets of scalograms (Fig. 5.25, Fig. 5.26, and Fig. 5.27) that refer to the four reference SHSs (i.e., the 4 SHSs related to the pavement un-cracked and cracked with 1, 2, and 3 lines of holes), one meaningful feature was extracted (cf. task I. Features in Fig. 5.21). Several features have been considered, but the overall area occupied by all the ridges of the scalograms is the most representative, i.e. the area that has been associated to the colors in the interval 20-64 (cf. color palette plotted beside each scalogram). The value of the feature *per* each reference SHSs was obtained by summing the percentage of the scaled energy of the CWCs (herein called Eng_{CWC}) above the threshold 20 (out of 64; cf. color palette plotted beside each scalogram). The values of the above-mentioned feature were plotted as a function of the road SHS (i.e., the 4 reference SHSs; see Fig. 5.28).

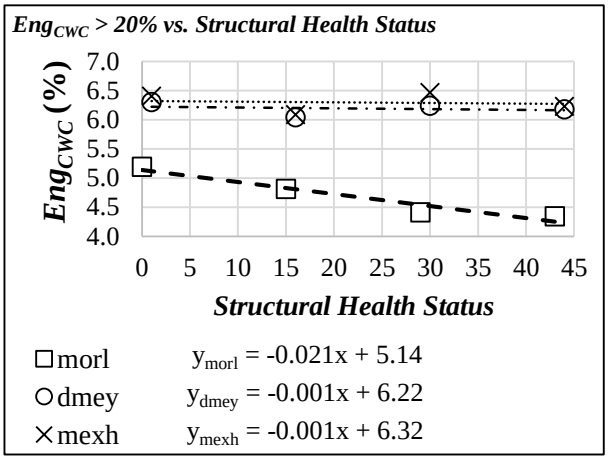

Fig. 5.28 Scatterplot of the feature Eng_{CWC} extracted from the scalograms displayed in Figs. 5.25, 5.26, and 5.27, which represents the energy of the CWCs over the normalized and scaled value 20.

By analyzing this scatterplot, it is possible to conclude that: 1) similar results were obtained if the MWs indicated by the three MW selection methods as the worst and the intermediate, and they do not allow identifying any variation of the signals when the SHS of the monitored pavement gets worse; 2) the best MW (morl) allows better identifying the dissipation of the energy of the signals, and, consequently, using the best MW (morl) it is possible to better identify the variation of the structural health status (SHS) of the

pavement over time; 3) it is possible to use this NDT-SHM method proposed in this thesis to monitor the SHS of a road pavement using scalograms or proper features extracted from them.

The results of this study are shown, in terms of hierarchical clustering, in the following tables (as in section 5.1.3). It is important to underline that, to better show the importance of including an efficient MW selection method in the NDT-SHM method, and compare the last results with the previous results (section 5.1.3), the MW meyr was used as "intermediate quality" MW instead the dmey. Furthermore, the meyr was the only MW used in section 5.1.3, and allowed built Tab. 5.9, which were replicated in Tab. 5.13.

Tab. 5.12 Hierarchical clustering of the features extracted from the 2200 ARs, using the "best" MW (morl) to derive the feature in the T-F domain.

#F	*F*		SHS				*Max* OPC_{AV} (%)
			SHS0	SHS1	SHS2	SHS3	
1	8	*PC* *Max OPC (%)*	2 100	1 76	4 65	3 75	79
2	*1+8* *2+8*	*PC* *Max OPC (%)*	4 100	3 70	2 65	1 75	78
3	***2+3+7***	***PC*** ***Max OPC (%)***	**2** **100**	**1** **77**	**3** **77**	**4** **95**	**87**
4	*2+3+7+9*	*PC* *Max OPC (%)*	4 100	3 52	2 81	1 92	81
5	*4+5+7+8+9*	*PC* *Max OPC (%)*	4 100	3 72	1 76	2 70	80
	3+5+7+8+9 *2+5+7+8+9* *2+3+5+7+8*	*PC* *Max OPC (%)*	4 100	3 70	2 91	1 58	80
	2+3+7+8+9	*PC* *Max OPC (%)*	4 100	3 72	2 90	1 58	80
6	*2+3+5+7+8+9*	*PC* *Max OPC (%)*	4 100	3 70	2 91	1 58	80
	1+4+5+7+8+9 *1+2+3+4+5+8*	*PC* *Max OPC (%)*	4 100	3 72	2 82	1 66	80
	1+2+3+4+8+9	*PC* *Max OPC (%)*	4 100	3 72	2 83	1 63	80
7	*1+2+4+5+7+8+9* *1+2+3+4+5+8+9*	*PC* *Max OPC (%)*	4 100	3 72	2 82	1 66	80
8	*1+2+3+5+6+7+8+9*	*PC* *Max OPC (%)*	3 100	4 70	2 67	1 74	78
9	*n.a.*	*PC* *Max OPC (%)*	- -	- -	- -	- -	-

Symbols. ARs = Acoustic Responses of the road pavement under test in different Structural Health Statuses (SHSs); SHS0 = Un-Cracked pavement, i.e. without holes; SHS1 = Cracked pavement with 1 line of holes (i.e., 15 holes); SHS2 = Cracked pavement with 2 lines of holes (i.e., 29 holes); SHS3 = Cracked pavement with 3 lines of holes (i.e., 43 holes); #F = number of features used as input during the clustering; F = Features from the first one of the Time domain to the last one of the Time-Frequency domain; *PC (%)*= Predicted cluster; *Max OPC (%)* = highest percentage of observations associated to *PC (%)*; *Max* OPC_{AV} *(%)*= average of the values *Max OPC (%);* n.a. = misclassification.

Tab. 5.13 Hierarchical clustering of the features extracted from the 2200 AARs, using the "intermediate quality" MW (meyr) to derive the feature in the T-F domain (cf. Tab. 5.9).

#F	*F*		SHS				*Max* OPC_{AV} (%)
			SHS0	SHS1	SHS2	SHS3	
1	2	*PC*	3	4	2	1	78
		Max OPC (%)	98	79	56	80	
2	**2+9**	***PC***	**4**	**3**	**1**	**2**	**87**
		Max OPC (%)	**98**	**79**	**82**	**89**	
3	*2+3+9*	*PC*	4	3	1	2	85
		Max OPC (%)	98	75	68	97	
4	*2+3+5+9*	*PC*	4	3	1	2	83
		Max OPC (%)	98	76	57	99	
5	*3+4+5+6+7*	*PC*	2	1	4	3	74
		Max OPC (%)	100	66	58	71	
	2+3+5+6+9	*PC*	1	2	4	3	74
		Max OPC (%)	96	68	82	50	
	1+2+6+8+9 *1+2+5+6+8* *1+2+3+6+8*	*PC*	2	1	4	3	74
		Max OPC (%)	100	67	68	61	
6	*1+2+5+6+8+9* *1+2+3+6+8+9* *1+2+3+5+6+8*	*PC*	2	1	4	3	74
		Max OPC (%)	100	67	68	61	
	1+2+4+5+7+9	*PC*	1	2	3	4	74
		Max OPC (%)	84	67	61	85	
7	*1+2+3+5+6+8+9*	*PC*	2	1	4	3	74
		Max OPC (%)	100	67	68	61	
8	*n.a.*	*PC*	-	-	-	-	-
		Max OPC (%)	-	-	-	-	
9	*n.a.*	*PC*	-	-	-	-	-
		Max OPC (%)	-	-	-	-	

Symbols. See Tab. 5.12.

Tab. 5.14 Hierarchical clustering of the features extracted from the 2200 ARs, using the "worst" MW (mexh) to derive the feature in the T-F domain.

#F	F		SHS				*Max OPC_{AV}* (%)
			SHS0	SHS1	SHS2	HS3	
1	2	*PC*	3	4	2	1	78
		Max OPC (%)	98	79	56	80	
2	*2+9*	*PC*	1	2	4	3	81
		Max OPC (%)	98	74	54	98	
3	*1+4+8*	*PC*	3	4	2	1	77
		Max OPC (%)	100	69	76	61	
	2+3+9	***PC***	**1**	**2**	**4**	**3**	**85**
		Max OPC(%)	**98**	**81**	**66**	**94**	
4	*4+5+6+8* *3+4+6+8*	*PC*	3	4	2	1	78
		Max OPC (%)	100	73	78	61	
5	*4+6+7+8+9*	*PC*	3	4	2	1	78
		Max OPC (%)	100	73	69	68	
6	*2+3+4+6+8+9*	*PC*	3	4	2	1	78
		Max OPC (%)	100	73	81	59	
7	*2+4+5+6+7+8+9* *2+3+4+6+7+8+9*	*PC*	3	4	2	1	77
		Max OPC (%)	100	73	74	61	
	1+3+4+5+7+8+9	*PC*	3	4	2	1	77
		Max OPC (%)	100	69	76	61	
	1+2+4+5+6+8+9	*PC*	3	4	2	1	77
		Max OPC (%)	100	73	71	63	
	1+2+3+4+6+8+9	*PC*	3	4	2	1	77
		Max OPC (%)	100	73	64	71	
	1+2+3+4+5+8+9	*PC*	3	4	2	1	77
		Max OPC (%)	100	71	76	61	
8	*2+3+4+5+6+7+8+9*	*PC*	3	4	2	1	77
		Max OPC (%)	100	73	74	61	
9	*n.a.*	*PC*	-	-	-	-	-
		Max OPC (%)	-	-	-	-	

Symbols. See Tab. 5.12.

Based on the results reported in the three table above (Tabs. 5.12, 5.13, and 5.14), it is possible to state that:

- The best results are obtained using the "best" MW. In fact, the values assumed by the parameter *Max OPC_{AV}* (maximum average percentage of observations associated to the predicted cluster) range from 78% and 87% (average = 82.5%) using the "best" MW, while between 74% and 87% (average = 80.5%) using the "intermediate quality" MW, and between 77% and 85% (average = 81%) using the "worst" MW.

- The highest value of *Max* OPC_{AV} is 87% obtained using the "best" and the "intermediate quality" MWs using combinations of 3 and 2 features, respectively.
- None of the three MW that were taken into account allow obtain a correct classification using all the 9 features. The "best" and the "worst" provide similar results if 8 features over 9 are used, showing that all the features extracted in the T-F domain (number 7, 8, and 9) are included in both the successful combinations.
- The "worst" MW allows to use 6 combinations of 7 features, even though the *Max* OPC_{AV} is 77%.

Finally, if the trends of the three features extracted in the T-F domain are compared (see Fig. 5.29): i) the three MWs provides similar trend of the feature 7 and 8 (i.e., the Ent_{CWC} , and the $p\text{-}f_{WR}$; see Fig. 5.29); ii) only the "best" MW allows confirming the expected reduction of the energy (feature number 9, Eng_{CWC}, i.e. the maximum energy of the CWCs greater than 60 out of 64), as shown in the following figure.

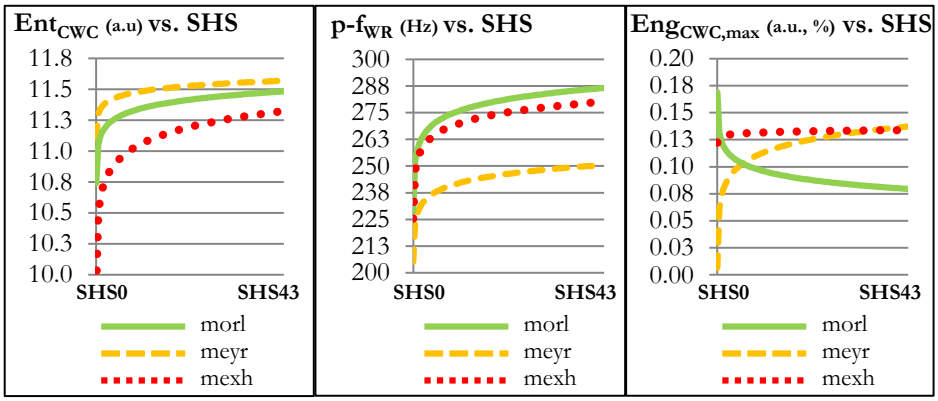

Fig. 5. 29 Trends (logarithmic scale) of the features extracted from the T-F domain using three different MWs: a) Entropy of the CWCs; b) Pseudo-frequency of the scalogram wavelet ridges; c) Energy of the CWCs.

5.2. On-site experiments using the car pass-by as source

This section refers to two different experimental investigations in which the vibro-acoustic signatures of the road pavement under test were recorded during the passage of a car, i.e. the car pass-by was used as source of vibration and sounds (hereafter called CAR).

Seismic and acoustic waves produced by traffic affect both people and infrastructures (Praticò and Vaiana 2015). The impact of the traffic depends on different factors like vehicles, drivers, and pavement characteristics (Covaciu, Florea, and Timar 2015). Rolling noise is the main factor at high speeds (higher than 40-80 km/h), while the engine has a dominant contribution to the traffic noise at low speeds (lower than 40 km/h) (Covaciu et al. 2015; Praticò and Vaiana 2015) By referring to the acoustic response of a pavement as perceived by a bystander who is close to the road, note that in order to reflect more accurately the frequency response of the human ear, the "A-weighting" scale is commonly used (dBA), in which the sound pressure levels (SPL, expressed in dBA) for the lower frequency bands and higher frequency bands are reduced by certain amounts before they are being combined together to give one single sound pressure level value (Sandberg and Ejsmond 2002). Traffic noise level (SPL) is about 70-80 dBA at 10 m from traffic (Annecke et al. 2008; Buratti and Moretti 2010; Cavanaugh and Tocci 1998; Guarnaccia 2013; Ow and Ghosh 2017; V. S. Wang et al. 2016). In more detail, it is very important to consider not only overall amplitude characteristics (SPL) but also noise composition with regard to frequency (spectral content). Typical traffic noise spectra cover the bandwidth from 700 Hz to 2 kHz (Buratti and Moretti 2010; Saboonchi, Ozevin, and Kabir 2016).

Generally, the traffic noise level is measured through sound level meters (which consist on a microphone, a data processor, and a display) or through microphone-based systems (e.g., standards ISO 11819-1 (ISO 1997), ISO 11819-2 (ISO 2017)). Microphone-based systems are also used for tests on road pavements in order to measure the sound absorption coefficient (e.g., according to the standards: ISO 13472-1 (ISO 2002), ISO 13472-2 (ISO 2002), ISO 10354-2 (ISO 2002)).

The experiments were carried out using the same measurement system used in the experimental investigations described in the previous section (see section 5.1), and the procedure described in the following. The same car passed, at an average speed of 20 km/h, 10 times in front of the microphone of the system presented in the sections above. The microphone was placed 2 m away from the line where the wheel of the car passed (see Fig. 5.30a). During this experiments, four structural health statuses (SHSs) of the road pavement under test were considered, i.e. SHS0 (un-cracked), SHS1 (cracked with 1 line of 16 holes), SHS2 (cracked with 1 line of 15 holes), and SHS3 (cracked with 1 line of 15 holes). Note that: i) the acoustic signals were recorded with a sampling frequency of 192 kS/s; ii) each passage of the car had a duration of 3 s; iii) 10 passages for each SHS were considered (see Fig. 5.30b), hence 40 ARs were collected.

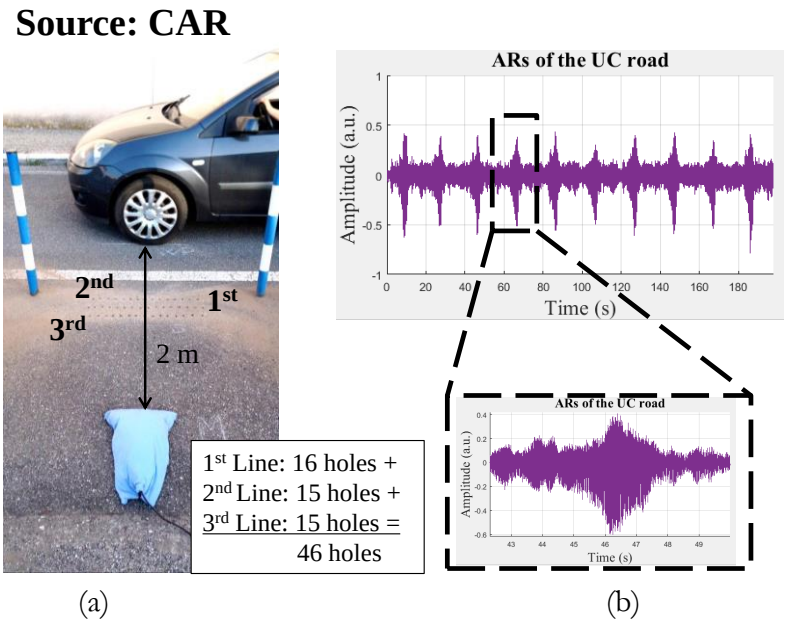

Fig. 5.30 Experimental investigation using (a) the car pass-by as a mechanical source to generate vibro-acoustic signals (b).

As is possible to see from the figure above, the shapes of the signals in this case is completely different from the signals recorded using the LWD as a source. In fact, the LWD-generate signals are transient, while these latter can be considered as pseudo-random.

5.2.1.Feature-based approach: road pavement classification from CAR-related signals[8]

This approach was applied on the 40 ARs collected using the CAR as a mechanical source, and on different (from those used in the previous studies) features extracted from the time domain, the frequency domain and the time-frequency domain. The following flow chart summarize the study.

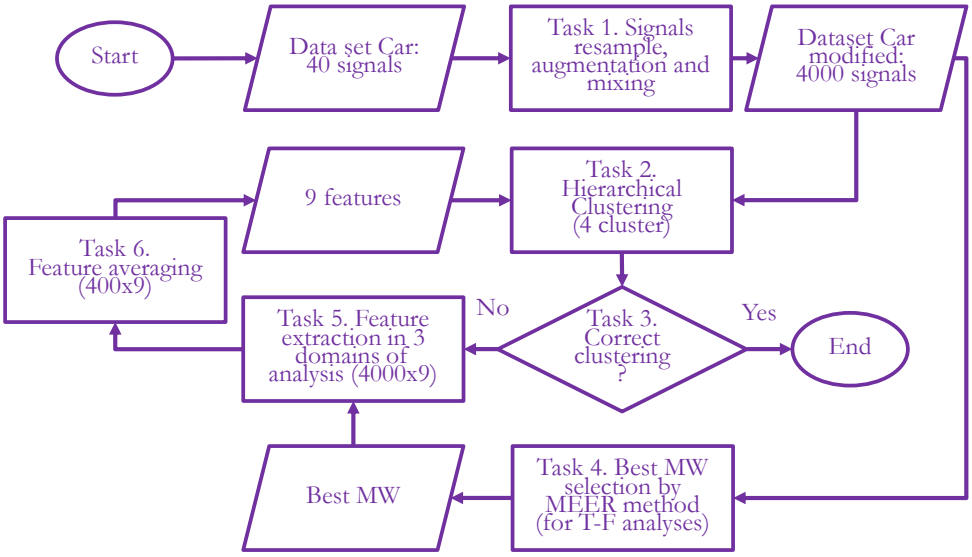

Symbols: MW=Mother Wavelet; MEER=Maximum Energy to Shannon Entropy Ratio criterion; T-F= Time-Frequency domain of analysis.

Fig. 5.31 Feature-based approach on the signals generated by pass-by vehicles.

It is needed to underline that the main difference with the previous procedure (see section 5.1.4) refers to the tasks 1 and 6, called "Signal resample, augmentation, and mixing", and "Feature averaging", respectively. In particular, the following processes were applied:

- Task1: this tasks consisted of three sub-tasks, i.e.:
  - Task 1.1: the 40 ARs recorded during the experimental investigation were resampled (from 1 Million of Samples *per* AR, to 7 kilo samples *per* AR) in order to investigate on the possibility of using a sampling frequency lesser than that used in this experiments (i.e., 192 kHz), and on the improvement (speed-up) of the data processing;

[8] This section mainly refers to the papers 3.2, and 3.9 (see Scientific production).

- Task 1.2: the 40 resampled ARs were augmented (see Fig. 5.32), i.e. each signal was cut moving a window with a constant width of 7 kilo samples, 100 times on the sample in order to obtain 4000 ARs from 40 ARs. This process was carried out in order to reduce the error due to incorrect cutting of the signal and to make the dataset more representative (i.e., similar to a dataset gathered in real traffic conditions).
- Task 1.3: the 4000 ARs were related to 4 SHSs of the road pavement. Hence, the first 1000 rows were referred to the SHS0 (i.e., the un-cracked road pavement), the rows between 1001 and 2000 were referred to the SHS1 (i.e., road cracked with one lines of 15 holes), and so on. During this process, the 1000 rows corresponding to each SHS were randomly mixed in order to obtain a dataset more representative of the real traffic (i.e., different vehicles produce different AR during the monitoring);

➢ Task 6: the 9 features extracted from the three domains of analysis consisted in a matrix of size 4000×9. Before the application of the clustering procedure, the elements of the matrix mentioned above were averaged. In particular, the 4000 elements of each column (namely the i-th feature) were assembled in 400 groups, and the 10 values of each group were averaged in order to obtain 400 averaged values per column.

Fig. 5.32 provides a representation of the augmentation procedure that was applied on the dataset used in this study (i.e.., 40 ARs). In particular, it shows how from one signal (e.g., the 4th AR, corresponding to the SHS0; see AR #4 in Fig. 5.32), shifting 100 times the same window over the signal, and cutting the samples included in the window, 100 signals can be generated (i.e., the AR #4 becomes the 400th AR, and from this latter moving the window 50, and 100 times the AR #450, and #500, can be obtained; see Fig. 5.32).

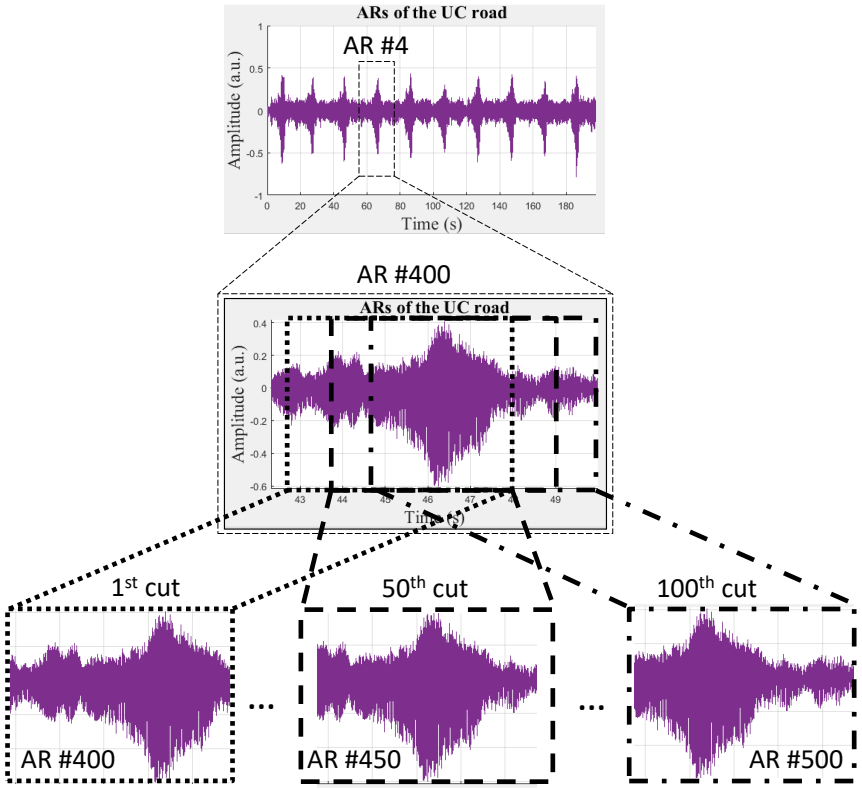

Fig. 5.32 Schematic representation of signal augmentation.

At first (Task 1 and Task 2.), the hierarchical clustering procedure was applied on the 4000 ARs in order to understand if it was possible to recognize the 4 SHSs of the road pavement under test from the ARs. Tab. 5.15 reports the results of this attempt of classification.

Tab. 5.15 Confusion matrix derived using the hierarchical clustering procedure and, as input, the 4000 ARs of the road pavement using a pass-by car as source.

SHS	CL_1	CL_2	CL_3	CL_4	***PC***	***Max OPC* (%)**
SHS0	249	302	163	286	**2**	**30**
SHS1	252	292	260	196	**2**	**29**
SHS2	217	302	240	241	**2**	**30**
SHS3	148	268	222	362	**4**	**36**

Symbols. SHS = Structural Health Status; SHS0 = pavement without holes; SHS1 = pavement with 1 line of holes (i.e., 15 holes); SHS2 = pavement with 2 lines of holes (i.e., 29 holes); SHS3 = pavement with 3 lines of holes (i.e., 43 holes); CLn = Cluster number n, with n = 1, 2, 3, 4; *PC* = Predicted Cluster; *Max OPC (%)* = highest percentage of observations associated to *PC* (%).

Based on the results reported in the table above, it is possible to state that the ARs do not allow the detection of the holes in the road pavement. For this reason, nine features were extracted from the ARs (Task 5) in three domain of analysis, i.e. the Time (T), the Frequency (F), and the Time-Frequency (TF) domain. The feature extraction was preceded by the selection of the best Mother Wavelet (MW) needed to carry out an efficient analysis in the TF domain using the Continuous Wavelet Transform, CWT (cf. section 5.1.4). The Maximum Energy to Shannon Entropy Ratio (MEER) method was used to select the best MW according to the results of the section 5.1.4. The above-mentioned nine features are described in the following table.

Tab. 5.16 Features considered in this study (mechanical source: CAR).

Feature #	Symbol	Feature definition	Unit of measure	Domain/ Feature Source
1	Δa	Amplitude difference between the absolute maximum P and the absolute minimum N of the AR amplitudes.	a.u.	Time/Signal
2	Δt	Time Delay of N from P	ms	
3	σ	Standard deviation of the ARs.	a.u.	
4	PSD_{max}	Maximum of the PSD of the ARs into the range 20-500 Hz.	dBW/Hz	Frequency/ Periodogram
5	S	Slope of the linear regression model of the PSD of the ARs into the frequency range 20-500 Hz.	dBW	
6	f_c	Spectral centroid of the periodogram (PSD vs. frequency) in the frequency range 20-500 Hz.	Hz	
7	*Ent*	Maximum Entropy of the CWCs.	a.u.	Time-Frequency/ CWT scalogram
8	$p\text{-}f_{WR}$	Pseudo-frequency of the WR (from the y-axis of the scalogram).	Hz	
9	*%Eng*	Energy of the CWCs above a given threshold (30 out of 64, i.e. red areas of the scalogram).	a.u.	

Symbols. *AR*s = Acoustic Responses; a.u. = arbitrary unit; dim. = dimensionless; ms = milliseconds; dB = decibel; dBW/Hz = decibel Watt per Hertz; Hz = Hertz; s = seconds; *Ent* = Entropy; CWC = Continuous Wavelet Coefficients; WR = Wavelet Ridges; *p-f* = pseudo-frequency; *Eng* = Energy; max =maximum; min = minimum.

Note that, in this study the frequency ranges used in the F domain, and the 6th and the 9th features were changed or adapted in comparison with the those used in the previous analyses (see section 5.1.3, and Tab. 5.3). In particular: i) the range 20-500 Hz was used, instead of the ranges 20-250 Hz and 20-450 Hz, to derive the feature 5th and 6th; ii) the maximum of the PSD were used as feature 4th instead of the minimum; iii) the value of energy of the wavelet coefficients (CWCs) greater than 30 out of 64 was used as feature 9th instead of greater than 60 out of 64.

Fig. 5.33 shows the spectral content of the ARs in the range 20-500 Hz, and between -100 dBW/Hz and 0 dBW/Hz. This section of the periodogram was selected because of the fact it contains the highest value of PSD.

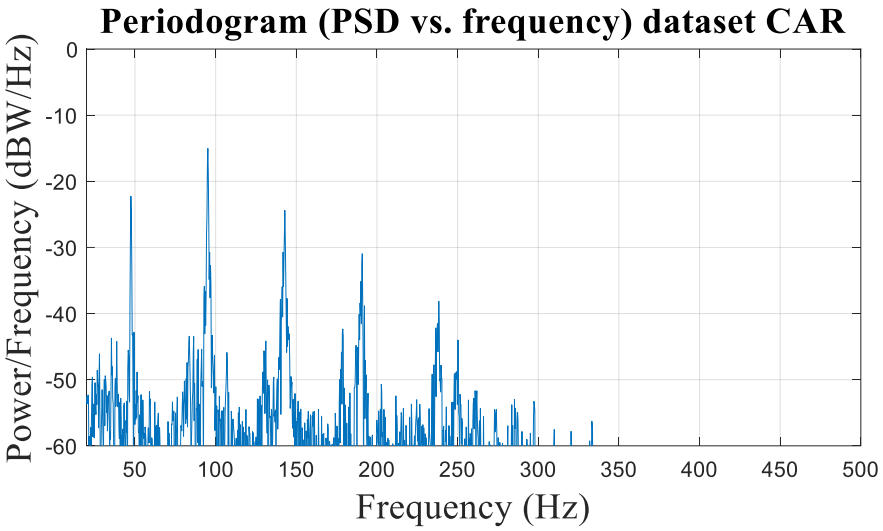

Fig. 5.33 Example of periodogram of one AR using the source CAR (AR #1000).

The features extracted in the Time-Frequency domain refer to the scalograms (e.g., Fig. 5.34). The scalograms were obtained using the best Mother Wavelet (MW) "morl", which were defined applying the selection method MEER. In more detail, the MEER method was applied as in the section 5.1.4., i.e. using 99 MWs. The results are reported in Tab. 5.17.

Tab. 5.17 Results of the MEER method on the dataset CAR (not normalized).

MEER method	
MW	***R(a)***
morl	368
sym44	260
db44	249
meyr	246
dmey	245
coif5	223
mexh	140

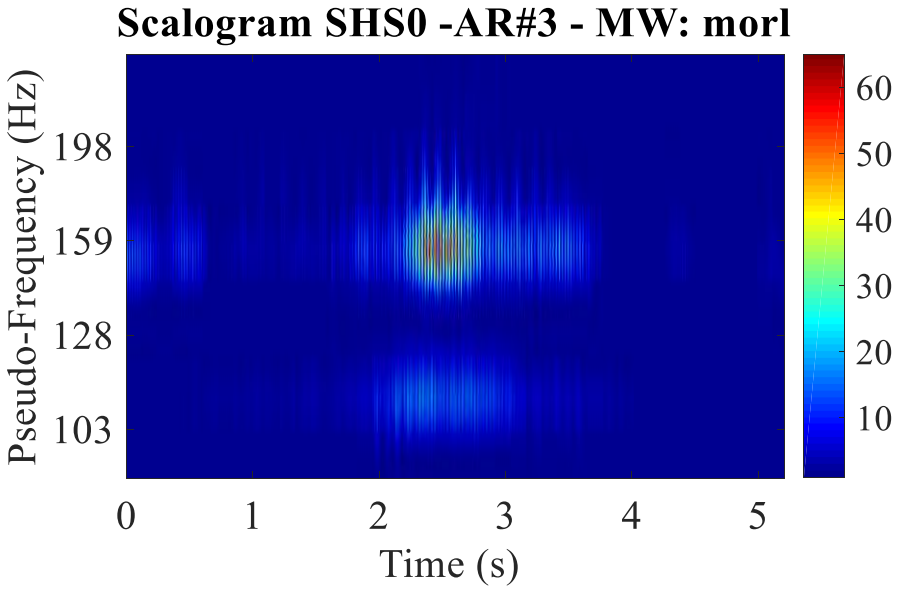

Fig. 5.34 Example of scalogram of one AR (i.e., AR #3) related to the un-cracked road pavement (i.e., Structural Health Status #0 = SHS0) using the source CAR and the best Mother Wavelet (MW) "morl".

The following figures (Figs. 5.35, 5.36, and 5.37) report the trends of the nine features extracted (see Tab. 5.16) from the ARs of the road pavement under investigation. These ARs correspond to 4 SHSs of the road pavement, which varied between SHS0 (i.e. the un-cracked condition) and SHS3 (i.e. the presence of 3 lines of drilled holes). It should be noted that, the values of the features are those derived in Task 6 (cf. Fig. 5.31). Furthermore, Fig. 5.38 was reported in order to show the difficulties in recognizing the variation of the SHS of the pavement using only the scalograms, and to underline that meaningful features should be instead used for SHS purposes.

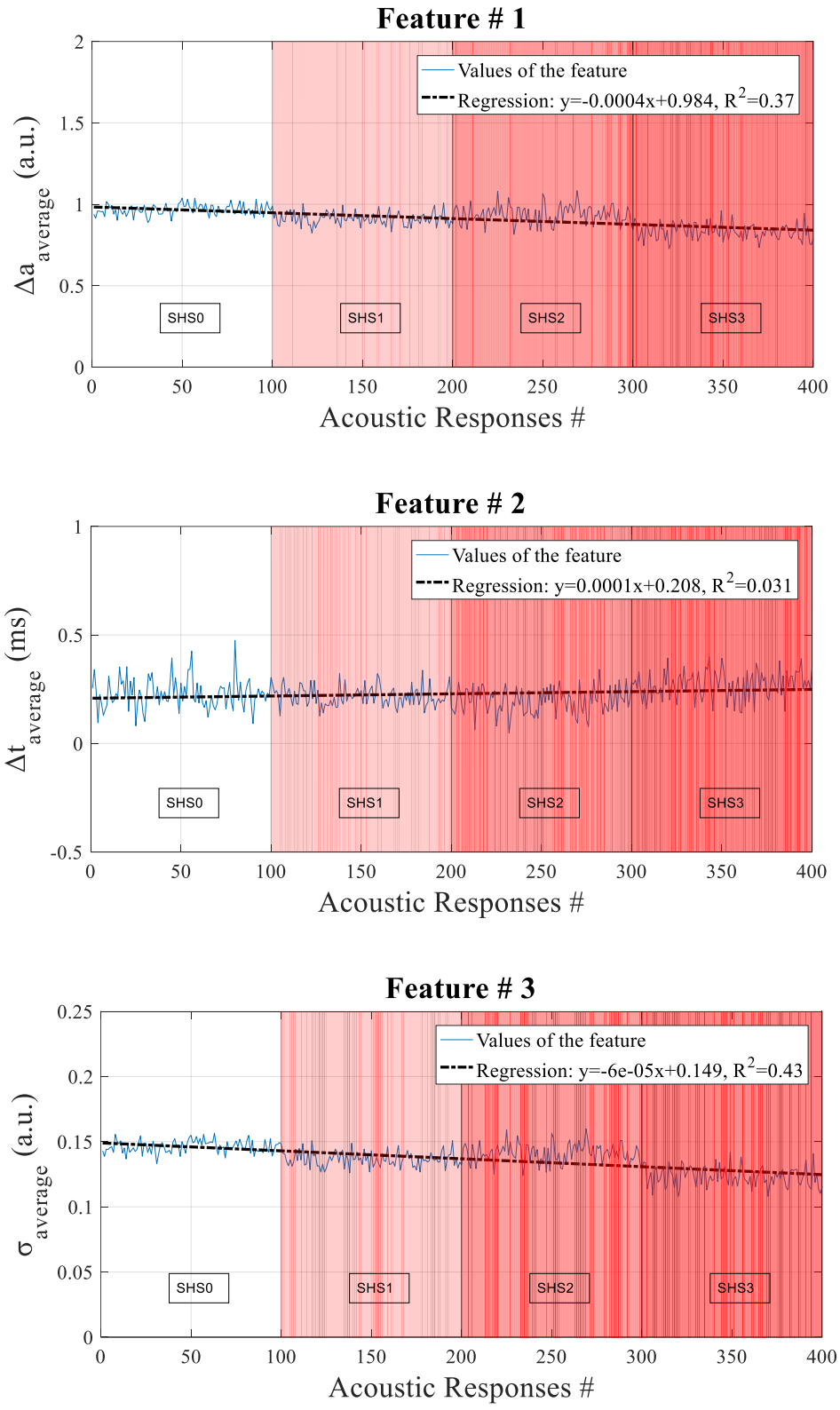

Fig. 5.35 Trends of the features extracted in the Time domain as a function of the SHS worsening (from SHS0 to SHS3) (source: CAR).

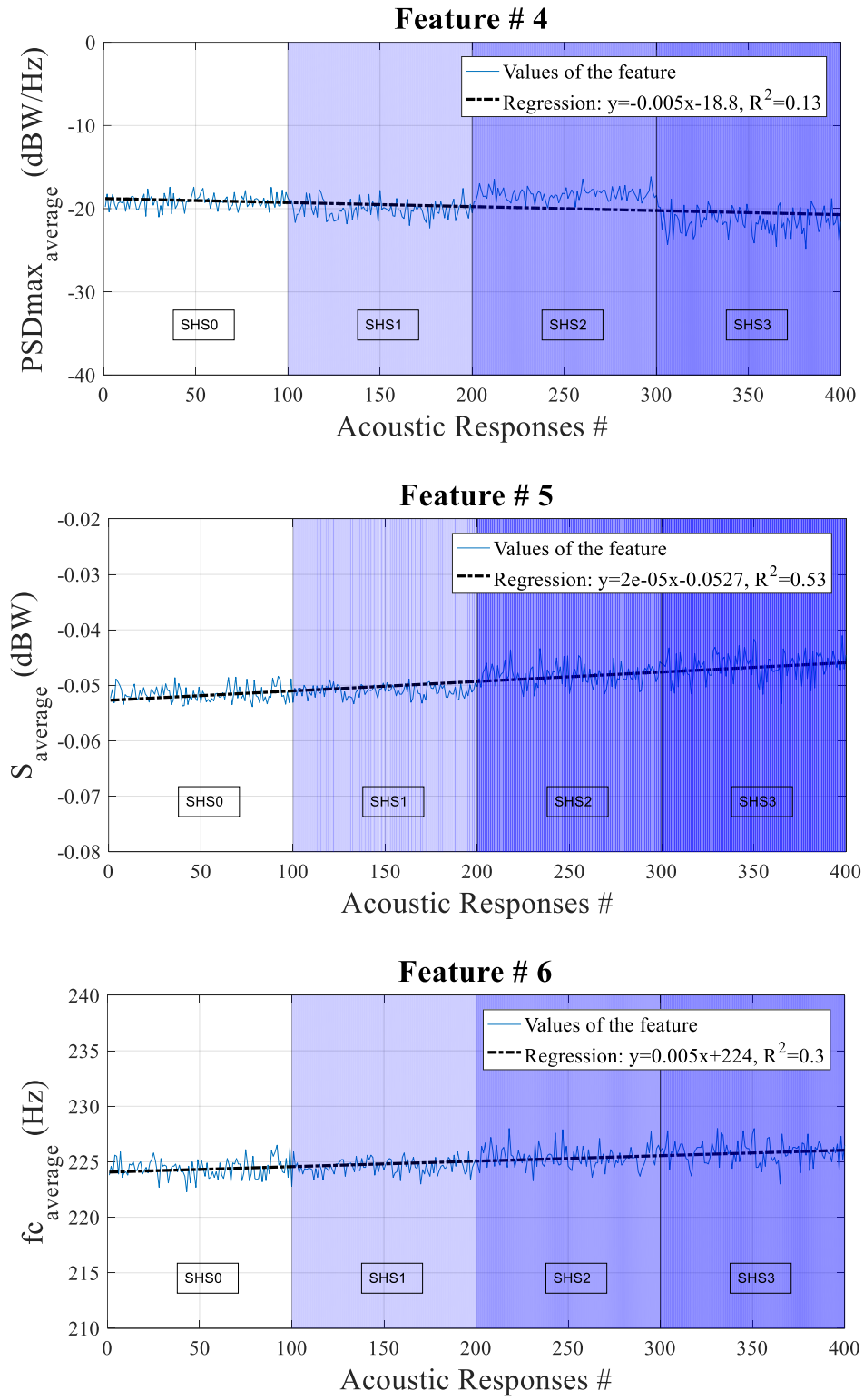

Fig. 5.36 Trends of the features extracted in the Frequency domain as a function of the SHS worsening (from SHS0 to SHS3) (source: CAR).

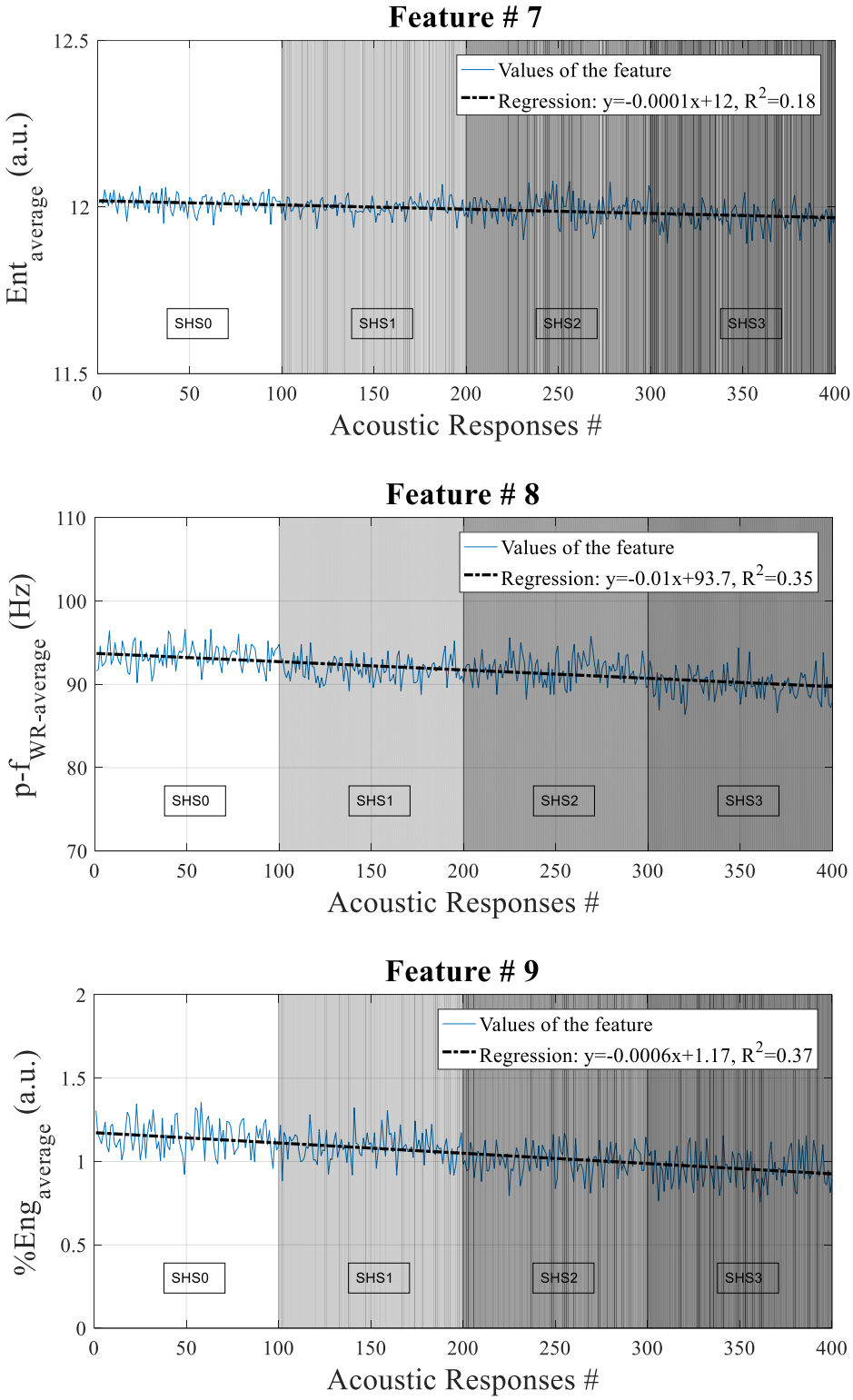

Fig. 5.37 Trends of the features extracted in the Time-Frequency domain as a function of the SHS worsening (from SHS0 to SHS3) (source: CAR).

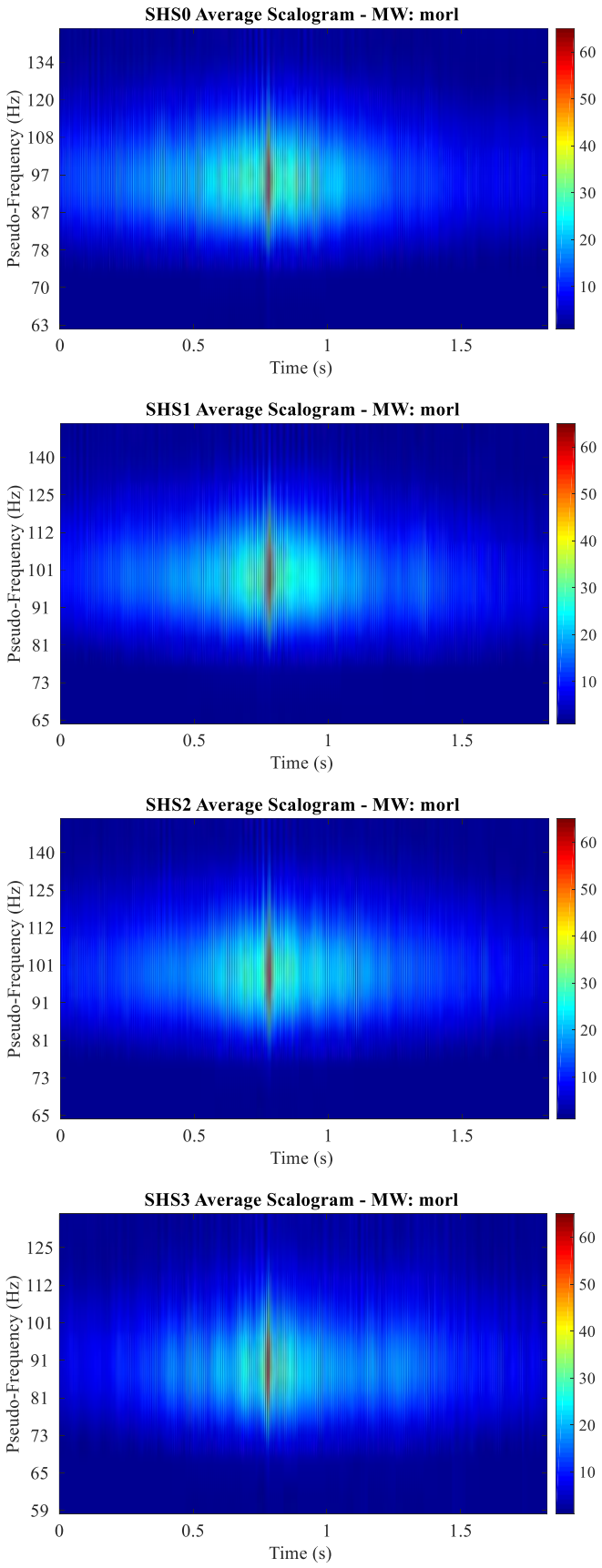

Fig. 5.38 Average scalograms related to the 4 SHSs of road (source: CAR).

Fig. 5.38 shows the 4 average scalograms related to the 40 ARs, namely the 4 scalograms obtained averaging the 10 scalograms obtained applying the CWT to each set of ARs related to the each of the 4 SHSs that were taken into account in this study. By comparing the above-mentioned scalograms, it is possible to state that they can be used to observe the dissipation of the AR energy (see the red spots in the scalograms, namely the feature #9). Indeed, this dissipation (when there are cracks) is even more evident when the feature number 9 in Table 5.16 is considered. In this case (cf. Figure 5.37 feature #9) the higher the quantity of cracks (x-axis), the lower the level of energy (y-axis). This dissipation can be associated to the worsening of the SHS of the road pavement under test (due to the presence and the increase of the number of the drilled holes). Furthermore, according to the considerations made in section 5.1.3 and related to the dataset LWD, the dissipation of the ARs energy can be seen also using the feature #1 and #3 (namely the variation of amplitude between the absolute maxima and the absolute minima, and the standard deviation of the signals, respectively). Another noteworthy result that emerged analyzing the trends of all the features used in this thesis (i.e., in the study reported in section 5.1.3 and in the current section), refers to the correlations between the features #2 and #6 (namely the time lag between the absolute maxima and the absolute minima, and the spectral centroid, respectively), and the features #7 and #8 (i.e., the Shannon's entropy of the wavelet coefficients, and the pseudo-frequency of the wavelet ridges, respectively). In particular, the first couple showed a monotone decreasing trend, while the second one exhibited a monotone increasing trend for the LWD-related couples of features. Importantly, these trends are opposite for the CAR-related couples of features.

These differences may be attributed to the two sources used in the experimental investigations, which produce signals characterized by dissimilar spectral contents. Hence, the interaction of these signals (and their spectral contents) with the holes drilled into the pavement (which modify the frequency range that "our filter" allows to passes through) led to different results. It is important to highlight the reduction of the Shannon's entropy of the wavelet coefficients (herein called feature #7). This feature can show the

amount of information carried by the signals (cf. considerations and references included in section 5.1.3). Consequently, the reduction of the feature #7 can be associated to a loss of "information" (e.g., of some spectral components, or of energy), which in turn can be associated to the worsening of the SHS of the road pavement.

The feature trends above can be used to define the boundary between different SHSs (or hopefully useful thresholds, such as between the "normal zone" related to the absence of failures and the "warning zone" related to the occurrence of potential failures, or between the "warning zone" and the "alert zone" related to the presence of functional failures; cf. section 5.1.2). Anyhow, a more powerful tool is needed to derive the SHS from the ARs. For this reason, the hierarchical clustering procedure used in the previous studies and recalled above (see Tab. 5.15) was applied on the features extracted from the ARs. In particular, the tables below report the result of the hierarchical clustering procedure that was applied on the 400 features obtained following the procedure described in Fig. 5.31 (i.e., from Task 1 to Task 6).

Tab. 5.18 Results of the hierarchical clustering of the nine features extracted from the 4000 ARs (mechanical source: CAR) based on the domains of analysis.

Domain		SHS			
		SHS0	SHS1	SHS2	SHS3
T	*PC*	1	3	3	4
	Max OPC (%)	56	71	37	52
F	*PC*	1	1	2	4
	Max OPC (%)	70	46	60	56
TF	*PC*	3	2	2	4
	Max OPC (%)	45	49	36	46
T + F	*PC*	2	4	2	4
	Max OPC (%)	65	78	86	82
T + TF	*PC*	4	2	2	3
	Max OPC (%)	57	48	68	59
F + TF	*PC*	2	4	4	4
	Max OPC (%)	57	71	66	62
T + F + TF	*PC*	4	2	2	3
	Max OPC (%)	57	48	68	58

Symbols. T = feature extracted in the Time domain; F = feature extracted in the Frequency domain; TF = feature extracted in the Time-Frequency domain; SHSi = i-th Structural Health Status of the road pavement under test, where i=0, 1, 2, and 3, corresponding to 0, 16, 31, and 46 drilled holes; *PC* = Predicted cluster; *Max OPC (%)* = highest percentage of observations associated to *PC*.

Tab. 5.19 Results of the hierarchical clustering of the nine features extracted from the ARs (source: CAR) based on all the possible combinations of the features

#F	*F*		SHS				*Max OPC$_{AV}$* (%)
			SHS0	SHS1	SHS2	SHS3	
1	*n.a.*	*PC*	-	-	-	-	-
		Max OPC (%)	-	-	-	-	
2	*n.a.*	*PC*	-	-	-	-	-
		Max OPC (%)	-	-	-	-	
3	*n.a.*	*PC*	-	-	-	-	-
		Max OPC (%)	-	-	-	-	
4	*2+4+6+8*	*PC*	4	1	2	3	50
		Max OPC (%)	60	41	42	56	
5	*2+4+5+6+8* *2+3+4+6+8*	*PC*	4	1	2	3	50
		Max OPC (%)	60	41	42	56	
6	***1+2+4+7+8+9***	***PC***	**3**	**2**	**1**	**4**	**61**
		Max OPC (%)	**78**	**60**	**45**	**60**	
7	*1+2+4+5+7+8+9* *1+2+3+4+7+8+9*	*PC*	3	2	1	4	61
		Max OPC (%)	78	60	45	60	
8	*1+2+3+4+5+7+8+9*	*PC*	3	2	1	4	61
		Max OPC (%)	78	60	45	60	
9	*n.a.*	*PC*	-	-	-	-	-
		Max OPC (%)	-	-	-	-	

Symbols. *#F* = number of features used as input during the clustering; *F* = combination of features that led to a correct classification; SHSi = i-th Structural Health Status of the road pavement under test, where i=0, 1, 2, and 3, corresponding to 0, 16, 31, and 46 drilled holes; *PC* = Predicted cluster; *Max OPC (%)* = highest percentage of observations associated to *PC*; *Max OPC$_{AV}$ (%)* = average of the values *Max OPC;* n.a. = not available because of misclassification.

Based on the results of the clustering reported in the Tabs. 5.18 and 5.19, it is possible to conclude that:

- It seems not possible to correctly classify the structural condition (SHS) of the road pavement under test using (cf. Tab. 5.18) the three features extracted in each domain of analysis (e.g., the 1st, 2nd, and 3rd feature extracted in the time domain, T), and all the possible combinations among the domains (e.g., the six feature belonging to the two domains T and F; see T+F in Tab. 5.18);
- It is possible to correctly classify the 50% of the ARs using one combination of 4 features (i.e., 2+4+6+8; cf. Tab. 5.19), or two combinations of 5 features;

- The best results can be obtained using one combination of 6 features that allows properly classifying the 61% of the ARs. This percentage can be achieved using also two combinations of 7 features and one combinations of 8 features.
- It is no possible to correctly classify the ARs using all the possible combinations of 2, 3, and 9 features. The result is the same using only one feature at time.
- The data processing allows to understand that: i) based on the high variability of the ARs obtained using the vehicle pass-by as a source of noise and vibration, a suitable number of ARs are needed to identify cracks in road pavement using the feature-based approach described in this section of the thesis; ii) in order to reduce the computational complexity and speed-up the data processing (which is a crucial factor of the SHM), it is possible to use sampling frequency lesser than 192 kHz (e.g., 100 times lesser); iii) the augmentation process can be used if the number of the ARs are not enough for the SHM purposes (e.g., at the beginning of the monitoring); iv) the number of features seems unrelated to the efficacy of the SHM. Only meaningful features ensure to succeed in clustering, and for this reason they should be selected based on their ability to represent relevant variations of the signals that are due to variation of the structural condition of the monitored asset.

Finally, it is important to underline that the real application of the proposed method, using the traffic as source of sound and vibration, will produce a big amount of data with a high variability. In fact, it is expected that different vehicles, periodical changes of the environmental conditions, different boundary conditions, and unexpected or infrequent phenomena will affect the vibro-acoustic responses of the monitored road pavement. Despite the evident high complexity of the problem (multivariate problem), two crucial aspects make the proposed method suitable for real applications, i.e.:

1. the possibility to handle big datasets: this allows reducing the variability associated to the signals because of the fact that machine learning-based or statistical-based approaches can be used to carry

out data processing (e.g., for feature extraction, data compression, classification, pattern recognition, etc.). Consequently, benchmarks related to the type of vehicles (e.g., heavy and light vehicles), patterns related to the environmental conditions (e.g., daily, seasonal, or annual changes), and unexpected and infrequent phenomena can be recognized and used to avoid mistakes during the monitoring (false alarm minimization);

2. the ability of carry out differential diagnoses: despite the moment in which the method is applied on an asset to be monitored, it is possible to define one or more benchmark(s) of the asset response(s) (e.g., of an as-built road), which will be compared with the successive asset responses during the asset life-time in order to recognize its SHS (e.g., absence of failures, occurrence of a potential failure, or presence of a functional failure).

Consequently, it is possible to state that, although the validation of the proposed NDT-SHM method refers to experimental investigations that 1) cannot take into account all the variables of the problems, and 2) was limited to work on datasets smaller than those related to real applications, the proposed method showed the full potential of being a powerful tool for the SHM of real assets, such as road pavements.

6
Complex system: design and set up of a system able to apply the proposed NDT-SHM method

The real-scale implementation of the proposed NDT-SHM method was taken into account through a specifically designed electronic system. Low- and ultra-low-power devices (e.g. sensors and wireless data transmitter), hopefully powered using renewable energy (e.g., photovoltaic), are recommended for this type of applications in order to reduce the energy consumption, and allow efficient and useful data transmission. The objective of this section are: 1) drawing useful guidelines for the design of NDT-SHM systems, focusing on the energy consumption, the typology and number of sensors, the frequency of measurements, the duty cycles of the devices, and the days of autonomy of the system; 2) describing a possible application of the proposed system related to the SHM of a road pavement.

6.1. Design of a system able to apply the proposed method: component's characteristics[9]

This section of the thesis refers to the application of the NDT-SHM method presented in the preceding sections. Based on the literature and the experience made during the experimental investigations carried out during all the research project, a Wireless Sensor Network (WSN) system was selected as the more appropriate type of system to apply the proposed monitoring method. In more detail, this section aims at presenting all the components of the WSN system (see Fig. 6.1, system design), and defining the criteria that were used for the selection of the components mentioned above. While, in the following section, one possible application of the proposed WSN system is reported (see Fig. 6.1, system set up), i.e. a case study related the monitoring of a road pavement, which was used to estimate the power consumption of the proposed system (Fedele, Merenda, et al. 2018).

[9] This section mainly refers to the paper 1.8 (see Scientific production).

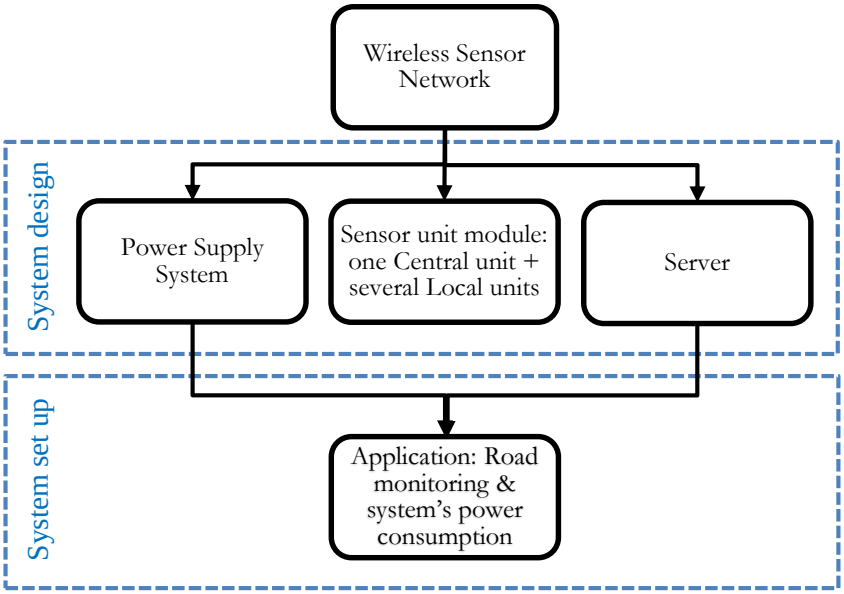

Fig. 6.1 Flow chart that summarize the Chapter 6.

As shown in Fig. 6.1, the WSN system presented in this thesis consists of a modular system, which includes several sensor units (herein called SUs), a power supply system, and a server. More details are provided in Fig. 6.2.

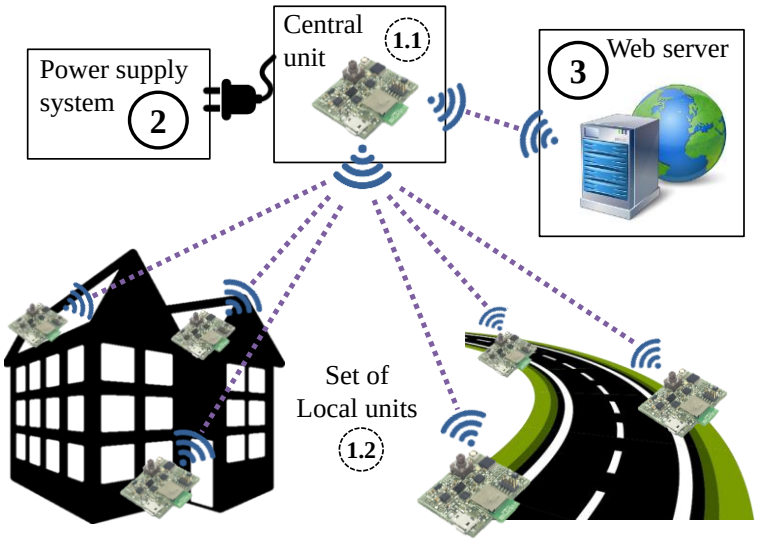

Fig. 6.2 Schematic representation of the proposed Wireless Sensor Network (WSN), which consists of (1) sensor units (1.1: Central, and 1.2: Local), (2) Power supply system, and (3) Web server.

The sensor units are the core of the system. Two different types of sensor units were designed, i.e. the Central unit (see Fig. 6.2, component 1.1), and

the Local unit (see Fig. 6.2, component 1.2). In particular, each module of the network includes several Local units that are wirelessly connected to one Central unit. The main components of the sensor units (see Fig. 6.3) are a dc-dc regulator or a battery (i.e., the dc-dc regulator is needed by the Central unit, and the battery is needed by each Local unit), a microcontroller, a wireless transmitter, and a Micro-Electro-Mechanical System (MEMS) microphone.

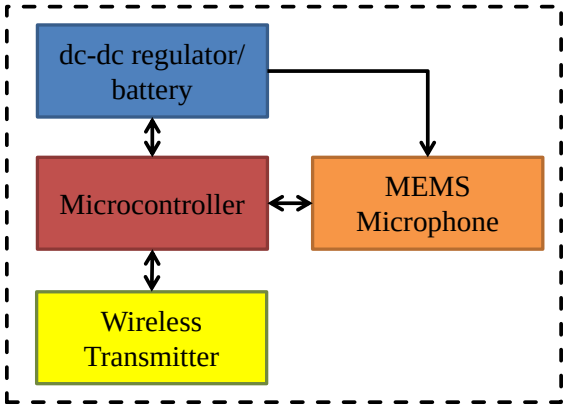

Fig. 6.3 Block diagram of the main components of the sensor units.

Note that, the Central unit is located in a safe site acting as an airplane's black box. In fact, this unit receives the data from each Local unit, temporally stores them, and then sends them to a server unit wirelessly a wireless transmitter.

The core of each sensor unit is the microcontroller. This component is needed because of the fact it allows the local management of the data. In fact, this component is devoted to execute software routines, to control the sensors, gather and transmit data, and to manage logical and power states.

The use of a MEMS microphone relates to the main advantages offered by the MEMS technology (Biprasish 2016) i.e.: i) minimization of energy and raw materials needed for their production; ii) high reproducibility, sensibility, sensitivity, accuracy, and reliability; iii) reduced costs and energy consumption.

A noteworthy effort was dedicated, during the research project, to define the more suitable wireless transmitter, because of the fact that a reliable monitoring system should be able to ensure a prompt transmission of data

and information. In addition, in order to provide crucial information for the design of an efficient monitoring system, the data transmission/interchange among all the devices of this type of systems, and different Radio Frequency (RF)-based technologies have been considered in this study. In particular, among all the recent protocols for low-power long-distance data transmission developed in the last years, we considered: i) several Low-Power Wireless (LPW; cf. (Mannion 2018)), i.e. ANT, 2.4 and 5 GHz Wi-Fi, ZigBee, RF4CE, Bluetooth Low Energy (BLE), and Bluetooth 5; ii) two Low-Power Wide-Area Networks (LPWAN; cf. (Mekki et al. 2018)), i.e. Narrow Band-Internet of Things (NB-IoT), and Long Range, low power wireless platform (LoRa). The more suitable protocol should be selected considering frequency band(s), network topology support, data transmission rate, range or transmission capability, and coexistence (Dementyev et al. 2013; Mannion 2018), and making a trade-off between power consumption, bandwidth occupation, and transmission range. Usually, the peak transmit power must be lower than +21 dBm (decibel-milliWatts, cf. (Mannion 2018)), and several factors (e.g., average receive, transmit, and sleep currents, data rate used, time taken for a node to connect to the hub after waking up, the use of sleep between individual Radio Frequency, RF, packets, packet size variations, transmitter and receiver distance, and hub parameters) must be considered to determine the actual power consumption of these technologies (Dementyev et al. 2013). Generally, in order to succeed in high-speed data transmission, during the design process, attention must be paid to the following aspects (Mannion 2018): i) technologies with high power transmission and high sensitivity (i.e., high Signal-to-Noise Ratio, SNR) should be used; ii) the operating environment should be carefully analyzed (e.g., the presence of ceilings, or walls, or human bodies can affect the transmission length), instead of using "ideal" conditions; iii) frequency of the RF carrier should be considered; iv) design layout, mechanics, and coding schemes should be adapted to the specific application (Farris et al. 2017; Merenda, M., Felini, C., Della Corte 2016).

ANT (and the most recent ANT+ and ANT BLAZE) is an ultra-LPW protocol, which operates in the 2.4 GHz ISM band (Mannion 2018). Suitable

for coin cell powered sensors, allows months or years of battery life. Originally targeted for sports and fitness, recently it is adopted in the home/industrial automation sectors.

Wi-Fi is very efficient for large data transfers using high-speed throughput, but it has high energy consumption (Mannion 2018). Although improvements have been made to solve this weakness (e.g., Wi-Fi "HaLow", which was presented in 2017), it is still unsuitable for low power operation (e.g., coin cell). It operates at 2.4 and 5 GHz bands, while the new low-power, and extended range version, i.e. the Wi-Fi "HaLow", works at 90 MHz ISM band (where ISM stands for Industrial, Scientific and Medical Radio).

ZigBee (and ZigBee PRO) is a LPW specification designed for high security mesh networking in industrial/home automation sectors (Mannion 2018). It operates in the 2.4 GHz ISM band (as well as 784 MHz in China, 868 MHz in Europe, and 915 MHz in the USA and Australia). It has a data rates of 20 kilobits per second, kbps, at 868 MHz, and 250 kbps at 2.4 GHz.

RF4CE stands for Radio Frequency for Consumer Electronics (Mannion 2018), and is a customization of ZigBee for RF remote control applications (e.g., television set-top boxes). Using RF, it improves interoperability, line-of-sight (straight path between transmitting antenna and receiving antenna), and limited feature drawbacks of infrared (IR) remote control. It is in competition with ZigBee and Bluetooth low energy.

Bluetooth low energy is one of the new wireless interfaces/protocols that have recently emerged to address the needs of the IoT (e.g., micro-amp average current require, or small battery capacities for wearable devices; cf. (Mannion 2018)). Its operation frequency of 2.4 GHz is suitable for asynchronous communication, and infrequent exchange of low volume of data.

Bluetooth 5 increased raw data rate (Mbit/s) by up to 2x, and transmission range by up to 4x compared to the Bluetooth low energy.

The main difference between the LPW and LPWAN devices concerns the transmission capacity, i.e. the first ones allow transmission for distance lesser than 150 m (Mannion 2018), while the second one up to 20 km in rural zones, and 1–5 km in urban zones (Mekki et al. 2018). Narrowband (NB)-IoT

technology offers very low latency, high quality of service, reliability, and high transmission range to the IoT markets (Mekki et al. 2018; Sinha, Wei, and Hwang 2017). It works at 700-900 MHz, in a bandwidth of 200 Hz, with data rate lesser than 200 kbps, it covers from 1 km (urban) to 10 km (rural), and has low interference immunity.

Lo-Ra has advantages in terms of battery lifetime, capacity, cost device, transmission range (high coverage; cf. (Mekki et al. 2018; Sinha et al. 2017)). It is suitable for infrequent communication rate, for local network deployment, for devices that move at high speeds, and for transmitting tiny amounts of data in long range. It operates at ISM bands of 868 MHz in Europe, 915 MHz in North America, and 433 MHz in Asia. Its bandwidths are 125 and 250 kHz, its data rate is lesser than 50 kbps, it covers from 5 km (urban) to 20 km (rural), and it has a high interference immunity. The following table shows the expected transmission capability of the technologies mentioned above.

Tab. 6.1 Transmission capability of different Low-Power technologies for data transmission.

Technology	Transmission capability (m)	Reference
ANT	< 30	(Darshana Thomas, Edward Wilkie 2016; Mannion 2018)
5 GHz Wi-Fi	< 50	
ZigBee/RF4CE	< 100	
BLE	< 70	
2.4 GHz Wi-Fi	< 150	
Bluetooth 5	< 200	
NB-IoT	< 20000	(Mekki et al. 2018)
LoRa	< 10000	

Based on the above, possible solutions can be represented by Central units equipped with a Wi-Fi Transmitter (e.g., 2.4 GHz Wi-Fi), and Local units equipped with devices with transmission capability lower than those installed in the Central units (e.g., Bluetooth low energy, BLE, or ANT).

The system was designed to power the Central unit with a power supply system, while the Local units are powered by battery (e.g., by means of button or coin cell batteries, e.g., CR2032). The next section contains one example of

power supply system that was designed taking into account the different technologies described in section 2.6 that allow energy harvesting in transportation.

An efficient WSN needs a server to collect, save, process, and analyze the data that are gathered using the sensor units, and to provide the results of the above-mentioned analysis to the user of the WSN system. In more detail, it is always important to find a trade-off between the local and remote data processing. In order to achieve this goal, each operation should be carefully analyzed. Possible trade-off solutions can be the followings: i) to minimize the amount of data exchanged on the network (e.g., preferring local data processing, or reducing the sampling frequency of the sensors); ii) to offload burdensome and important tasks to a more powerful machine (e.g., a remote server), saving time and energy (otherwise locally required by the sensor units); iii) to use custom developed Application Programming Interfaces (APIs) that allow secure data transmission, especially toward the platform users, or the other stakeholders. For instance, using a cloud server to process the acoustic data collected by the MEMS microphones of the WSN, the following benefits can be obtained: 1) the power consumption of the battery-powered local sensor units is reduced; 2) it is possible to use more powerful computational hardware and more performing software; 3) each Local unit, instead of consuming power in calculations, will continue running smoothly, staying focused on quickly collecting data. Meanwhile, with the exception of the occurrence of an alert condition, the environmental data (e.g., the air temperature) could be processed locally with a low periodicity, reducing the data flow in the network. In order to provide more information about the design of the APIs, the terms REST and JSON should be defined. REST stands for Representational State Transfer (Lanthaler and Gütl 2012) and is the most widespread style used in the mobile world to design APIs. REST relies on stateless, client-server, cacheable communications. RESTful services (i.e., the REST applications; see (Lanthaler and Gütl 2012)) use the Hyper Text Transfer Protocol (HTTP) requests to carry out the four CRUD (Create/Read/Update/Delete) operations, i.e. POST = create, PUT = create and/or update, GET = make queries, and DELETE = delete data. JSON

stands for Java Script Object Notation. It is a language independent format (lightweight text-based open standard) used for serializing and transmitting structured human-readable data over network connection (Afsari, Eastman, and Castro-Lacouture 2017), which was mainly designed for server-web applications communications. Finally, specific needs for performance, scalability, administrative features, resources scaling, costs, migration features, data protection, and data export should be considered to select the best-fit server option. Bearing in mind all the considerations defined above, a Web Server (cloud-hosted solution), with proper scaling and migration features at a reasonable cost (guaranteed by the provider), was considered as a suitable solution for the WSN system proposed in this thesis.

6.2. Application: road monitoring and system's energy consumption[10]

This section reports a possible application (road pavement monitoring) of the proposed WSN that which was used to estimate the power consumption of the proposed system.

As is well known, a well-designed monitoring system should be able to carry out a real-time assessment of the overall road conditions, hopefully in a non-destructive, efficient, safe, and sustainable way (i.e., save energy, time, and other resources). Furthermore, in order to monitor the structural health conditions of a road pavement, the action of the vehicular traffic (e.g., vibrations, noise, loads) and the boundary conditions (e.g., temperature, humidity, presence of water in the bottom layers, availability of electricity) should be taken into account.

Consequently, in the application described in this section, in order to minimize energy consumption (sustainability), state-of-art extreme low power devices and techniques have been taken into account. Hence, the WSN was equipped with a low-power transmission system, and a Photovoltaic Standalone System (PVSS). Fig. 6.4 recalls the Fig. 6.2 and provides more

[10] This section mainly refers to the paper 2.1 (see Scientific production).

detail about the components of the power supply system, which were dimensioned as described in this section. In particular, the Power Supply System includes: 1) one photovoltaic panel (i.e., the component 2.1 in Fig. 6.4); 2) one recharge circuit (i.e., the component 2.2 in Fig. 6.4); 3) one battery (i.e., the component 2.3 in Fig. 6.4).

An important component of the Power Supply System is the recharging circuit. It consists of an electronic card that efficiently converts the variable voltage obtained from the solar panel, during the operating time, to a fixed voltage (or fixed current, depending on the type of recharge) for the optimal recharge of the battery. Nevertheless, the recharging circuit is also deputed to the charge control of the batteries to avoid overcharging and unwanted issues. Finally, each Local unit of the WSN system should be installed on the road pavement in conditions of non-destructivity and safety (e.g., attaching them on the road pavement along the road's edges), should be powered through batteries (aiming at system sustainability), and should be wirelessly connected to one Central unit.

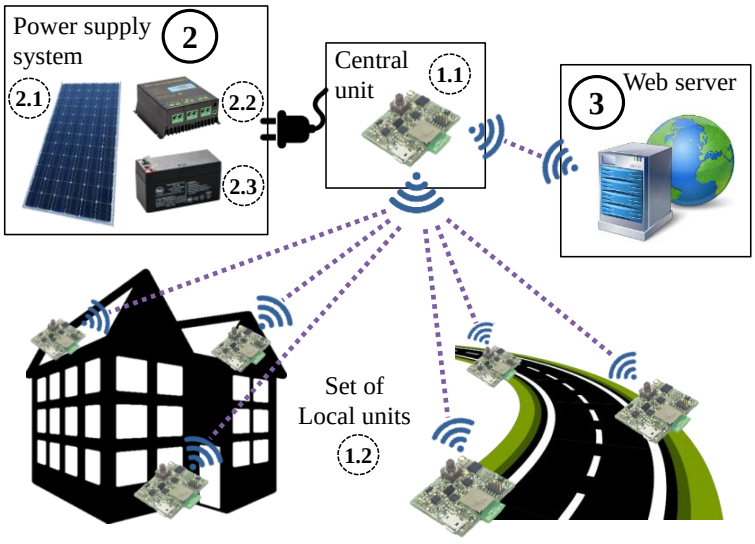

Fig. 6.4 Schematic representation of the proposed Wireless Sensor Network (WSN), which consists of (1) sensor units (1.1: Central, and 1.2: Local), (2) Power supply system (i.e., 2.1: photovoltaic system, 2.2: recharge circuit, and 2.3: battery), and (3) Web server.

Each sensor unit contains (see Fig. 6.5): i) different MEMS sensors, i.e. those chosen to detect the vibro-acoustic responses of the pavement to the traffic

(i.e., a microphone), and those needed to detect important environmental parameters (i.e., temperature and humidity sensors, accelerometer and gyroscope); ii) the microcontroller used to manage the sensors; iii) the wireless transmitter unit (RF transmitter), which consists of an integrated transmitter and an antenna; iv) the dc-dc regulator used by the Central units to control the energy provided by the PSSV, or by the batteries used in the Local units.

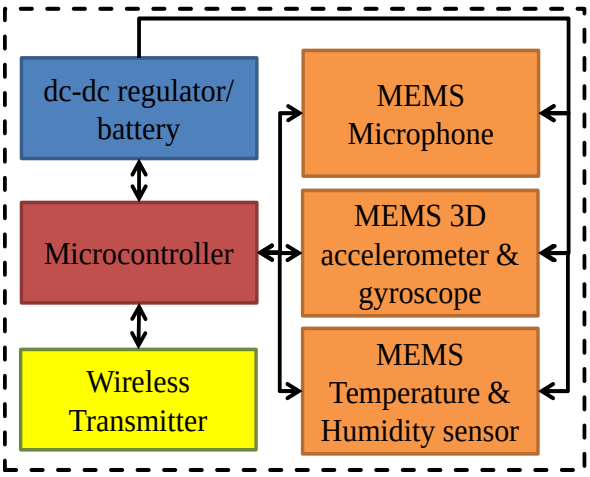

Fig. 6.5 Block diagram of a sensor unit used for road pavement SHM.

The energy consumption of the system depends on the configuration of the devices used inside the sensor units (i.e., type, model, etc.), and of some important parameters related to their operation (i.e., sampling frequencies of the sensors, and duty cycles of all the devices). For this reason, in Tabs. 6.2 and 6.3, values for these two parameters have been reported together with the sensors used to derive the power consumption of the system. It should be noted that, the values of Tab. 6.3, were derived based on the content of Tab. 6.2. In more detail, the sampling frequencies that are shown in Tab. 6.2: i) have been chosen based on a previous study (i.e., Chapters 4 and 5); ii) might allow gathering a sufficient amount of data from which the structural conditions of the pavement can be extracted; iii) have been used to calculate the energy consumption of each component of the system.

Tab. 6.2 Sensor unit characteristics: devices, sampling frequencies, and power consumptions.

Device	Sampling frequency [kHz]	Power consumption	References
Accelerometer	1	< 2 mW	(STMicroelecronics 2018a)
Gyroscope	1		
Microphone	44		(Knowles 2018)
Temperature/ Humidity sensor	0.1		(STMicroelecronics 2018b)
Microcontroller	N/A	150 µW/MHz in low power mode	(Microchip 2018)
Low-Power RF Transmitter	N/A	550 µW in low power mode	(Prasad 2018)

The current consumption of each component of the sensor unit (see Tab. 6.3) was derived considering the sensors set chosen (see references in Tab. 6.2), a voltage of 3 V, a microcontroller with a clock frequency f_{clk} = 40 MHz, and defining the duty cycles reported in Tab. 6.3.

Tab. 6.3 Duty cycles and current consumption of each component of the sensor unit during the system operation @ f_{clk} = 40 MHz.

		Duty cycle of operation (%)				
Operational condition[1]		0	1	2	3	
Device	State					CC[5]
M[2]	Sleep	99	99	99	99	0.01
	Run	1	1	1	1	15
S[3]	Sleep	90	60	30	0	0.1
	Run	10	40	70	100	5
RF/Wi-Fi or BLE[4]	Sleep	90	95	97.5	99	0.1
	Run	10	5	2.5	1	150

Notes: 1. Operational conditions; 2. Microcontroller; 3. Sensors; 4. Transmitter system/protocol; 5. Current consumption at 3 V (mA).

Based on Tab. 6.3, it is possible to calculate the average daily power consumption of the WSN, for one sensor unit (i.e., M + S + RF/Wi-Fi): i) for each device (e.g., M), the current consumption (A) is derived considering two different working states of the devices, namely the sleep time and the run time); ii) the average current consumption (A) is then derived; iii) the average

power consumption is calculated (A×V=W); iv) the 24h-related energy consumption is derived (W×h). Hence, it was estimated that about 380 mWh/day are needed by one sensor unit. This result will be used in the following section to properly size the power supply system.

The characterization and sizing of the power supply system were based on the energy consumption of the system with the operating condition specified in Tab. 6.3, and under the hypothesis of installing the monitoring system on a road in Reggio Calabria (Italy), herein called "reference road". This road was selected as an example of road that needs to be monitored because: 1) it is located very close to a small river (creek), and for this reason, it is subjected to high hydrogeological risk; 2) section location and characteristics easily allow gathering information about traffic spectrum and solar radiation. Indeed, in order to define the characteristics of the power supply system (i.e., the dimensions, peak power, etc.), the solar radiation (i.e., irradiation) is required.

Different tools are available online that allow estimating the solar radiation, and sizing photovoltaic (PV) grid-connected and off-grid systems (e.g., (ENEA 2018; JRC 2018; Oregon Embedded 2018)). In this study, one of these tools (JRC 2018) was used to estimate the annual solar irradiation on the reference road (see Fig. 6.7).

In particular, the highest values of irradiation refer to the optimal inclination (*Iopt*) of the solar panel (i.e., the acute angle between a horizontal plane and an inclined plane facing south). The *Iopt* allows gathering the maximum amount of solar energy because it varies during the year. From the *Iopt* curve, the average optimal inclination was calculated (i.e., 36°), and the irradiation *H(36)* was determined. The annual averages (av) values are the following:

- Irradiation on horizontal plane *Hh_av* = 4889 Wh/m^2/day;
- Direct normal irradiation (*DNI*) = 5306 Wh/m^2/day;
- Irradiation on optimally inclined plane *Hopt_av* = 5523 Wh/m^2/day;
- Irradiation on plane at the average optimal inclination angle of 36°, *H(36)av* = 5508 Wh/m^2/day.

Because of the fact that, *H(36)av* is very close to the maximum irradiation (*Hopt_av*), it is possible to assume this value as the input parameter of the PV panel (i.e., the panel inclination was assumed as 36°).

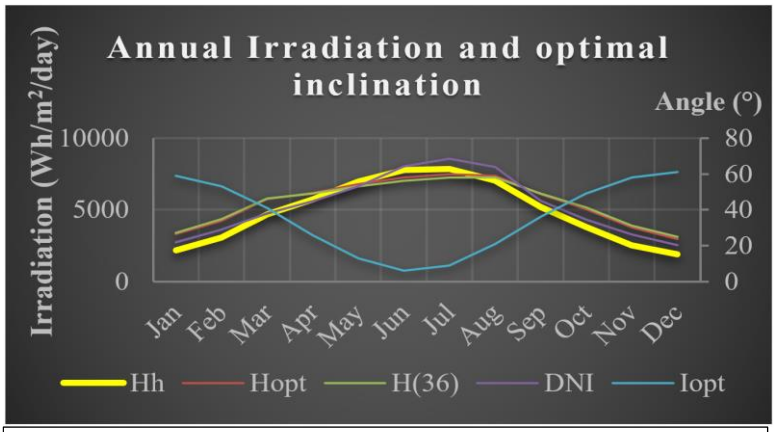

Symbols. Hh: Irradiation on horizontal plane; Hopt: Irradiation on optimally inclined plane; H(36): Irradiation on plane at the average optimal inclination angle of 36°; DNI: Direct normal irradiation; Iopt: Optimal inclination (°).

Fig. 6. 6 Annual trend of the daily irradiation on the reference road obtained for the optimal inclination (angle) of the panel.

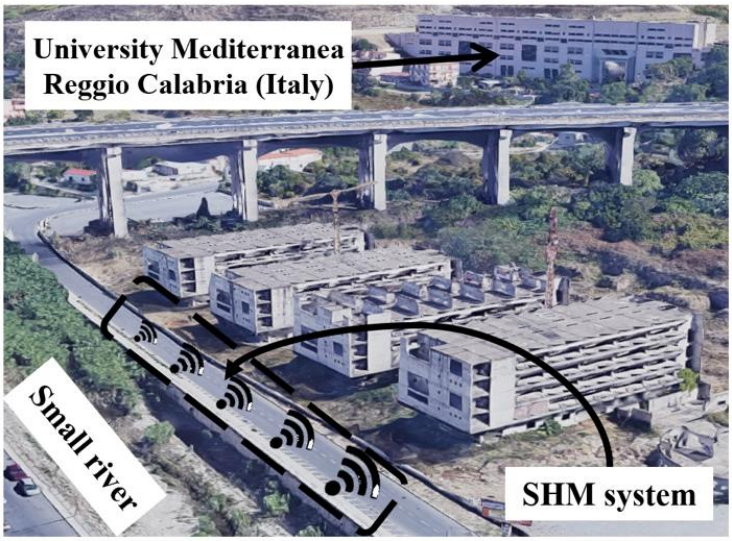

Fig. 6. 7 Road reference beside a small river in Reggio Calabria (Italy) where we suppose to install the SHM system.

The main parts of the power supply unit (PV panel, and battery) was designed using the following equations (Kazem, Khatib, and Sopian 2013):

$$A_{PV} = \frac{E_{PV}}{H \times \eta_{PV} \times \eta_{wire}}, \quad (6.1)$$

where A_{PV} is the area of the PV panel (m^2); E_{PV} is the energy produced by the PV panel in one day (Wh/day); H stands for the annual irradiation ($Wh/m^2/day$); η_{PV} is the efficiency of the PV panel (%; as reported into the manufacturer data sheet; e.g., 14%); η_{wire} is the efficiency of the wire used (%; this value is a function of quality and length of the wires used).

In this study, a battery was included in the power supply unit because of the fact that this allows increasing the reliability of the system. In more detail, if the sizing of the battery is conveniently carried out, the system will be able to perform its work even in the case of the failure of the PV panel. This will permit, to the decision maker (e.g., authority or the company that are responsible of the system maintenance), to define and make the proper intervention to solve the failure, and rehabilitate the system.

The following equation was used to size the battery:

$$C_B = \frac{E_L \times n}{DOD \times \eta_B \times V_B}, \quad (6.2)$$

where C_B is the capacity of the battery (Ah); E_L is the daily energy load (or daily energy consumption, i.e. the energy required by the sensor unit (SU) of the system as a function of the operational condition in a day); n represents the autonomy of the system provided by the battery (day); DOD stands for the maximum Depth Of Discharge of the battery (%; usually, greater than 20%, e.g., 50%.; cf. (Kazem et al. 2013)); η_B is the efficiency of the battery (%); V_B is the nominal voltage of the battery (V).

Based on the equations and the assumptions reported above, useful curves and guidelines are reported in the following. In particular, the average solar radiation (5508 $Wh/m^2/day$) for the reference road, and the energy load of system (380 mWh/day = 0.380 Wh/day), in the benchmark condition 0 (see Tabs. 6.2 and 6.3), and equipped with one sensor unit (#SU = 1), were calculated. In order to compensate for the losses of the monitoring system,

the energy load of the system was assumed as 1 Wh/day. This value was used into the following examples. The first set of curves (see Fig. 6.8) concerns the sizing of the power unit supply (i.e., the PV panel and the battery) of the WSN monitoring system (at the benchmark condition 0, and #SU = 1). Appling Eq. 6.1, using as input E_{PV} = 1 Wh/day, H = 5508 Wh/m^2/day, η_{PV} = 14%, and η_{wire} = 85%, the area of the panel required by the system equipped with 1 SU was 0.0015 m^2 (e.g., a panel with an area of 10 × 15 cm^2). After that, using the Eq. 6.2 and considering a PV panel with an area equal to 0.0015 m^2, the following curves were drawn (see Fig. 6.8). These curves show how the capacity of the battery (C_B) is influenced by the days of autonomy (n), and the voltage of the battery (V_B), while the other parameters are fixed (i.e., E_L = 1 Wh/day, DOD = 50%, and η_B = 80%).

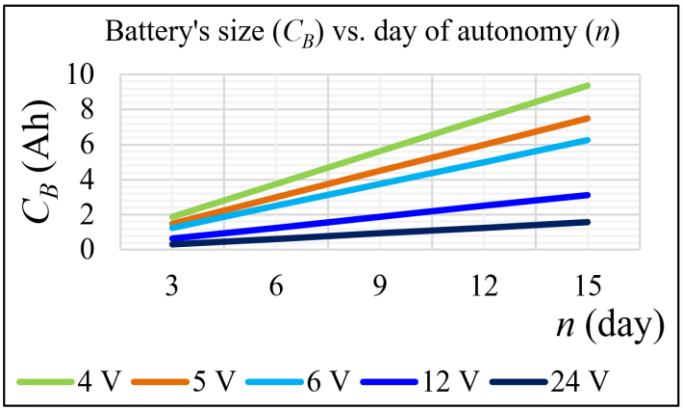

Fig. 6.8 Capacity of the battery (C_B) as a function of the day of autonomy (n), and battery voltage (V_B).

If the benchmark conditions or the number of SUs change, the energy consumption of the monitoring system changes as well. For this reason, in the next example, the energy consumption of the system equipped with 1 SU was estimated changing the benchmark conditions as in Tab. 6.3.

Fig. 6.9 shows: i) the operational conditions 0, 1, 2, 3 (x-axis, cf. Tab. 6.3); ii) the run time percentage, *per* given device (R_M, R_S, R_RF, respectively, cf. y-axis, left); iii) the energy load *per* day needed *per* given operational condition (E_L, y-axis, right). The results shown in Fig. 6.9 demonstrate that it is possible to optimize the system, reducing the energy consumption and

improving the performances of the system (in terms of duty cycle) at the same time.

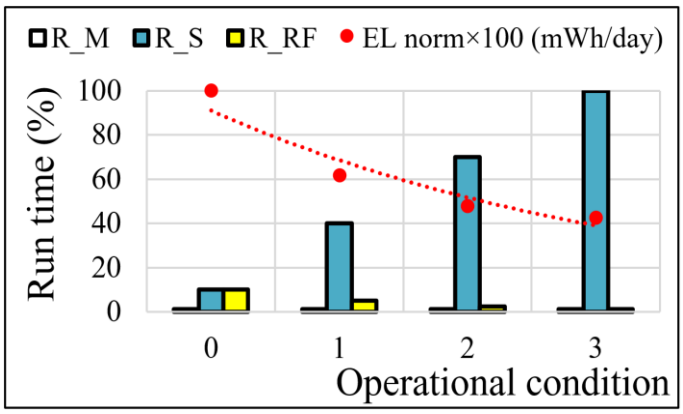

Fig. 6. 9 Energy consumption of the system, E_L , equipped with 1 SU (containing the microcontroller, M, the sensors, S, and the data transmitter, RF, as a function of the duty cycle

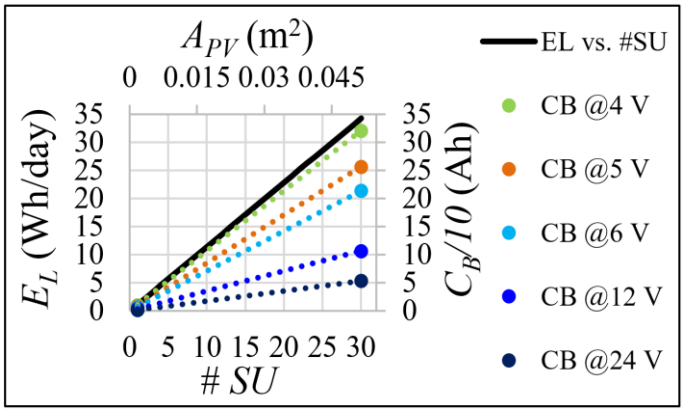

Fig. 6. 10 Energy load of the system *per* day, E_L , battery capacity, C_B , at different voltages, V_B , and area of the PV panel, A_{PV}, as a function of the number of sensor unit (#SU)

In addition, Fig. 6.10 shows: i) the energy consumption *per* day, E_L, of the WSN system (at the benchmark condition 0 defined in Tabs. 6.2 and 6.3) as a function of the number of SU used, #SU; ii) the area of a PV panel, A_{PV}, that should be used to power the WSN system equipped with a network of SUs (#SU); iii) the capacity of the battery, C_B (expressed in Ah divided by 10 to be plotted in this graph) at different voltages (i.e., 4, 5, 6, 12, 24 V), which should be used to power the monitoring system equipped with a network of SUs (#SU) in order to ensure 15 days of autonomy.

Finally, considering that a real WSN monitoring system consists in a network of SUs wireless connected to a Central unit (HUB), the design of all the system components should be carefully carried out. For this reason, the following procedure was drawn:

2) Consider the number of SUs per linear meter (e.g., 0.1) controlled by one HUB.
3) Consider a standalone power supply that consists of the following components:
    i. photovoltaic modules;
    ii. batteries;
    iii. dc-dc regulator.
4) Define sampling frequencies, and duty cycles of the devices of the WSN system. Note that, in order to define these parameters, a trade-off between real-time monitoring and the energy consumption is needed.
5) Calculate the energy consumption of the devices above as a function of the sampling frequency, and the duty cycles defined in the previous point.
6) Define a RF transmission system and the relative energy consumption (derived from the datasheet of the devices used).
7) Calculate the maximum irradiation (best angle and orientation) in the place where the WSN system has to be installed.
8) Calculate the dimension of a PV panel (or more than one) that is able to produce the energy daily required by the WSN System.
9) Determinate the characteristics of a battery that allows gathering enough energy to power the system, even in case of failure or reduction of energy production of the PV panel.

Conclusions

The worsening of the road pavement performances is mainly caused by concealed distresses that are generated by several factors such as the vehicular traffic. The propagation of these distresses, from the bottom of the pavements to the upper layers, is one of the main causes of surface damage. All these damages represent a real problem for the authorities that are responsible for the road infrastructures (mismanagement, and risks), and for the users of these assets (discomfort, and risks).

Consequently, different literature reviews were carried out to obtain a comprehensive overview about the causes that lead to the generation and propagation of the distresses mentioned above, and the strategies that were carried out to face this problem. In particular, the following topics were investigated: i) the various phenomena that lead to the failure of road pavements; ii) the state-of-the-art of the solutions adopted to increase the sustainability and the efficiency of road pavements; iii) the Pavement Management Systems (PMSs) currently applied on road infrastructures; iv) the state-of-the-art of the methods, techniques, devices, systems, and patents related to the field of the Structural Health Monitoring (SHM) of civil engineer structures and infrastructures; v) the techniques and methods used to carry out efficient data processing to analyze the data gathered using SHM systems; vi) the Energy Harvesting Technologies (EHTs) designed for, or implemented on road pavements in order to increase the sustainability of this type of asset, and to gather the energy required to power the SHM systems eventually installed.

These literature reviews show that:

- Several solutions are currently adopted to improve the sustainability and efficiency of the road pavements construction and operational phases, and one of the most effective refers to Intelligent Transportation System (ITS).

- An ideal ITS should include as a fundamental component a Pavement Management Systems (PMSs) based on Structural Health Monitoring (SHM) solutions, efficient data processing methods, and EHTs.
- The authorities that are responsible for the management of road pavements could improve the management process by using innovative ITSs that enable them: i) to switch from the failure-based to the condition- or predictive-based maintenance; ii) to move from the current destructive, un-sustainable, and limited traditional measurements systems to non-destructive, sustainable, and specially designed innovative ones.
- Despite the high number of solutions designed for the SHM of civil engineering assets (e.g., building, bridge, and roads), there is a lack in implementation of these solutions in real contexts. In addition, it is difficult to find solutions applied on road infrastructures that are able to: a) monitor the structural conditions of the internal layers of the road pavements; b) detect any temporal and spatial variations of the road conditions due to the occurrence, or the propagation, of internal distresses; c) share the above-mentioned information with the appropriate authorities and the asset users. In fact, this crucial information is strongly requested from the future smart cities that need smart infrastructures (i.e., assets that are able to efficiently gather and share such information).
- Efficient data processing can be carried out using Wavelet Transform and Artificial Neural Network. The first one can be used for different purposes (time-frequency analyses, signal decomposition, denoising, compression, etc.), but it is recommended when signal singularities, which can be related with the occurrence of asset distresses, should be detected and monitored. While, the second one can be used to implement algorithm that are able "to learn" from the signals gathered from the monitoring system, and this ability can be effectively used to recognize the occurrence of asset distresses, and the type of distress.

- High levels of efficiency, sustainability, connectivity, performance, durability, and comfort can be reached implementing ITSs based on Internet of Things (IoT) solutions, such as Wireless Sensor Network (WSN) monitoring systems that are able to gather data using Non-Destructive Test (NDT) and Micro Electro-Mechanical Systems (MEMS)-sensor, hopefully powered using specially designed Energy Harvesting Technologies (EHTs).

Bearing in mind all the above-mentioned problems and solutions, this thesis aimed at presenting an innovative NDT-SHM method, and at providing significant guidelines to design a MEMS-based WSN that is able to implement the proposed NDT-SHM method.

The proposed method aims at monitoring the Structural Health Status (SHS) of the internal layers of the road pavement through the analysis of its acoustic signatures, i.e. their acoustic responses (ARs) to different conventional and un-conventional loads. The set up and the validation of the NDT-SHM method mentioned above was carried out through:

1. several in-lab and on-site experimental investigations on road pavements and asphalt concrete samples (slabs) characterized by different SHSs (induced cracks). A wheel tracking machine was used during the in-lab tests as conventional load. On the other hand, during the on-site experiments, a Light Weight Deflectometer (LWD) was used as un-conventional load, and the vehicular traffic was used as conventional load;
2. a specially designed data processing that aimed at identifying the variation over time of the SHS of road pavements, or its samples (slabs), using meaningful features extracted from the ARs, analyzed in the time domain, in the frequency domain (i.e., from the ARs' spectral contents obtained applying the Fast Fourier Transform, FFT), and in the time-frequency domains (i.e., applying the Wavelet Transform, WT). Ten different features were recognized in the three above-mentioned domains of analysis (i.e., three in the Time

domain, four in the Frequency domain, and three in the Time-Frequency domain; cf. Tabs. 5.3 and 5.16).

The validation of the NDT-SHM method consists in the results obtained during the data processing (i.e., the analyses in above-mentioned domains of the different data set (ARs) collected during the experiments cited above). In more detail:

- The analyses carried out in the time domain showed that the best three meaningful features are related to the amplitudes and the arrival time of the ARs absolute maxima and minima (herein called $\measuredangle a$ and $\measuredangle t$, respectively), and the variance of the ARs (herein called σ).
- The analyses of the spectral content of the ARs (frequency domain), expressed in terms of Power Spectral Density (PSD), pointed out as the most meaningful feature the spectral centroid (herein called fc). Furthermore, case by case, features related to the PSD (e.g., the minimum, the average, or the slope of the PSD in specific frequency domains) can be defined and efficiently used.
- Based on the results obtained in the time-frequency domain, the scalograms (wavelet-based analysis) resulted more efficient to extract features in this domain than the spectrograms (Fourier-based analysis). Among a variety of features extracted and analyzed in the time-frequency domain using the Continuous Wavelet Transform (CWT), the energy and the entropy of the wavelet coefficients, and the pseudo-frequency of the scalograms ridges resulted the best ones to identify and monitor the change of the road pavement SHS.
- The analyses in the time-frequency domain can be improved through the application of quantitative methods and criterions for the selection of the proper wavelet (usually called mother wavelet) that should be used during the application of the CWT. Different methods were taken into account and, among them, three were applied and compared. Results showed that the Maximum Energy to Shannon Entropy ratio criterion (a.k.a., MEER method) allows obtaining good results in terms of SHS change identification.

- Hierarchical clustering can be efficiently used to classify the ARs based on the features extracted in the three domain mentioned above. ARs related to un-convention load (i.e., LWD), and conventional (i.e., vehicle pass-by) can be effectively classified using a small number of features.

The proposed NDT-SHM method may be implemented through a specifically designed WSN system. Low- and ultra-low-power devices (e.g., MEMS sensors and wireless data transmitter), hopefully powered using renewable energy (e.g., produced by a mini-photovoltaic panel), are recommended for this type of application in order to reduce the energy consumption, and allow efficient and useful data transmission.
The implementation of the above-mentioned WSN system and the application of the NDT-SHM method proposed in this thesis can successfully increase the current transportation infrastructure management process (e.g., the Pavement Management Systems, PMS), or the emergency management process.
Future works will involve: i) the application of the machine learning approach for data processing and data mining; ii) the inclusion of accelerometers in the monitoring system.
In particular, the widespread machine learning approach allows carrying out several tasks, and is more and more frequently used in a multitude of fields. In the application described in this thesis, this approach may be used for:

- the automatic extraction of features using the feature learning or representation learning.
- the classification of the vibro-acoustic signature of the road pavement using neural network or deep learning.

Finally, although vibration-based methods represent a well-known and widespread approach in the field of the SHM, the use of vibrational signals can actually improve the proposed NDT-SHM method. In fact, these signals can increase the chances of defining significant and useful characteristics that can lead to the success of the NDT-SHM method.

References

1. AASHTO. 1993. *AASHTO Guide for Design of Pavement Structures*.
2. Abdolmaleki, Mehdi, Morteza Tabaei, Nader Fathianpour, and Ben G. H. Gorte. 2017. "Selecting Optimum Base Wavelet for Extracting Spectral Alteration Features Associated with Porphyry Copper Mineralization Using Hyperspectral Images." *International Journal of Applied Earth Observation and Geoinformation*.
3. Abtahi, Sayyed Mahdi, Mohammad Sheikhzadeh, and Sayyed Mahdi Hejazi. 2010. "Fiber-Reinforced Asphalt-Concrete - A Review." *Construction and Building Materials*.
4. Achenbach, Jan. 1973. *Wave Propagation in Elastic Solids*.
5. Adamo, Francesco, Gregorio Andria, Filippo Attivissimo, Anna Maria Lucia Lanzolla, and Maurizio Spadavecchia. 2013. "A Comparative Study on Mother Wavelet Selection in Ultrasound Image Denoising." *Measurement: Journal of the International Measurement Confederation*.
6. Afsari, Kereshmeh, Charles M. Eastman, and Daniel Castro-Lacouture. 2017. "JavaScript Object Notation (JSON) Data Serialization for IFC Schema in Web-Based BIM Data Exchange." *Automation in Construction*.
7. Aggelis, D. G., E. Z. Kordatos, D. V. Soulioti, and T. E. Matikas. 2010. "Combined Use of Thermography and Ultrasound for the Characterization of Subsurface Cracks in Concrete." *Construction and Building Materials*.
8. Al-Khoury, R., C. Kasbergen, A. Scarpas, and J. Blaauwendraad. 2002. "Poroelastic Spectral Element for Wave Propagation and Parameter Identification in Multi-Layer Systems." *International Journal of Solids and Structures*.
9. Al-Qazzaz, Noor Kamal, Sawal Ali, Siti Anom Ahmad, Md Shabiul Islam, and Mohd Izhar Ariff. 2014. "Selection of Mother Wavelets Thresholding Methods in Denoising Multi-Channel EEG Signals during Working Memory Task." in *IECBES 2014, Conference Proceedings - 2014 IEEE Conference on Biomedical Engineering and Sciences: "Miri, Where Engineering in Medicine and Biology and Humanity Meet."*
10. Al-Qazzaz, Noor Kamal, Sawal Hamid Bin Mohd Ali, Siti Anom Ahmad, Mohd Shabiul Islam, and Javier Escudero. 2015. "Selection of Mother Wavelet Functions for Multi-Channel EEG Signal Analysis during a Working Memory Task." *Sensors (Switzerland)*.
11. Alhasan, Ahmad, David J. White, and Kris De Brabanterb. 2016. "Continuous Wavelet Analysis of Pavement Profiles." *Automation in Construction*.
12. ANAS S.p.a. 2008. *Capitolato ANAS: GESTIONE DELLE PAVIMENTAZIONI STRADALI, LINEE GUIDA DI PROGETTO E NORME TECNICHE PRESTAZIONALI*.
13. Annecke, R., T. Berge, S. Crawshaw, L. Ellebjerg, S. Mårdh, E. Pullwitt, H. Steven, A. Wiberg, and U. Zimmermann. 2008. *SILENCE Project - Noise Reduction in Urban Areas from Traffic and Driver Management*.
14. Appiah, Johnson Kwabena, Victor Nana Berko-Boateng, and Trinity Ama Tagbor. 2017. "Use of Waste Plastic Materials for Road Construction in Ghana." *Case Studies in Construction Materials*.
15. Asphalt-Institute. 1991. *Thickness Design—Asphalt Pavements for Highways and Streets*. Lexington, KY.
16. Asset Insights.net. 2018. "Failure Replacement (Policy)." Retrieved (http://www.assetinsights.net/Glossary/G_Failure_Replacement_%28Policy%29.html%0A).
17. ASTM. 2003. *ASTM D1194-94 - Standard Test Method for Bearing Capacity of Soil for Static Load and Spread Footings (Withdrawn 2003)*.
18. ASTM. 2015. *ASTM E2583 - 07(2015) - Standard Test Method for Measuring Deflections with a Light Weight Deflectometer (LWD)*.
19. ASTM. 2016. *ASTM D1196 / D1196M - 12(2016) - Standard Test Method for Nonrepetitive Static Plate Load Tests of Soils and Flexible Pavement Components, for Use in Evaluation and*

Design of Airport and Highway Pavements.

20. Balaguera, Alejandra, Gloria Isabel Carvajal, Jaume Albertí, and Pere Fullana-i-Palmer. 2018. "Life Cycle Assessment of Road Construction Alternative Materials: A Literature Review." *Resources, Conservation and Recycling*.
21. Bandara, Rupika P., Tommy HT Chan, and David P. Thambiratnam. 2014. "Structural Damage Detection Method Using Frequency Response Functions." *Structural Health Monitoring*.
22. Behnia, Arash, Hwa Kian Chai, and Tomoki Shiotani. 2014. "Advanced Structural Health Monitoring of Concrete Structures with the Aid of Acoustic Emission." *Construction and Building Materials*.
23. Bendat, A. G. and J. S. Piersol. 2000. "Random Data Analysis and Measurement Procedures." *Measurement Science and Technology*.
24. Benedetto, Andrea, Fabio Tosti, Luca Bianchini Ciampoli, and Fabrizio D'Amico. 2017. "An Overview of Ground-Penetrating Radar Signal Processing Techniques for Road Inspections." *Signal Processing*.
25. Beskou, Niki D., Stephanos V. Tsinopoulos, and George D. Hatzigeorgiou. 2016. "Fatigue Cracking Failure Criterion for Flexible Pavements under Moving Vehicles." *Soil Dynamics and Earthquake Engineering*.
26. Bevacqua, Martina T. and Tommaso Isernia. 2018. "Boundary Indicator for Aspect Limited Sensing of Hidden Dielectric Objects." *IEEE Geoscience and Remote Sensing Letters*.
27. Bigerelle, M., G. Guillemot, Z. Khawaja, M. El Mansori, and J. Antoni. 2013. "Relevance of Wavelet Shape Selection in a Complex Signal." *Mechanical Systems and Signal Processing*.
28. Biprasish, Ray. 2016. "Mems Technologies and Analysis of Merits and Demerits." *NVIDIA*. Retrieved (https://www.slideshare.net/Biprasish/mems-technologies-and-analysis-of-merits-and-demerits).
29. Blache, Y., C. Hautier, F. Lefebvre, A. Djordjevic, T. Creveaux, and I. Rogowski. 2017. "Analysis of the Tennis Racket Vibrations during Forehand Drives: Selection of the Mother Wavelet." *Journal of Biomechanics*.
30. British Standards Institution. 1990. *BS 1377-9:1990 - Methods for Test for Soils for Civil Engineering Purposes. In-Situ Tests*.
31. Bucket.sunshineworks.com. 2018. "Solar Tree." Retrieved (http://bucket.sunshineworks.com/images/solar-panel-mounts/pv-tree/pv-tree-1r.jpg).
32. Buratti, C. and E. Moretti. 2010. "Traffic Noise Pollution : Spectra Characteristics and Windows Sound Insulation in Laboratory and Field Measurements." *Journal of Environmental Science and Engineering*.
33. Cafiso, S., C. D'Agostino, E. Delfino, and A. Montella. 2017. "From Manual to Automatic Pavement Distress Detection and Classification." in *5th IEEE International Conference on Models and Technologies for Intelligent Transportation Systems, MT-ITS 2017 - Proceedings*.
34. Calvert, S. C., H. Taale, M. Snelder, and S. P. Hoogendoorn. 2018. "Improving Traffic Management through Consideration of Uncertainty and Stochastics in Traffic Flow." *Case Studies on Transport Policy*.
35. Le Cam, V., M. Doehler, M. Le Pen, and L. Mevel. 2013. "Embedded Modal Analysis Algorithms on the Smart Wireless Sensor Platform PEGASE." in *STRUCTURAL HEALTH MONITORING 2013, VOLS 1 AND 2*.
36. Carlos, Manuel Ricardo, Mario Ezra Aragon, Luis C. Gonzalez, Hugo Jair Escalante, and Fernando Martinez. 2018. "Evaluation of Detection Approaches for Road Anomalies Based on Accelerometer Readings--Addressing Who's Who." *IEEE Transactions on Intelligent Transportation Systems*.
37. Carr, T. A., M. D. Jenkins, M. I. Iglesias, T. Buggy, and G. Morison. 2018. "Road Crack Detection Using a Single Stage Detector Based Deep Neural Network." in *IEEE EESMS 2018*.

38. Cavanaugh, W. and G. Tocci. 1998. *Environmental Noise the Invisible Pollutant*.
39. Ceylan, Halil, Mustafa Birkan Bayrak, and Kasthurirangan Gopalakrishnan. 2014. "Neural Networks Applications in Pavement Engineering: A Recent Survey." *International Journal of Pavement Research and Technology*.
40. Chai, Mengyu, Zaoxiao Zhang, and Quan Duan. 2018. "A New Qualitative Acoustic Emission Parameter Based on Shannon's Entropy for Damage Monitoring." *Mechanical Systems and Signal Processing*.
41. Chapa, Jorge. 2007. "STUDENT DESIGN TURNS HIGHWAYS INTO WIND FARMS." Retrieved (https://inhabitat.com/student-designs-highway-power/).
42. Chen, Kongyang, Mingming Lu, Xiaopeng Fan, Mingming Wei, and Jinwu Wu. 2011. "Road Condition Monitoring Using On-Board Three-Axis Accelerometer and GPS Sensor." in *Proceedings of the 2011 6th International ICST Conference on Communications and Networking in China, CHINACOM 2011*.
43. Chen, Xiaodan and Hao Wang. 2018. "Life Cycle Assessment of Asphalt Pavement Recycling for Greenhouse Gas Emission with Temporal Aspect." *Journal of Cleaner Production*.
44. Cheng, H. D., Rui Min, and Ming Zhang. 2010. "Automatic Wavelet Base Selection and Its Application to Contrast Enhancement." *Signal Processing*.
45. Choi, Pangil, Dong Ho Kim, Bong Hak Lee, and Moon C. Won. 2016. "Application of Ultrasonic Shear-Wave Tomography to Identify Horizontal Crack or Delamination in Concrete Pavement and Bridge." *Construction and Building Materials*.
46. Chompusri, Yotaka, Kobchai Dejhan, and Surapun Yimman. 2012. "Mother Wavelet Selecting Method for Selective Mapping Technique ECG Compression." in *2012 9th International Conference on Electrical Engineering/Electronics, Computer, Telecommunications and Information Technology, ECTI-CON 2012*.
47. Colorado Department of Transportation, USA. 2015. *Colorado Procedure – Laboratory 5116-10*.
48. Commuri, S., M. Zaman, F. Beainy, D. Singh, M. Nazari, S. Imran, and M. Barman. 2012. *REPORT NO. OT-CREOS11.1-14-F - Pavement Evaluation Using a Portable Lightweight Deflectometer*.
49. Consiglio Nazionale delle Ricerche (CNR). 1992. *CNR B.U. A. XXVI N°146 - 1992*.
50. Covaciu, Dinu, Daniela Florea, and Janos Timar. 2015. "Estimation of the Noise Level Produced by Road Traffic in Roundabouts." *Applied Acoustics*.
51. Darshana Thomas, Edward Wilkie, James Irvine. 2016. "Comparison of Power Consumption of WiFi Inbuilt Internet of Things Device with Bluetooth Low Energy." *International Journal of Computer and Information Engineering* 10(10):1856–59.
52. Dementyev, Artem, Steve Hodges, Stuart Taylor, and Joshua Smith. 2013. "Power Consumption Analysis of Bluetooth Low Energy, ZigBee and ANT Sensor Nodes in a Cyclic Sleep Scenario." in *2013 IEEE International Wireless Symposium, IWS 2013*.
53. Dezfooli, Azin Sadeghi, Fereidoon Moghadas Nejad, Hamzeh Zakeri, and Sholeh Kazemifard. 2017. "Solar Pavement: A New Emerging Technology." *Solar Energy*.
54. Dhakar, Lokesh. 2017. *Triboelectric Devices for Power Generation and Self-Powered Sensing Applications*.
55. Du, Yinfei, Jiaqi Chen, Zheng Han, and Weizheng Liu. 2018. "A Review on Solutions for Improving Rutting Resistance of Asphalt Pavement and Test Methods." *Construction and Building Materials*.
56. Duarte, Francisco and Adelino Ferreira. 2016. "Energy Harvesting on Road Pavements: State of the Art." *Proceedings of the Institution of Civil Engineers - Energy*.
57. ENEA. 2018. "Radiazione Solare Globale Giornaliera Media Mensile Su Superficie Inclinata." Retrieved (http://www.solaritaly.enea.it/CalcRggmmIncl/Calcola1.php).
58. Engineersonline.nl. 2012. "Energie Opwekken Uit Trillingen Wegdek Blijkt Mogelijk." Retrieved (https://www.engineersonline.nl/nieuws/id19397-energie-opwekken-uit-trillingen-wegdek-blijkt-mogelijk.html).
59. Esfandiarpour, Saman (Sam) and Ahmed Shalaby. 2017. "Alternatives for Calibration of Dynamic Modulus Prediction Models of Asphalt Concrete Containing RAP."

International Journal of Pavement Research and Technology.
60. European Union. 2010. "Directive of the European Union 2010/40/EU."
61. Farrar, Charles R. and Keith Worden. 2010. "An Introduction to Structural Health Monitoring." in *CISM International Centre for Mechanical Sciences, Courses and Lectures*.
62. Farris, Ivan, Sara Pizzi, Massimo Merenda, Antonella Molinaro, Riccaro Carotenuto, and Antonio Iera. 2017. "6lo-RFID: A Framework for Full Integration of Smart UHF RFID Tags into the Internet of Things." *IEEE Network*.
63. Fedele R., Praticò F. G., Carotenuto R., and Della Corte F. G. 2017. "Structural Health Monitoring of Pavement Assets through Acoustic Signature." in *BCRRA 2017 (10th International Conference on the Bearing Capacity of Roads, Railways and Airfields)*.
64. Fedele, R., F. G. Della Corte, R. Carotenuto, and F. G. Praticò. 2017. "Sensing Road Pavement Health Status through Acoustic Signals Analysis." in *PRIME 2017 - 13th Conference on PhD Research in Microelectronics and Electronics, Proceedings*.
65. Fedele, R., M. Merenda, F. G. Praticò, R. Carotenuto, and F. G. Della Corte. 2018. "Energy Harvesting for IoT Road Monitoring Systems." *Instrumentation Mesure Metrologie* 17(4):605–23.
66. Fedele, R., F. G. Pratico, R. Carotenuto, and F. G. Della Corte. 2017. "Instrumented Infrastructures for Damage Detection and Management." in *5th IEEE International Conference on Models and Technologies for Intelligent Transportation Systems, MT-ITS 2017 - Proceedings*.
67. Fedele, R., F. G. Praticò, R. Carotenuto, and F. G. Della Corte. 2017. "Damage Detection into Road Pavements through Acoustic Signature Analysis: First Results." in *24th International Congress on Sound and Vibration, ICSV 2017*.
68. Fedele, R., F. G. Praticò, R. Carotenuto, and F. G. Della Corte. 2018. "Energy Savings in Transportation: Setting up an Innovative SHM Method." *Mathematical Modelling of Engineering Problems* 5(4):323–30.
69. Ferroudji, K., N. Benoudjit, M. Bahaz, and A. Bouakaz. 2012. "Selection of a Suitable Mother Wavelet for Microemboli Classification Using SVM and RF Signals." in *ICM 2012, Algiers, Algeria*.
70. FIAT. 2016. "Fiat 500." Retrieved (http://www.omniauto.it/download/fiat-500-scheda-tecnica.pdf%0A).
71. Finn, F., C. L. Saraf, R. Kulkarni, K. Nair, W. Smith, and A. Abdullah. 1986. *Development of Pavement Structural Subsystems*.
72. Gajewski, Jakub and Tomasz Sadowski. 2014. "Sensitivity Analysis of Crack Propagation in Pavement Bituminous Layered Structures Using a Hybrid System Integrating Artificial Neural Networks and Finite Element Method." *Computational Materials Science*.
73. Ganchev, Todor, Mihalis Siafarikas, Iosif Mporas, and Tsenka Stoyanova. 2014. "Wavelet Basis Selection for Enhanced Speech Parametrization in Speaker Verification." *International Journal of Speech Technology*.
74. Gandhi, Tapan, Bijay Ketan Panigrahi, and Sneh Anand. 2011. "A Comparative Study of Wavelet Families for EEG Signal Classification." *Neurocomputing*.
75. Gedafa, Daba S. 2007. *Performance Prediction and Maintenance of Flexible Pavement*.
76. German, Stephanie, Ioannis Brilakis, and Reginald Desroches. 2012. "Rapid Entropy-Based Detection and Properties Measurement of Concrete Spalling with Machine Vision for Post-Earthquake Safety Assessments." in *Advanced Engineering Informatics*.
77. Gosk, Wojciech. 2016. "Stiffness Estimation of the Soil Built-in Road Embankment on the Basis of Light Falling Weight Deflectometer Test." in *Procedia Engineering*.
78. Grace, R. 2015. "Sensors to Support the IoT for Infrastructure Monitoring: Technology and Applications for Smart Transport/Smart Buildings." in *MEPTEC-IoT*.
79. Grauers, Anders and Karthik Upendra. 2016. "Energy Based Method to Analyse Fuel Saving Potential of Hybrid Vehicles for Different Driving Cycles." *IFAC-PapersOnLine*.
80. Guarnaccia, Claudio. 2013. "Advanced Tools for Traffic Noise Modelling and Prediction." *WSEAS Transactions on Systems*.
81. Guo, Lukai and Qing Lu. 2017. "Modeling a New Energy Harvesting Pavement System

with Experimental Verification." *Applied Energy*.
82. Harcourt, Houghton Mifflin, ed. 2011. *The American Heritage Dictionary of the English Language*. Boston.
83. Harjit K.; Rajandeep K. 2017. "A Review on Crack Detection and Parameters Estimation on Road Images." *International Journal for Research in Applied Science & Engineering Technology* 5(2):1–4.
84. Hasni, Hassene, Amir H. Alavi, Karim Chatti, and Nizar Lajnef. 2017. "A Self-Powered Surface Sensing Approach for Detection of Bottom-up Cracking in Asphalt Concrete Pavements: Theoretical/Numerical Modeling." *Construction and Building Materials*.
85. Hassan, N., S. Mathavan, and K. Kamal. 2017. "Road Crack Detection Using the Particle Filter." in *IEEE ICAC 2017*.
86. Hassan, Norhidayah Abdul, Gordon D. Airey, Ramadhansyah Putra Jaya, Nordiana Mashros, and Maniruzzaman A. Aziz. 2014. "A Review of Crumb Rubber Modification in Dry Mixed Rubberised Asphalt Mixtures." *Jurnal Teknologi*.
87. He, Can, Xing Jianchun, and Qiliang Yang. 2014. "Optimal Wavelet Basis Selection for Wavelet Denoising of Structural Vibration Signal." *Applied Mechanics and Materials* 578–579:1059–63.
88. He, Hong, Yonghong Tan, and Yuexia Wang. 2015. "Optimal Base Wavelet Selection for ECG Noise Reduction Using a Comprehensive Entropy Criterion." *Entropy*.
89. He, Shiyong, Bo Liang, Guobing Pan, Feng Wang, and Lulu Cui. 2017. "Influence of Dynamic Highway Tunnel Lighting Environment on Driving Safety Based on Eye Movement Parameters of the Driver." *Tunnelling and Underground Space Technology*.
90. Hebel, G. C. and T. G. Dorbit. 2018. "Road Resurfacing Program." *Harford County, USA*. Retrieved (http://www.harfordcountymd.gov/615/Road-Resurfacing-Program).
91. Heisey, J. S. S., K. H. Stokoe II, A. H. H. Meyer, I. I. Stokoe, A. H. H. Meyer, and others. 1982. "Moduli of Pavement Systems from Spectral Analysis of Surface Waves." *Transportation Research Record*.
92. Hemmati, Farzad, Wasim Orfali, and Mohamed S. Gadala. 2016. "Roller Bearing Acoustic Signature Extraction by Wavelet Packet Transform, Applications in Fault Detection and Size Estimation." *Applied Acoustics*.
93. Hoegh, Kyle, Lev Khazanovich, and H. Yu. 2011. "Ultrasonic Tomography for Evaluation of Concrete Pavements." *Transportation Research Record: Journal of the Transportation Research Board*.
94. Hola, J. and K. Schabowicz. 2010. "State-of-the-Art Non-Destructive Methods for Diagnostic Testing of Building Structures – Anticipated Development Trends." *Archives of Civil and Mechanical Engineering*.
95. Hu, Xiaosong, Yuan Zou, and Yalian Yang. 2016. "Greener Plug-in Hybrid Electric Vehicles Incorporating Renewable Energy and Rapid System Optimization." *Energy*.
96. Huang, Yang Hsien. 2003. *Pavement Analysis and Design*.
97. Hüthwohl, Philipp and Ioannis Brilakis. 2018. "Detecting Healthy Concrete Surfaces." *Advanced Engineering Informatics*.
98. Hyder, Farhan, K. Sudhakar, and Rizalman Mamat. 2018. "Solar PV Tree Design: A Review." *Renewable and Sustainable Energy Reviews*.
99. International Atomic Energy Agency. 2002. *Guidebook on Non-Destructive Testing of Concrete Structures*.
100. Intmensorg.com. 2018. "Turbine Light Concept." Retrieved (http://www.intmensorg.com/science4.htm).
101. Iodice, M., J. Muggleton, and E. Rustighi. 2016. "The Detection of Vertical Cracks in Asphalt Using Seismic Surface Wave Methods." in *Journal of Physics: Conference Series*.
102. ISO. 1997. *ISO 11819-1:1997 Acoustics -- Measurement of the Influence of Road Surfaces on Traffic Noise -- Part 1: Statistical Pass-By Method*.
103. ISO. 1998. *ISO 10534-2:1998 Acoustics -- Determination of Sound Absorption Coefficient and Impedance in Impedance Tubes -- Part 2: Transfer-Function Method*.
104. ISO. 2002. *ISO 13472-1:2002 Acoustics -- Measurement of Sound Absorption Properties of Road Surfaces in Situ -- Part 1: Extended Surface Method*.

105. ISO. 2017. *ISO 11819-2:2017 Acoustics -- Measurement of the Influence of Road Surfaces on Traffic Noise -- Part 2: The Close-Proximity Method*.
106. J. Moubray. 1997. *Reliability-Centered Maintenance "Proactive Maintenance 2: Predictive Tasks."* New York, USA: Ind. Press Inc.
107. Jamshidi, Ali, Kiyofumi Kurumisawa, Toyoharu Nawa, Mao Jize, and Gregory White. 2017. "Performance of Pavements Incorporating Industrial Byproducts: A State-of-the-Art Study." *Journal of Cleaner Production*.
108. Jose, C. Principe, R. Euliano Neil, and W. Curt. 2001. "Neural and Adaptive Systems: Fundamentals Through Simulations." *IEEE Transactions on Neural Networks*.
109. JRC. 2018. "Photovoltaic Geographical Information System - Interactive Maps." Retrieved (http://re.jrc.ec.europa.eu/pvgis/apps4/pvest.php?lang=en&map=europe).
110. Kankar, P. K., Satish C. Sharma, and S. P. Harsha. 2011. "Fault Diagnosis of Ball Bearings Using Continuous Wavelet Transform." in *Applied Soft Computing Journal*.
111. Karlaftis, M. G. and E. I. Vlahogianni. 2011. "Statistical Methods versus Neural Networks in Transportation Research: Differences, Similarities and Some Insights." *Transportation Research Part C: Emerging Technologies*.
112. Kashif Ur Rehman, Sardar, Zainah Ibrahim, Shazim Ali Memon, and Mohammed Jameel. 2016. "Nondestructive Test Methods for Concrete Bridges: A Review." *Construction and Building Materials*.
113. Katicha, Samer Wehbe, Gerardo Flintsch, James Bryce, and Brian Ferne. 2014. "Wavelet Denoising of TSD Deflection Slope Measurements for Improved Pavement Structural Evaluation." *Computer-Aided Civil and Infrastructure Engineering*.
114. Kazem, Hussein A., Tamer Khatib, and K. Sopian. 2013. "Sizing of a Standalone Photovoltaic/Battery System at Minimum Cost for Remote Housing Electrification in Sohar, Oman." *Energy and Buildings*.
115. Kim, Dong Soo and Jin Sun Lee. 2000. "Propagation and Attenuation Characteristics of Various Ground Vibrations." *Soil Dynamics and Earthquake Engineering*.
116. Kim, Hansang and Hani Melhem. 2004. "Damage Detection of Structures by Wavelet Analysis." *Engineering Structures*.
117. Knowles. 2018. *MEMS Microphone (Model: SPM0687LR5H-1)*.
118. Koch, Christian, Kristina Georgieva, Varun Kasireddy, Burcu Akinci, and Paul Fieguth. 2015. "A Review on Computer Vision Based Defect Detection and Condition Assessment of Concrete and Asphalt Civil Infrastructure." *Advanced Engineering Informatics*.
119. Krysinski, Lech and Jacek Sudyka. 2013. "GPR Abilities in Investigation of the Pavement Transversal Cracks." *Journal of Applied Geophysics*.
120. Kulkarni, P. G. and A. D. Sahasrabudhe. 2017. "Investigations on Mother Wavelet Selection for Health Assessment of Lathe Bearings." *International Journal of Advanced Manufacturing Technology*.
121. Kumar, H. S., P. Srinivasa Pai, N. S. Sriram, and G. S. Vijay. 2014. "Selection of Mother Wavelet for Effective Wavelet Transform of Bearing Vibration Signals." *Advanced Materials Research* 1039:169–76.
122. Kumar, Praveen and Efi Foufoula-Georgiou. 1997. "Wavelet Analysis for Geophysical Applications." *Reviews of Geophysics*.
123. Lafarge, B., C. Delebarre, S. Grondel, O. Curea, and A. Hacala. 2015. "Analysis and Optimization of a Piezoelectric Harvester on a Car Damper." in *Physics Procedia*.
124. Lajnef, N., Chatti, K., Chakrabartty, S., Rhimi, M. & Sarkar, P. 2013. *Smart Pavement Monitoring System*.
125. Lamothe, Sébastien, Daniel Perraton, and Hervé Di Benedetto. 2015. "Contraction and Expansion of Partially Saturated Hot Mix Asphalt Samples Exposed to Freeze–thaw Cycles." *Road Materials and Pavement Design*.
126. Lanthaler, Markus and Christian Gütl. 2012. "On Using JSON-LD to Create Evolvable RESTful Services." in *Proceedings of the Third International Workshop on RESTful Design - WS-REST '12*.
127. Lee, Jaeyun and Bumkyoo Choi. 2014. "Development of a Piezoelectric Energy

Harvesting System for Implementing Wireless Sensors on the Tires." *Energy Conversion and Management*.

128. Lenglet, C., J. Blanc, and S. Dubroca. 2017. "Smart Road That Warns Its Network Manager When It Begins Cracking." *The Institution of Engineering and Technology (IET) Intelligent Transport Systems* 11(3):152–57.
129. Li, Fucai, Guang Meng, Kazuro Kageyama, Zhongqing Su, and Lin Ye. 2009. "Optimal Mother Wavelet Selection for Lamb Wave Analyses." *Journal of Intelligent Material Systems and Structures*.
130. Licitra, G., L. Teti, and M. Cerchiai. 2014. "A Modified Close Proximity Method to Evaluate the Time Trends of Road Pavements Acoustical Performances." *Applied Acoustics*.
131. Lin, Shibin, Jeramy C. Ashlock, and R. Christopher Williams. 2016. "Nondestructive Quality Assessment of Asphalt Pavements Based on Dynamic Modulus." *Construction and Building Materials*.
132. Liu, Tao, Xiao Ning Zhang, Zhi Li, and Zhou Quan Chen. 2014. "Research on the Homogeneity of Asphalt Pavement Quality Using X-Ray Computed Tomography (CT) and Fractal Theory." *Construction and Building Materials*.
133. Lonbar, M. S., S. M. Nasrazadani, and A. Shafaghat. 2015. "Investigation of Aggregate and Binder Types Effects on the Microsurfacing Rutting Properties." in *ICICA15 Annual Meeting*.
134. Lu, George and Y. J. Yang. 2017. "Structural Health Monitoring." in *Internet of Things and Data Analytics Handbook*.
135. Maheswaran, R. and Rakesh Khosa. 2012. "Comparative Study of Different Wavelets for Hydrologic Forecasting." *Computers and Geosciences*.
136. Mannion, P. 2018. "Comparing Low-Power Wireless Technologies (Part 1)." *Digi-Key's North American Editors*. Retrieved (https://www.digikey.it/en/articles/techzone/2017/oct/comparing-low-power-wireless-technologies).
137. Marecos, Vânia, Mercedes Solla, Simona Fontul, and Vitor Antunes. 2017. "Assessing the Pavement Subgrade by Combining Different Non-Destructive Methods." *Construction and Building Materials*.
138. Masino, Johannes, Jakob Thumm, Michael Frey, and Frank Gauterin. 2017. "Learning from the Crowd: Road Infrastructure Monitoring System." *Journal of Traffic and Transportation Engineering (English Edition)*.
139. Mathworks. 2006. "Hierarchical Clustering." Retrieved (https://it.mathworks.com/help/stats/hierarchical-clustering.html).
140. Mathworks. 2008. "Wscalogram - Scalogram for Continuous Wavelet Transform." Retrieved (https://it.mathworks.com/help/wavelet/ref/wscalogram.html).
141. Mathworks. 2018a. "Introduction to Wavelet Families." Retrieved (https://it.mathworks.com/help/wavelet/gs/introduction-to-the-wavelet-families.html).
142. Mathworks. 2018b. "Mathworks - Wavedec." Retrieved (https://it.mathworks.com/help/wavelet/ref/wavedec.html).
143. Megahed, A. I., A. Monem Moussa, H. B. Elrefaie, and Y. M. Marghany. 2008. "Selection of a Suitable Mother Wavelet for Analyzing Power System Fault Transients." in *IEEE Power and Energy Society 2008 General Meeting: Conversion and Delivery of Electrical Energy in the 21st Century, PES*.
144. Mekki, Kais, Eddy Bajic, Frederic Chaxel, and Fernand Meyer. 2018. "A Comparative Study of LPWAN Technologies for Large-Scale IoT Deployment." *ICT Express*.
145. Merenda, M., Felini, C., Della Corte, F. G. 2016. "An Autonomous and Energy Efficient Smart Sensor Platform." Pp. 1208–11 in *IEEE Sensors 2014*. art. no. 6985226.
146. Microchip. 2018. *Microcontroller - Model: ATSAMD20E17*.
147. Miraliakbari, A., M. Hahn, and H. G. Maas. 2014. "Development of a Multi-Sensor System for Road Condition Mapping." in *International Archives of the Photogrammetry, Remote Sensing and Spatial Information Sciences - ISPRS Archives*.

148. Moghadas Nejad, Fereidoon and Hamzeh Zakeri. 2011. "An Expert System Based on Wavelet Transform and Radon Neural Network for Pavement Distress Classification." *Expert Systems with Applications*.
149. Moghaddam, Taher Baghaee, Mohamed Rehan Karim, and Mahrez Abdelaziz. 2011. "A Review on Fatigue and Rutting Performance of Asphalt Mixes." *Scientific Research and Essays*.
150. Morgan, P. A. and G. R. Watts. 2003. "A Novel Approach to the Acoustic Characterisation of Porous Road Surfaces." *Applied Acoustics*.
151. Moriarty, Patrick and Stephen Jia Wang. 2017. "Could Automated Vehicles Reduce Transport Energy?" in *Energy Procedia*.
152. Morova, N., S. Serin, S. Terzi, and M. Saltan. 2013. "Prediction of the Pavement Serviceability Ratio of Rigid Highway Pavements by Artificial Neural Networks." *Journal of Advanced Technology Sciences* 2(1):12–25.
153. Morsi, Walid G. and M. E. El-Hawary. 2008. "The Most Suitable Mother Wavelet for Steady-State Power System Distorted Waveforms." in *Canadian Conference on Electrical and Computer Engineering*.
154. Mounier, Damien, Hervé Di Benedetto, and Cédric Sauzéat. 2012. "Determination of Bituminous Mixtures Linear Properties Using Ultrasonic Wave Propagation." *Construction and Building Materials*.
155. Mubaraki, Muhammad. 2016. "Highway Subsurface Assessment Using Pavement Surface Distress and Roughness Data." *International Journal of Pavement Research and Technology*.
156. Muench, S. T., J. P. Mahoney, and L. M. Pierce. 2003. "The WSDOT Pavement Guide Interactive."
157. Nair, K. Krishnan and Anne S. Kiremidjian. 2009. "Derivation of a Damage Sensitive Feature Using the Haar Wavelet Transform." *Journal of Applied Mechanics*.
158. National Center for Pavement Preservation (NCPP). 2018. "Pavement Deterioration Curve." Retrieved (http://images.slideplayer.com/35/10456260/slides/slide_34.jpg).
159. Nazarko, Joanicjusz, Piotr Radziszewski, Katarzyna Dębkowska, Joanna Ejdys, Alicja Gudanowska, Katarzyna Halicka, Jarosław Kilon, Anna Kononiuk, Karol J. Kowalski, Jan B. Król, Łukasz Nazarko, Michał Sarnowski, and Tatjana Vilutiene. 2015. "Foresight Study of Road Pavement Technologies." in *Procedia Engineering*.
160. Ngui, Wai Keng, M. Salman Leong, Lim Meng Hee, and Ahmed M. Abdelrhman. 2013. "Wavelet Analysis: Mother Wavelet Selection Methods." *Applied Mechanics and Materials*.
161. Nguyen, Sy Tuan, Quy Dong To, and Minh Ngoc Vu. 2017. "Extended Analytical Solutions for Effective Elastic Moduli of Cracked Porous Media." *Journal of Applied Geophysics*.
162. Nozarian, M. M. and A. Esfandiari. 2008. "Structural Damage Identification Using Frequency Response Function." in *Materials Forum*.
163. O'Kelly, Noel. 2016. "Use of Machine Learning Technology in the Diagnosis of Alzheimer's Disease." Dublin City University.
164. Oliveira, Henrique and Paulo Lobato Correia. 2013. "Automatic Road Crack Detection and Characterization." *IEEE Transactions on Intelligent Transportation Systems*.
165. Ooms Avenhorn Holding BV. 2003. "Solar Roadway." Retrieved (https://www.restreets.org/case-studies/solar-roadway).
166. Oregon Embedded. 2018. "Battery Life Calculator."
167. Ouma, Yashon O. and M. Hahn. 2017. "Pothole Detection on Asphalt Pavements from 2D-Colour Pothole Images Using Fuzzy c-Means Clustering and Morphological Reconstruction." *Automation in Construction*.
168. Ouma, Yashon O. and Michael Hahn. 2016. "Wavelet-Morphology Based Detection of Incipient Linear Cracks in Asphalt Pavements from RGB Camera Imagery and Classification Using Circular Radon Transform." *Advanced Engineering Informatics*.
169. Ow, L. F. and S. Ghosh. 2017. "Technical Note Urban Cities and Road Traffic Noise: Reduction through Vegetation." *Applied Acoustics* 120:15–20.
170. Pahlavan, Lotfollah, Mariana M. Mota, and Gerrit Blacquière. 2016. "Influence of

Asphalt on Fatigue Crack Monitoring in Steel Bridge Decks Using Guided Waves." *Construction and Building Materials*.

171. Pal, Sukhomay, P. Stephan Heyns, Burkhard H. Freyer, Nico J. Theron, and Surjya K. Pal. 2011. "Tool Wear Monitoring and Selection of Optimum Cutting Conditions with Progressive Tool Wear Effect and Input Uncertainties." *Journal of Intelligent Manufacturing*.
172. Pan, Pan, Shaopeng Wu, Yue Xiao, and Gang Liu. 2015. "A Review on Hydronic Asphalt Pavement for Energy Harvesting and Snow Melting." *Renewable and Sustainable Energy Reviews*.
173. Papagiannakis, A. T., S. Dessouky, A. Montoya, and H. Roshani. 2016. "Energy Harvesting from Roadways." in *Procedia Computer Science*.
174. Papagiannakis, A. T. and E. A. Masad. 2012. *Pavement Design and Materials*.
175. Pavementinteractive.org. 2018. "Pavement Distresses." Retrieved (https://www.pavementinteractive.org/reference-desk/pavement-management/pavement-distresses/).
176. Pedret Rodés, J., V. Pérez-Gracia, and A. Martínez-Reguero. 2015. "Evaluation of the GPR Frequency Spectra in Asphalt Pavement Assessment." *Construction and Building Materials*.
177. Peng, Bo, Xueyong Fan, Xunjie Wang, and Wenying Li. 2017. "Key Steps of Carbon Emission and Low-Carbon Measures in the Construction of Bituminous Pavement." *International Journal of Pavement Research and Technology*.
178. Perles, Angel, Eva Pérez-Marín, Ricardo Mercado, J. Damian Segrelles, Ignacio Blanquer, Manuel Zarzo, and Fernando J. Garcia-Diego. 2018. "An Energy-Efficient Internet of Things (IoT) Architecture for Preventive Conservation of Cultural Heritage." *Future Generation Computer Systems*.
179. Pitoňák, Martin and Ján Filipovsky. 2016. "GPR Application - Non-Destructive Technology for Verification of Thicknesses of Newly Paved Roads in Slovakia." in *Procedia Engineering*.
180. Pokorski, Piotr, Piotr Radziszewski, and Michał Sarnowski. 2016. "Fatigue Life of Asphalt Pavements on Bridge Decks." in *Procedia Engineering*.
181. Pop, Mădălin-Dorin and Octavian Proştean. 2018. "A Comparison Between Smart City Approaches in Road Traffic Management." *Procedia - Social and Behavioral Sciences*.
182. Porubiaková, Andrea, Michal Grinč, and Martin Slabej. 2014. "Non-Invasive and Effective Method of the Pavement Investigation: Ground Penetrating Radar." in *Procedia Engineering*.
183. Posenato, Daniele, Francesca Lanata, Daniele Inaudi, and Ian F. C. Smith. 2008. "Model-Free Data Interpretation for Continuous Monitoring of Complex Structures." *Advanced Engineering Informatics*.
184. Poulikakos, L. D., C. Papadaskalopoulou, B. Hofko, F. Gschösser, A. Cannone Falchetto, M. Bueno, M. Arraigada, J. Sousa, R. Ruiz, C. Petit, M. Loizidou, and M. N. Partl. 2017. "Harvesting the Unexplored Potential of European Waste Materials for Road Construction." *Resources, Conservation and Recycling*.
185. Prasad, Pratiksha R. 2018. "BLE vs Wi-Fi: Which Is Better for IoT Product Development?" Retrieved (https://www.cabotsolutions.com/2018/02/ble-vs-wi-fi-which-is-better-for-iot-product-development).
186. Praticò, F. G., F. G. Della Corte, and M. Merenda. 2016. "Self-Powered Sensors for Road Pavements." in *Functional Pavement Design - Proceedings of the 4th Chinese-European Workshop on Functional Pavement Design, CEW 2016*.
187. Praticò, F. G., A. Moro, and R. Ammendola. 2009. "Factors Affecting Variance and Bias of Non-Nuclear Density Gauges for PEM and DGFC." *The Baltic Journal of Road and Bridge Engineering* 4(3):99–107.
188. Praticò, F. G., A. Moro, S. Noto, and G. Colicchio. 2016. "Three-Year Investigation on Hot and Cold Mixes with Rubber." in *8th International Conference on Maintenance and Rehabilitation of Pavements, MAIREPAV 2016*.
189. Praticò, F. G. and R. Vaiana. 2013. "A Study on Volumetric versus Surface Properties of Wearing Courses." *Construction and Building Materials*.

190. Praticò, F. G. and R. Vaiana. 2015. "A Study on the Relationship between Mean Texture Depth and Mean Profile Depth of Asphalt Pavements." *Construction and Building Materials*.
191. Praticò, F. G., R. Vaiana, and R. Fedele. 2015. "A Study on the Dependence of PEMs Acoustic Properties on Incidence Angle." *International Journal of Pavement Engineering* 16(7).
192. Praticò, F. G., R. Vaiana, M. Giunta, T. Iuele, and A. Moro. 2013. *Recycling PEMs Back to TLPAs: Is That Possible notwithstanding RAP Variability?*
193. Praticó, Filippo Giammaria. 2011. *QA/QC in Transport Infrastructures: Issues and Perspectives, Modern Approaches To Quality Control*. Ahmed Badr.
194. Qin, Li, Lili Dong, Wenhai Xu, Lidong Zhang, Qiubo Yan, and Xiaodong Chen. 2017. "A 'Vehicle in, Light Brightens; Vehicle out, Light Darkens' Energy-Saving Control System of Highway Tunnel Lighting." *Tunnelling and Underground Space Technology*.
195. Qureshi, H., R. Wilson, and N. Rajpoot. 2008. "Optimal Wavelet Basis for Wavelet Packets Based Meningioma Subtype Classification." in *MIUA 2008, Dundee, Scotland*.
196. Raab, Christiane, Ingrid Camargo, and Manfred N. Partl. 2017. "Ageing and Performance of Warm Mix Asphalt Pavements." *Journal of Traffic and Transportation Engineering (English Edition)*.
197. Radopoulou, Stefania C. and Ioannis Brilakis. 2016. "Improving Road Asset Condition Monitoring." in *Transportation Research Procedia*.
198. Rafiee, J., M. A. Rafiee, N. Prause, and M. P. Schoen. 2011. "Wavelet Basis Functions in Biomedical Signal Processing." *Expert Systems with Applications*.
199. Rafiee, J., M. A. Rafiee, and P. W. Tse. 2010. "Application of Mother Wavelet Functions for Automatic Gear and Bearing Fault Diagnosis." *Expert Systems with Applications*.
200. Rafiee, J. and P. W. Tse. 2009. "Use of Autocorrelation of Wavelet Coefficients for Fault Diagnosis." *Mechanical Systems and Signal Processing*.
201. Rafiee, J., P. W. Tse, A. Harifi, and M. H. Sadeghi. 2009. "A Novel Technique for Selecting Mother Wavelet Function Using an Intelli Gent Fault Diagnosis System." *Expert Systems with Applications*.
202. Rahman, A. S. M. A., Rafiqul A., and Tarefder. 2016. "Dynamic Modulus and Phase Angle of Warm-Mix versus Hot-Mix Asphalt Concrete." *Construction and Building Materials*.
203. Reda Taha, M. M., A. Noureldin, J. L. Lucero, and T. J. Baca. 2006. "Wavelet Transform for Structural Health Monitoring: A Compendium of Uses and Features." *Structural Health Monitoring*.
204. Rodrigues, A. P., Grynal D'Mello, and Pai Srinivasa. 2016. "Selection of Mother Wavelet for Wavelet Analysis of Vibration Signals in Machining." *Journal of Mechanical Engineering and Automation* 6(5A):81–85.
205. RPB HealTec, Review of highway standards and manuals, Deliverable D9. 2. 2016. *Road Pavements and Bridge Deck Health Monitoring/Early Warning Using Advanced Inspec-Tion Technologies*.
206. Ryden, Nils and Michael A. Mooney. 2009. "Analysis of Surface Waves from the Light Weight Deflectometer." *Soil Dynamics and Earthquake Engineering*.
207. Saadona, Salem and Sideka Othman. 2015. "Micro-Electro-Mechanical System (MEMS)-Based Piezoelectric Energy Harvester for Ambient Vibrations." *Procedia - Social and Behavioral Sciences* 195:2353 – 2362.
208. Saboonchi, Hossain, Didem Ozevin, and Minoo Kabir. 2016. "MEMS Sensor Fusion: Acoustic Emission and Strain." *Sensors and Actuators, A: Physical*.
209. Saikar, Anurag, Mihir Parulekar, Aditya Badve, Sagar Thakkar, and Aaradhana Deshmukh. 2017. "TrafficIntel: Smart Traffic Management for Smart Cities." in *2017 International Conference on Emerging Trends and Innovation in ICT, ICEI 2017*.
210. Saito, Naoki. 1994. "Simultaneous Noise Suppression and Signal Compression Using a Library of Orthonormal Bases and the Minimum Description Length Criterion." *Wavelet Analysis and Its Applications*.

211. Salman, M., S. Mathavan, K. Kamal, and M. Rahman. 2013. "Pavement Crack Detection Using the Gabor Filter." in *IEEE Conference on Intelligent Transportation Systems, Proceedings, ITSC*.
212. Sandberg, U. and J. A. Ejsmond. 2002. *Tyre/Road Noise Reference Book*.
213. Saraswathy, J., M. Hariharan, Thiyagar Nadarajaw, Wan Khairunizam, and Sazali Yaacob. 2014. "Optimal Selection of Mother Wavelet for Accurate Infant Cry Classification." *Australasian Physical and Engineering Sciences in Medicine*.
214. Scarpati, W. and J. Guerra. 2013. "Investing in Pavement Management Can Improve Roads, Save Money." vol. 27, N. 2, pp. 22–25.
215. Schnebele, E., B. F. Tanyu, G. Cervone, and N. Waters. 2015. "Review of Remote Sensing Methodologies for Pavement Management and Assessment." *European Transport Research Review*.
216. Schubert, E. and J. Wolfe. 2006. "Timbral Brightness and Spectral Centroid." *Acta Acustica United with Acustica* 92:820–825.
217. Seljuq, Usman, Faraz Himayun, and Haroon Rasheed. 2014. "Selection of an Optimal Mother Wavelet Basis Function for ECG Signal Denoising." in *17th IEEE International Multi Topic Conference: Collaborative and Sustainable Development of Technologies, IEEE INMIC 2014 - Proceedings*.
218. Selvi, P. 2015. "Fatigue and Rutting Strain Analysis on Lime Stabilized Subgrades to Develop a Pavement Design Chart." *Transportation Geotechnics*.
219. Sheerin Sitara, N., S. Kavitha, and G. Raghuraman. 2018. "Review and Analysis of Crack Detection and Classification Techniques Based on Crack Types." *International Journal of Applied Engineering Research*.
220. Shi, Arthur and Xiao-Hua Yu. 2012. "Structural Damage Detection Using Artificial Neural Networks and Wavelet Transform." in *2012 IEEE International Conference on Computational Intelligence for Measurement Systems and Applications (CIMSA) Proceedings*.
221. Shoaib, Muhammad, Asaad Y. Shamseldin, and Bruce W. Melville. 2014. "Comparative Study of Different Wavelet Based Neural Network Models for Rainfall–runoff Modeling." *Journal of Hydrology* 515:47–58.
222. Siekmeier, John, Cassandra Pinta, Scott Merth, Jensen Julie, Peter Davich, Felipe Camargo, and Matthew Beyer. 2009. "Using the Dynamic Cone Penetrometer and Light Weight Deflectometer for Construction Quality Assurance." *Minnesota Department of Transportation*.
223. Silva, D. 2016. "World's First Solar Road Opens in Normandy, France." *NBC NEWS*.
224. Singh, Brij N. and Arvind K. Tiwari. 2006. "Optimal Selection of Wavelet Basis Function Applied to ECG Signal Denoising." *Digital Signal Processing: A Review Journal*.
225. Sinha, Rashmi Sharan, Yiqiao Wei, and Seung Hoon Hwang. 2017. "A Survey on LPWA Technology: LoRa and NB-IoT." *ICT Express*.
226. Sivakumar Babu, G. L., Sireesh Saride, and B. Munwar Basha. 2016. *Sustainability Issues in Civil Engineering*. Springer.
227. Smadi, O. 2004. "Quantifying the Benefits of Pavement Management." *Methodology*.
228. Smarsly, Kay and Kincho H. Law. 2013. "A Migration-Based Approach towards Resource-Efficient Wireless Structural Health Monitoring." *Advanced Engineering Informatics*.
229. Soenen, Hilde, Per Redelius, and Chantal De La Roche. 2003. "Fatigue Behaviour of Bituminous Materials: From Binders to Mixes." *Road Materials and Pavement Design*.
230. Solanki, Pranshoo and Musharraf Zaman. 2017. "Design of Semi-Rigid Type of Flexible Pavements." *International Journal of Pavement Research and Technology*.
231. Solla, M., S. Lagüela, H. González-Jorge, and P. Arias. 2014. "Approach to Identify Cracking in Asphalt Pavement Using GPR and Infrared Thermographic Methods: Preliminary Findings." *NDT and E International*.
232. Springfield Department of Public Work. 2009. "Pavement Life Curve." Retrieved (https://www.springfield-ma.gov/dpw/index.php?id=121).
233. STMicroelecronics. 2018a. "MEMS 3D Accelerometer and Gyroscope." Retrieved (https://www.st.com/resource/en/datasheet/lsm6ds3.pdf).

234. STMicroelecronics. 2018b. "MEMS Temperature and Humidity." Retrieved (https://www.st.com/resource/en/datasheet/hts221.pdf).
235. Subirats, Peggy, Jean Dumoulin, Vincent Legeay, and Dominique Barba. 2006. "Automation of Pavement Surface Crack Detection Using the Continuous Wavelet Transform." in *Proceedings - International Conference on Image Processing, ICIP*.
236. Taha, Mohd Raihan, Sentot Hardwiyono, Nur Izzi Md Yusoff, Mohd Rosli Hainin, Jiantao Wu, and Khairul Anuar Mohd Nayan. 2013. "Study of the Effect of Temperature Changes on the Elastic Modulus of Flexible Pavement Layers." *Research Journal of Applied Sciences, Engineering and Technology*.
237. Technology, Federal Highway Administration Research and. 2013. *FHWA-HRT-13-038*.
238. Tedeschi, A. and F. Benedetto. 2017. "A Real-Time Automatic Pavement Crack and Pothole Recognition System for Mobile Android-Based Devices." *Advanced Engineering Informatics*.
239. Tong, Zheng, Jie Gao, and Haitao Zhang. 2017. "Recognition, Location, Measurement, and 3D Reconstruction of Concealed Cracks Using Convolutional Neural Networks." *Construction and Building Materials*.
240. Tosti, Fabio, Luca Bianchini Ciampoli, Fabrizio D'Amico, Amir M. Alani, and Andrea Benedetto. 2018. "An Experimental-Based Model for the Assessment of the Mechanical Properties of Road Pavements Using Ground-Penetrating Radar." *Construction and Building Materials*.
241. Tsui, Patrick P. C. and Otman A. Basir. 2006. "Wavelet Basis Selection and Feature Extraction for Shift Invariant Ultrasound Foreign Body Classification." *Ultrasonics*.
242. Uddin, W. 2014. "An Overview of GPR Applications for Evaluation of Pavement Thickness and Cracking." in *15th International Conference on Ground Penetrating Radar - GPR 2014*.
243. UNI. 2007a. *UNI EN 12697-22:2007 Miscele Bituminose - Metodi Di Prova per Conglomerati Bituminosi a Caldo - Parte 22: Metodo Della Traccia Delle Ruote (Wheel Tracking)*.
244. UNI. 2007b. *UNI EN 12697-33:2007 - Miscele Bituminose - Metodi Di Prova per Conglomerati Bituminosi a Caldo - Parte 33: Provino Preparato Con Compattatore a Rullo*.
245. UNI. 2016. *UNI EN 12697-35:2016 - Miscele Bituminose - Metodi Di Prova - Parte 35: Miscelazione in Laboratorio*.
246. Vakharia, V., V. K. Gupta, and P. K. Kankar. 2017. "Efficient Fault Diagnosis of Ball Bearing Using ReliefF and Random Forest Classifier." *Journal of the Brazilian Society of Mechanical Sciences and Engineering*.
247. Vanderhawk Consulting LLC. 2011. "Road Maintenance Philosophy: Best First vs. Worst First." Retrieved (http://vanderhawk.net).
248. Vasudevan, R., A. Ramalinga Chandra Sekar, B. Sundarakannan, and R. Velkennedy. 2012. "A Technique to Dispose Waste Plastics in an Ecofriendly Way - Application in Construction of Flexible Pavements." *Construction and Building Materials*.
249. Vitillo, N. 2018. *Pavement Management Systems*.
250. Vujnovic, Sanja, Zeljko Djurovic, and Goran Kvascev. 2016. "Fan Mill State Estimation Based on Acoustic Signature Analysis." *Control Engineering Practice*.
251. Wang, T., Gopalakrishnan, K., Smadi, O. Somani, A. K. 2018. "Automated Shape-Based Pavement Crack Detection Approach." *Transportation* 33(3):598–608.
252. Wang, Chao, Lei Xue, Wei Xie, Zhanping You, and Xu Yang. 2018. "Laboratory Investigation on Chemical and Rheological Properties of Bio-Asphalt Binders Incorporating Waste Cooking Oil." *Construction and Building Materials*.
253. Wang, Deng, Duoqian Miao, and Chen Xie. 2011. "Best Basis-Based Wavelet Packet Entropy Feature Extraction and Hierarchical EEG Classification for Epileptic Detection." *Expert Systems with Applications*.
254. Wang, Hao, Abbas Jasim, and Xiaodan Chen. 2018. "Energy Harvesting Technologies in Roadway and Bridge for Different Applications – A Comprehensive Review." *Applied Energy*.
255. Wang, Haopeng, Jun Yang, Hui Liao, and Xianhua Chen. 2016. "Electrical and

Mechanical Properties of Asphalt Concrete Containing Conductive Fibers and Fillers." *Construction and Building Materials*.

256. Wang, Liang and Tommy H. T. Chan. 2009. "Review of Vibration-Based Damage Detection and Condition Assessment of Bridge Structures Using Structural Health Monitoring." in *Proc 2nd Infrastructure Theme Postgrad Conf*.
257. Wang, T., K. Gopalakrishnan, A. Somani, O. Smadi, and H. Ceylan. 2016. *Machine-Vision-Based Roadway Health Monitoring and Assessment: Development of a Shape-Based Pavement-Crack-Detection Approach*.
258. Wang, Tao, Feipeng Xiao, Xingyi Zhu, Baoshan Huang, Jingang Wang, and Serji Amirkhanian. 2018. "Energy Consumption and Environmental Impact of Rubberized Asphalt Pavement." *Journal of Cleaner Production*.
259. Wang, V. S., Ei Wen Lo, Chih Hsiang Liang, Keh Ping Chao, Bo Ying Bao, and Ta Yuan Chang. 2016. "Temporal and Spatial Variations in Road Traffic Noise for Different Frequency Components in Metropolitan Taichung, Taiwan." *Environmental Pollution*.
260. Wang, Xianglong and Zhaozheng Hu. 2017. "Grid-Based Pavement Crack Analysis Using Deep Learning." in *2017 4th International Conference on Transportation Information and Safety, ICTIS 2017 - Proceedings*.
261. Wang, Y., S. J. Chen, S. J. Liu, and H. X. Hu. 2016. "Best Wavelet Basis for Wavelet Transforms in Acoustic Emission Signals of Concrete Damage Process." *Russian Journal of Nondestructive Testing* 52(3):125–133.
262. Wenlong, Sun, Chen Xiaokai, and Wang Lu. 2016. "Analysis of Energy Saving and Emission Reduction of Vehicles Using Light Weight Materials." in *Energy Procedia*.
263. Wijaya, Dedy Rahman, Riyanarto Sarno, and Enny Zulaika. 2017. "Information Quality Ratio as a Novel Metric for Mother Wavelet Selection." *Chemometrics and Intelligent Laboratory Systems*.
264. Wilberforce, Tabbi, Zaki El-Hassan, F. N. Khatib, Ahmed Al Makky, Ahmad Baroutaji, James G. Carton, and Abdul G. Olabi. 2017. "Developments of Electric Cars and Fuel Cell Hydrogen Electric Cars." *International Journal of Hydrogen Energy*.
265. Woods, R. D. and LP. Jedele. 1985. "Energy Attenuation Relationships from Construction Vibrations." *ASCE Convention* 229–46.
266. Worden, Keith, Charles R. Farrar, Graeme Manson, and Gyuhae Park. 2007. "The Fundamental Axioms of Structural Health Monitoring." *Proceedings of the Royal Society A: Mathematical, Physical and Engineering Sciences*.
267. Wright, D. 2014. *Monitoring Structural and Surface Conditions*.
268. Wulandari, Paravita Sri and Daniel Tjandra. 2017. "Use of Crumb Rubber as an Additive in Asphalt Concrete Mixture." in *Procedia Engineering*.
269. Xiang, Bo, Xiaoling Cao, Yanping Yuan, Liangliang Sun, Hongwei Wu, and Fariborz Haghighat. 2018. "A Novel Hybrid Energy System Combined with Solar-Road and Soil-Regenerator: Dynamic Model and Operational Performance." *Energy Conversion and Management*.
270. Xiong, Haocheng and Linbing Wang. 2016. "Piezoelectric Energy Harvester for Public Roadway: On-Site Installation and Evaluation." *Applied Energy*.
271. Xu, Xiaochen, Dongwei Cao, Hailu Yang, and Ming He. 2018. "Application of Piezoelectric Transducer in Energy Harvesting in Pavement." *International Journal of Pavement Research and Technology*.
272. Yan, R. 2007. "Base Wavelet Selection Criteria for Non-Stationary Vibration Analysis in Bearing Health Diagnosis." UMass Amherst.
273. Yan, R. and R. X. Gao. 2009. "Base Wavelet Selection for Bearing Vibration Signal Analysis." *Int. J. Wavel. Multiresol. Inform. Proces.* 7(4):411–426.
274. Yang, Hailu, Linbing Wang, Bin Zhou, Ya Wei, and Qian Zhao. 2018. "A Preliminary Study on the Highway Piezoelectric Power Supply System." *International Journal of Pavement Research and Technology*.
275. Yang, L., M. D. Judd, and C. J. Bennoch. 2004. "Denoising UHF Signal for PD Detection in Transformers Based on Wavelet Technique." in *Conference on Electrical*

Insulation and Dielectric Phenomena.
276. Yang, S. 2014. "Health Monitoring of Pavement Systems Using Smart Sensing Technologies."
277. Yang, Shih Hsien and Try Suciptan. 2016. "Rheological Behavior of Japanese Cedar-Based Biobinder as Partial Replacement for Bituminous Binder." *Construction and Building Materials*.
278. Yi, Chih Wei, Yi Ta Chuang, and Chia Sheng Nian. 2015. "Toward Crowdsourcing-Based Road Pavement Monitoring by Mobile Sensing Technologies." *IEEE Transactions on Intelligent Transportation Systems*.
279. Yoomak, Suntiti and Atthapol Ngaopitakkul. 2018. "Optimisation of Lighting Quality and Energy Efficiency of LED Luminaires in Roadway Lighting Systems on Different Road Surfaces." *Sustainable Cities and Society*.
280. Yousaf, Muhammad Haroon, Kanza Azhar, Fiza Murtaza, and Fawad Hussain. 2018. "Visual Analysis of Asphalt Pavement for Detection and Localization of Potholes." *Advanced Engineering Informatics*.
281. Yousuf, M.; Morton, T. 2014. *Use of Vehicle Noise for Roadways, Bridge, and Infrastructure Health Monitoring*.
282. Yu, Yan, Xuefeng Zhao, Yan Shi, and Jinping Ou. 2013. "Design of a Real-Time Overload Monitoring System for Bridges and Roads Based on Structural Response." *Measurement: Journal of the International Measurement Confederation*.
283. Zalama, Eduardo, Jaime Gómez-García-Bermejo, Roberto Medina, and José Llamas. 2014. "Road Crack Detection Using Visual Features Extracted by Gabor Filters." *Computer-Aided Civil and Infrastructure Engineering*.
284. Zang, C., M. I. Friswell, and M. Imregun. 2004. "Structural Damage Detection Using Independent Component Analysis." *Structural Health Monitoring*.
285. Zelelew, H. M., A. T. Papagiannakis, and E. D. De León Izeppi. 2013. "Pavement Macro-Texture Analysis Using Wavelets." *International Journal of Pavement Engineering*.
286. Zhang, Lei, Paul Bao, and Xiaolin Wu. 2005. "Multiscale LMMSE-Based Image Denoising with Optimal Wavelet Selection." *IEEE Transactions on Circuits and Systems for Video Technology*.
287. Zhang, Y., C. Chen, Q. Wu, Q. Lu, S. Zhang, G. Zhang, and Y. Yang. 2018. "A Kinect-Based Approach for 3D Pavement Surface Reconstruction and Cracking Recognition." *IEEE Transaction on Intelligent Transportation Systems* in press.
288. Zhao, J., J. N. Ivan, and J. T. DeWolf. 1998. "Structural Damage Detection Using Artificial Neural Networks." *Journal of Infrastructure Systems*.
289. Zheng, Chunhua, Guoqing Xu, Kun Xu, Zhongming Pan, and Quan Liang. 2015. "An Energy Management Approach of Hybrid Vehicles Using Traffic Preview Information for Energy Saving." *Energy Conversion and Management*.
290. Zheng, Zuduo and Simon Washington. 2012. "On Selecting an Optimal Wavelet for Detecting Singularities in Traffic and Vehicular Data." *Transportation Research Part C: Emerging Technologies*.
291. Zhou, Zhi, Wanqiu Liu, Ying Huang, Huaping Wang, He Jianping, Minghua Huang, and Ou Jinping. 2012. "Optical Fiber Bragg Grating Sensor Assembly for 3D Strain Monitoring and Its Case Study in Highway Pavement." *Mechanical Systems and Signal Processing*.

Scientific production

1. Scientific production – already present on Scopus

1.1. Fedele, R., Della Corte, F.G., Carotenuto, R., and Praticò, F.G. 2017. Sensing road pavement health status through acoustic signals analysis. Presented at PRIME 2017 (13th Conference on PhD Research in Microelectronics and Electronics), 12-15 June 2017, Giardini Naxos – Taormina, Italy. Proceedings 7974133, pp. 165-168. DOI: 10.1109/PRIME.2017.7974133.

1.2. Fedele, R., Praticò, F.G., Carotenuto, R., and Della Corte, F.G. 2017. Damage detection into road pavements through acoustic signature analysis: First results. Presented at ICSV 2017 (24th International Congress on Sound and Vibration), 23-27 July 2017, London, UK.

1.3. Fedele, R., Pratico, F.G., Carotenuto, R., and Della Corte, F. G. 2017. Instrumented infrastructures for damage detection and management. Presented at MT-ITS 2017 (5th IEEE International Conference on Models and Technologies for Intelligent Transportation Systems), 29-28 June 2017, Naples, Italy. Proceedings 8005729, pp. 526-531. DOI: 10.1109/MTITS.2017.8005729.

1.4. Praticò, F.G., Fedele, R., and Vizzari, D. 2017. Significance and reliability of absorption spectra of quiet pavements. Construction and Building Materials, Vol. 140, pp. 274-281. DOI: 10.1016/j.conbuildmat.2017.02.130.

1.5. Praticò, F.G., Vizzari, D., and Fedele, R. 2017. Estimating the resistivity and tortuosity of a road pavement using an inverse problem approach. Presented at ICSV 2017 (24th International Congress on Sound and Vibration), 23-27 July 2017, London, UK.

1.6. Praticò, F.G., Vaiana, R., and Fedele, R. 2015. A study on the dependence of PEMs acoustic properties on incidence angle. International Journal of Pavement Engineering, Vol. 16, No. 7, pp. 632-645. DOI: 10.1080/10298436.2014.943215.

1.7. Fedele R., Praticò F. G., Carotenuto R., and Della Corte F. G. Structural health monitoring of pavement assets through acoustic signature. Presented at the conference BCRRA 2017 (10th International Conference on the Bearing Capacity of Roads, Railways and Airfields), 28-30 June 2017, Atene, Greece. DOI: 10.1201/9781315100333-127.

1.8. Fedele R., Merenda M., Praticò F. G., Carotenuto R., and Della Corte F. G. 2018. Energy harvesting for IoT road monitoring systems. Instrumentation Mesure Metrologie. Vol. 17, No. 4, pp. 605-623. DOI: 10.3166/I2M.17.605-623

1.9. Fedele R., Praticò F. G., Carotenuto R., and Della Corte F. G. 2018. Energy savings in transportation: setting up an innovative SHM method. Mathematical Modelling of Engineering Problems, Vol. 5, No. 4, pp. 323-330. DOI: 10.18280/mmep.050408.

2. Scientific production – proceeding of international conferences/meetings

2.1. Praticò F.G., Fedele R., and Vizzari D. A comprehensive study on the precision and accuracy of in/lab and on/site measurement of pavement acoustic absorption. Presented at TRB 2017 (96th Annual Meeting of Transportation Research Board), 8–12 January 2017, Washington D.C., USA.

3. Scientific production – submitted to Journals and Conferences

3.1. Fedele R., Praticò F.G., Carotenuto R., Della Corte F.G., and Vizzari D. A novel approach for the monitoring of road infrastructure performance. Presented at ADC40 (Transportation Research Board ADC40 Transportation-Related Noise + Vibration Committee, Summer Meeting), 23-26 July 2017, Minneapolis, Minnesota, USA.

3.2. Fedele R., Praticò F.G., Carotenuto R., Della Corte F.G. Intelligent road pavements monitoring through acoustic signature. Submitted to the Journal IEEE Transaction on Intelligent Transportation System in January 2018.

3.3. Praticò F.G., Fedele R., Merenda M., Carotenuto R., and Della Corte F. G. Real-time decision platform for the management of structures and infrastructures in theme parks. Submitted to the Journal NDT & E International in January 2018.

3.4. Fedele R., Praticò F.G., Carotenuto R., Della Corte F.G. Structural health monitoring of road pavements using acoustic signature: The Mother Wavelet choice. Submitted to the Journal Mechanical System and Signal Processing in October, 2018.

3.5. Fedele R., Praticò F. G., Carotenuto R., and Della Corte F. G. Comparing mother wavelet selection criteria for road pavements NDT monitoring. Presented at ICONFBMP 2019 (7th International Conference on Bituminous

Mixtures and Pavements), 12-14 June, 2019, Thessaloniki, Greece. Accepted for oral presentation.

3.6. Praticò F. G., Fedele R., Merenda M., Carotenuto R., and Della Corte F. G. NDT-based platform for road infrastructures management and decision support in emergency situations. Presented at ICONFBMP 2019 (7th International Conference on Bituminous Mixtures and Pavements), 12-14 June, 2019, Thessaloniki, Greece. Accepted for oral presentation.

3.7. Praticò F. G., Colicchio G., Fedele R., and Briante, P. G. M. Surface properties of porous asphalt concretes: time, position, and treatment impact. Presented at ICONFBMP 2019 (7th International Conference on Bituminous Mixtures and Pavements), 12-14 June, 2019, Thessaloniki, Greece. Accepted for oral presentation.

3.8. Praticò F.G., Astolfi A., and Fedele R. Analysis and modelling of the main causes of unsatisfactory quality of transportation infrastructures. Submitted to the Journal of Construction Engineering and Management in December 2018.

3.9. Fedele R, Praticò F. G., Carotenuto R., Merenda M., and Della Corte F. G. Monitoring infrastructure asset through its acoustic signature. Submitted to the Conference INTERNOISE 2019 in February 2019.

3.10. F.G. Praticò, P.G. Briante, G. Colicchio, and R. Fedele. Optimal design of premium surface courses: methodology and experiments. Submitted to the Journal of Traffic and Transportation Engineering (English Edition) in February 2019.

3.11. Praticò F.G., Naumov V., and Fedele R. Identification and monitoring of concealed cracks in road pavement using a machine-learning approach. Submitted to the Conference MT-ITS 2019, 5-7 June, Kraków, Poland, http://www.mt-its2019.pk.edu.pl/ in February 2019

4. Scientific production – patents

4.1. Carotenuto R., Della Corte F.G., Fedele R., Merenda M., and Praticò F.G. Metodo e sistema per il monitoraggio strutturale di corpi solidi per identificare e monitorare la crescita di anomalie interne (System and method for the structural monitoring of solid bodies to identify and monitor the growth of internal anomalies). Submitted to Ufficio Italiano Brevetti e Marchi (UIBM): 22 November 2017. Patent application number: 102017000133871.